ASC

ASTRO SCIENCES CENTER

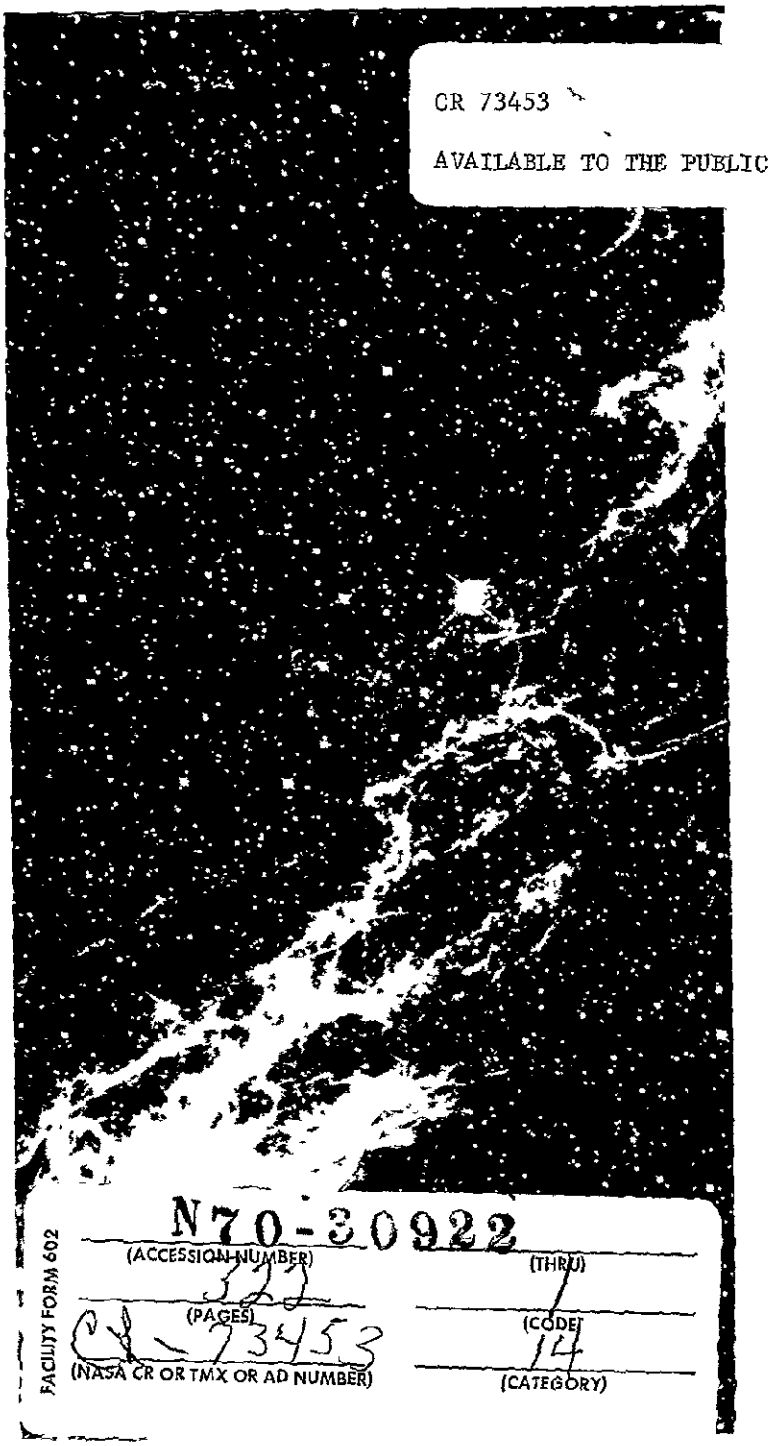

ORBITAL IMAGERY FOR PLANETARY EXPLORATION

VOLUME IV

IMAGING SENSOR SYSTEM SCALING LAWS

IITRI

IIT RESEARCH INSTITUTE

10 West 35 Street
Chicago, Illinois 60616

ORBITAL IMAGERY FOR PLANETARY EXPLORATION

VOLUME IV

IMAGING SENSOR SYSTEM SCALING LAWS

by

D. Klopp

Contributors

H. Borrough
H. Goldman
J.C. Jones
D. Roberts
A. Weigandt

for

Mission Analysis Division
NASA
Office of Advanced Research and Technology
Moffett Field, California

Contract No. NAS2-4494

APPROVED:

D L Roberts

D.L. Roberts, Manager
Astro Sciences Center

September 1969

IIT RESEARCH INSTITUTE

Table of Contents

List of Tables

List of Figures

VOLUME IV

IMAGING SENSOR SYSTEM SCALING LAWS

"Such things and deeds as are
not written down are covered
with darkness, and given over
to the sepulchre of oblivion"

- Ivan Bunin

INTRODUCTION

This volume describes the origin, development, and utilization of scaling laws which characterize the operation of selected imaging sensor systems. These scaling laws permit preliminary design of space-orbital imaging systems with due regard to the nature of the desired imagery and the orbit configuration. Companion volumes to this report are:

Volume I - Technical Summary

Volume II - Definition of Scientific Objectives

Volume III - Orbit Selection and Definition

Volume V - Support Requirements for Planetary Orbital Imaging

The purpose of this study has been to identify the requirements imposed upon spacecraft subsystems by the use of orbital imaging systems in unmanned planetary exploration. Attention has been focused upon the 1975-1995 epoch and the planets Mercury, Venus, Mars and Jupiter. Meaningful experiment support requirements must be based upon an appreciation of those bits of scientific knowledge which can be usefully acquired by imaging systems in planetary orbit. Volume II of this series examines those planetary phenomena which can be observed by remote sensing techniques, and identifies those cases in which orbital imagery can be expected to contribute materially to an understanding of the planets and their history.

Scientific requirements for orbital imagery have been distilled into a table of image specifications presented in Volume I. These specifications set forth, for each planetary phenomenon, the nature of the desired imagery in terms of ground resolution, ground area to be observed, planetary coverage, solar illumination, coverage repetition rate, etc. For each planetary observable, one or more spacecraft orbits has been selected. These orbits are described in Volume III. Each orbit has been selected to provide imagery at the desired solar illumination, repetition rate, etc. The imaging system scaling laws presented in this volume are designed to bridge the gap between the image specifications and orbit description and the requirements demanded of the spacecraft subsystems by the imaging sensor system, as schematically indicated in Figure 1. The scaling laws parametrically describe each type of imaging system in such a manner that the system performance is related both to achievement of the image specifications and to demands imposed upon the spacecraft subsystems.

The types of imaging systems considered have been determined by the spectral bands identified in the image specifications (ultraviolet, visible, infrared, microwave, and radio frequency). Only passive systems, except for microwave (radar), have been considered. In each spectral region, the scaling laws have been developed by collecting empirical and design data and attempting to relate the support requirements to the sensor system characteristics. For example, the weight of a television camera system is found to depend upon the size of the TV image tube. Such empirical relations are, of course, dependent upon the current level of technological capability. Thus the scaling laws reflect the current imaging sensor system state-of-art. In those few cases where an increased capability can be foreseen clearly, the effect of such technological advancements upon the scaling laws have been identified. In general, the experiment support requirements

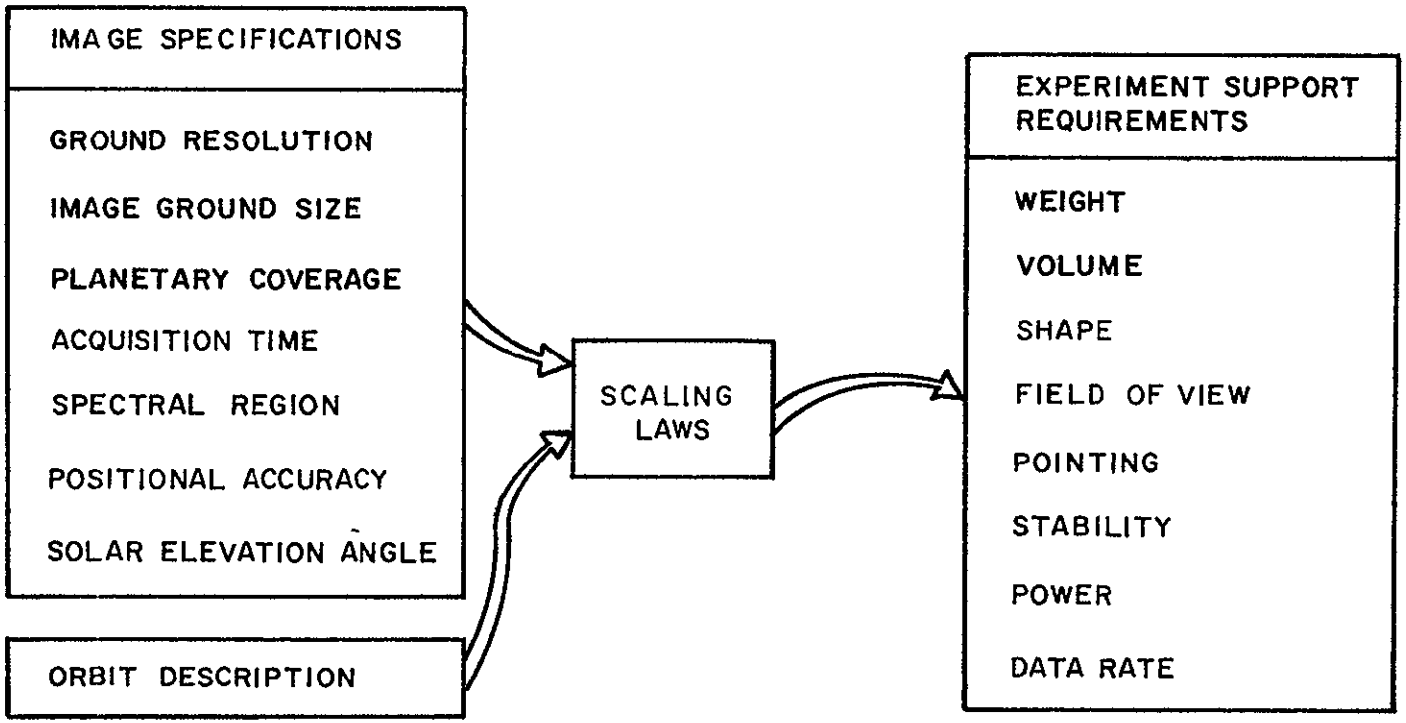

FIGURE I FUNCTION OF SCALING LAWS

cannot be directly related to the image specifications or the orbit parameters, but must be related instead to the sensor system variables, which in turn are related to the image specifications and orbit parameters. For example, radar antenna weight depends upon the antenna size, which depends upon the required ground resolution, the orbit altitude, and the operating frequency. Only the sensor system field-of-view and pointing accuracy requirements can be related directly to the image specifications and orbit parameters. Therefore this volume also presents design equations which relate the sensor system variables to the image specifications and to the orbit parameters for each type of sensor system. Scaling laws and design equations are developed for the following types of imaging systems:

1. ultraviolet scanning
2. television
3. photographic film
4. infrared scanning
5. passive microwave
6. noncoherent radar
7. synthetic aperture radar

Scaling laws and design equations for infrared television systems are contained in a classified appendix to this volume.

Section 1 of this volume presents an analysis of the planet-sensor geometrical relationship, while Section 2 discusses solar radiation reflection and thermal radiation emission as appropriate to imagery of Mercury, Venus, Mars, and Jupiter. Each following section deals with a single type of imaging system, in the order given above. The first part of each sensor system section analyzes the relationships between the image specifications and the sensor system design variables, for that type of imaging system. The second part presents empirical data from which scaling laws relating the sensor system design variables to the support requirements are

developed. Each sensor system section concludes with a logic diagram and a scaling law chart which summarize a suggested procedure for design of the imaging system and estimation of support requirements. The results obtained by use of this procedure are presented in Volume V of this series.

Although the imaging system scaling laws provided here are intended primarily for the estimation of orbital experiment support requirements based on a specific set of image specifications and orbit selections, the scaling laws can be used to identify advances which must be made in imaging system technology if orbital imagery is to be exploited fully as a useful planetary investigative technique. In addition, the scaling laws may be used to compare the efficacy of one spectral region or one type of system to another for acquiring imagery in the study of a specific planetary observable or for achievement of a specific imaging requirement. For example, television systems may be compared to photographic film systems or radar systems. Such comparisons depend, of course, upon the establishment of suitable criteria. As a trivial example, television and film systems are useless in studying surface topography at Venus from orbital altitudes; radar systems should be employed.

The scaling laws may also be used to study tradeoffs in imaging experiment design. For a specific set of image specifications and a specific orbit, various alternatives exist in the design of an imaging system which will achieve the image specifications from that orbit. For example, within well-defined limits the optical aperture stop and the exposure time of a camera system may be adjusted to provide short exposure times at large apertures or long exposure times at small apertures. The small aperture systems tend to weigh less than large aperture systems, while short exposure times imply less stringent platform stability requirements than for long exposure times. That is, system weight may be traded for

platform stability requirements, without influencing achievement of the image specifications. For a specific orbit, the image specifications may be varied to study the dependence of support requirements upon the image specifications. For example, for a fixed altitude the scaling laws may be used to discover how sensor system weight depends upon ground resolution. Alternatively, the system weight may be fixed, and the achievable ground resolution may be determined as a function of orbital altitude. Thus the imaging system scaling laws presented in this volume provide the planetary mission analyst with a powerful tool for mission comparisons and evaluations. The scaling laws are not restricted to orbital sensor systems, and could be used as well for study of flyby and atmospheric probe imaging experiment design.

The imager scaling laws are not intended to be a substitute for detailed experiment design. They are intended to provide representative sensor system configurations, thus permitting estimation of typical support requirements demanded by specific imaging experiments. Scaling laws have been provided only for those types of imaging systems which appear to be particularly useful in planetary exploration from orbit and for which a substantial operational or design experience is available. Unless a sensor system is useful, there is no point in developing scaling laws, and unless the characteristics of a sensor system can be predicted over fairly wide ranges, scaling laws cannot be developed. A number of potentially useful imaging systems (multifrequency radar, radio frequency imagers, and multiband systems) fall into this second category. The potential value of multiband systems, that is, those systems which collect data in more than one spectral region, is clearly established by the analysis of planetary phenomena presented in Volume II. Very little experience exists in the design and use of even multispectral instruments. Therefore no unique set of scaling laws has been developed for multiband systems. A crude,

and perhaps unreliable, estimate of support requirements for specific multiband experiments could be made by using the scaling laws for the different spectral regions and using a common optical or collecting system.

1. ORBITAL VIEWING GEOMETRY

This section discusses the geometrical relationships between the imaging sensor system on board an orbiting spacecraft and the planetary scene viewed by the sensor system. In particular, the relation between angular resolution at the sensor system and ground resolution in the planetary scene is developed for vertically-oriented imagers, vertically-oriented scanning systems, and side-looking systems. The stereo parallax equiations are developed, and finally the dependence of apparent ground velocities upon orbital altitude and velocity is identified.

1.1 Vertically-Oriented Imagers

Figure 1-1 represents a sensor system at a known altitude H above a planetary surface with radius of curvature R, i.e., R is the radius of the planet. Suppose that it is desired to image a square scene of linear dimensions W by W on the planet. The planetocentric half-angle γ subtended by the great-circle arc formed by W on the planetary surface is given by

$$\gamma = \frac{W}{2R} \text{ radians.} \qquad (1\text{-}1)$$

The maximum arc length which can be seen from a given altitude is constrained by the viewing angle ϕ_h to the planetary horizon. If γ_h is the planetocentric angle corresponding to ϕ_h,

$$\sin \phi_h = \cos \gamma_h = \frac{R}{R+H} \; . \qquad (1\text{-}2)$$

Using eq. (1-1), the image ground size is limited by

$$W \leq 2 R \cos^{-1} \frac{R}{R+H} \; . \qquad (1\text{-}3)$$

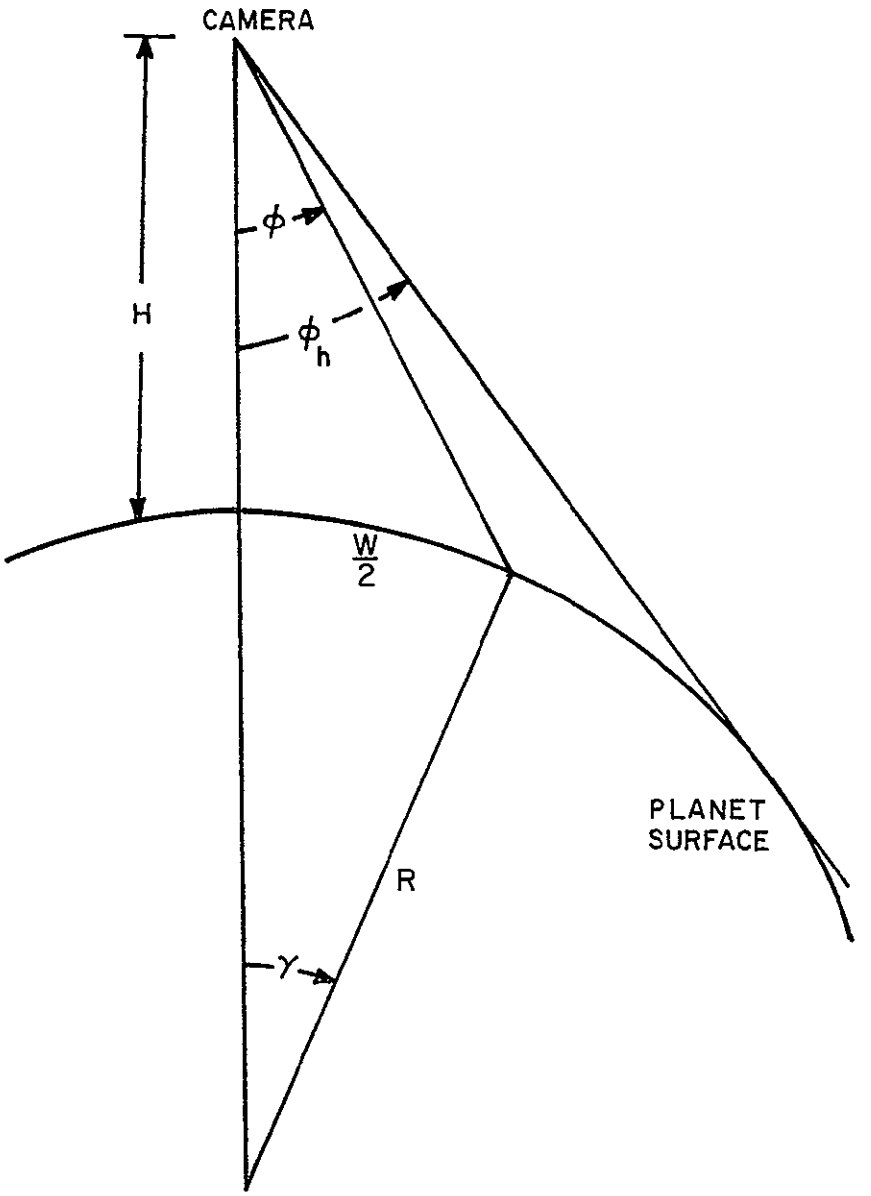

FIGURE 1-1. VERTICAL VIEWING GEOMETRY

In any practical case, the image ground size must be considerably less than the limit given here because of the degradation in scene resolution near the horizon.

Widger[1] has shown how the half-angle field-of-view ϕ is related to W, provided that $\phi \leq \phi_h$. Using Figure 1-1 and the law of sines,

$$\sin(\pi - \phi - \gamma) = \sin(\phi + \gamma) = \frac{R+H}{R} \sin\phi. \quad (1\text{-}4)$$

Solving for ϕ,

$$\phi = \cot^{-1}\left(\frac{R+H}{R \sin\gamma} - \cot\gamma\right). \quad (1\text{-}5)$$

Thus for a given planet radius R, sensor altitude H, and image size W, eq. (1-1) gives γ and then the required half-angle field-of-view is given by eq. (1-5). For small γ, eq. (1-5) reduces to the flat planet result

$$\phi = \tan^{-1}\frac{W}{2H}. \quad (1\text{-}6)$$

Eq. (1-4) may also be solved for γ in terms of ϕ,

$$\gamma = \sin^{-1}\left(\frac{R+H}{R} \sin\phi\right) - \phi. \quad (1\text{-}7)$$

Differentiating with respect to ϕ,

$$\frac{d\gamma}{d\phi} = \frac{\cos\phi}{\left[\left(\frac{R}{R+H}\right)^2 - \sin^2\phi\right]^{\frac{1}{2}}} - 1 \quad (1\text{-}8)$$

For a sensor system with a fixed angular resolution $\Delta\phi$, this result may be used to show how ground resolution varies with the view angle ϕ. The geometry is shown in Figure 1-2. For small $\Delta\phi$ and $\Delta\gamma$,

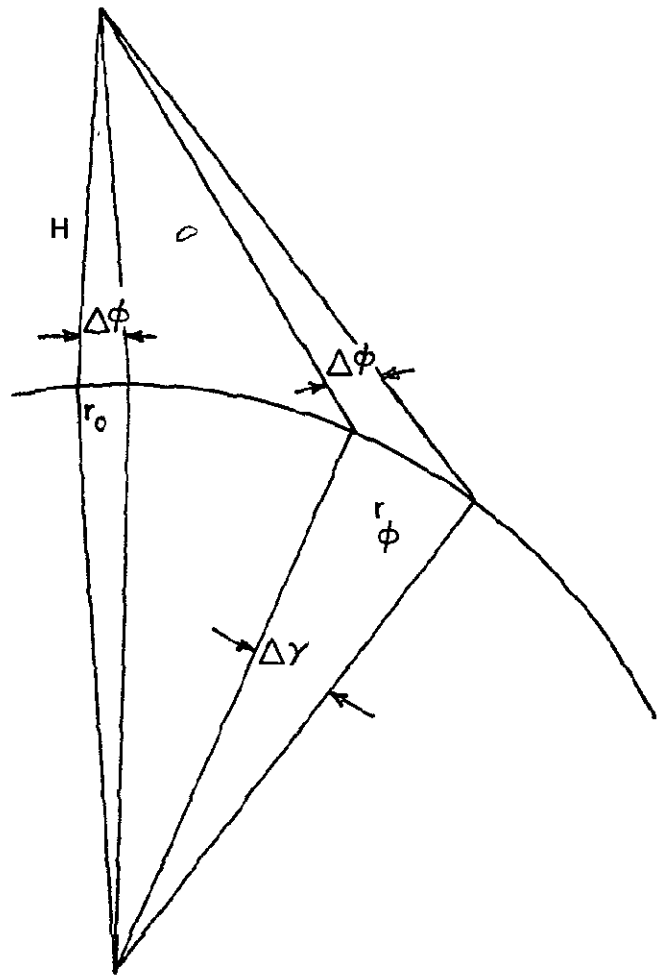

FIGURE 1-2. VARIATION OF RESOLUTION WITH VIEW ANGLE

$$\frac{\Delta\gamma}{\Delta\phi} = \frac{\cos\phi}{\left[\left(\frac{R}{R+H}\right)^2 - \sin^2\phi\right]^{\frac{1}{2}}} - 1 \qquad (1\text{-}9)$$

If r_0 is the ground (scene) resolution corresponding to $\Delta\phi$ at the subsatellite point, and r_ϕ is the ground resolution at the view angle ϕ, then

$$\frac{r_\phi}{r_0} = \frac{R}{H} \cdot \left\{ \frac{\cos\phi}{\left[\left(\frac{R}{R+H}\right)^2 - \sin^2\phi\right]^{\frac{1}{2}}} - 1 \right\}. \qquad (1\text{-}10)$$

It is easily seen that $r_\phi \geq r_0$, i.e., the best resolution is obtained at the subsatellite point and the ground resolution degrades with increasing view angle. For convenience, Table 1-1 gives r_ϕ/r_0 as a function of ϕ and H/R. A non-entry in the table indicates that $\phi > \phi_h$, i.e., ϕ is greater than the view angle to the horizon. If the ground resolution r is desired throughout the entire image of ground size W by W, then the imaging system angular resolution $\Delta\phi$ must satisfy

$$\Delta\phi \leq \frac{r}{H(r_\phi/r_0)} \quad , \qquad (1\text{-}11)$$

where r_ϕ/r_0 is obtained with ϕ equal to the half-angle field of view given by eq. (1-5).

The system angular resolution has been assumed above to be independent of view angle. It will now be shown that this is a reasonable assumption. Consider an imaging system with a vertical optical axis and a sensitive surface, of dimensions ℓ by ℓ, normal to the optical axis. As shown in Figure 1-3, F is the distance from the sensitive surface to the lens, i.e., F is the focal length. From the figure

$$\tan\phi = \frac{\ell}{2F} . \qquad (1\text{-}12)$$

Table 1-1

Values of r_ϕ/r_0

ALTITUDE RADIUS	Half-Angle Field-of-View Ø (Deg.)							
	10	20	30	40	50	60	70	80
0.01	1.03	1.13	1.34	1.72	2.47	4.19	9.66	69.9
0.02	1.03	1.14	1.35	1.74	2.53	4.40	11.2	--
0.03	1.03	1.14	1.35	1.76	2.59	4.64	13.4	--
0.04	1.03	1.14	1.36	1.78	2.65	4.92	17.0	--
0.05	1.03	1.14	1.37	1.80	2.72	5.24	24.1	--
0.06	1.03	1.15	1.38	1.82	2.79	5.61	51.6	--
0.07	1.03	1.15	1.38	1.84	2.87	6.04	--	--
0.08	1.04	1.15	1.39	1.87	2.95	6.58	--	--
0.09	1.04	1.15	1.40	1.89	3.04	7.24	--	--
0.1	1.04	1.16	1.41	1.92	3.13	8.08	--	--
0.2	1.04	1.18	1.50	2.22	4.80	--	--	--
0.3	1.05	1.21	1.60	2.71	27.3	--	--	--
0.4	1.05	1.25	1.74	3.65	--	--	--	--
0.5	1.06	1.28	1.93	6.66	--	--	--	--
0.6	1.07	1.33	2.18	--	--	--	--	--
0.7	1.07	1.38	2.56	--	--	--	--	--
0.8	1.08	1.43	3.22	--	--	--	--	--
0.9	1.09	1.50	4.74	--	--	--	--	--
1.0	1.10	1.58	--	--	--	--	--	--
2.0	1.23	--	--	--	--	--	--	--
3.0	1.49	--	--	--	--	--	--	--
4.0	2.23	--	--	--	--	--	--	--

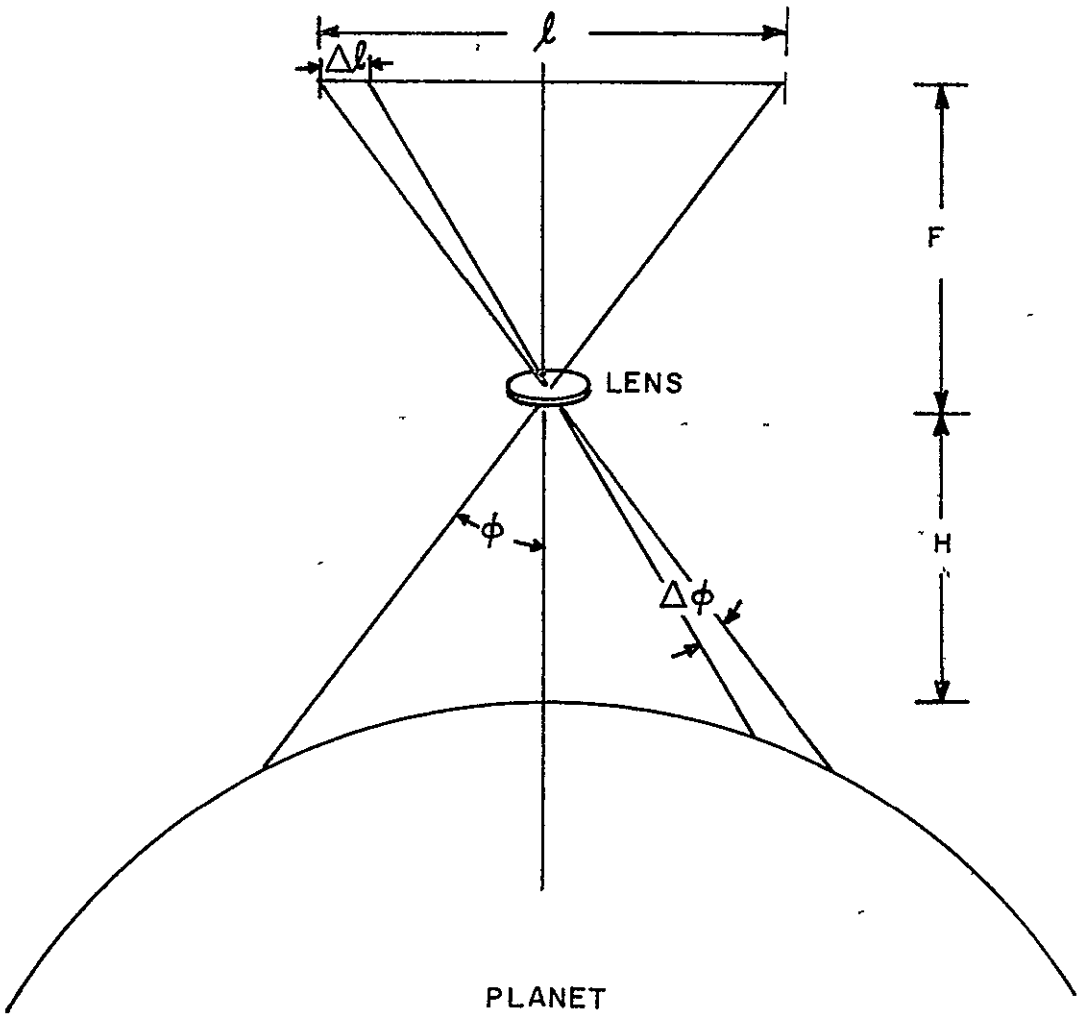

FIGURE 1-3. CAMERA VIEWING GEOMETRY

Solving for ϕ, and differentiating with respect to ℓ,

$$\frac{d\phi}{d\ell} = \frac{\cos^2 \phi}{2F} . \qquad (1\text{-}13)$$

If $\Delta\ell$ is the linear dimension of a resolution element on the sensitive surface, and if $\Delta\ell$ and $\Delta\phi$ are small,

$$\Delta\phi = \frac{\cos^2 \phi}{2F} \cdot \Delta\ell . \qquad (1\text{-}14)$$

Assuming that $\Delta\ell$ is constant across the entire sensitive surface (which is true for silver halide film and nearly so for television cameras), the effect of geometry alone is to improve the sensor system angular resolution in areas of the image farthest from the image center. This purely geometrical effect is opposed by lens distortion in any refractive lens system. For any real lens, the angular resolution capability of the lens degrades rapidly as one moves off the optical axis. It is assumed in this study that, to a first approximation, these two effects counterbalance one another, and hence the sensor system angular resolution is independent of view angle.

1.2 Vertically-Oriented Scanning Systems

The scanning systems considered here operate by scanning the planetary scene with a fixed angular field-of-view in a direction perpendicular to the heading line. The heading line is formed by the instantaneous intersection of the orbital plane with the planetary surface. The direction of flight and the direction of scan are shown in Figure 1-4(a). If W is the length of scan along a great-circle arc, then

$$\gamma = \frac{W}{2R} , \qquad (1\text{-}15)$$

and

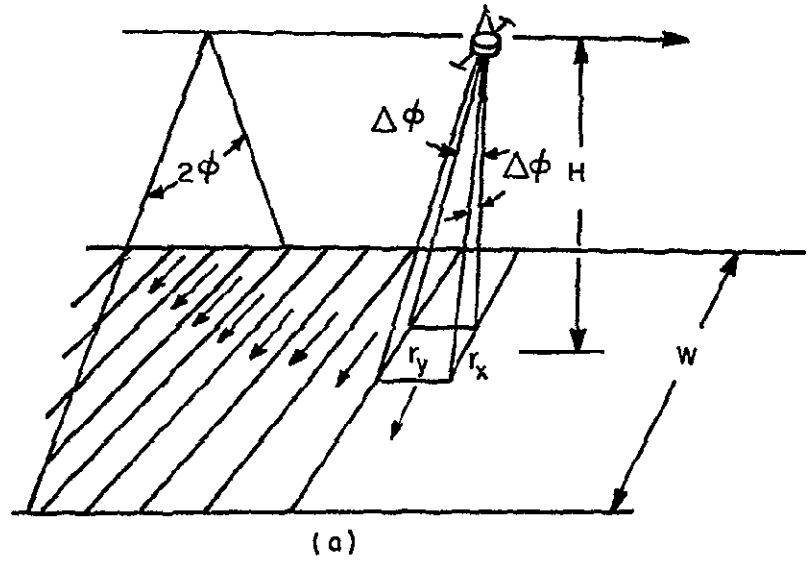

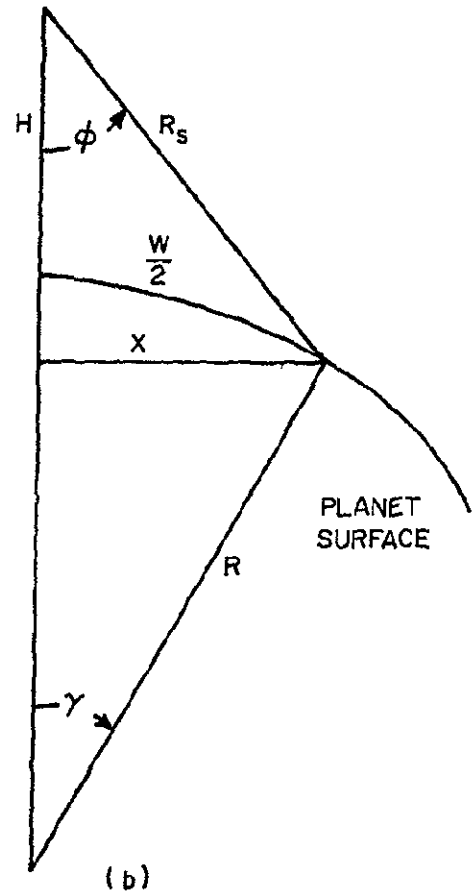

FIGURE 1-4. SCANNING SYSTEM GEOMETRY

$$\phi = \cot^{-1}\left(\frac{R + H}{R \sin \gamma} - \cot \gamma\right) , \qquad (1\text{-}16)$$

as in the previous section. Similarly, if $\Delta\phi$ is the angular size of the scanning beam, and r_x is the corresponding ground resolution normal to the heading line,

$$r_x = \Delta\phi \cdot R \left\{ \frac{\cos \phi}{\left[\left(\frac{R}{R+H}\right)^2 - \sin^2 \phi\right]^{\frac{1}{2}}} - 1 \right\} , \qquad (1\text{-}17)$$

which is obtained from eq. (1-10) by identifying r_x with r_ϕ.

The resolution degradation in the direction parallel to the heading line is not as serious as the resolution degradation normal to the heading line, as given by eq. (1-17). From Figure 1-4(b), the slant range R_s is

$$R_s = \frac{R \sin \gamma}{\sin \phi} . \qquad (1\text{-}18)$$

If r_y is the ground resolution corresponding to $\Delta\phi$, parallel to the heading line, then

$$r_y = \Delta\phi \cdot R_s . \qquad (1\text{-}19)$$

Thus

$$r_y = \frac{\Delta\phi \cdot R \sin \gamma}{\sin \phi} , \qquad (1\text{-}20)$$

and it can be shown that $r_y \leq r_x$. If r is the ground resolution required throughout the entire scan line, the sensor system angular resolution is constained by

$$\Delta\phi \leq \frac{r}{H(r_\phi / r_0)} , \qquad (1\text{-}21)$$

as in the previous section, where r_ϕ/r_0 has been given by eq. (1-10) and Table 1-1.

1.3 Side-Looking Systems

Consider a side-looking sensor system at an altitude H above the planetary surface, as shown in Figure 1-5. The field-of-view in the plane normal to the heading line is β_r, while in the plane parallel to the heading line it is β_a. The great-circle arc-length W subtends the angle β_r at the sensor system and the angle $\gamma_2 - \gamma_1$ at the planet center. The sensor system field-of-view is depressed an angle α from the local horizontal plane. The depression angle to the horizon is easily found to be

$$\alpha_h = \cos^{-1}\left(\frac{R}{R+H}\right) . \qquad (1\text{-}22)$$

If the horizon is not to be included in the image, clearly $\alpha < \alpha_h$.

The field-of-view β_r is related to the image size W, the altitude H, the planet radius R, and the depression angle α. Using the diagram and the law of sines,

$$\frac{H + R}{\sin\left(\frac{\pi}{2} + \Psi_2\right)} = \frac{R}{\sin\left(\frac{\pi}{2} - \alpha\right)} = \frac{R_2}{\sin \gamma_2} , \qquad (1\text{-}23)$$

where Ψ_2 is the grazing angle at the far edge of the field-of-view, and R_2 is the slant range to the far edge. Solving for R_2 and Ψ_2,

$$R_2 = \frac{R \sin \gamma_2}{\cos \alpha} , \qquad (1\text{-}24)$$

$$\Psi_2 = \cos^{-1}\left(\frac{R+H}{R} \cos \alpha\right). \qquad (1\text{-}25)$$

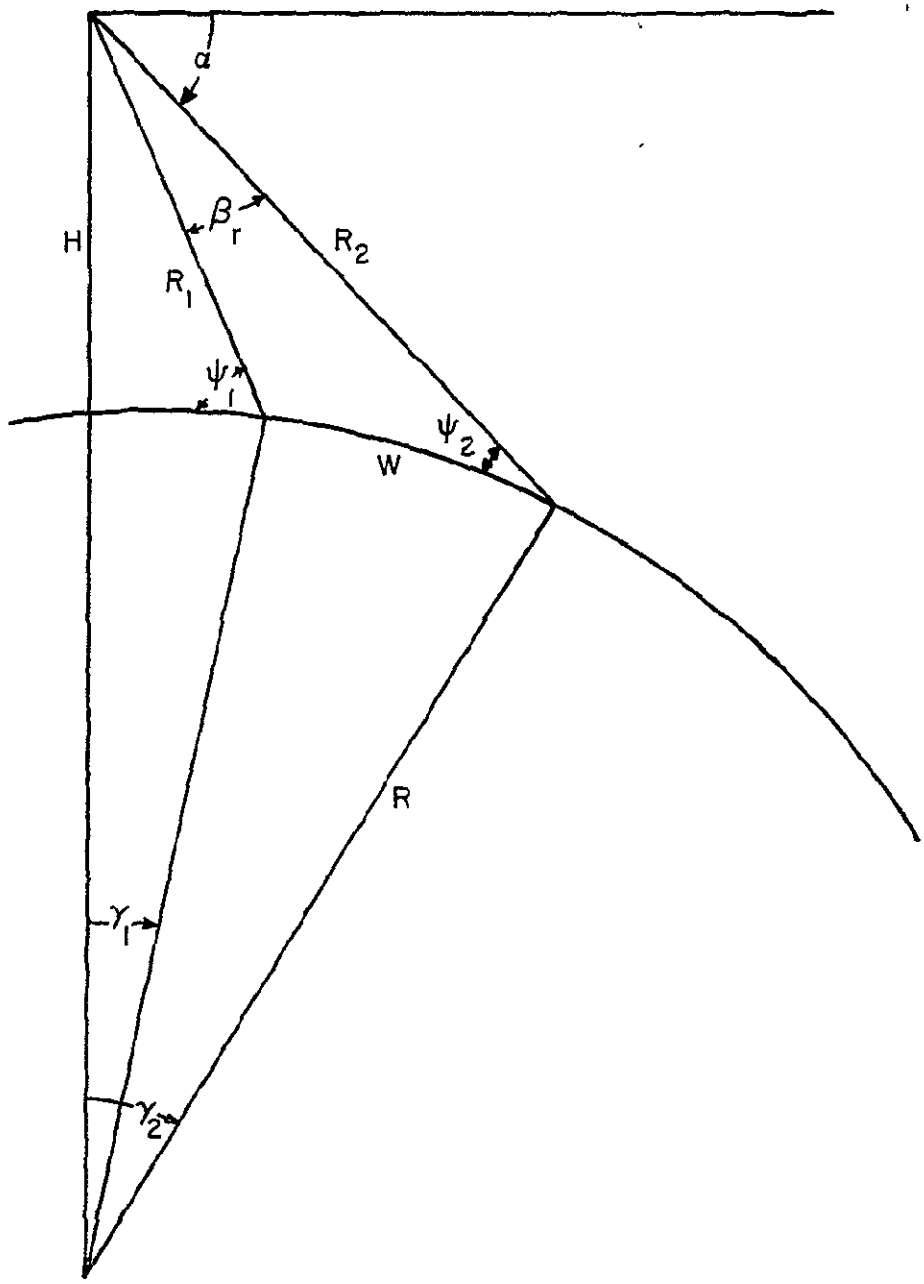

FIGURE I-5. SIDE-LOOKING GEOMETRY

The angle γ_2 may be found by summing the angles in a triangle to find

$$\gamma_2 = \alpha - \Psi_2 . \tag{1-26}$$

Again using the law of sines,

$$\frac{W'}{\sin \beta_r} = \frac{R_2}{\sin(\pi - \Psi_1 + \delta)} = \frac{R_1}{\sin(\Psi_2 + \delta)} , \tag{1-27}$$

where W' is the chord length associated with the arc length W, and δ is the angle at the edges of the field of view between the chord W' and the tangent to the arc W. It can be shown that

$$\Psi_1 = \Psi_2 + \beta_r + \frac{W}{R} . \tag{1-28}$$

Now since

$$W' = 2R \sin \frac{W}{2R} , \tag{1-29}$$

and

$$\delta = \frac{W}{2R} , \tag{1-30}$$

eq. (1-28) may be substituted into eq. (1-27), and some minor manipulation yields

$$\beta_r = \tan^{-1} \left[\frac{W' \sin(\Psi_2 + \delta)}{R_2 - W' \cos(\Psi_2 + \delta)} \right] . \tag{1-31}$$

For a flat planet, it can be shown that this reduces to

$$\beta_r = \tan^{-1} \left(\frac{W \sin^2 \alpha}{H - W \sin \alpha \cos \alpha} \right) . \tag{1-32}$$

For completeness, it may be noted that if β_a, the field-of-view in the plane parallel to the heading line, is to subtend the great-circle arc W at the slant range R_1, then

$$\beta_a = 2 \sin^{-1} \left[\frac{\sin \beta_r}{2 \sin(\Psi_2 + \delta)} \right] . \qquad (1\text{-}33)$$

This field-of-view will, of course, subtend a great-circle arc longer than W at the slant range R_2.

If the sensor system has a fixed angular resolution $\Delta\phi$, then the poorest resolution in the image will occur along the direction normal to the heading line and at the slant range R_2. As in the previous sections, if r is the desired ground resolution, then

$$\Delta\phi \leq \frac{r}{H(r_\phi/r_0)} , \qquad (1\text{-}34)$$

where r_ϕ/r_0 is evaluated at $\phi = \pi/2 - \beta_r - \alpha$.

1.4 Stereo Parallax

Vertical relief information on the planetary surface may be deduced from image measurements of shadows or from stereo parallax. Suppose it is desired to detect vertical height differences of h on the planetary surface. Stereo parallax is achieved by acquiring images from different positions (1 and 2) on the same side of the target, as shown in Figure 1-6(a), it is seen from similar triangles, that

$$\frac{P_1}{h} = \frac{S_1 + P_1}{H} , \qquad (1\text{-}35)$$

and

$$\frac{P_2}{h} = \frac{S_2 + P_2}{H} , \qquad (1\text{-}36)$$

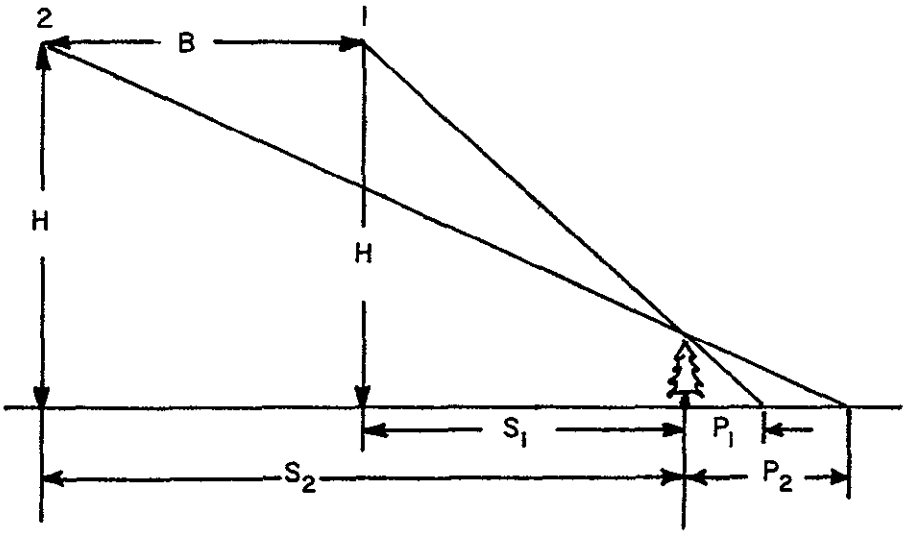

(a) ONE-SIDED MODE

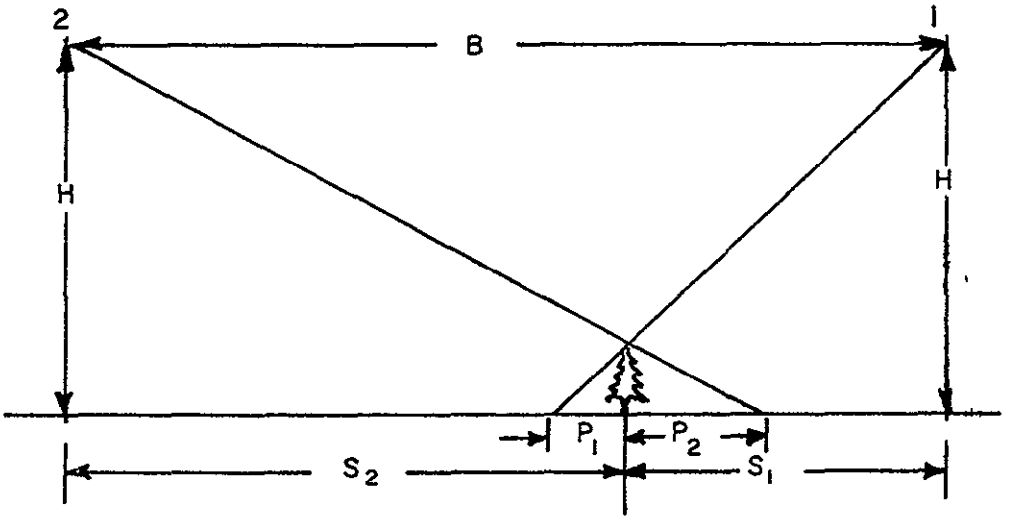

(b) TWO-SIDED MODE

FIGURE 1-6. STEREO GEOMETRY

where S_1 is the ground range of the target from position 1, P_1 is the apparent "length" of the target as viewed in the image acquired from position 1, and similarly for S_2 and P_2. Solving eq. (1-35) for S_1, substituting the result into eq. (1-36), and solving for h,

$$h = \frac{H(P_2 - P_1)}{B + P_2 - P_1} , \tag{1-37}$$

where B is the "base length" defined as $S_2 - S_1$. If ΔP is the parallax difference $P_2 - P_1$, and if the parallax difference is much smaller than the base length,

$$\frac{h}{H} = \frac{\Delta P}{B} . \tag{1-38}$$

Thus if the vertical resolution desired in the imagery is r_v, and r_g is the ground (horizontal) resolution required to achieve the desired vertical resolution by stereo parallax, then,

$$r_g = \frac{Br_v}{H} . \tag{1-39}$$

In many operational situations, this resolution will control the image. That is, in many cases where both a horizontal and vertical resolution have been given by the image specifications, the ground resolution computed by eq. (1-39) will be smaller than the horizontal resolution given in the image specifications.

The stereo parallax equation for the two-sided case illustrated in Figure 1-6(b) is identical to eq. (1-38) derived above, except that the base length B is defined as $S_2 + S_1$. Eq. (1-39) follows as before. The two-sided mode affords a better vertical resolution for a fixed horizontal resolution,

as compared with the one-sided mode, since the base length is longer.

Vertical heights may also be deduced by measuring the lengths of shadows in the imagery. Imagine that the Sun is at position 2 in either figure. The ground length P_2 of the shadow cast by an object of height h is

$$P_2 = h \tan i \ , \tag{1-40}$$

where i is the solar zenith angle (a noon Sun corresponds to zero zenith angle). Thus if vertical resolutions of r_v are desired, the necessary ground (horizontal) resolution is

$$r_g = r_v \tan i \ . \tag{1-41}$$

At low solar elevations, tan i is about 1.3 or greater, and the ground resolution given in the image specifications is usually adequate to achieve the desired vertical resolution.

1.5 Apparent Ground Velocities

The orbiting spacecraft maximum velocity in the local horizontal plane at the spacecraft occurs at periapse and is

$$v_s = \left[\mu \left(\frac{2}{R+H_p} - \frac{1}{a} \right) \right]^{\frac{1}{2}} , \tag{1-42}$$

where μ is the planetary gravitational constant given in Table 1-2, R is the planet radius (also shown in the table), H_p is the orbit altitude at periapse, and a is the semi-major axis of the orbit. In particular

$$a = R + \tfrac{1}{2}(H_p + H_a) \ , \tag{1-43}$$

where H_a is the orbit altitude at apoapse. For a circular orbit, eq. (1-42) reduces to

$$v_s = \left(\frac{\mu}{R + H}\right)^{\frac{1}{2}}. \qquad (1\text{-}44)$$

The maximum horizontal velocity of the subsatellite point, as it moves over the surface of a non-rotating planet in the direction of the heading line, is

$$v_p = \frac{R}{R + H_p} v_s . \qquad (1\text{-}45)$$

The maximum apparent horizontal velocity v_h of the planetary surface as seen by the sensor system (which is regarded as fixed in space) is obtained by adding vectorially the velocity of planetary rotation to v_p. For a planet with posigrade rotation, the result is

$$v_h = (v_p^2 + v_r^2 - 2v_p v_r \cos I)^{\frac{1}{2}}, \qquad (1\text{-}46)$$

where v_r is the equatorial velocity of planet rotation (given in Table 1-2), and I is the orbit inclination. For the Moon, Mercury, and Venus, the rotation rate is sufficiently small that v_r may be neglected in comparison with v_p, and v_h is then equal to v_p.

Table 1-2

Planetary Constants

Planet	μ (km^3/sec^2)	Radius (km)	v_r (km/sec)
Moon	4.903×10^3	1740	--
Mercury	2.169×10^4	2420	--
Venus	3.248×10^5	6100	--
Mars	4.298×10^4	3380	0.2396
Jupiter	1.267×10^8	71,350	12.65

The radial velocity v_v of the spacecraft is given by[2]

$$v_v = \left\{ \frac{\mu[a^2e^2 - (a - r)^2]}{ar^2} \right\}^{\frac{1}{2}}, \qquad (1\text{-}47)$$

where e is the orbit eccentricity, and r is the radial distance from the planet's center to the spacecraft. Of course, v_v vanishes for a circular orbit. For an elliptical orbit, v_v vanishes at periapse, increases with radial distance until reaching a maximum value at the radial distance $a(1 - e^2)$, after which v_v decreases with increasing radial distance, vanishing at apoapse. Thus if $R + H_{max}$ is less than $a(1 - e^2)$, where H_{max} is the maximum altitude from which imagery is to be obtained, the maximum vertical (radial) velocity of the spacecraft during imaging operations is given by eq. (1-47) with r equal to $R + H_{max}$. On the other hand, if $R + H_{max}$ is greater than $a(1 - e^2)$, then the maximum vertical velocity during imaging operations is equal to the maximum vertical velocity attained by the spacecraft during orbit,

$$v_{v,max} = \left[\frac{\mu e^2}{a(1 - e^2)} \right]^{\frac{1}{2}}. \qquad (1\text{-}48)$$

In any case, the effect of a vertical velocity during acquisition of an image is an apparent horizontal motion of points near the periphery of the image towards or away from the apparent center of the image. That is, the imaged area grows larger as the spacecraft climbs and smaller as the spacecraft dives.

2. PLANETARY REFLECTION AND EMISSION

Both active and passive imaging sensor systems are useful in achieving the scientific objectives of planetary exploration. Active systems (e.g., radar) direct a source of electromagnetic energy toward the planetary surface. The sensor system receiver then detects the amount of energy reflected from the planet in the direction of the receiver. Passive systems detect solar radiation reflected from the planet, or thermal radiation emitted by the planet. Passive systems tend to be smaller, lighter, and consume less power than active systems, but are frequently subject to operational constraints, such as requiring adequate solar illumination of the planetary scene. This section deals with the computation of the amount of solar and thermal energy emanating from the planetary scene. Radar reflectivity of planetary surfaces is discussed in the sections of this volume treating radar imaging systems.

2.1 Reflected Solar Energy

Imagery of the planets can be obtained by detecting reflected solar energy of wavelengths from about 2000 Å to 2 or 2.5 microns. Other energy sources which might be detected are excitation emission of discrete spectral lines and luminescence or fluorescence of lunar-type minerals. These extraneous sources are not considered here. At wavelengths shorter than 2000 Å, there is little solar energy available for reflection from the planets (and fortunately no obvious imaging requirements which cannot be just as well performed above 2000 Å), while at wavelengths longer than 2 microns in the case of Mercury, and 2.5 microns in the case of Mars and the Moon, thermally emitted radiation interferes with detection of reflected solar radiation, thus complicating interpretation of the imagery.

The solar energy spectrum is peaked at about 4800 Å. The spectral energy distribution[3] at one astronomical unit

(AU) from the sun is shown in Figure 2-1. In the visible and ultraviolet portion of the spectrum, a number of emission and absorption lines are evident. The solar irradiance is expected to be inversely proportional to the square of the planet's distance from the Sun. Thus the solar irradiance at Jupiter, whose average distance from the Sun is 5.2 AU, is about one-twentyfifth of the irradiance shown in the figure. This may be a slight overestimate of the irradiance in the case of Jupiter, since there may be some screening or absorption of solar energy by the asteroid belt.

The amount of solar energy per unit time reflected by the observed scene per unit area per unit solid angle is[4]

$$I(i, \epsilon, \alpha, \lambda) = \frac{H(\lambda)}{\pi} a(\lambda) f(i,\epsilon,\alpha) \cos \epsilon \ , \qquad (2\text{-}1)$$

where I is the spectral radiance, $H(\lambda)$ is the solar spectral irradiance, $a(\lambda)$ is the surface normal albedo, and f is the photometric function of the surface. In addition to the physical properties of the surface, and the wavelength of the incident radiation, the photometric function depends upon the angle of incidence i, (measured from the normal to the surface), the angle of reflection ϵ, and the luminance longitude α defined as shown in Figure 2-2. For vertical viewing of a planetary scene from orbital altitude, both the angle of reflection and the luminance longitude may be taken as zero. In this case, the phase angle g (as defined in the figure) is identical to the angle of incidence.

Rennilson et al.[5] have reported the lunar photometric function as measured in the visible portion of the spectrum by Surveyor I. The results are shown in Figure 2-3, along with a zero luminance longitude photometric function deduced from Earth-based measurements by Orlova[6], as quoted by Burkhard and Ashby[4]. Also shown for comparison is the zero luminance longitude photometric function for a Lambertian

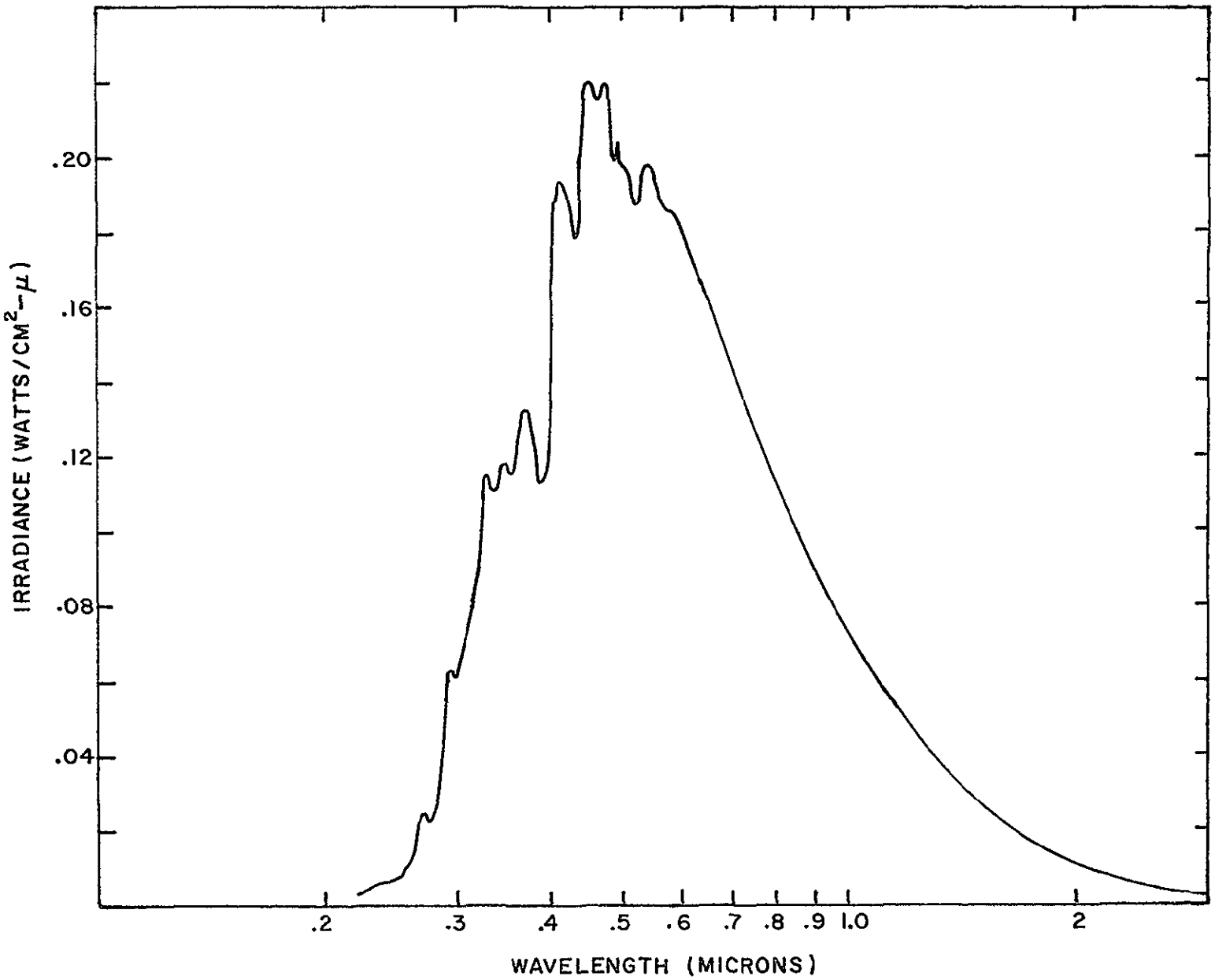

FIGURE 2-1. SOLAR SPECTRAL IRRADIANCE AT ONE AU.

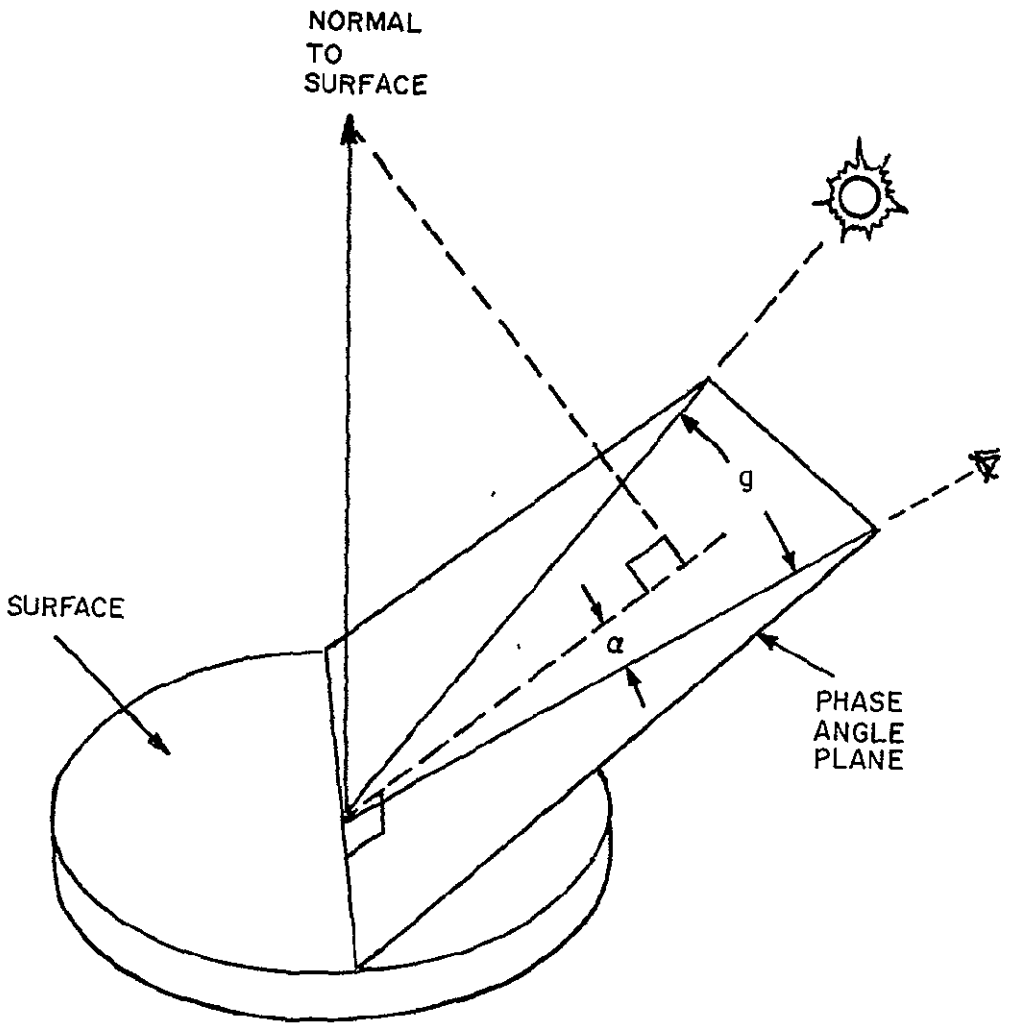

FIGURE 2-2. PHOTOMETRIC FUNCTION GEOMETRY

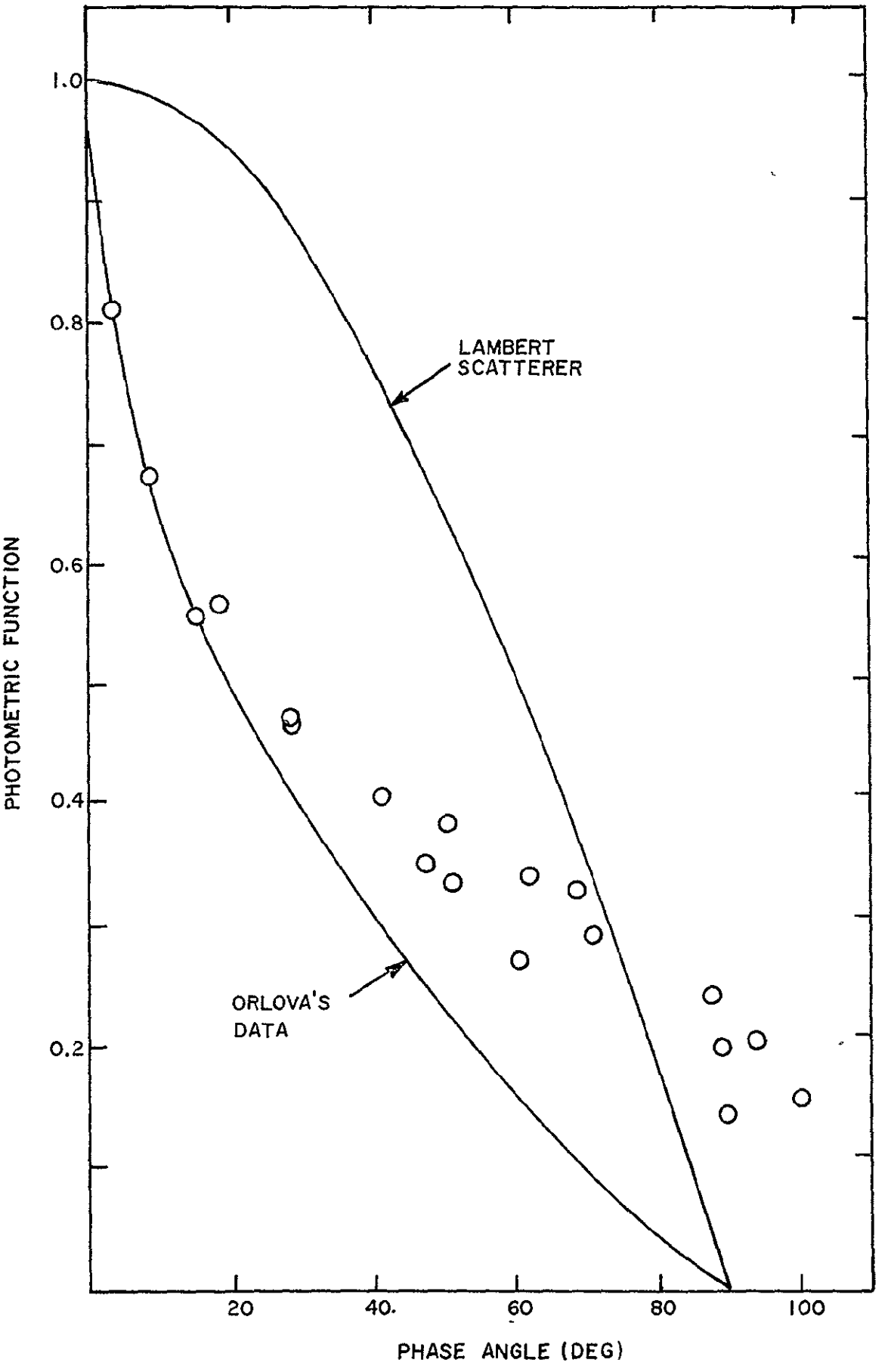

FIGURE 2-3. LUNAR PHOTOMETRIC FUNCTION

surface. Clearly, the lunar surface is poorly approximated by a Lambert scatterer. There is good agreement between the Surveyor I data (shown by the experimental points) and Orlova's data, since the Surveyor data was obtained at luminance longitudes ranging from -30° to -80° and therefore should result in larger values than the zero luminance longitude photometric function, particularly for phase angles larger than 30°. This conclusion is based on a lunar photometric model due to Hapke[7,8], who regards the surface as composed of dark material containing a large proportion of void holes or tunnels. Without specific evidence to the contrary, it is assumed here that all planetary surfaces, which can be imaged from orbital altitudes, have photometric functions identical to that of the lunar surface.

For Venus and Jupiter, the incident solar radiation is absorbed or reflected by the atmosphere. That is, no solar radiation which might be reflected from the surface can be observed from orbital altitude. Therefore, the lunar photometric function should not be used in estimating planetary scene radiance for Venus and Jupiter. Unfortunately, no photometric function has been observed for other than the Earth and the Moon. Measurements are available for the phase function, which is essentially the integral of the photometric function over the visible disk as seen from the Earth. Figure 2-4 shows a comparison of the measured phase function of Venus in the visible portion of the spectrum, as deduced by Harris[9] from Danjon's measurements[10], to the phase function for a Lambert scatterer. The fractional error in assuming a Lambertian surface is large at large phase angles where the phase function is dominated by the contribution from large angles of reflection. However, large angles of reflection are inappropriate for imagery from orbit. Therefore when the planetary scene radiance is dominated by atmospheric reflection, the radiance may be approximated by assuming a Lambert scatterer.

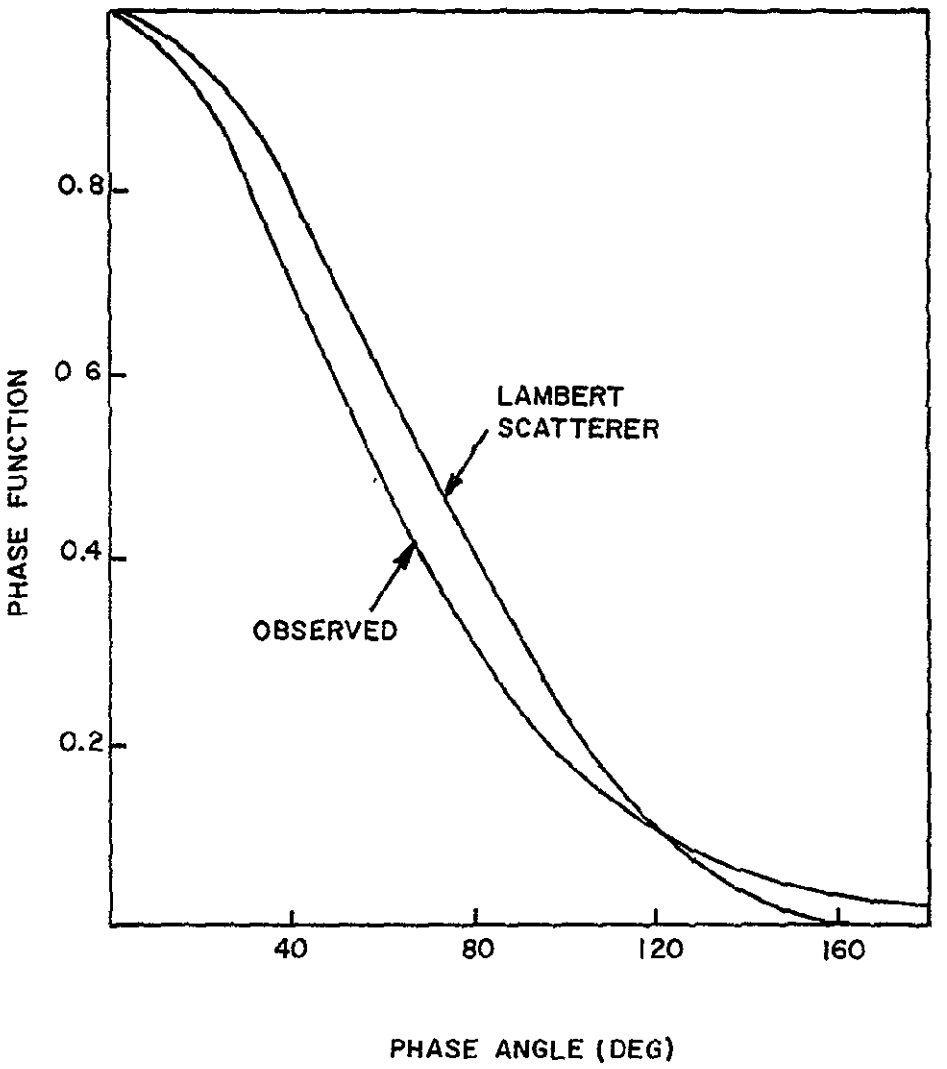

FIGURE 2 - 4 VENUS PHASE FUNCTION

That is, the photometric function is taken as cos i, where i is the angle of incidence (equal to the solar zenith angle for a flat surface). Table 2-1 indicates the preferred approximation to the scene photometric function for different planets and different regions of the spectrum.

Table 2-1

Planetary Photometric Functions

Planet	Spectral Region		
	UV	Visible	Near IR
Moon	Fig. 2-3	Fig. 2-3	Fig. 2-3
Mercury	Fig. 2-3	Fig. 2-3	Fig. 2-3
Venus	cos i	cos i	cos i
Mars	cos i	Fig. 2-3	Fig. 2-3
Jupiter	cos i	cos i	cos i

The remaining factor required to estimate scene radiance by eq. (2-1) is the normal albedo $a(\lambda)$, which is the surface reflectivity for normal angles of incidence and reflection. Unfortunately, the normal albedo is known only for the Moon, and then in the visible spectral band. Burkhard and Ashby[4] have examined data from several sources and conclude that the average visible normal albedo for the Moon is 0.106. Normal albedoes for specific areas range from 0.50 - 0.65 in the Ocean of Storms to 0.13 at Clavius.

Other types of albedoes have been measured or deduced for the planets. The geometric albedo p is the ratio of the luminous intensity of the planet at full phase ($g = 0$) to that of a Lambert disk of equal diameter normally

illuminated. For Lambertian planetary surfaces, the geometric albedo is equal to the normal albedo. The geometric albedoes of the planets have been determined in standard spectral bands defined by specified filter-photodetector combinations. The symbols and effective wavelengths for these standard bands[11] are given in Table 2-2. Geometric albedoes in these bands have been given by Harris[9] and de Vaucouleurs[11], and are shown in Figure 2-5. More detailed measurements[12] have been made for the Moon and Mars and these data are shown by the solid lines in the figure. The increasing albedo for Mars below 0.4 microns is presumably due to Rayleigh scattering in the atmosphere. This effect is probably absent for the Moon and Mercury, but does occur at Venus and Jupiter. In fact, Jenkins[13] has found that, for Venus, the albedo increases with decreasing wavelength from 0.3 microns to 0.22 microns, with a decrease at shorter wavelengths due to absorption by an unknown trace atmospheric compound. A similar increase in the albedo occurs for Jupiter[13,14].

Table 2-2

Effective Wavelengths of Standard Spectral Bands

Symbol	Effective Wavelength (microns)
U'	0.33
U	0.37
B	0.445
V	0.555
R	0.69
I	0.82

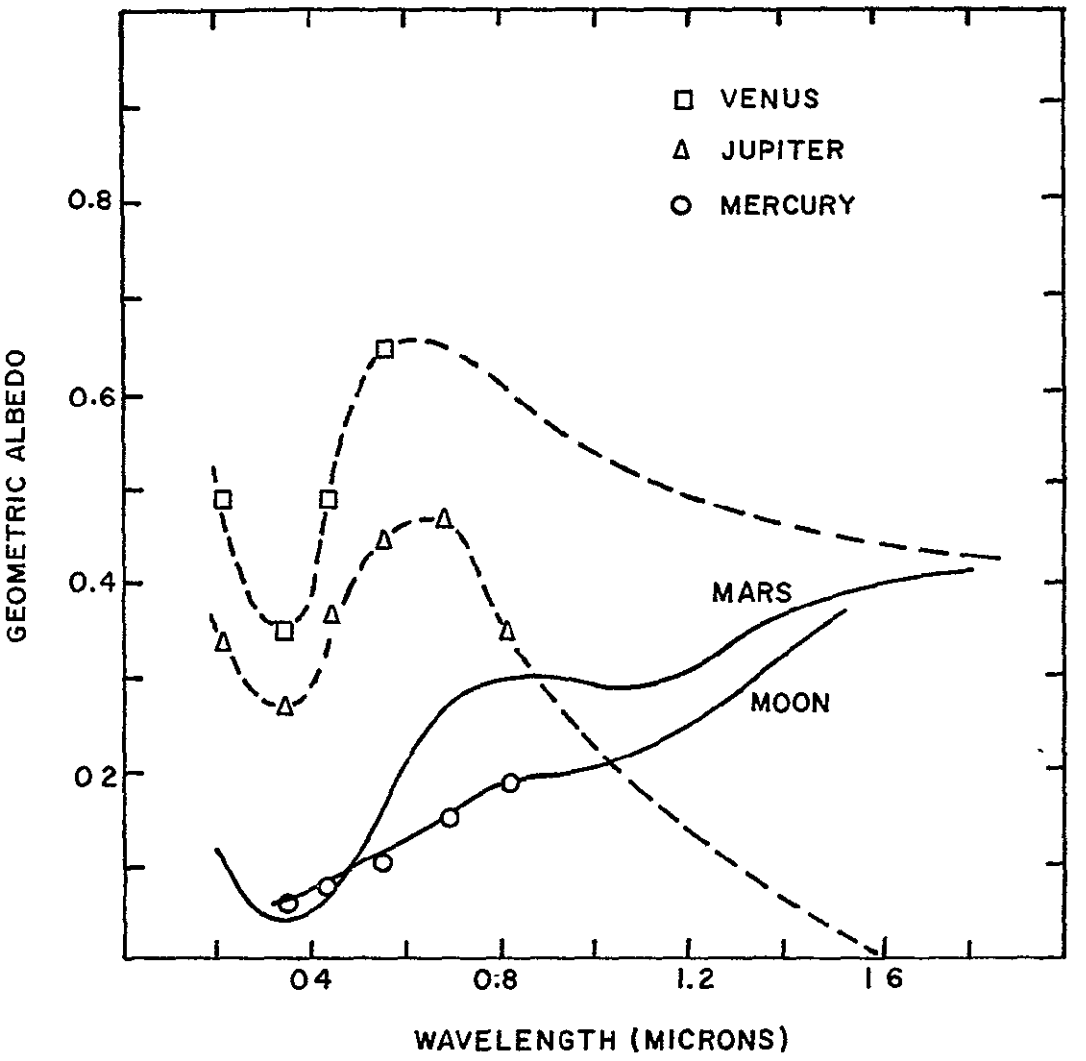

FIGURE 2-5. PLANETARY ALBEDOES

Virtually no data is available in the near infrared for Mercury, Venus, and Jupiter. Hayakawa et al.[15] have obtained lunar albedoes ranging from 0.3 to 0.6 at about 2.2 microns, depending upon the specific area under observation. The dashed curves shown in the figure are extrapolated into the infrared on the basis of preliminary data from Binder[16].

For accurate computations, eq. (2-1) should be used to obtain the spectral radiance as a function of wavelength. In this study, however, averages over broad spectral bands have been used. The spectral regions of interest are the ultraviolet 0.2-0.4 micron band, the visible 0.4 - 0.7 micron band, and the near infrared 1 - 2.5 microns (or 2 microns in the case of Mercury). Averages of the solar irradiance at one AU, and planetary albedoes over these spectral bands, are given in Tables 2-3 and 2-4.

Table 2-3

Average Solar Irradiance (watts/cm^2)
at one Astronomical Unit

Spectral Band		
UV	Visible	Near IR
0.0126	0.0557	0.0322 (1-2 μ) 0.0347 (1-2.5 μ)

Table 2-4

Average Planetary Albedoes

Planet	Spectral Band UV	Visible	Near IR
Moon	0.07	0.11	0.30
Mercury	0.07	0.10	0.30
Venus	0.35	0.65	0.50
Mars	0.05	0.15	0.35
Jupiter	0.27	0.45	0.15

2.2 Thermally Emitted Energy

The spectral radiant emittance of a black body, i.e., a perfect radiator, is given by Planck's law,

$$R(\lambda,T) = \frac{2\pi c^2 h}{\lambda^5[\exp(hc/\lambda kT)-1]} \qquad (2\text{-}2)$$

where

R = black body spectral radiant emittance,
λ = wavelength of emitted energy,
T = temperature of emitting surface,
c = speed of light (3×10^8 meters/sec),
h = Planck's constant (6.626×10^{-34} joule sec),
k = Boltzmann's constant (1.381×10^{-23} joule/deg K).

The spectral radiant emittance is the power radiated in the wavelength interval from λ to $\lambda + d\lambda$ into a hemisphere, per unit area of radiating surface. By integrating eq. (2-2) over all wavelengths from zero infinity, the Stefan-Boltzmann

law is obtained. That is, the power per unit area radiated into a hemisphere by a blackbody is σT^4, where σ is the Stefan-Boltzmann constant equal to 5.669×10^{-8} watts/meter^2-deg K^4.

Because $R(\lambda,T)$, as expressed by eq. (2-2), cannot be integrated directly in closed form over a finite wavelength interval, various approximations are often made[17]. At high temperatures or long wavelengths, more rigorously whenever $hc/\lambda kT$ is sufficiently small that $\exp(hc/\lambda kT)$ can be approximated by $1 + (hc/\lambda kT)$, eq. (2-2) reduces to

$$R(\lambda,T) \simeq \frac{2\pi ckT}{\lambda^4} \quad , \tag{2-3}$$

which is the Rayleigh-Jeans approximation. At low temperatures or short wavelengths, more rigorously whenever $hc/\lambda kT$ is sufficiently large that $\exp(hc/\lambda kT)$ is much larger than unity, eq. (2-2) reduces to

$$R(\lambda,T) \simeq 2\pi c^2 h\lambda^{-5} \exp(-hc/\lambda kT) \quad , \tag{2-4}$$

which is the Wien approximation. Both of these expressions can be easily integrated over an arbitrary wavelength interval. Although it has been reported[18] that at λT equal to about 2×10^4 micron-deg K the Rayleigh-Jeans approximation is ten percent too large, and the Wien approximation is ten percent too small, these error estimates appear to be unduly optimistic. A simple calculation will show that at λT equal to about 1.37×10^4 micron-deg K the Rayleigh-Jeans and Wien approximations have equal errors, of about fifty percent, but of opposite sign. The Rayleigh-Jeans approximation is good to within ten percent for λT greater than 2.7×10^5 micron-deg K, while the Wien approximation is good to within ten percent for λT less than 6×10^3 micron-deg K. It may be noted, however, that the error in integration over any appreciable wavelength interval will be less than the maximum error of the integrated function within the interval. Therefore, eq. (2-3) is preferred above

λT equal to 1.37×10^4 micron-deg K, and eq. (2-4) is preferred below.

For a black body, the spectral radiance is

$$N(\lambda,T) = \frac{1}{\pi} R(\lambda,T) \cos \epsilon \ , \qquad (2\text{-}5)$$

where ϵ is the angle of emittance measured from the normal to the surface. The spectral radiance is the power per unit wavelength per unit solid angle radiated by a unit area of surface.

In practice, the quantity of interest is the difference in radiance between two surface resolution elements of slightly different temperatures. Thus, if two adjacent, small, black body areas are observed from sufficiently far away that differences in the angle of emittance are negligible, and if one area is at the temperature T and the other at $T + \Delta T$, the resulting difference in radiance over the spectral region from λ_1 to λ_2 is

$$\Delta N = \frac{\cos \epsilon}{\pi} \int_{\lambda_1}^{\lambda_2} [R(\lambda,T + \Delta T) - R(\lambda,T)] \, d\lambda \ . \qquad (2\text{-}6)$$

If ΔT is small,

$$R(\lambda,T + T) - R(\lambda,T) \simeq \frac{\partial R(\lambda,T)}{\partial T} \cdot \Delta T \ , \qquad (2\text{-}7)$$

and hence

$$\Delta N = \frac{\Delta T \cos \epsilon}{\pi} \int_{\lambda_1}^{\lambda_2} \frac{\partial R(\lambda,T)}{\partial T} \, d\lambda \ . \qquad (2\text{-}8)$$

The error in using eq. (2-8), rather than the more correct eq. (2-6), has been evaluated for typical temperature and spectral

bands of interest. Even for ΔT for 5 deg K, eq. (2-8) gives results well within ten percent of the values resulting from use of eq. (2-6). Thus, using the Rayleigh-Jeans approximation,

$$\Delta N = \frac{2}{3} ck\, \Delta T \cos \epsilon \left(\frac{1}{\lambda_1^3} - \frac{1}{\lambda_2^3} \right) , \qquad (2\text{-}9)$$

and using the Wien approximation,

$$\Delta N = 2\, kc \left(\frac{kT}{hc}\right)^3 \Delta T \cos \epsilon \left[e^{-x} (x^4 + 4x^3 + 12x^2 + 24x + 24) \right]_{x_1}^{x_2} , \qquad (2\text{-}10)$$

where

$$x_i = \frac{hc}{\lambda_i kT} . \qquad (2\text{-}11)$$

The development above leading to eqs. (2-9) and (2-10) has ignored the spectral sensitivity of the sensor system, and hence is valid only for the case where the sensor sensitivity is independent of wavelength throughout the pass band from λ_1 to λ_2. For many sensors, the sensitivity is proportional to λ, in which case the quantity of interest is

$$\Delta(N\lambda) = \frac{\Delta T \cos \epsilon}{\pi} \int_{\lambda_1}^{\lambda_2} \frac{\partial R(\lambda, T)}{\partial T} \lambda d\lambda . \qquad (2\text{-}12)$$

Using the Rayleigh-Jeans approximation yields

$$\Delta(N\lambda) = ck\, \Delta T \cos \epsilon \left(\frac{1}{\lambda_1^2} - \frac{1}{\lambda_2^2} \right) , \qquad (2\text{-}13)$$

while the Wien approximation gives

$$\Delta(N\lambda) = 2kc \left(\frac{kT}{hc}\right)^2 \Delta T \cos \epsilon \left[e^{-x}(x^3 + 3x^2 + 6x + 6x)\right]_{x_1}^{x_2} , \qquad (2\text{-}14)$$

where x_i is defined above in eq. (2-11).

Application of these results to imagery of planetary scenes presumes that the thermally emitting bodies behave as perfect radiators. All known materials radiate somewhat less energy than would be radiated by a black body at the same physical temperature. The "blackness" of most nonmetallic substances increases with decreasing temperature, and at 350 deg K most nonmetallic substances emit more than eighty percent of the energy emitted by a perfect radiator. Therefore, little error is introduced by regarding the Moon, Mars, and Jupiter as black bodies. Larger errors may result at Mercury, at least on the sunlit side, and Venus. Still, the error introduced by the black body assumption is probably less than the errors introduced by uncertainties in the measured planetary temperatures.

3. ULTRAVIOLET SCANNING SYSTEMS

3.1 Design Equations

The following paragraphs develop the mathematical and physical relations useful in estimating design variables of space-orbital optical-mechanical scanning systems for obtaining imagery in the ultraviolet portion of the spectrum. Section 3.2 presents empirical data useful in estimating support requirements, while Section 3.3 summarizes a logical design procedure for ultraviolet scanning systems.

3.1.1 Scanning Operation

The relationships between sensor system field-of-view and imaged area on the planetary surface, and between sensor system angular resolution and ground resolution parallel to and normal to the heading line, have been discussed in Section 1.2. It was shown that if a great-circle arc-length W on the planetary surface is to be scanned, the total angle through which the scanning beam must rotate is 2ϕ, where

$$\phi = \cot^{-1}\left(\frac{R + H}{R \sin \gamma} - \cot \gamma\right) . \qquad (3\text{-}1)$$

Here R is the radius of the planet, H is the altitude of the sensor system, and γ is W/2R radians. For small values of W/R, eq. (3-1) reduces to the flat planet result,

$$\phi = \tan^{-1}\left(\frac{W}{2H}\right). \qquad (3\text{-}2)$$

The ground resolution r_x normal to the heading line is

$$r_x = \Delta\phi \cdot R\left\{\frac{\cos \phi}{\left[\left(\frac{R}{R+H}\right)^2 - \sin^2 \phi\right]^{\frac{1}{2}}} - 1\right\}, \qquad (3\text{-}3)$$

while the ground resolution r_y parallel to the heading line is

$$r_y = \Delta\phi \cdot R_s = \frac{\Delta\phi \cdot R \sin \gamma}{\sin \phi} \quad . \tag{3-4}$$

Here $\Delta\phi$ is the angular resolution of the sensor system, and R_s is the slant range. If $\Delta\phi$ is independent of ϕ, as has been assumed, both r_x and r_y increase with ϕ. That is, the ground resolution degrades as one moves away from the sub-satellite point. If r is the ground resolution which must be achieved throughout the entire scan, the angular resolution is constrained by

$$\Delta\phi \leq \frac{r}{H(r_\phi/r_0)} \quad , \tag{3-5}$$

where r_ϕ/r_0 has been given in Table 1-1 as a function of ϕ and H/R.

The scanning beam, of angular size $\Delta\phi$ by $\Delta\phi$, is swept across the planetary surface by the rotation of a multi-faced scanning mirror, schematically shown in Figure 3-1. To avoid gaps between successive scan lines on the planetary surface, the distance traveled along the heading line by the sensor in the time taken to scan a single line must be less than the width of the scan line. Thus if t is the time required to scan the great-circle arc-length W, then

$$v_h t \leq H \cdot \Delta\phi \quad , \tag{3-6}$$

where v_h is the apparent speed of the sensor along the heading line. The computation of v_h has been discussed in Section 1.5. If the scanning mirror has m faces,

$$t = \frac{2\pi}{m\omega} \quad , \tag{3-7}$$

where ω is the angular rotation rate (in radians per second)

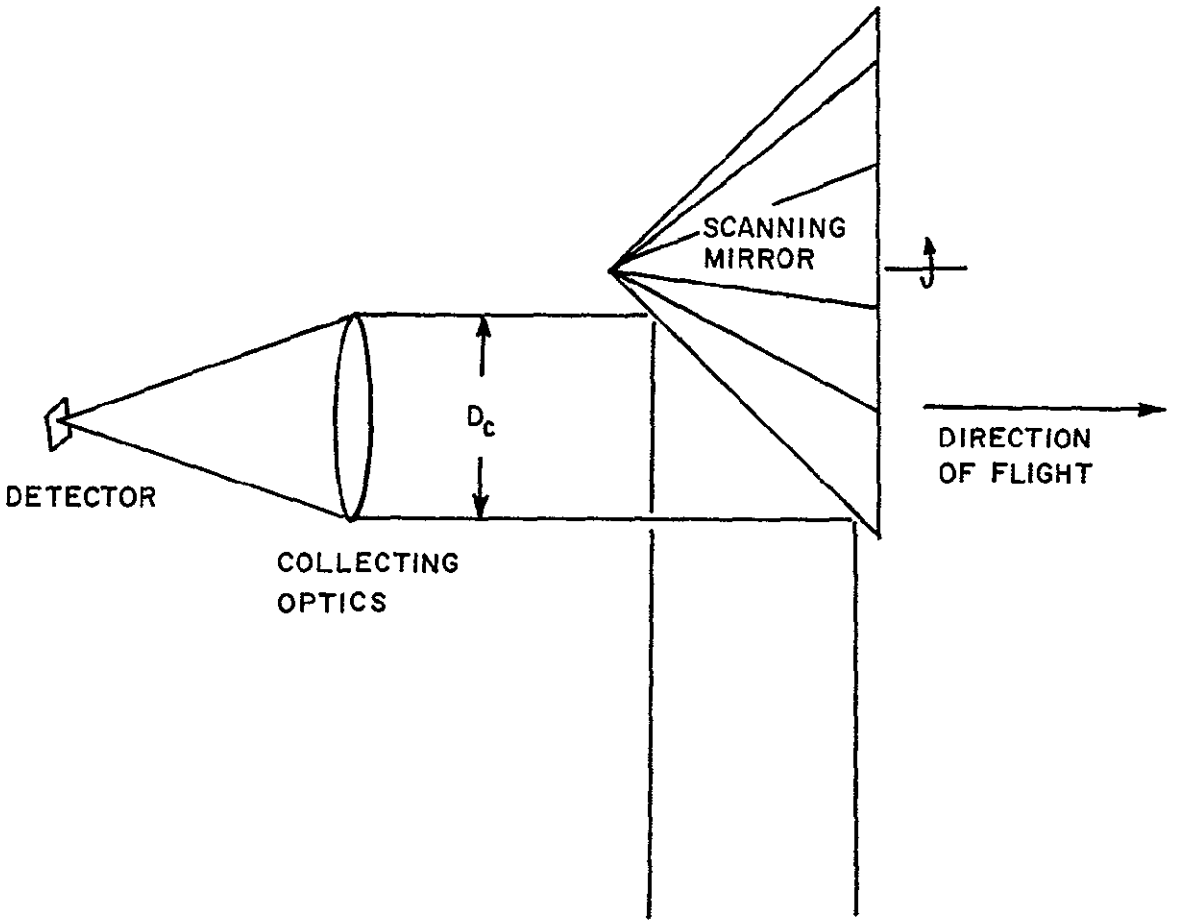

FIGURE 3-1. OBJECT PLANE SCANNING

of the scanning mirror. It should be noted that each face of the scanning mirror observes the planetary scene through a rotation angle of $2\pi/m$ radians, centered on the vertical. If each face is to observe the great-circle arc-length W by rotating through an angle $2\emptyset$, then m must be less than $\pi/\emptyset$. Substituting eq. (3-7) into eq. (3-6), and rearranging, the scanning mirror rotation rate is constrained by

$$\omega \geq \frac{2\pi v_h}{m H \cdot \Delta\emptyset} , \tag{3-8}$$

if gaps are not to appear between the scan lines. A rotation rate larger than the required minimum value will result in some overlap of scan lines. By using more than one detector, multiple scan lines can be swept out simultaneously. Thus for a linear array of p detectors[19],

$$\omega \geq \frac{2\pi v_h}{pm H \cdot \Delta\emptyset} , \tag{3-9}$$

and the rotation rate of the mirror may be reduced from the single detector case.

For some orbital imaging experiments, such as those designed to obtain images of cloud formation, the image specifications given in Volume I indicate that data from all the resolution elements within the scene area (W by W) should be procured in some time interval less than the maximum allowable image acquisition time t_a. Except for exceedingly small values of t_a, the condition expressed by eq. (3-6) suggests that data from a single scan line will be procured in a time interval much less than t_a. However, it is also necessary to procure data from all the scan lines in the scene dimension W <u>along</u> the heading line in a time interval less than t_a. This implies that

$$v_h \, t_a \leq W \, . \tag{3-10}$$

The scanning rate is also constrained by the response time of the detector. That is, if the detector response time is τ, the scanning beam must observe each resolution element on the planetary surface for a length of time longer than τ. It is assumed here that 2τ is a sufficient time, hence

$$\omega \leq \frac{\Delta\phi}{2\tau} \, . \tag{3-11}$$

The rotation rate of the scanning mirror is also limited by distortion of the optically flat surfaces. Chase and Kaisler[20] have studied such mechanical problems, and have shown that the bursting speed of a thin-walled cylinder is

$$\omega = \frac{6.26}{D_s} \left(\frac{S}{\rho}\right)^{\frac{1}{2}} , \tag{3-12}$$

where D_s is the cylinder diameter in meters, S is the yield stress in kg/m^2, and ρ is the wall density in kg/m^3. Representative values of S/ρ are 1.78×10^4 meters for aluminum, 1.52×10^4 meters for beryllium, and 6.35×10^3 meters for stainless steel. Assuming that the scanning mirror may be treated as a thin-walled cylinder, and that significant optical distortion will occur at rotational speeds of one-fourth the bursting speed, the scanning mirror rotation rate is limited by

$$\omega \leq \frac{193}{D_s} \text{ radians/sec}, \tag{3-13}$$

for a beryllium mirror.

These operational and mechanical constraints confine the scanning mirror rotation rate to the range

$$\frac{2\pi\, v_h}{pm\, H \cdot \Delta\phi} \leq \omega \leq \frac{\Delta\phi/2\tau}{193/D_s}$$

For high resolution (small $\Delta\phi$) systems, it is evident that simultaneous scans may be required. This can best be accomplished by an array of solid-state detectors, although the current state-of-art probably limits p to ten or less. Since only the product pm occurs, it is equally effective to increase the number of faces on the scanning mirror. Aside from the necessity of $m < \pi/\phi$, increasing m much beyond four may result in unreasonably large scanning mirrors, since it is evident from Figure 3-1 that each face must be at least as large as the collecting aperture. Rotating scanning mirrors of base diameters larger than one or two meters are impractical. Finally, although eq. (3-13) implies that rotation rates for very small scanning mirrors are limitless, a reasonable upper limit for the drive mechanism is probably 200,000 rpm or about 2×10^6 radians per second.

3.1.2 Photomultiplier Tube Detectors

The spectral response of photomultiplier tubes used in the spectral region from 1000 Å to 4000 Å is usually expressed in terms of the cathode quantum efficiency, defined as the number of photoelectrons emitted from the cathode per photon incident upon the cathode. The spectral response curves for four typical EMR phototubes are shown in Figure 3-2. The response curves for phototubes from other manufacturers are similar. The short wavelength cut-off shown is due to a sapphire window for curves 1, 2, and 4, and a Vycor glass window for curve 3. All other glasses have a short wavelength cut-off at 3000 Å or higher. Use of a lithium window would result in a 1050 Å cut-off. However, the transmittance of lithium fluoride is seriously degraded by exposure to Van Allen electron radiation[21]. Curve 1 represents a multi-alkali

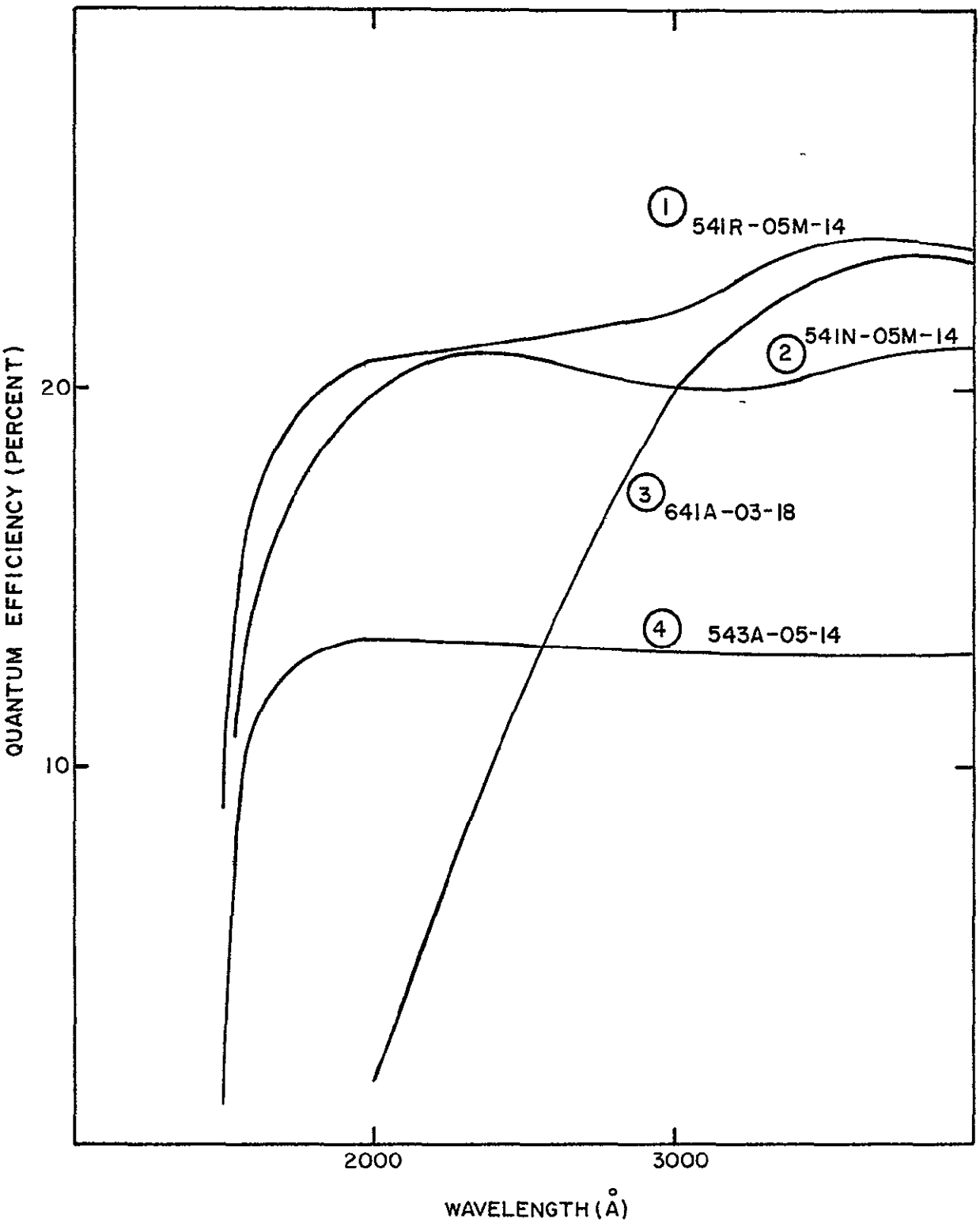

FIGURE 3-2. TYPICAL QUANTUM EFFICIENCIES

photocathode, curve 2 a bi-alkali, and curves 3 and 4 a cesium antimonide. The figure shows that quantum efficiencies are approximately constant over a limited spectral interval, and that efficiences of twenty percent are attainable. The phototube sensitivity S, defined as the cathode current per unit of incident power, is

$$S = \frac{nqe}{n(\frac{hc}{\lambda})} = \frac{qe\lambda}{hc} , \qquad (3\text{-}14)$$

where

n = number of photons incident per unit time,
q = quantum efficiency,
e = electron charge (1.602×10^{-19} coulombs),
h = Planck's constant (6.626×10^{-34} joule-sec),
c = speed of light (3×10^{8} meters/sec),
λ = wavelength of incident photon.

Noise in a photomultiplier tube may arise from a number of sources[22], including:

(a) Johnson noise due to thermal motion of conducting electrons in the load resistance. With proper circuit design, the large internal electron multiplication factors of photomultiplier tubes permit detection of even single photon events without interference from Johnson noise. Therefore, Johnson noise is ignored here.

(b) Dark current. Even when a photomultiplier tube is operated in complete darkness, electrons are still emitted by the cathode. This dark current is amplified by the internal gain, setting a lower limit on the minimum light intensity which can be detected unambiguously. However, when a photon flux is incident upon the tube, the total noise increases rapidly[23] and the dark current noise becomes negligible in comparison to the total noise. Dark current noise, therefore, is neglected here.

(c) Random fluctuations in the incident photon flux, or "quantum noise". If $\bar{n}$ is the average number of photons incident upon the phototube during the dwell time $\Delta\phi/\omega$ for a planetary scene resolution element, the corresponding cathode current I is

$$I = \frac{\bar{n}qe}{(\Delta\phi/\omega)} = \int M(\lambda)\, S(\lambda)\, d\lambda \,, \qquad (3\text{-}15)$$

where $M(\lambda)$ is the incident photon spectral power flux in watts per unit wavelength, $S(\lambda)$ is the phototube sensitivity, and the right-hand equality follows from the definition of sensitivity. The limits of integration are determined by the spectral bandpass of the sensor system. The standard deviation in the number of detected photons is then

$$\sigma = (\bar{n}q)^{\frac{1}{2}} \,, \qquad (3\text{-}16)$$

and the corresponding quantum noise current is

$$I_q = \frac{e(\bar{n}q)^{\frac{1}{2}}}{(\Delta\phi/\omega)} \,. \qquad (3\text{-}17)$$

Solving eq. (3-15) for $\bar{n}q$ in terms of I, and substituting into eq. (3-17), the quantum noise current may be written as

$$I_q = \left(\frac{e\omega I}{\Delta\phi}\right)^{\frac{1}{2}} \qquad (3\text{-}18)$$

(d) The electron current, or "shot noise". The cathode noise current I_s due to shot noise is given by[22]

$$I_s = (2eI\Delta f)^{\frac{1}{2}} \,, \qquad (3\text{-}19)$$

where I is the average cathode current, and Δf is the electronic detection bandwidth. The detection bandwidth is inversely proportional to the dwell time, and no large error is

introduced[24] by assuming that the proportionality constant is unity. Also, the noise current is increased by a factor of about $(2)^{\frac{1}{2}}$ due to the electron multiplication process. Thus the shot noise current is approximately

$$I_s = \left(\frac{4e\omega I}{\Delta\phi}\right)^{\frac{1}{2}} . \qquad (3\text{-}20)$$

Now by using eqs. (3-18) and (3-20), the ratio of signal current to rms noise current is

$$\frac{S}{N} = \frac{I}{I_q + I_s} = \frac{1}{3}\left(\frac{I \cdot \Delta\phi}{e\omega}\right)^{\frac{1}{2}} . \qquad (3\text{-}21)$$

Substituting for I from eq. (3-15), and using eq. (3-14),

$$\frac{S}{N} = \left(\frac{q \cdot \Delta\phi}{9\ hc\omega} \int \lambda M(\lambda)\, d\lambda\right)^{\frac{1}{2}} . \qquad (3\text{-}22)$$

Thus for photomultiplier tubes, the signal-to-noise ratio is proportional to the square root of the number of detected photons from a planetary surface resolution element. The signal-to-noise ratio may be enhanced by increasing the quantum efficiency of the tube, the resolution element dwell time, or the size of the collecting optics.

Quantum efficiencies for typical photomultiplier tubes have been given in Figure 3-2. In the absence of the selection of a specific tube, the quantum efficiency may be taken as 0.2 throughout the spectral region of interest (2000 - 4000 Å). It was also shown above that the maximum permissible scan rate is related to the detector time constant. The minimum response time attainable with a photomultiplier tube is limited by the anode pulse rise time, which has been tabulated for many commercially available tubes by Van Slyke[25]. With few exceptions, the tabulated rise times are less than about

ten nanoseconds. Thus, the detector time constant τ for photomultiplier tubes is taken here as 10^{-8} seconds.

3.1.3 Solid-State Photoconductor Detectors

Stannic oxide (SnO_2) and solid solutions of MgS in ZnS have recently been developed[26] as photoconductive detectors for the spectral region below 3000 Å, which is the long wavelength cut-off for both materials. The sensitivity of solid-state photon detectors is commonly represented[17] by the quantity D^*, defined as

$$D^* = \frac{(A \cdot \Delta f)^{\frac{1}{2}}}{NEP} \quad , \tag{3-23}$$

where A is the area of the detector, Δf is the noise bandwidth, and NEP is the noise equivalent power. For solid-state photon detectors, the response is proportional to the rate at which photons are detected. No photons are detected, however, unless the photon energy is greater than some threshold value. Since photon energy is inversely proportional to wavelength, the response of an idealized photon detector per unit photon energy increases with wavelength, and suddenly vanishes at a wavelength corresponding to the threshold energy. Thus the wavelength dependence of D^* for a solid-state photon detector is often approximated by

$$D^*(\lambda) = \frac{\lambda}{\lambda_p} D_p^* \quad , \tag{3-24}$$

where λ_p is the wavelength of peak response, and D_p^* is the value of $D^*(\lambda)$ at λ_p. For both types of solid-state detectors considered here, λ_p is about 3000 Å. Schultz and Harty[26] have measured D_p^* at 10^{11} cm-Hz$^{\frac{1}{2}}$/watt for SnO_2, and about 4×10^{11} cm-Hz$^{\frac{1}{2}}$/watt for MgS-ZnS. It is possible that higher values of D_p^* can be obtained, since many of the measurements were limited by amplifier noise, due to the very high

resistance of the detectors. Time constants in the range of 1-10 milliseconds were observed for both materials. Since there is some evidence that the time constants can be shortened in the near future, the detector time constant is taken here as one millisecond for both SnO_2 and MgS-ZnS. Detector areas as small as 10^{-3} cm^2 are available.

Solving eq. (3-23) for the noise equivalent power, and using eq. (3-24),

$$NEP = \frac{\lambda_p (A\Delta f)^{\frac{1}{2}}}{\lambda D^*_p} . \qquad (3\text{-}25)$$

Since $M(\lambda)$ has been previously defined as the spectral power incident upon the detector, the signal-to-noise ratio is

$$\frac{S}{N} = \frac{D^*_p}{\lambda_p} \left(\frac{\Delta\phi}{A\omega}\right)^{\frac{1}{2}} \int \lambda M(\lambda) d\lambda , \qquad (3\text{-}26)$$

where Δf has been taken as $\omega/\Delta\phi$. This derivation has been somewhat less than rigorous, but essentially the same result has been obtained by Jamieson[24] and by Hawkins[27]. Jamieson also suggested that for chopped systems, eq. (3-26) should be multiplied by $\sqrt{2}/\pi$ to obtain an effective rms signal-to-noise ratio, since the rms value of the fundamental harmonic of a square wave form is $\sqrt{2}/\pi$ of the peak-to-peak value of the modulation. With this correction,

$$\frac{S}{N} = \frac{D^*_p}{\pi\lambda_p} \left(\frac{2\Delta\phi}{A\omega}\right)^{\frac{1}{2}} \int \lambda M(\lambda) d\lambda \qquad (3\text{-}27)$$

for solid-state ultraviolet systems.

3.1.4 Collecting Optics

For either photomultiplier or solid-state photoconductive detectors, it has been shown that that signal-to-noise ratio depends upon the product $\lambda M(\lambda)$, which is proportional to the number of photons incident upon the detector. Since $M(\lambda)$ is the power per unit wavelength incident on the detector,

$$M(\lambda) = \frac{\pi D_c^2 r_x r_y \eta(\lambda) I(\lambda)}{4 R_s^2} \qquad (3\text{-}28)$$

where $I(\lambda)$ is the amount of solar power reflected by the observed scene per unit area per unit solid angle, $r_x r_y$ is the area of a resolution element, $\pi D_c^2/4R_s^2$ is the solid angle subtended by the collecting optics of diameter D_c at the range R_s, and $\eta(\lambda)$ is the optical efficiency of the system. The estimation of $I(\lambda)$ has been discussed in Section 2.1, where it was shown that

$$I(\lambda) = \frac{1}{\pi} H(\lambda)\ a(\lambda)\ f(i)\ \cos \epsilon \qquad (3\text{-}29)$$

The functional dependence of I upon several other variables is suppressed in this notation; $H(\lambda)$ is the solar spectral irradiance, $a(\lambda)$ is the planetary albedo, $f(i)$ is the photometric function as a function of solar zenith angle i, and ϵ is the angle of reflection measured from the normal to the surface. The quantity which is needed in eqs. (3-22) and (3-27) is then

$$\int \lambda M(\lambda) d\lambda = \frac{0.2\ D_c^2 r_x r_y\ f(i)\ \cos \epsilon}{R_s^2} \int \lambda H(\lambda) a(\lambda) d\lambda\ , \qquad (3\text{-}30)$$

where $\eta(\lambda)$ has been taken as 0.8, independent of wavelength. The integral on the right-hand side has been evaluated for

the planets of interest, using the data presented in Section 2.1, over two spectral ranges: 2200 - 3000 Å and 2200 - 4000 Å. The planet's distance from the sun has been accounted for in computing the solar irradiance, $H(\lambda)$. The results are shown in Table 3-1, where C_s signifies the integral evaluated from 2200 to 3000 Å (the spectral range of solid-state detectors), and C_p from 2200 to 4000 Å (the spectral range of photomultiplier tubes).

Table 3-1

Values of C (watts/meter)

Planet	C_s	C_p
Moon	2.08×10^{-7}	2.67×10^{-6}
Mercury	1.39×10^{-6}	1.78×10^{-5}
Venus	3.26×10^{-6}	3.00×10^{-5}
Mars	1.16×10^{-7}	8.68×10^{-7}
Jupiter	4.86×10^{-8}	4.49×10^{-7}

By using the geometrical relations developed in Section 1, it can be shown that

$$\frac{r_x r_y \cos \epsilon}{R_s^2} = (\Delta\emptyset)^2 , \qquad (3\text{-}31)$$

which is independent of the view angle $\emptyset$, hence eq. (3-30) reduces to

$$\int \lambda M(\lambda) d\lambda = 0.2\ CD_c^2\ (\Delta\emptyset)^2\ f(i) . \qquad (3\text{-}32)$$

Substituting this result into eqs. (3-22) and (3-27), and solving for the diameter of the collecting optics gives

$$D_{c,p} = 3 \times 10^{-12} \frac{(S/N)}{\Delta\phi} \left(\frac{\omega}{qC_p f\, \Delta\phi}\right)^{\frac{1}{2}} \qquad (3\text{-}33)$$

for photomultiplier systems, and

$$D_{c,s} = \frac{3.33}{\Delta\phi} \left(\frac{\lambda_p \cdot S/N}{D_p^* C_s f}\right)^{\frac{1}{2}} \left(\frac{A\omega}{\Delta\phi}\right)^{\frac{1}{4}} , \qquad (3\text{-}34)$$

for solid-state detector systems, where the argument of f has been omitted for simplicity. Dividing eq. (3-33) by eq. (3-34),

$$\frac{D_{c,p}}{D_{c,s}} = 9 \times 10^{-13} \left(\frac{C_s D_p^* \cdot S/N}{C_p \lambda_p q}\right)^{\frac{1}{2}} \left(\frac{\omega}{A \cdot \Delta\phi}\right)^{\frac{1}{4}} \qquad (3\text{-}35)$$

which indicates whether a photomultiplier system or a solid-state system will require the larger optical system, for a given application. For a rough estimate, D_p^* may be taken as 4×10^{11} cm-Hz$^{\frac{1}{2}}$/watt, λ_p as 3×10^{-5} cm (3000 Å), A as 10^{-7} meters^2, and q as 0.2. Table 3-1 indicates that C_s/C_p is approximately 0.1 for all the planets. Then

$$\frac{D_{c,p}}{D_{c,s}} \simeq 0.0041\ (S/N)^{\frac{1}{2}} \left(\frac{\omega}{\Delta\phi}\right)^{\frac{1}{2}} . \qquad (3\text{-}36)$$

The signal-to-noise ratio required of the sensor system clearly influences the optical design. Smith and Wood[28], along with other workers, have reviewed this problem, and it appears that for visual imagery an S/N of about three is required to resolve a standard high-contrast three bar pattern. Presumably, similar resolution would be obtained in the ultraviolet portions of the spectrum. For a low contrast

target, the signal must be increased to afford the same probability of detection or image quality. Suppose that the target or scene consists of small areas whose reflectivities differ by five percent. This corresponds roughly to a scene contrast of 1.05:1, and the modulation transfer for this contrast is about 0.025. If a signal-to-noise ratio of three is required for a scene of high contrast, then a signal-to-noise ratio of 3/0.025 or 120 is required for reliable detection of reflectivity differences of five percent. Although for some applications, such as study of lithologic contacts, it may be argued that detection of reflectivity differences on the order of one percent are desirable, such highly precise measurements are probably best performed by spectroscopic, rather than imaging, experiments. Assuming a required signal-to-noise ratio of 120, eq. (3-36) becomes

$$\frac{D_{c,p}}{D_{c,s}} \simeq 0.045 \left(\frac{w}{\Delta\phi}\right)^{\frac{1}{4}} . \qquad (3\text{-}37)$$

For high resolution (small $\Delta\phi$) experiments, it would appear that the use of solid-state detectors is advantageous.

The maximum size of the collecting optics depends upon whether reflective or refractive optical systems are used. Both types of systems have been used in the ultraviolet. Refractive UV lenses are generally made of quartz, with either a lithium fluoride or calcium fluoride coating. The maximum lens diameter is currently limited to about 20 cm or less, because of problems with the coating. Reflective systems can be much larger. For example, the OAO UV telescopes have reflecting mirrors of 16 inches diameter. Reflective mirrors of 200 inches diameter are certainly possible, although such systems are hardly space-qualified at the current state-of-art. In either case, optical efficiencies of 0.8 are commonly achieved as implied earlier.

The collecting optics diameter is also controlled by image plane resolution and must be larger than the diffraction limit,

$$D_c > \frac{1.22\lambda}{\Delta\phi} \qquad (3\text{-}38)$$

The focal length of a simple optical system is

$$F = \frac{\ell}{\Delta\phi} \ , \qquad (3\text{-}39)$$

where ℓ is the linear size of a single detector. The effective f-number of the system is

$$f\# = \frac{F}{D_c} = \frac{\ell}{D_c \Delta\phi} \ . \qquad (3\text{-}40)$$

For reasonable optical systems, the f-number must be one or larger. For solid-state detectors, reasonable values of ℓ may range from 0.1 to 3 mm. For photomultiplier tubes, ℓ may range from about 0.1 mm to 10 cm for single detectors. For arrays of photomultiplier tubes, quartz fiber optics may be used and the effective ℓ is about 0.1 mm.

3.2 Support Requirements

3.2.1 System Weight

The total weight of the imaging system may be estimated by approximating the weights of the system components. Slater and Johnson[29] have studied the dependence of optical system weight upon collecting optics diameter for space-qualified systems. Figure 3-3 is reproduced from their report. Their results can be reasonably well approximated by

$$M_c = 168\ D_c^2 \ , \qquad (3\text{-}41)$$

where M_c is the mass of the optical system in kilograms, and D_c is the diameter of the collecting optics in meters. Bashe and Kennedy[30] have examined the weights of long focal length optical systems with the results shown in Figure 3-4, which is taken from their report. For comparison, the dashed line in the figure shows the results of using eq. (3-41). The

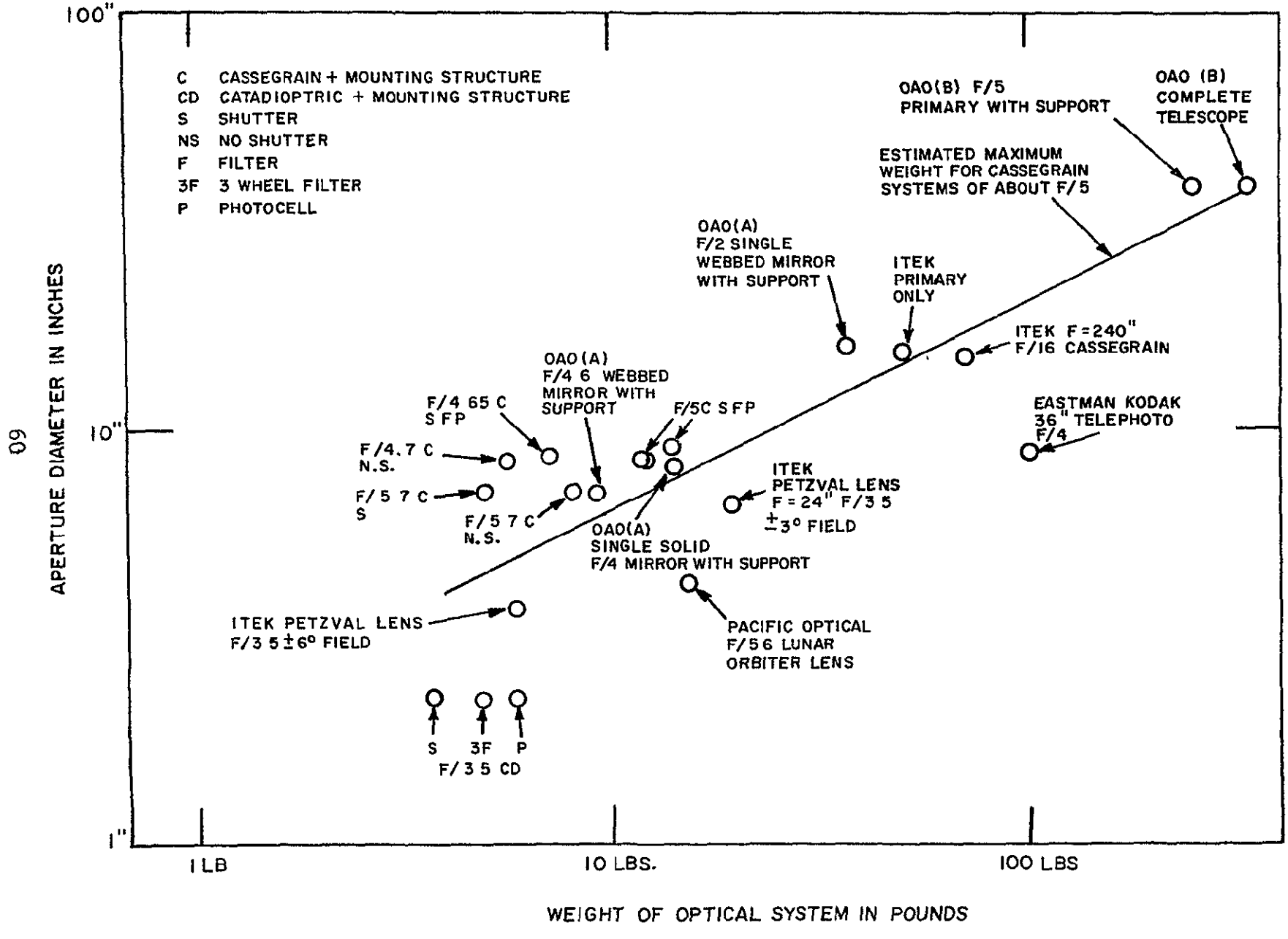

FIGURE 3-3 APERTURE DIAMETER VERSUS WEIGHT FOR A VARIETY OF SPACE OPTICAL SYSTEMS

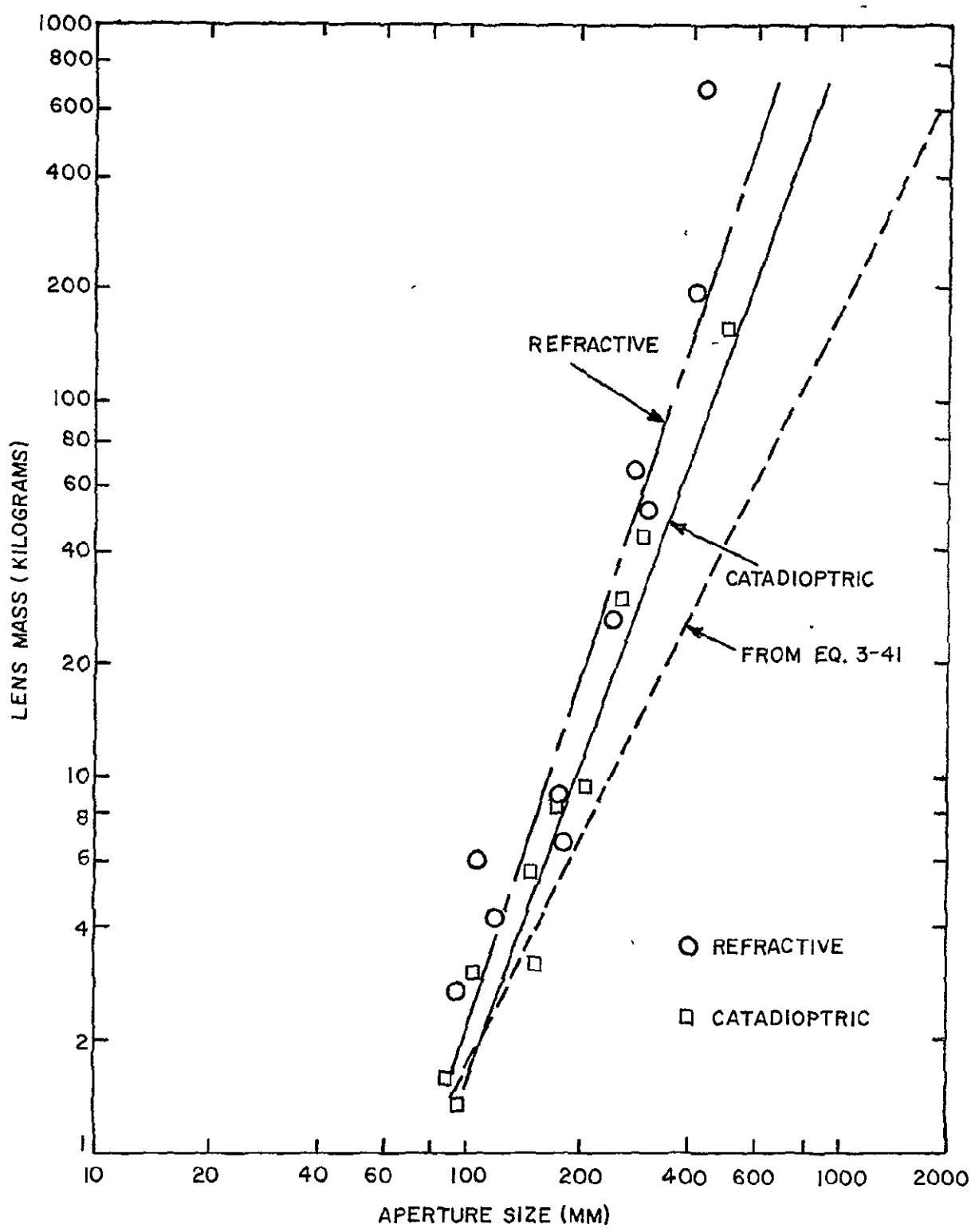

FIGURE 3-4. APERTURE SIZE VS. MASS FOR REFRACTIVE AND CATADIOPTRIC OPTICAL SYSTEMS.

Slater and Johnson analysis predicts smaller weights than those of Bashe and Kennedy, presumably because emphasis is placed upon weight reduction in the design of large optical systems for use in space. The data of Bashe and Kennedy are not confined to space-qualified systems. It is assumed here that the weights of ultraviolet optical systems are sufficiently similar to optical systems used in the visible portion of the spectrum that eq. (3-41) can be used for ultraviolet optics. For comparison, the OAO ultraviolet nebular telescope has a 16-inch diameter parabolic reflector. Eq. (3-41) predicts that such an optical system will have a mass of 28 kg, or 61 lbs, which is consistent with the reported[31] experiment weight of 74 lbs, including the photometer and electronics.

As mentioned above, reflecting system diameters of larger than two meters are probably unrealistic for the current state-of-art, while refractive systems are limited to about twenty centimeters. Reflecting system diameters of up to five meters may be possible in the 1980's and 1990's, but the weight scaling law above is of questionable validity for diameters larger than two meters. An additional constraint is optical quality of the surface. Surface deviations of larger than $\lambda/20$ will degrade the optical system performance. Thus for systems operating at 2000 Å, optical surface deviations must be limited to about 100 Å.

The size of the scanning mirror is related to the diameter of the collecting optics. Each face of the scanning mirror must have an area at least as large as the area of the collecting optics. If D_s is the diameter of the scanning mirror base, some simple analysis will show that

$$\frac{D_s}{D_c} = \begin{cases} 2^{\frac{1}{2}} & \text{for } m = 1, \\ 1 + \dfrac{1}{\cos \phi} & \text{for } m = 2, \\ \left[1 + \csc \left(\dfrac{\pi}{m} - \phi\right)\right] \sec \dfrac{\pi}{m} & \text{for } m \geq 3. \end{cases} \qquad (3\text{-}42)$$

By assuming that the thickness of the scanning mirror assembly is $D_s/10$ for m equal to one, $D_s/15$ for m equal to two, and $D_s/20$ for m greater than two, and that the mass of the scanner shaft and bearings, the drive motor, and the scanner housing is 0.1, 0.1, and 0.5 times the mirror mass, respectively, the total mass of the scanning assembly is estimated as

$$M_s = \begin{cases} 0.13\ \rho\ D_s^3 & \text{for } m = 1, \\ 0.22\ \rho\ D_s^3 & \text{for } m = 2, \\ 0.015\ \rho m\ D_s^3 \sin \frac{2\pi}{m} & \text{for } m \geq 3. \end{cases} \qquad (3\text{-}43)$$

Here ρ is the density of the construction material. Suggested values are 1.85×10^3 kg/m^3 for beryllium, 2.7×10^3 kg/m^3 for aluminum, and 7.9×10^3 kg/m^3 for stainless steel.

Each detector (whether a photomultiplier or a solid-state device) and its associated electronics is assumed to have a mass of one kilogram. Although the electronics weight is not expected to be directly proportional to the number of detectors, this assumption is probably valid (within a factor of three) for as many as ten detectors. The total sensor system weight is the sum of the optical system weight, the scanning system weight, and the detector and electronics weight. However, unless the power available to a photomultiplier sensor system is constant to within one percent[32], additional weight must be provided for power conditioning. The minimum system mass of one kilogram implied above is consistent with the three-pound single - channel UV photometers flown aboard Aerobee rockets.

3.2.2 System Volume

The volume of the scanning assembly may be approximated by a right circular cylinder of diameter $1.1\ D_s$ and height $0.6\ D_s$. Similarly, the volume of the collecting optics

may be approximated by a right circular cylinder of diameter 1.1 D_s and height 1.1 F. Thus the sensor system volume is approximately

$$V = \frac{\pi}{4} (0.73\ D_s^3 + 1.3\ F\ D_c^2). \qquad (3\text{-}44)$$

Unless the scanning and optical systems are very small, this estimate should be generous enough that it includes the detector and electronics volume. The minimum sensor system volume is taken as 10^{-3} cubic meters.

3.2.3 System Power

Each detector and its associated electronics are assumed to consume one watt of power. The sensor system power requirement is then

$$P = p \text{ watts}, \qquad (3\text{-}45)$$

where p is the number of detectors. The power estimate afforded by eq. (3-45) is consistent with the 0.5 watt consumption by Aerobee UV photometer experiments, and is expected to be accurate within a factor of three for up to ten detectors. The development and use of advanced electronic components, including field effect transistors, may reduce the power requirements as much as a factor of ten[33].

3.2.4 Data Acquisition Rate

The system data acquisition rate is very simply

$$DR = \frac{p\ G\ \omega}{\Delta\emptyset} \text{ bits/sec}, \qquad (3\text{-}46)$$

where p is the number of detectors, G is the number of binary bits required for each resolution element, and $\omega/\Delta\emptyset$ is the number of resolution elements scanned per second. For high

quality imagery, 64 shades of gray are required; G has been taken as six in this study.

3.2.5 Pointing and Platform Stability

If Δr is the desired positional accuracy of the image, that is, if the planetary location of the resolution element at the center of the scan line is to be known with an accuracy of Δr unit lengths, then the required pointing accuracy is

$$\Delta\theta = \frac{\Delta r}{H} \text{ radians.} \tag{3-47}$$

An estimate of the permissible angular rotation rates of the scanning beam is afforded by noting that the dwell time on each resolution element is $\Delta\phi/\omega$. Limiting the sensor system roll, yaw, and pitch rates to those resulting in apparent image movements of one-half resolution element gives

$$\dot{\Delta\theta} = \frac{\omega}{2} \text{ rad/sec,} \tag{3-48}$$

where $\dot{\theta}$ is the maximum allowable roll, yaw, or pitch rate.

3.2.6 State-of-Art Constraints

Throughout the above development of scaling laws for ultraviolet optical-mechanical scanning systems, operational and mechanical constraints due to current state-of-art limitations have been pointed out, where appropriate. The major constraints deal with the optical system and the detector system. For photomultiplier systems, quantum efficiencies of twenty percent and response times of 10^{-8} seconds appear attainable. For solid-state detectors, specific detectivities (D_p^*) of 4×10^{11} cm-Hz$^{\frac{1}{2}}$/watt and response times of 10^{-3} seconds are reasonable.

The scanning mechanism appears to be limited to angular rotation rates of 10^6 radians/second, although this estimate is based on currently operating aircraft systems,

and it is not clear how much this constraint can be relaxed in the vacuum of space. Although reflective ultraviolet optical systems of greater than one meter in diameter appear feasible, this would imply scanning mirrors greater than two meters or so in diameter for object-plane scanners. Such mirrors are so far beyond the range of current operating experience that two meter scanning mirrors and one meter collecting optics are a prudent practical limit. Scanning mechanisms other than the type discussed here are feasible. For example, split-field scanning optics may be more suitable when large collecting optics are required. For the imaging experiments considered in this study, each scan line must include a minimum of one hundred resolution elements. To do away with the rotating scanning mechanism entirely and employ some sort of "push-broom" or rake technique, would require a band of more than 100 detectors scanning forward along the heading line by virtue of spacecraft motion along the orbit. This technique is beyond current technological capabilities, and little experience in the design of such systems is available.

Aside from the scanning problem, there appear to be no fundamental limitations to the use of one or two meter diameter optical systems in the ultraviolet. In fact, much larger (200-inch) systems might be employed, but at great expense in weight. The scaling law given above for the weights of optical systems is unreliable for diameters much larger than two meters. Optical surfaces must be accurate to within about 100 Å, and this is clearly a problem for large surfaces. Since the OAO UV telescope systems are operable in the temperature range from -55 to +72 deg C, such a temperature environment should be comfortable for the systems of interest here.

3.3 Design Procedures

Figure 3-5 is a logic diagram which summarizes the design procedures developed above for ultraviolet scanning systems. Given a set of image specifications and a set of

orbit parameters, the logic diagram indicates each step in the estimation of the support requirements implied by any specific ultraviolet experiments. The square boxes in the figure represent steps in the design procedure, while the oval boxes represent estimation of specific support requirements. In this study, image specifications have been given in Volume I, and orbit parameters in Volume III. The design procedure and scaling laws are, of course, applicable to many situations beyond the scope of this study. The scaling laws are summarized in Figure 3-6, which is intended for use with Figure 3-5. Unless specified otherwise, the use of MKS units is implied. An example of the design procedure and the estimation of experiment support requirements is given in Section 6 of Volume I.

The attitude control requirement (step #1) is independent of detailed sensor system design, and hence can be estimated early in the design process. The field-of-view (step #4) is computed after determining the scan half-angle and the scanning beam angular size. No skillful design adjustments can circumvent the diffraction limit (step #5) on the optical system. Thus if the diffraction limit exceeds one meter, the experiment should be abandoned as beyond the current state-of-art. The system design and support requirements are sensitive to the number (p) of detectors and the number (m) of faces on the scanning mirror. Since system weight and power requirements usually increase with p and m, it is frequently convenient to initially select p and m (step #7) each equal to one. A minimum mirror rotation rate (step #8) is based on congruence of scan lines. The design rate may equal or exceed this minimum value. Since high rotation rates tend to increase the rate at which data is acquired and also requires use of detectors with short response times, the selected mirror rotation rate should normally be chosen equal to the minimum value. It should be noted, however, that the platform stability requirements are eased as the rotation rate increases.

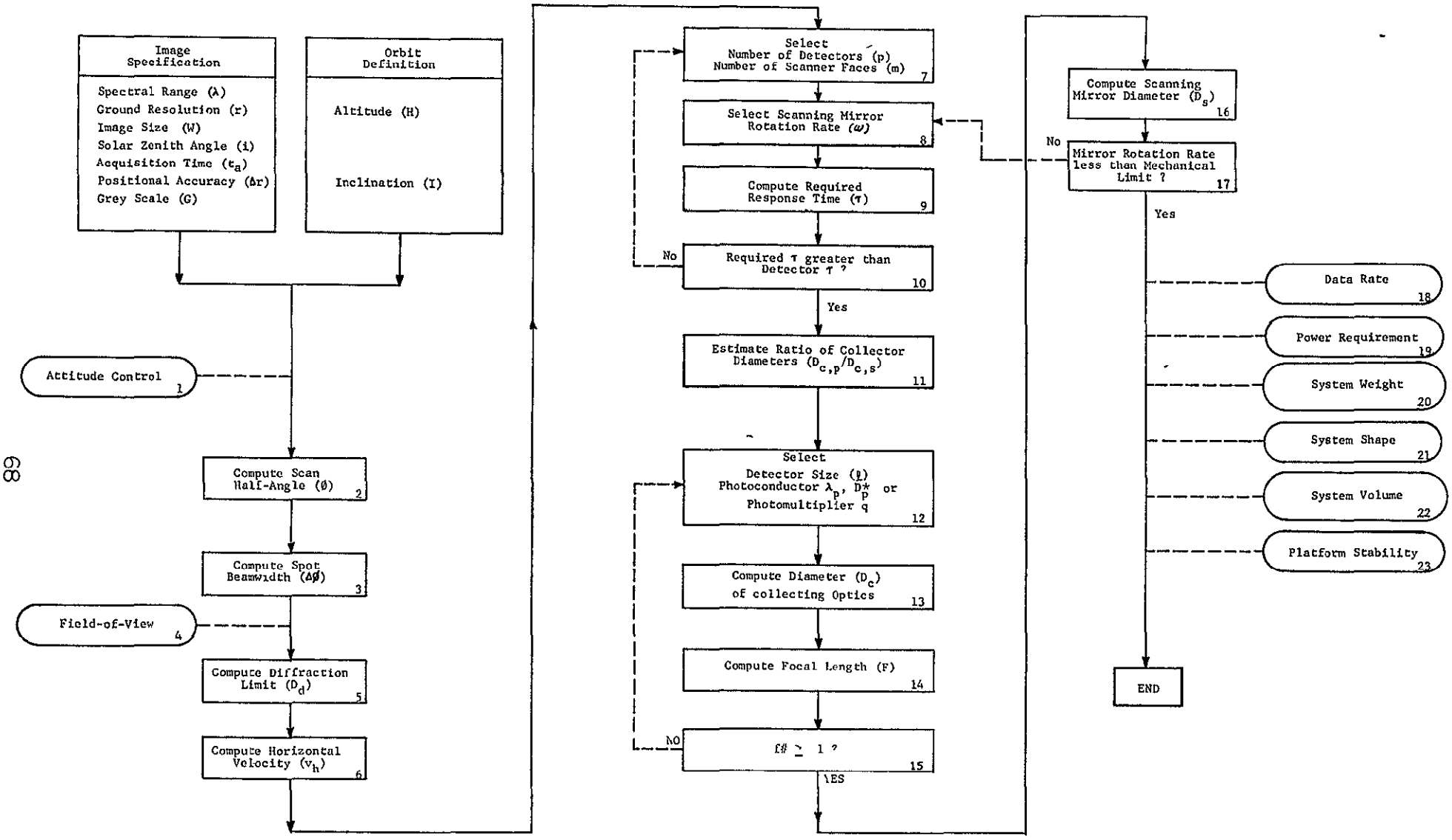

FIGURE 3-5 LOGIC DIAGRAM FOR ULTRAVIOLET SCANNING SYSTEMS

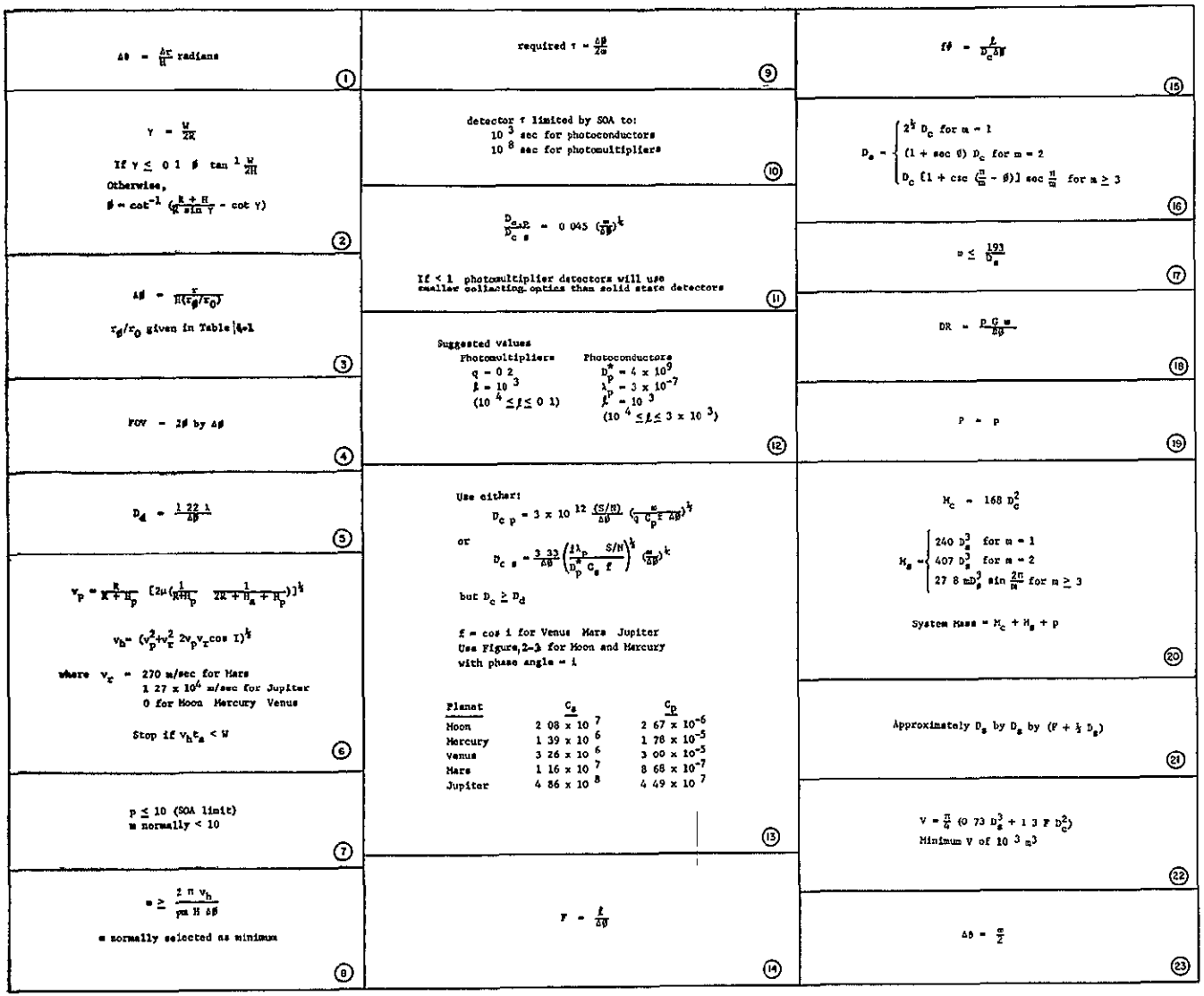

NOMENCLATURE
(MKS units implied)

D_c	Collecting aperture diameter
$D_{c\,p}$	D_c for photomultiplier system
$D_{c\,s}$	D_c for photoconductive system
D_d	Diffraction limit for D_c
D_p^*	Photoconductive detector peak detectivity
D_s	Scanning mirror diameter
DR	Data acquisition rate (bits/sec)
F	Optical focal length
f	Photometric function
$f\phi$	Aperture stop (f number)
FOV	Field of-view
G	Bits per resolution element (normally 6)
H	Sensor altitude
H_a	Orbit apoapse altitude
H_p	Orbit periapse altitude
I	Orbit inclination
i	Solar zenith angle
ℓ	Detector linear size
M_c	Mass of collecting optics
M_s	Mass of scanning mirror
m	Number of scanning faces
P	System power requirement
p	Number of detectors
q	Photomultiplier quantum efficiency
R	Planet radius
r	Ground resolution
S/N	Signal to noise ratio (normally 120)
V	System volume
v_h	Apparent horizontal ground speed
v_p	Speed of subsatellite point
v_r	Planet equatorial rotational speed
W	Linear ground size of image
γ	Planetocentric half angle subtended by W
Δr	Image location error on planet
$\Delta\theta$	Allowable pointing error
$\Delta\theta$	Allowable sensor roll or yaw rate
$\Delta\phi$	Scanning beam angular size
λ	Wavelength
λ_p	Photoconductive detector cutoff wavelength
ϕ	Half angle of scan
τ	Response time
w	Scanning mirror rotation rate

FIGURE 3-6 SCALING LAWS FOR ULTRAVIOLET SCANNING SYSTEMS

Having selected a mirror rotation rate, the constraints upon the detector response time may be evaluated (step #9). By comparing the required response time to the detector response times available (step #10), the number of design choices may be narrowed down. That is, if the required response time is less than one millisecond, no currently available solid-state detector can be used. However, if desired, the response time required of the detector may be made less demanding by increasing p or m. This possible design iteration is indicated by the dashed line in the logic diagram. Since the system weight, power, and data acquisition rate all increase with p, it is usually preferable to increase m rather than p. However, for all but small values of the scan half-angle, the scanning mirror size and weight increase rapidly with m.

If both photomultiplier and solid-state detectors provide adequate response times, an estimate may be made (step #11) of which detector type will require the larger optical system. Once either photomultiplier or solid-state detectors are selected, the appropriate detector parameters are used to estimate the minimum collecting aperture size (step #13) which will provide adequate energy focused on the detector. The collecting aperture size must, of couse, equal or exceed that size determined by the diffraction limit. The focal length (step #14) is easily obtained, and the relative aperture stop, or f-number (step #15), is computed. If the f-number is less than one, it can be most easily increased by increasing the detector size. This iteration is also shown by a dashed line in the logic diagram.

The last stage of the design procedure is to determine the approximate size of the scanning mirror (step #16), and to ensure that the design rotation rate will not result in serious dynamical distortion of the scanning mirror (step #17). The sensor system design is now sufficiently well-defined that the remaining support requirements (steps #18-23) may be estimated in a straightforward manner.

4. TELEVISION SYSTEMS

4.1 Design Equations

The following paragraphs develop the mathematical and physical relationships useful in estimating design variables of space-orbital television systems. Only the visible portion of the spectrum is considered here. Infrared television systems are discussed in a separately bound (and classified) Appendix. Techniques for estimating support requirements of visual television systems are presented in Section 4.2, while Section 4.3 summarizes the design procedure.

4.1.1 Planet-Sensor Geometry

The geometry involved in obtaining planetary images from orbit with a vertical viewing axis has been discussed in Section 1.1. To summarize, if the linear extent of the image along a great-circle arc is denoted by W, then the half-angle subtended at the planet center by the arc W on the planet surface is

$$\gamma = \frac{W}{2R} \text{ radians}, \tag{4-1}$$

where R is the planet radius. Widger[1] has shown that the half-angle camera field-of-view is then

$$\phi = \cot^{-1} \left(\frac{R + H}{R \sin \gamma} - \cot \gamma \right), \tag{4-2}$$

where H is the camera altitude. The geometry is shown in Figure 4-1. Unless full-disk imagery is desired, ϕ should be less than the view angle to the horizon,

$$\phi_h = \sin^{-1} \left(\frac{R}{R + H} \right). \tag{4-3}$$

For vertical viewing of small arc-lengths, that is, if γ is less than about 0.1 radians, eq. (4-2) reduces to the flat-

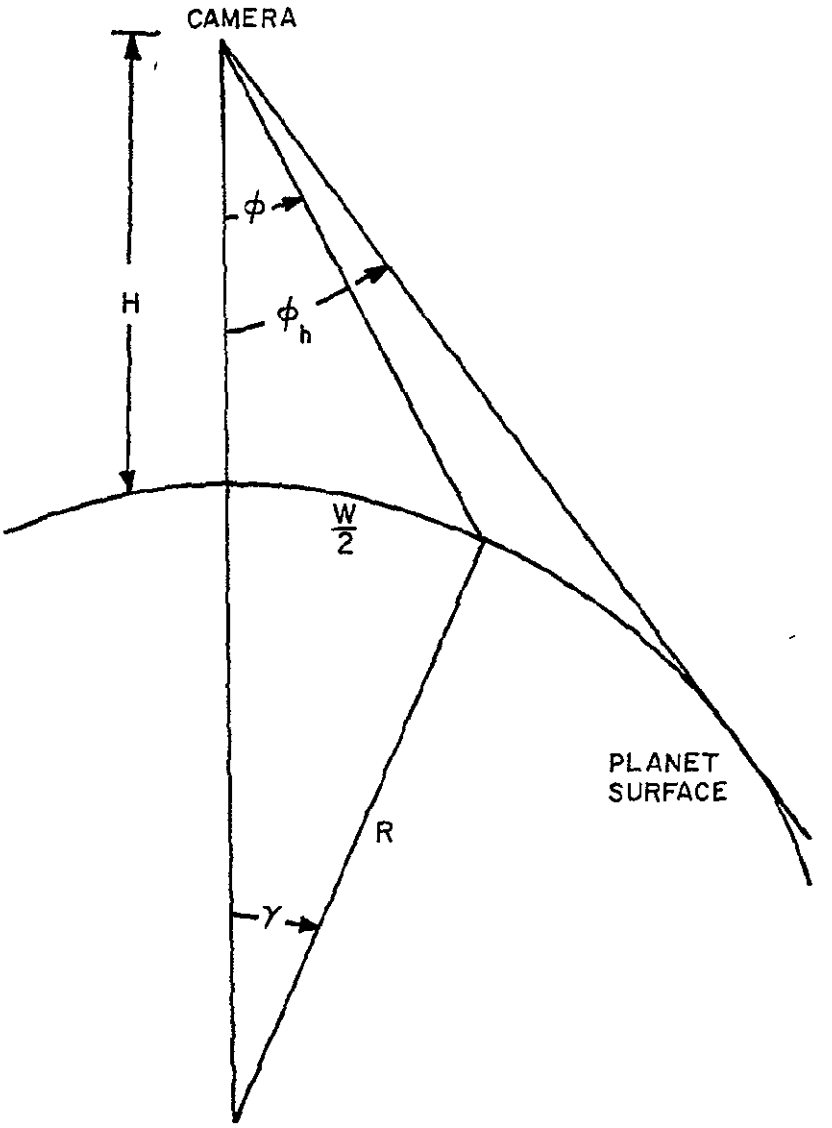

FIGURE 4-1. VERTICAL VIEWING GEOMETRY

planet result,

$$\phi \simeq \tan^{-1} \left(\frac{W}{2H}\right). \tag{4-4}$$

If the angular resolution is constant across the field-of-view, the ground resolution r_ϕ at the angle ϕ degrades with viewing angle according to

$$\frac{r_\phi}{r_0} = \frac{R}{H}\left\{\frac{\cos\phi}{\left[\left(\frac{R}{R+H}\right)^2 - \sin^2\phi\right]^{\frac{1}{2}}} - 1\right\}, \tag{4-5}$$

where r_0 is the ground resolution at the nadir point (where ϕ is zero). Table 4-1 gives r_ϕ/r_0 as a function of ϕ and H/R. A non-entry in the table indicates that $\phi > \phi_h$.

It is assumed here that areas on the planetary surface can be resolved (detected) if their linear dimensions correspond to the width of a TV line on the face of the camera tube. In practice it has been found that the minimum detectable linear size in the image plane is somewhat larger than the TV line width, because of the raster characteristics of the imagery. This effect is approximately accounted for by introduction of the "Kell factor". Thus the minimum total number of TV lines required to obtain a ground resolution r in an image of ground size W by W is

$$L \geq \frac{W}{0.7\,r}, \tag{4-6}$$

where the Kell factor has been taken as 0.7. This equation, because of its simplicity, is useful in obtaining an initial estimate of the required line capability of the TV camera tube. Because of the curvature of the planetary surface, the number of TV lines actually required is

Table 4-1

Values of r_ϕ/r_0

ALTITUDE RADIUS	Half-Angle Field-of-View ϕ (Deg.)							
	10	20	30	40	50	60	70	80
0.01	1.03	1.13	1.34	1.72	2.47	4.19	9.66	69.9
0.02	1.03	1.14	1.35	1.74	2.53	4.40	11.2	--
0.03	1.03	1.14	1.35	1.76	2.59	4.64	13.4	--
0.04	1.03	1.14	1.36	1.78	2.65	4.92	17.0	--
0.05	1.03	1.14	1.37	1.80	2.72	5.24	24.1	--
0.06	1.03	1.15	1.38	1.82	2.79	5.61	51.6	--
0.07	1.03	1.15	1.38	1.84	2.87	6.04	--	--
0.08	1.04	1.15	1.39	1.87	2.95	6.58	--	--
0.09	1.04	1.15	1.40	1.89	3.04	7.24	--	--
0.1	1.04	1.16	1.41	1.92	3.13	8.08	--	--
0.2	1.04	1.18	1.50	2.22	4.80	--	--	--
0.3	1.05	1.21	1.60	2.71	27.3	--	--	--
0.4	1.05	1.25	1.74	3.65	--	--	--	--
0.5	1.06	1.28	1.93	6.66	--	--	--	--
0.6	1.07	1.33	2.18	--	--	--	--	--
0.7	1.07	1.38	2.56	--	--	--	--	--
0.8	1.08	1.43	3.22	--	--	--	--	--
0.9	1.09	1.50	4.74	--	--	--	--	--
1.0	1.10	1.58	--	--	--	--	--	--
2.0	1.23	--	--	--	--	--	--	--
3.0	1.49	--	--	--	--	--	--	--
4.0	2.23	--	--	--	--	--	--	--

$$L = \frac{W(r_\phi/r_0)}{0.7\ r} \qquad (4\text{-}7)$$

where (r_ϕ/r_0) has been given above. Currently available TV camera tubes provide a theoretical maximum of about 6000 lines. It will be shown later that only about 3000 lines can be achieved in practice, because of low scene contrast, lens resolution degradation, and image motion effects.

4.1.2 Illumination

In Section 2.1 it was shown that the amount of solar power reflected by a planetary scene per unit area into a unit solid angle is

$$I(\lambda) = \frac{1}{\pi} H(\lambda) a(\lambda) f(i) \cos \epsilon\ , \qquad (4\text{-}8)$$

where $I(\lambda)$ = spectral luminance of scene,
$H(\lambda)$ = solar spectral illuminance,
$a(\lambda)$ = surface normal albedo,
$f(i)$ = photometric function,
λ = wavelength,
i = angle of incidence,
ϵ = angle of reflection.

The angles are measured from the normal to the surface, and the photometric function depends only upon the angle of incidence (solar zenith angle) for the viewing geometry considered here. For visual imagery at Venus and Jupiter, the photometric function is approximated by cos i; for visual imagery at the Moon, Mercury, and Mars the photometric function has been given in Figure 2-3, where the phase angle may be taken equal to the solar zenith angle (for vertical viewing). For convenience, the photometric function is given in Table 4-2 for selected values of the zenith angle.

Table 4-2

Values of the Photometric Function

Solar Zenith Angle (deg)	Photometric Function
20	0.49
40	0.31
60	0.15
75	0.06

The solar illuminance is taken as 12,500 footcandles at the Earth's heliocentric radius, and is assumed to vary inversely as the square of the distance from the Sun. Planetary albedoes in the visible portion of the spectrum have been given in Table 2.4. For viewing along a vertical axis, the scene angle of reflection is nearly zero, and hence cos ϵ may be taken as unity throughout the image. Thus for visual imagery, the scene luminance is approximately

$$B = B_o f \ , \qquad (4\text{-}9)$$

where B_o is given in Table 4-3 for the different planets. The notation has been changed from eq. (4-8) to agree with standard practice, and B_o is given in footlamberts for the same reason.

Table 4-3

Values of B_o

Planet	B_o (footlamberts)
Moon	1,400
Mercury	8,300
Venus	15,500
Mars	800
Jupiter	200

If the camera tube face is exposed to the scene for t_e seconds, the illumination on the face is

$$E = \frac{B\,\eta\,t_e}{4(f\#)^2 \cdot FF} \text{ ft-candle-sec}, \qquad (4\text{-}10)$$

where E is the illumination, η is the optical transmission factor, f# is the relative aperture of the lens (the f-number), and FF is the filter factor. Optical transmission factors of 0.9 are common with currently available lenses. As the number of lens elements increases, the optical transmission decreases. For example, a typical zoom lens has an optical transmission factor of about 0.8. The filter factor depends upon both the spectral transmission of the lens and the spectral sensitivity of the camera tube. Figure 4-2 shows the measured spectral sensitivity of the Mariner 4 vidicon[34], along with the spectral sensitivity of other commercially available tubes. If $R(\lambda)$ denotes the relative spectral response of the camera tube, and $T(\lambda)$ the measured transmission of the filter as a function of wavelength, the filter factor is computed from

$$FF = \frac{\int R(\lambda)d\lambda}{\int T(\lambda)R(\lambda)d\lambda} . \qquad (4\text{-}11)$$

Filter factors for selected filters are given in Table 4-3. In each case, the integration indicated in eq. (4-11) was performed numerically from 4000 to 7000 Å, using the Mariner 4 spectral response and the measured filter transmission[35].

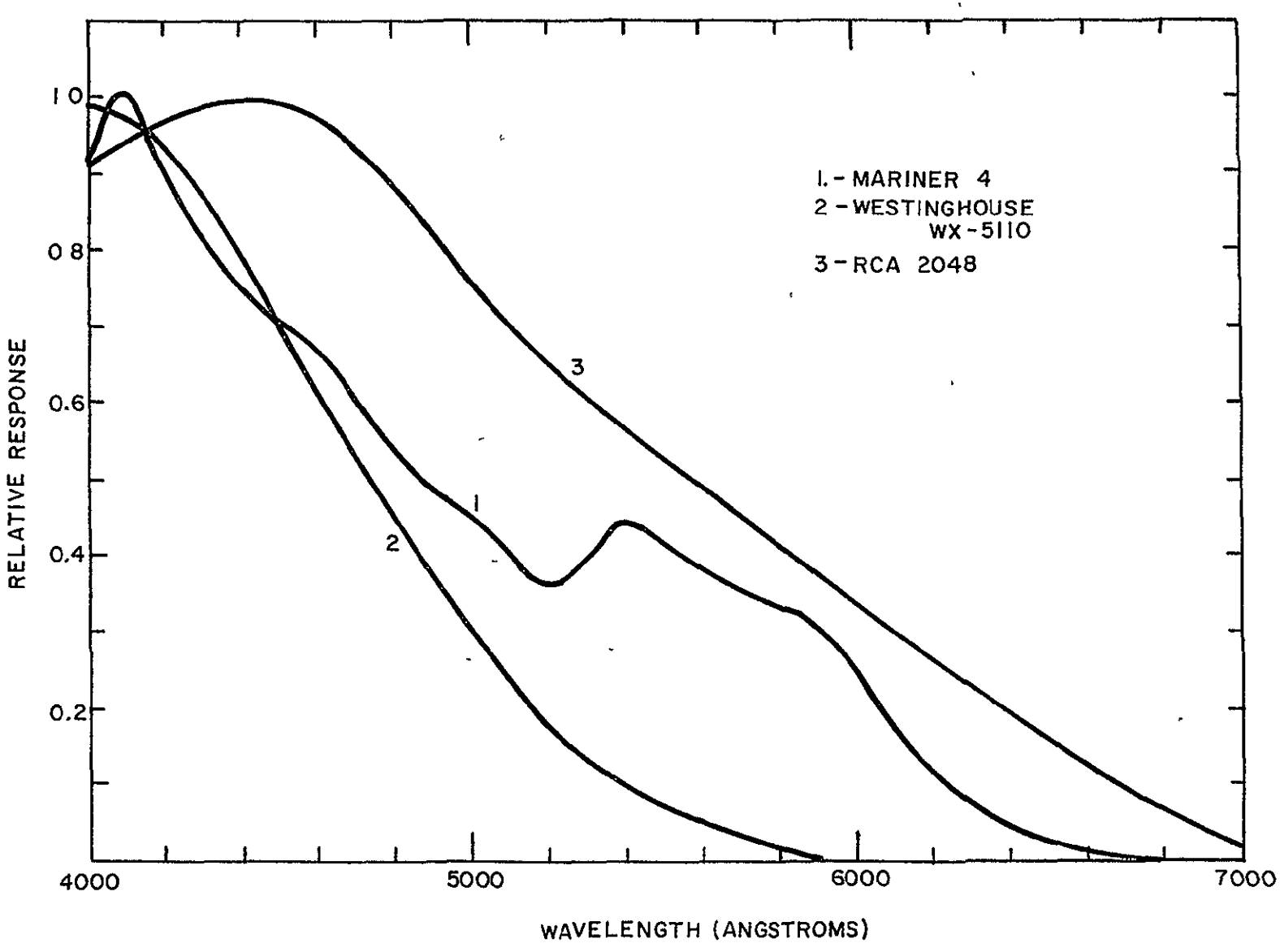

FIGURE 4-2. TV TUBE SPECTRAL SENSITIVITY

Table 4-4

TV Tube Filter Factors

Filter Type	Filter Factor
500 mμ	3.7
WRATTEN 47 Blue	5.3
WRATTEN 58 Green	9.8
WRATTEN 25A Red	27

Eq. (4-10) may be solved for the exposure time required to provide a given tube illumination. Thus if S is the minimum illumination required for satisfactory operation of the camera tube, the minimum exposure time is

$$t_e \geq \frac{4S(f\#)^2 \cdot FF}{B\,\eta} \quad . \tag{4-12}$$

Maximum exposure times based on image motion considerations are discussed below. Approximate minimum illumination values have been obtained from manufacturer's data, and are listed in Table 4-4 for various types of TV tubes.

Table 4-5

TV Tube Minimum Illumination

Tube Type	Illumination (foot-candle-sec)
Vidicon	3×10^{-3}
Plumbicon	2×10^{-3}
Return Beam Vidicon	1×10^{-3}
SEC Vidicon	5×10^{-5}
Image Orthicon	2×10^{-6}

4.1.4 Noise

The number of grey levels available for image interpretation depdns upon the signal-to-noise ratio of the imagery. This topic was first discussed by Rose[36], and more recently by Morton[37] and by Sadashige[38]. Consider two adjacent picture elements A and B, and let N_A and N_B be the number of photons incident upon these respective elements. The signal may be regarded as $N_A - N_B$, while the noise due to the random nature of photon arrivals is $(N_A + N_B)^{\frac{1}{2}}$. Thus the signal-to-noise ratio is

$$\frac{S}{N} = \frac{N_A - N_B}{(N_A + N_B)^{\frac{1}{2}}} \quad . \tag{4-13}$$

Assuming that the density of the processed image is proportional to the logarithm of the incident photon flux, the density difference between the image elements A and B is

$$D_{AB} = \log_{10} \frac{N_A}{N_B} \quad , \tag{4-14}$$

and the contrast is

$$C_{AB} = \frac{N_A}{N_B} \quad . \tag{4-15}$$

If k shades of grey are required in the imagery, then the minimum detectable density difference is

$$d = \frac{D}{k} \quad , \tag{4-16}$$

where D is the density difference between the brightest and darkest picture elements. If the dynamic range of the tube is known, D may be taken as the log (base 10) of the dynamic range. Thus if the dynamic range is 100:1, the maximum density

difference is 2. If 8 shades of grey are desired to span this density range, then using eq. (4-16) a density difference of 2/8 or 0.25 must be discernable. Now if elements A and B represent a difference of one shade of grey, and if $N_A - N_B$ is much less than N_B,

$$d = \log_{10} \frac{N_A}{N_B} \simeq \frac{N_A - N_B}{2.3\ N_B} \quad . \tag{4-17}$$

Substituting into eq. (4-13),

$$\frac{S}{N} = 2.3\ d \left(\frac{N_B}{2}\right)^{\frac{1}{2}} \quad . \tag{4-18}$$

Thus far the tube has been treated as a perfect detector. If q is the quantum efficiency of the tube, eq. (4-18) implies that when a signal-to-noise ratio of S/N is desired, the required number of incident photons per picture element is

$$N = \frac{2}{q} \left(\frac{S/N}{2.3\ d}\right)^2 \text{ photons/element.} \tag{4-19}$$

Assuming a picture of L^2 elements and an image format size of ℓ^2, the required incident photon flux is

$$N = \frac{2}{q} \left(\frac{S/N \cdot L}{2.3\ d\ \ell}\right)^2 \text{ photons/unit area.} \tag{4-20}$$

This may be converted to more convenient units by noting that for average white light 3×10^{16} photons/second correspond to one lumen, or

$$N = \frac{2}{3 \times 10^{16}\ \eta q} \left(\frac{S/N \cdot L}{2.3\ d\ell}\right)^2 \text{ ft-candle-sec} \tag{4-21}$$

If the illumination N is known, one may solve for the S/N attained. Thus if eq. (4-10) is used for N, the signal-to-noise ratio is

$$\frac{S}{N} = \frac{4.6 \times 10^5 \, D\ell}{L \, (f\#) \, k} \left(\frac{q \, B\eta \, t_e}{FF} \right)^{\frac{1}{2}}, \qquad (4\text{-}22)$$

where ℓ is the image format size in millimeters, and B is the low-level scene brightness in footlamberts. A signal-to-noise ratio of three is generally regarded as a minimum acceptable value. Typical values of D and q are given in Table 4-5 for different image tubes. The dependence of the format size upon the type and size of the camera tube will be discussed later.

Table 4-6

TV Tube Dynamic Ranges and Efficiencies

Tube Type	Dynamic Range	Max. Density Difference (D)	Quantum Efficiency (q)
Vidicon	100:1	2.0	0.2
Plumbicon	200:1	2.3	0.2
Return Beam Vidicon	100:1	2.0	0.2
SEC Vidicon	60:1	1.8	0.3
Image Orthicon	100:1	2.0	0.3

4.1.5 Modulation Transfer

The analysis of visual imaging systems is often performed using the Modulation Transfer Function (MTF) technique. The MTF, which is a measure of contrast transfer, is defined as the ratio of the output to the input modulation intensity of a sinusoidal pattern at a given spatial frequency. Thus, a value of 1.0 corresponds to a faithful reproduction of the input pattern, and a value of zero represents no signal transfer.

Consider a scene in which the intensity varies as

$$I_o = I_{Ao} + I_{Vo} \sin \frac{2\pi x}{x_o} , \tag{4-23}$$

which represents a series of lines spaced x_o apart. The maximum intensity is $I_{Ao} + I_{Vo}$, while the minimum intensity is $I_{Ao} - I_{Vo}$. The scene modulation is

$$M_o = \frac{I_{max} - I_{min}}{I_{max} + I_{min}} = \frac{I_{Vo}}{I_{Ao}} , \tag{4-24}$$

while the scene contrast is

$$C_o = \frac{I_{max}}{I_{min}} = \frac{I_{Ao} + I_{Vo}}{I_{Ao} - I_{Vo}} . \tag{4-25}$$

The modulation is a more meaningful description than contrast ratio for visual imagery, since its rate of change agrees more closely with visual effect. The human eye sees little difference in contrast between a scene of 100:1 contrast and one of 1,000:1 contrast. This visual impression is in accord with the little difference in modulation between the scenes, the respective scene modulations being 0.9 and 1.0.

The intensity variation in an image of the scene represented by eq. (4-23) may be written

$$I_i = I_{Ai} + I_{Vi} \sin \frac{2\pi x'}{x'_o} \tag{4-26}$$

where I_{Ai} is the average intensity of the image. The sine waves in the image have amplitude I_{Vi} for wavelength x'_o. The image lengths x' and x'_o are related to the scene lengths x and x_o by the system magnification. In any real system,

$$I_{Ai} = \eta I_{Ao} \tag{4-27}$$

and

$$I_{Vi} = T(x'_o)\, I_{Vo} \,. \qquad (4\text{-}28)$$

Here η is the system transmission, and $T(x'_o)$ is the system modulation transfer function. If the system MTF is unity, the amplitude of the sine waves in the image is equal to the amplitude of the sine waves in the scene.

The system MTF is obtained by multiplying together the individual transfer functions of the system components. Every visual imaging system has a number of components common to other systems and some that are peculiar to the individual system. Factors such as scene luminance, scene contrast, atmospheric transmission and scattering, image motion, lens performance, data handling and transmission, and ground reconstruction (including reception, storage, and processing) are typical common components of all orbital imaging systems. For TV systems, the only additional element required is the camera TV tube and its associated electronics; for film systems, the additional elements are the film, the film processor and the film scanning system. It is assumed here that the data storage, transmission, and ground reconstruction elements of the system have transfer functions close to unity. Thus the system MTF is approximated by

$$T_{system} = T_C\, T_L\, T_{TV}\, T_M \qquad (4\text{-}29)$$

where T_C = apparent scene contrast transfer function,
T_L = lens transfer function,
T_{TV} = camera tube transfer function,
T_M = image motion transfer function.

Each of these transfer functions will be discussed separately, and an approximate method developed for determining the system design parameters. The method assumes that for adequate imagery a minimum modulation of 0.04 is required[39] in the

image, and therefore the system modulation transfer function must equal or exceed a value of 0.04.

Contrast Transfer Function

The transfer function for an apparent scene contrast of C is given by[40]

$$T_C = \frac{C - 1}{C + 1}, \qquad (4\text{-}30)$$

which is shown in Figure 4-3. For scenes of low contrast, or for high-contrast scenes viewed through a thick intervening atmosphere, low values of image modulation are unavoidable. Imaging experience at the Moon and Mars strongly suggests that visual imaging experiment design must be predicated upon low-contrast scenes. For this study, an apparent scene contrast of 1.6 has been used, implying a transfer function value of 0.23.

Lens Transfer Function

An estimate of the theoretical resolving power of a circular lens is often arrived at by considering the diameter of the first zone of the diffraction pattern for a point source produced by the lens. This simple analysis leads to the minimum lens diameter D_d required to achieve the angular resolution $\Delta\phi$:

$$D_d = \frac{1.22\,\lambda}{\Delta\phi}, \qquad (4\text{-}31)$$

where λ is the wavelength. A more thorough analysis by Scott[39] has shown that the lens modulation transfer function for a perfect (distortion-free) lens is

$$T_L = \frac{2}{\pi}\left\{ \cos^{-1} ka - ka\left[1 - (ka)^2\right]^{\frac{1}{2}} \right\} \qquad (4\text{-}32)$$

with

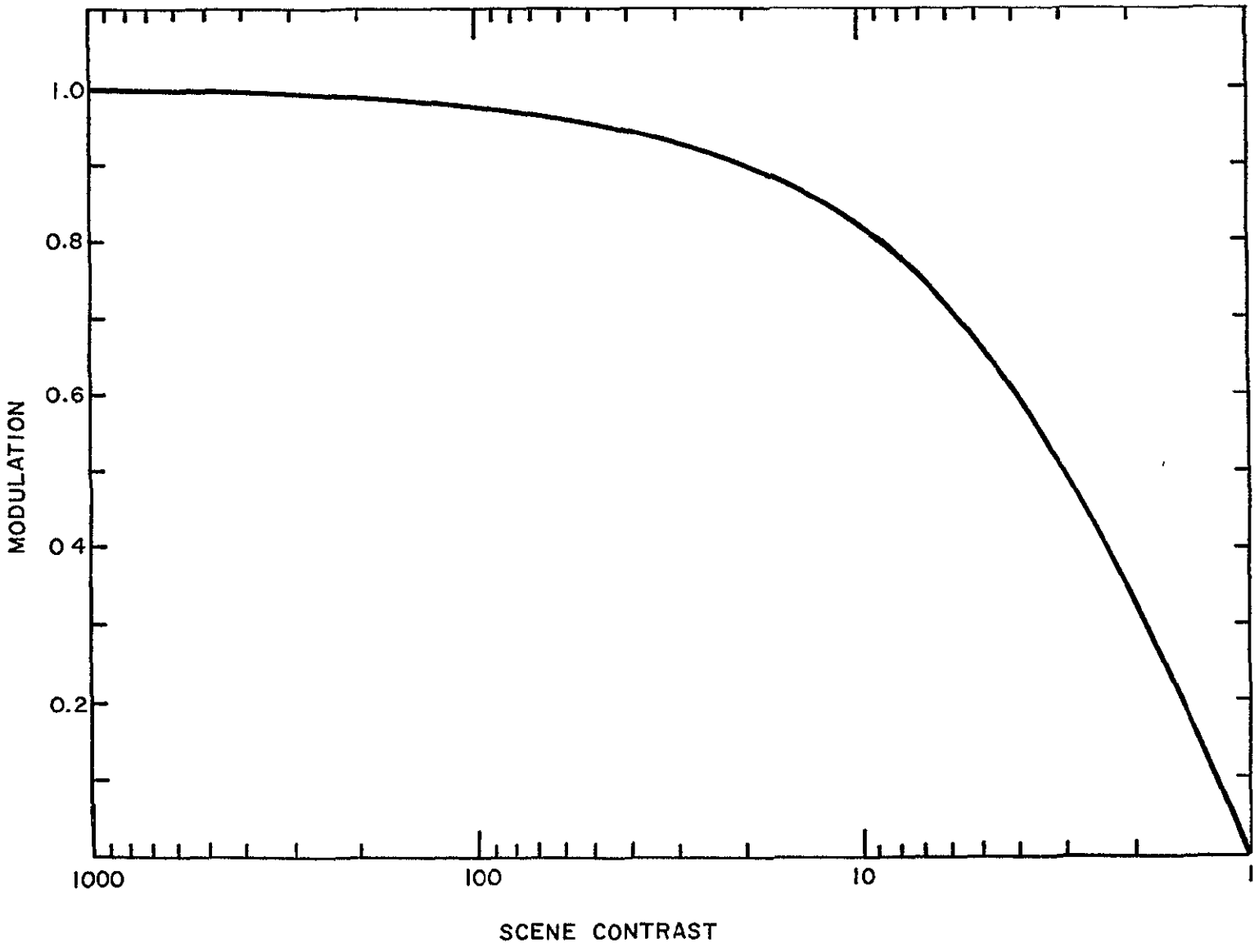

FIGURE 4-3. APPARENT CONTRAST TRANSFER FUNCTION

$$a = \frac{\lambda F}{D} , \qquad (4\text{-}33)$$

where $k = 1/x_o$,
F = lens focal length,
D = lens diameter.

Eq. (4-32) may be rewritten in terms of the ratio D/D_d, if x_o is identified with $F \cdot \Delta\emptyset$. Figure 4-4 shows then the lens transfer function dependence upon D/D_d. For a lens diameter equal to the diffraction limit of eq. (4-31), the figure shows that the transfer function is 0.085, which is near the limit of visual detection. Similarly, for a lens whose diameter is five times the diffraction limit, the transfer function is about 0.78.

Image Motion Transfer Function

During the camera exposure time, both the camera and the planetary surface are in motion. The effects of this relative motion may be analyzed by considering those components of the motion resulting in an apparent movement of the planetary scene in a horizontal plane normal to the viewing axis. Scott[39] has shown that the transfer function for such motion is

$$T_M = \frac{\sin \pi ka}{\pi ka} , \qquad (4\text{-}34)$$

where again k is the spatial frequency $(1/x_o)$, and a is the distance of the motion as measured in the image plane. If x_o is identified with $F \cdot \Delta\emptyset$, as before, then ka is simply the distance of the motion expressed in terms of ground resolution elements. Figure 4-5 shows T_M as a function of ka. For scene motion of one-half a resolution element, the transfer function has the value 0.64, while for scene motion of one resolution element, the transfer function vanishes.

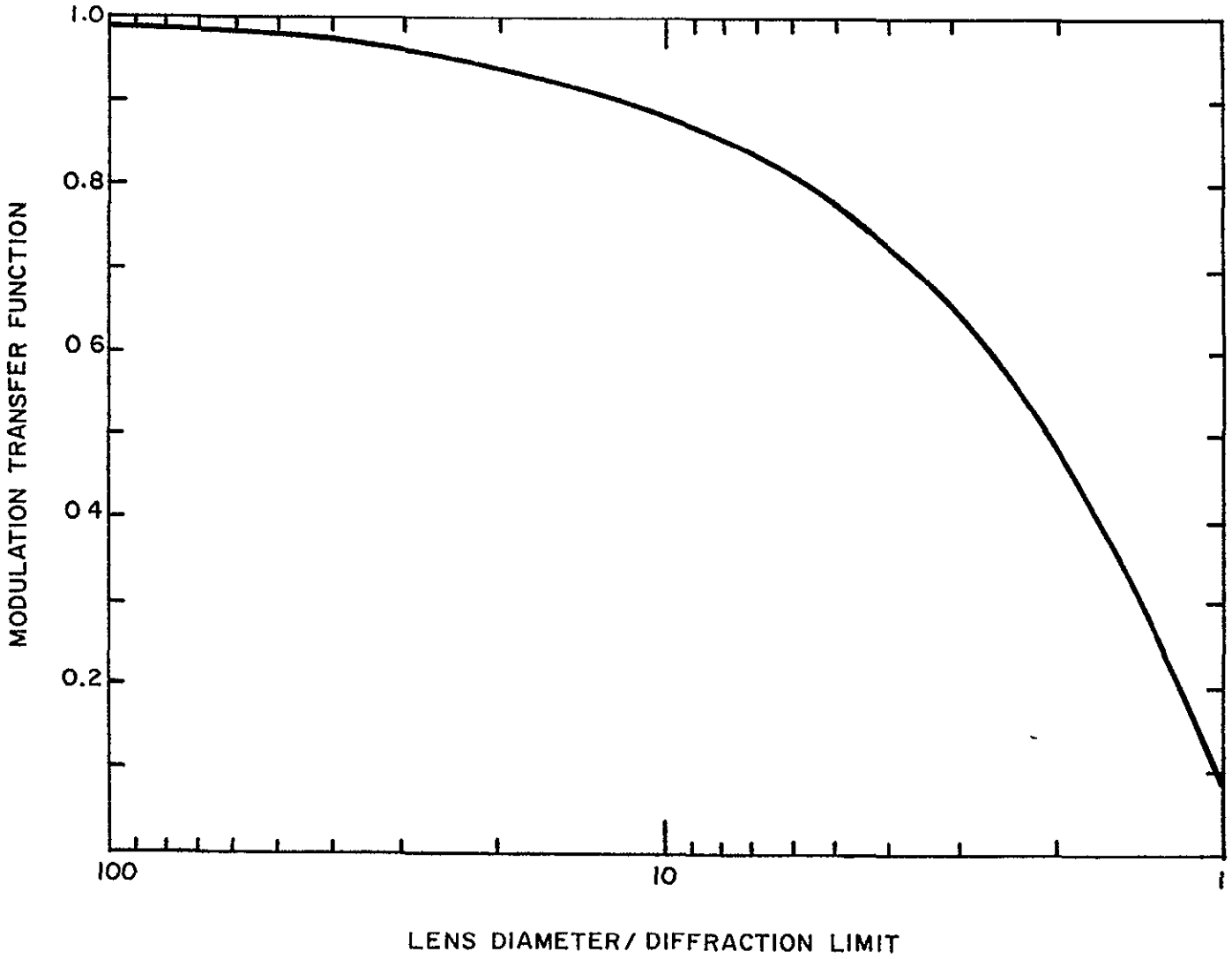

FIGURE 4-4 LENS TRANSFER FUNCTION

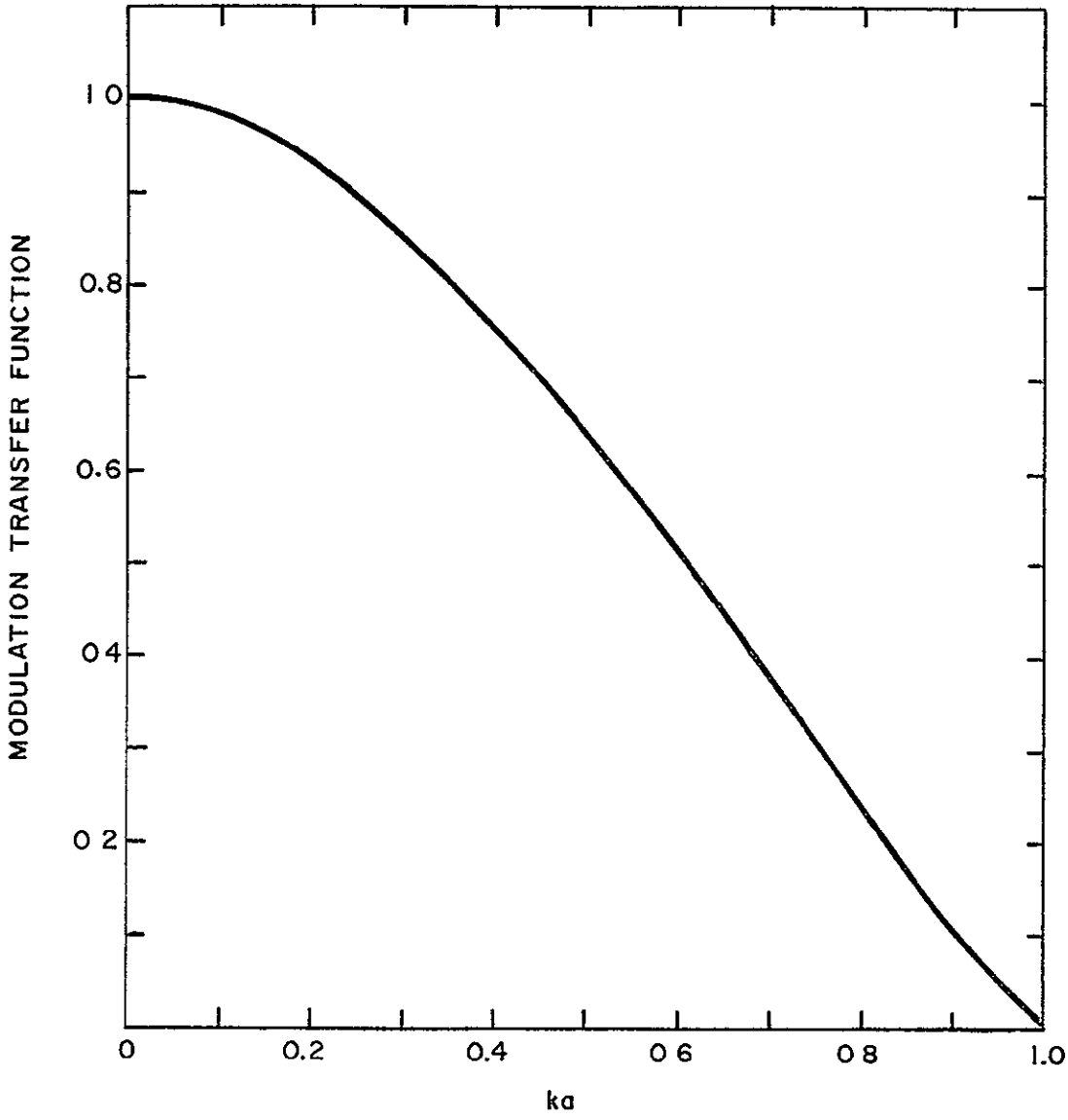

FIGURE 4-5. IMAGE MOTION TRANSFER FUNCTION

Television Camera Transfer Function

Very limited data is available for the modulation transfer function of TV camera tubes. The usual practice is to describe the tube resolution by quoting the "limiting resolution" in TV lines. For example, the RCA 2048 one-inch vidicon is characterized by a limiting resolution of 750 lines[41]. A less common, but considerably more useful, procedure is to describe the tube resolution characteristics by measuring the uncompensated peak-to-peak response, at the center of the picture, to a square-wave test pattern. Examples of these data are shown in Figure 4-6. Occassionally measurements are made of the corner response, as also shown in the figure.

It may be noted that since the limiting center resolution of the WX-30654 is quoted as 800 lines[42], the so-called limiting resolution corresponds to the number of lines at which the measured square-wave response is about 5 percent. The limiting resolution cannot be achieved when the TV tube is used in a planetary imaging application, because of low scene contrast, image motion, etc.

Approximate Analysis

Ignoring the difference between the TV tube square-wave response and its modulation transfer function (sine-wave response), system design can proceed by combining the scene contrast, lens, and image motion transfer functions, and then choosing a TV tube whose transfer function results in a final sensor system modulation of 0.04 or larger. In addition, of course, care must be taken that the camera tube provides a sensitivity adequate for the available faceplate illumination, and that a sufficient number of lines are available (at 0.04 modulation) to provide the desired ground resolution. Aside from the paucity of square-wave response data, such a detailed design procedure is beyond the scope of this study. Therefore, an approximate method of analysis which permits a more rapid estimation of experiment support requirements has been devised.

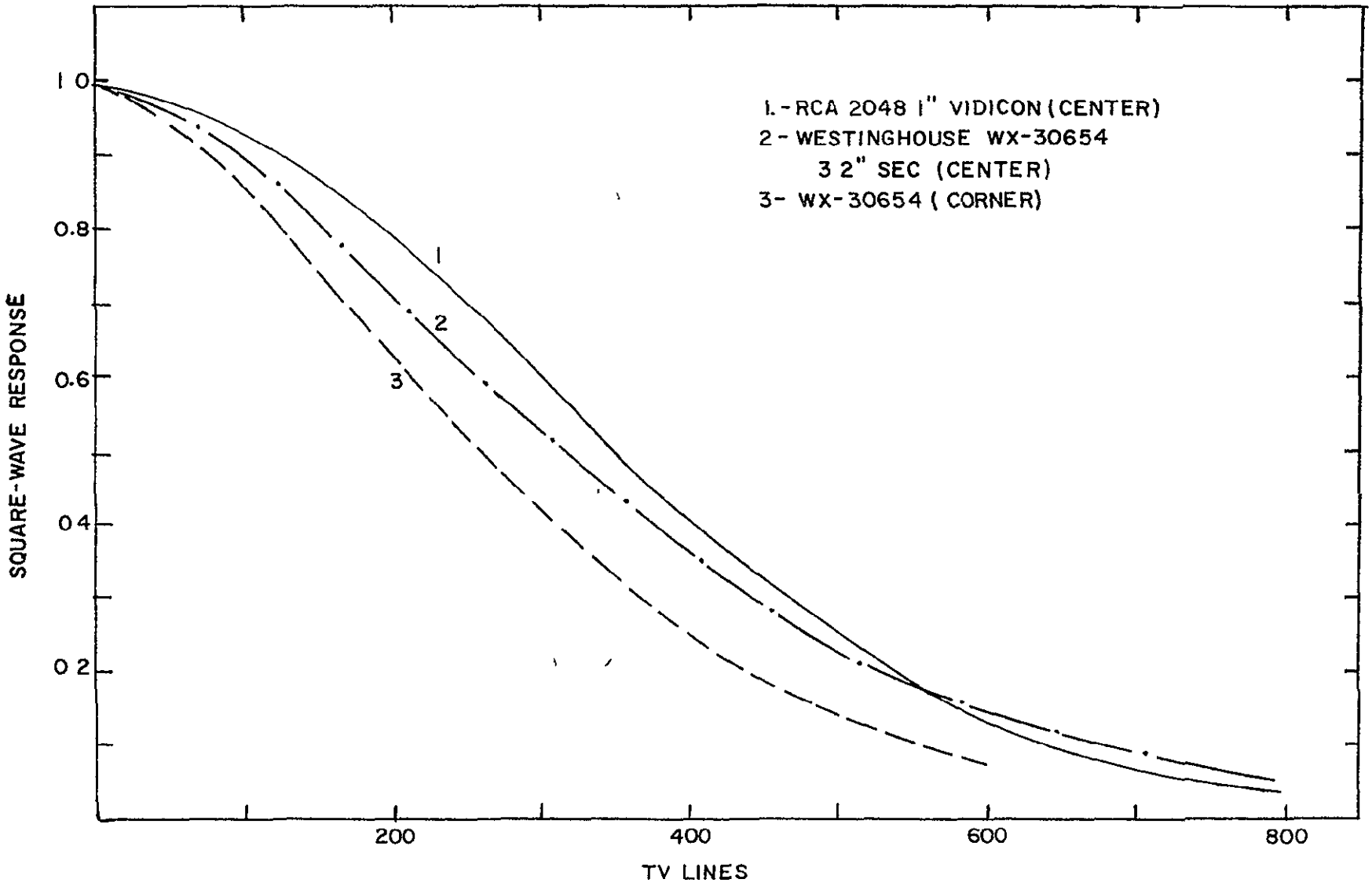

FIGURE 4-6 TV TUBE SQUARE-WAVE RESPONSE

The approximate solution also identifies marginal situations in which the experiment design could be considered in more detail.

The basis of the approximate method is to fix the apparent scene contrast, the lens diameter (relative to the diffraction limit), and the image motion. The remaining variable is the number of TV lines,and this may be chosen to provide the desired ground resolution. The tube type (rather than size) selected depends upon the available illumination. Assuming an apparent scene contrast of 1.6, an image motion of one-half a resolution element, and a lens diameter of five times the diffraction limit, the camera tube transfer function must be at least

$$T_{TV} = \frac{0.04}{T_C\ T_L\ T_M} = \frac{0.04}{0.23 \times 0.78 \times 0.64} = 0.35 \quad (4\text{-}35)$$

Clearly, the limiting resolution cannot be achieved under such operational conditions. However, the limiting resolution may be used to estimate the number of TV lines corresponding to a tube transfer function of 0.35.

Typical characteristics, including the limiting resolution, of various TV systems[30, 43-48] suitable for use in a space environment are summarized in Tables 4-6 and 4-7. These data suggest that the limiting resolution is related to tube type and size as shown in Figure 4-7. The dashed lines are speculative in that insufficient data is available on the variation of limiting resolution with tube size for image orthicons and Plumbicons. The square-wave response curves of Figure 4-6 show that at a response of 0.35, the center resolution corresponds to 410 TV lines on the 3.2-inch SEC tube. That is, the center resolution has been decreased to about fifty percent of the "limiting" resolution. Similarly, the resolution for the one-inch vidicon has been reduced from 800 to 430 lines, or to about fifty-five percent of the "limiting"

Table 4-7

TV Camera System Characteristics (Standard Vidicons)

	Tiros	RAE	Tiros X	Min. Vid.	Mar. IV	ATS AVCS	ATS AVCS	Nimbus AVCS	ESSA AVCS	APT	Rang. F	Rang. P	OAO	Surv
Tube Diameter (inches)	½	½	½	½	1	1	1	1	1	1	1	1	1	1
Resolution * (TV lines)	375		500	600	200	800	800	700	700	650	700	200	325	600
Focal Length (Millimeters)	5	5 5		28	305	12	200	17	5.7	5.7	25 76	25 76	5 5	100
Aperture Stop	f/1.5	f/1.8	f/1.5	f/2	f/8	f/1.5	f/4	f/4	f/1.8	f/1.8	f/1/2	f/1/2	f/1 8	f/4
Eff Lens Diam. (Millimeters)	3.3	3		14	38	8	50	4	3.2	3.2	38	38	3	25
Image Format (Millimeters)	6.4	6.4	6.4	6.4	5.5	11	11	11	12	11	11	2 8	11	
System Weight (lbs)	14	5	7	2	11	23	23	18	19	22	17	17	21	16
System Power (watts)	12	6	9	4	8	31	31	21	16	15	31	32	9	
System Volume (cu. in.)	340	150		20		610	1230	500	500	500	530	530	560	

* Limiting resolution at center of image plane for high contrast target.

Table 4-8

TV Camera System Characteristics (RBV and other types)

	RBV	RBV	I.O.	I.O.	I.O.	SEC	SEC	Plumbicon
Tube Diameter (inches)	2	4.5	3	3	2	2	3.2	1.3
Resolution * (TV lines)	5000-6000	6000-7000	400	200-600	650	300	1000	600
Focal Length (Millimeters)	125	150	215	25				
Aperture Stop	f/4	f/2.8	f/2.8	f/2.8				
Eff. Lens Diam. (Millimeters)	31	54	77	9				
Image Format (Millimeters)	25	51	30	36	22	14	25	14
System Weight (lbs)	18-30	50-75	60	40				
System Power (watts)	22-30	50-75	50	50				
System Volume (cu. in.)	1000-1500	2500	1500	1420				

* Limiting resolution at center of image plane for high contrast target.

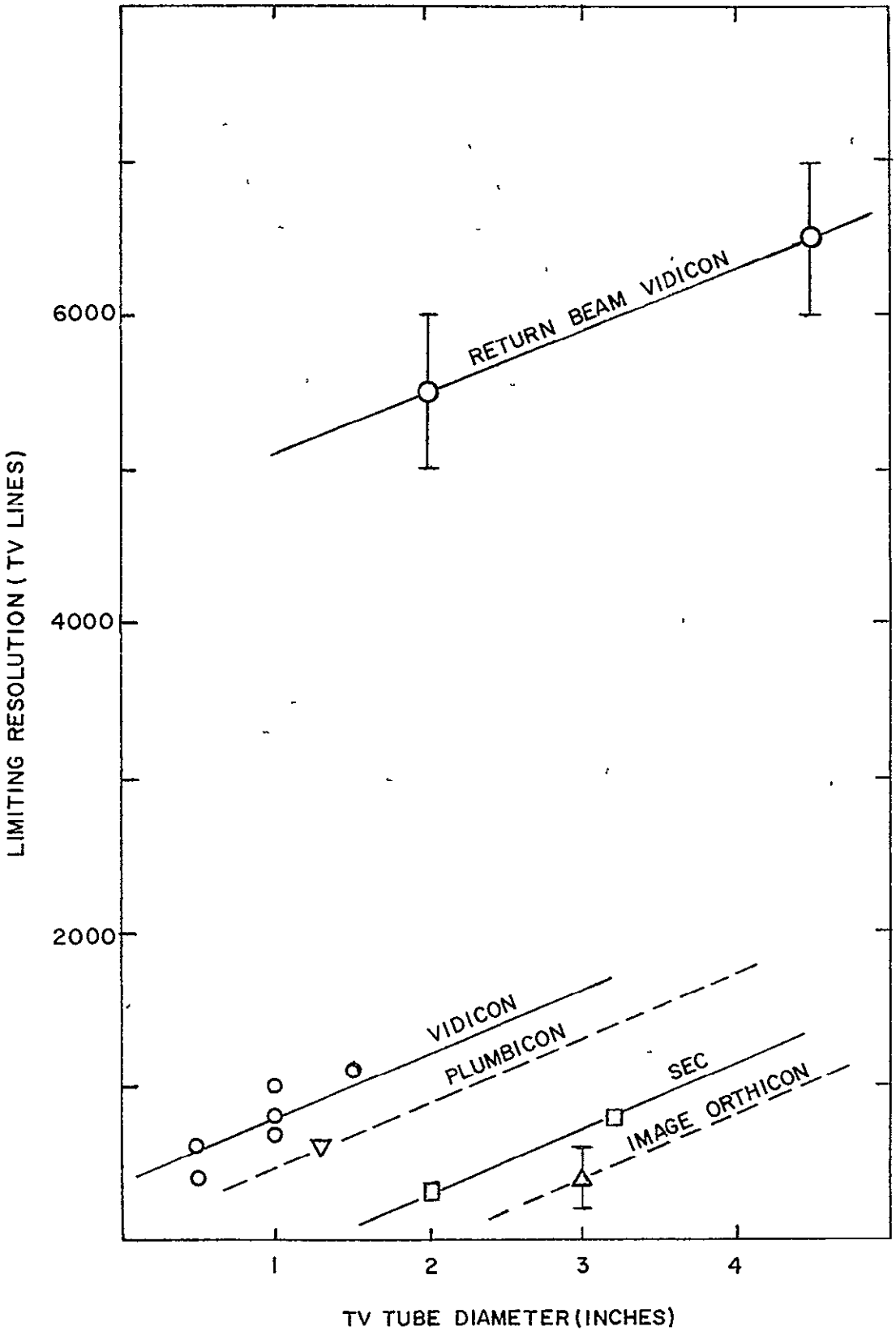

FIGURE 4-7 TV LIMITING RESOLUTION

resolution. The close similarity of these reductions, for a different tube size and type, suggests that for all sizes and types of TV tubes the center resolution at a square-wave response of 0.35 is about fifty-five percent of the limiting resolution. To ensure that adequate ground resolution is achieved throughout the picture format, the effects of resolution degradation in the corners of the picture should be accounted for. Figure 4-6 shows that at a response of 0.35, the corner resolution of the SEC tube corresponds to 340 lines, as opposed to 410 lines at the center. That is, the corner resolution is only slightly more than eighty percent of the center resolution. The approximation made in this study is that the corner resolution at a response of 0.35 corresponds to about forty-five percent of the limiting resolution (the center resolution at a response of 0.05), independent of the size or type of the TV tube. Figure 4-8 shows the "operational" resolution obtained in this manner.

As stated above, the simplified method of analysis assumes a lens diameter equal to or greater than five times the diffraction limit. If L is the total number of lines on the tube face, and ℓ is the linear size of the image format, the angular resolution is

$$\Delta\phi = \frac{\ell}{LF} , \qquad (4\text{-}36)$$

where F is the focal length. Using eq. (4-31) for the diffraction limit, the lens diameter must satisfy

$$D \geq \frac{3.66 \times 10^{-3}\ LF}{\ell} \text{ millimeters}, \qquad (4\text{-}37)$$

where λ has been taken as 6000 Å. The focal length is determined by the image format size and the camera field-of-view,

$$F = \frac{\ell}{2 \tan \phi} ; \qquad (4\text{-}38)$$

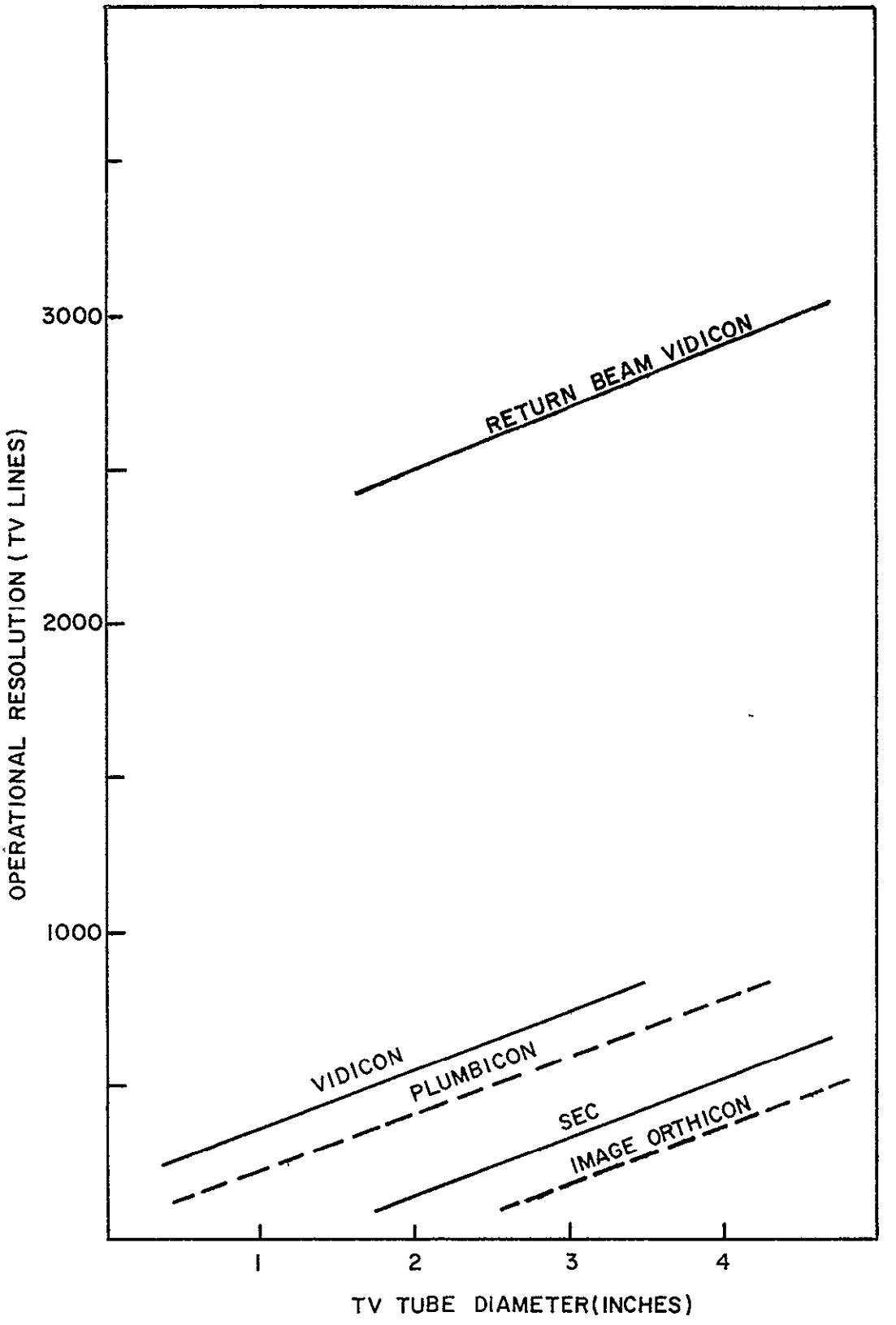

FIGURE 4-8. TV TUBE OPERATIONAL RESOLUTION

hence eq. (4-37) becomes

$$D \geq \frac{1.83 \times 10^{-3} L}{\tan \phi} \text{ millimeters,} \qquad (4\text{-}39)$$

and ϕ has been given by eq. (4-2).

Limiting the extent of image motion to one-half resolution element implies some limitation on the camera exposure time. That is, the product of the exposure time and the apparent velocity of the scene as it moves underneath the camera must be less than one-half the desired ground resolution. As shown in Section 1.5, the maximum apparent horizontal velocity of the planetary surface as seen by the camera is

$$v_h = (v_p^2 + v_r^2 + 2v_p v_r \cos I)^{\frac{1}{2}} \qquad (4\text{-}40)$$

where v_p is the horizontal speed of the subsatellite point, v_r is the equatorial speed due to planet rotation, and I is the orbit inclination. Vertical motion of the camera will also result in an apparent horizontal velocity of points on the imaged surface. For example, if the camera system moves vertically upward during the exposure time, points on the surface will appear to move horizontally toward the subsatellite point with a velocity proportional to the distance from the subsatellite point. It can be shown that the maximum apparent velocity of a point on the surface is $v_v \tan \phi$, where v_v is the vertical velocity of the camera, and ϕ is the half-angle field-of-view. The computation of v_v has been discussed in Section 1.5. The maximum apparent horizontal speed of any point on the imaged surface is then $v_h + v_v \tan \phi$.

In this study, two-thirds of the half-resolution element limit is allocated for translational motion effects, the remaining one-third being held in reserve for apparent motion due to rotation of the camera. Thus the maximum exposure

time is taken as

$$t_e \leq \frac{r}{3(v_h + v_v \tan \phi)} \quad \text{(w/o IMC)}, \qquad (4\text{-}41)$$

in absence of IMC (image motion compensation), where r is the desired ground resolution.

Campen and Stallkamp[49] have estimated that single-direction IMC can compensate for 90 percent of the apparent motion due to the spacecraft's horizontal speed, rotation normal to the optical axis, and planet rotation. Compensation for the apparent motion due to vertical movement of the camera would require a zoom lens coupled to an altitude sensor. Other authors[29,30] have suggested that 99 percent, or even 99.9 percent, of the spacecraft's horizontal motion can be compensated for. An accurate estimate of the uncompensated camera horizontal speed must take into account such factors as the camera true velocity, image format size, altitude, and the nature of the compensation mechanism. It is conservatively assumed here that a simple single-direction IMC mechanism will compensate for 90 percent of the camera horizontal speed and planet rotation. Thus, with IMC, the maximum exposure time is

$$t_e \leq \frac{r}{3(0.1\, v_h + v_v \tan \phi)} \quad \text{(w/IMC)}. \qquad (4\text{-}42)$$

Before passing on to the support requirements, an additional useful relation may be derived from the data presented in Tables 4-6 and 4-7. The image format size on the face of the TV tube is required in computing the signal-to-noise ratio and the lens focal length. The data presented in the tables suggests that the image format (for a 1:1 aspect ratio) is related to TV tube diameter as shown in Figure 4-9. Except for SEC vidicons, there appears to be about 11.3 mm of image length (or width) per inch of face plate diameter.

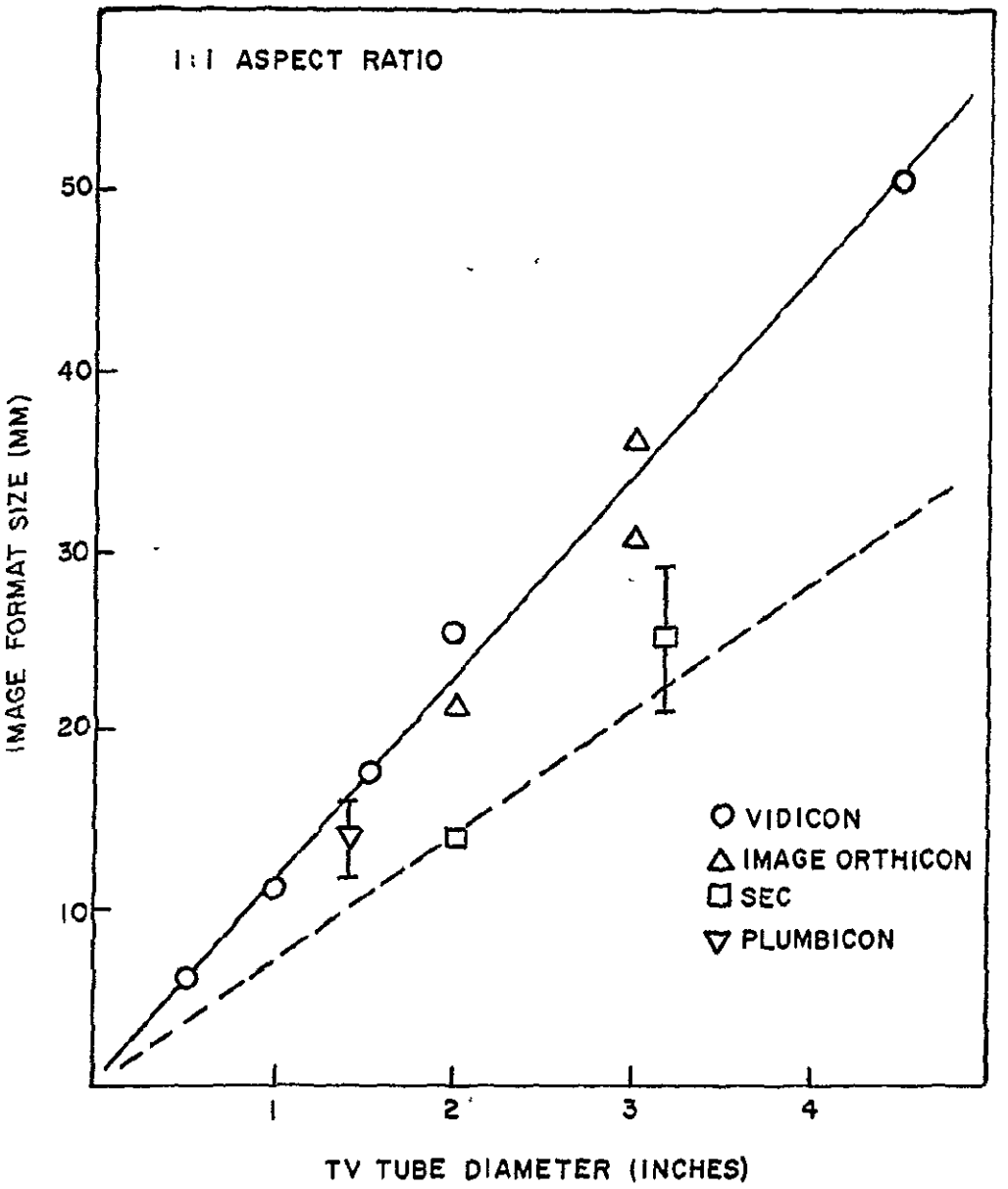

FIGURE 4-9. FORMAT SIZES

4.2 Support Requirements

4.2.1 Camera System Weight

The data presented in Tables 4-6 and 4-7 suggest that space-qualified TV camera system weights depend upon camera tube diameter as shown in Figure 4-10. Each inch of tube diameter is equivalent to about sixteen pounds of camera system weight. No dependence upon tube type (as opposed to size) is evident from the data shown. Current state-of-the-art limits TV tube diameters to 4.5 inches. Actually, the 4.5-inch RBV is in the development stage, rather than existing as a fully-qualified system. Some additional development could lead to TV tubes nearly six inches in diameter, but 4.5 inches is the maximum size considered in this study. For the range of tube sizes considered, camera system weights estimated by use of the solid line in the figure are accurate to within a factor of two. However, extensive use of micro-miniaturization techniques, as exemplified by the two-pound miniature half-inch vidicon, might result in system weights about one-fourth of those indicated by the solid line. The support requirements estimated in this study have been based upon sixteen pounds per inch diameter, i.e., the solid line in the figure. The system weights depicted in Figure 4-10 are appropriate for simple camera systems which do not utilize large optical subsystems, IMC devices, or zoom lenses. Additional weight is required for such refinements.

The largest effective lens diameter (obtained by dividing the focal length by the f-number) represented by the data shown in Figure 4-10 is about 87 millimeters. The estimated weight of an optical subsystem of this size is somewhat less than three pounds, which is a small fraction of the 21 pound total system weight. Optical subsystems containing lenses of one hundred millimeters or larger will constitute an appreciable fraction of the total system weight. Therefore, for lens diameters of ten centimeters or larger, an optical

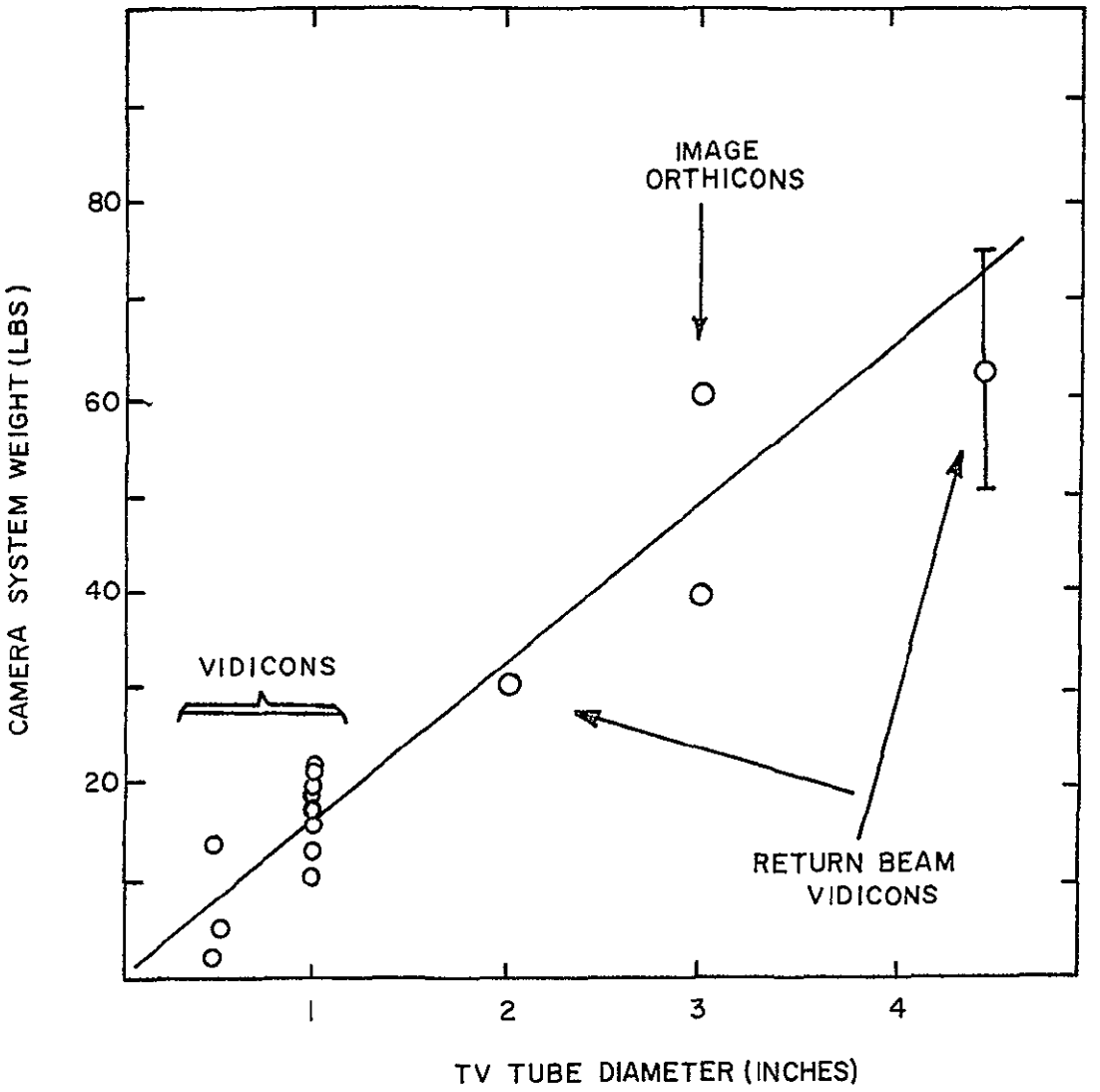

FIGURE 4-10. TV CAMERA SYSTEM WEIGHTS

subsystem weight must be added to the system weight estimated from Figure 4-10. Slater and Johnson[29] have studied the dependence of optical subsystem weight upon collecting optics diameter for space-qualified systems. Figure 4-11 is reproduced from their report. The data can be reasonably well approximated by

$$M_c = 0.037\ D_c^2 \qquad (4\text{-}43)$$

where M_c is the weight of the optical subsystem in pounds; and D_c is the diameter of the collecting optics in centimeters. Bashe and Kennedy[30] have examined the weights of long focal length optical subsystems with the results shown in Figure 4-12, which is reproduced from their report. For comparison, the dashed line in the figure shows weights estimated by using eq. (4-43). The data of Bashe and Kennedy are not confined to optical systems designed for space use, while the Slater and Johnson data are. Since emphasis is placed upon weight reduction in the design of space optical systems, it is not surprising that eq. (4-43) leads to lower weight estimates than implied by the analysis of Bashe and Kennedy.

There is, in principal, no limit to the size of optical systems, provided the necessary surface tolerances can be achieved and one is willing to pay a very high weight penalty, not only for the optics, but for the necessary thermal control. Although 200-inch optical systems have been used on Earth, a reasonable upper limit to the size of optical systems designed for space orbital use appears to be about two meters. Eq. (4-43) implies that such an optical system would weigh about 1500 pounds. For large reflective systems, a segmented mirror with active control aligning the segments is feasible[50]. In any case, the surface quality of the optical system should be characterized by rms deviations of $\lambda/20$ or less. Crane[50] has shown that at high spatial frequencies the system

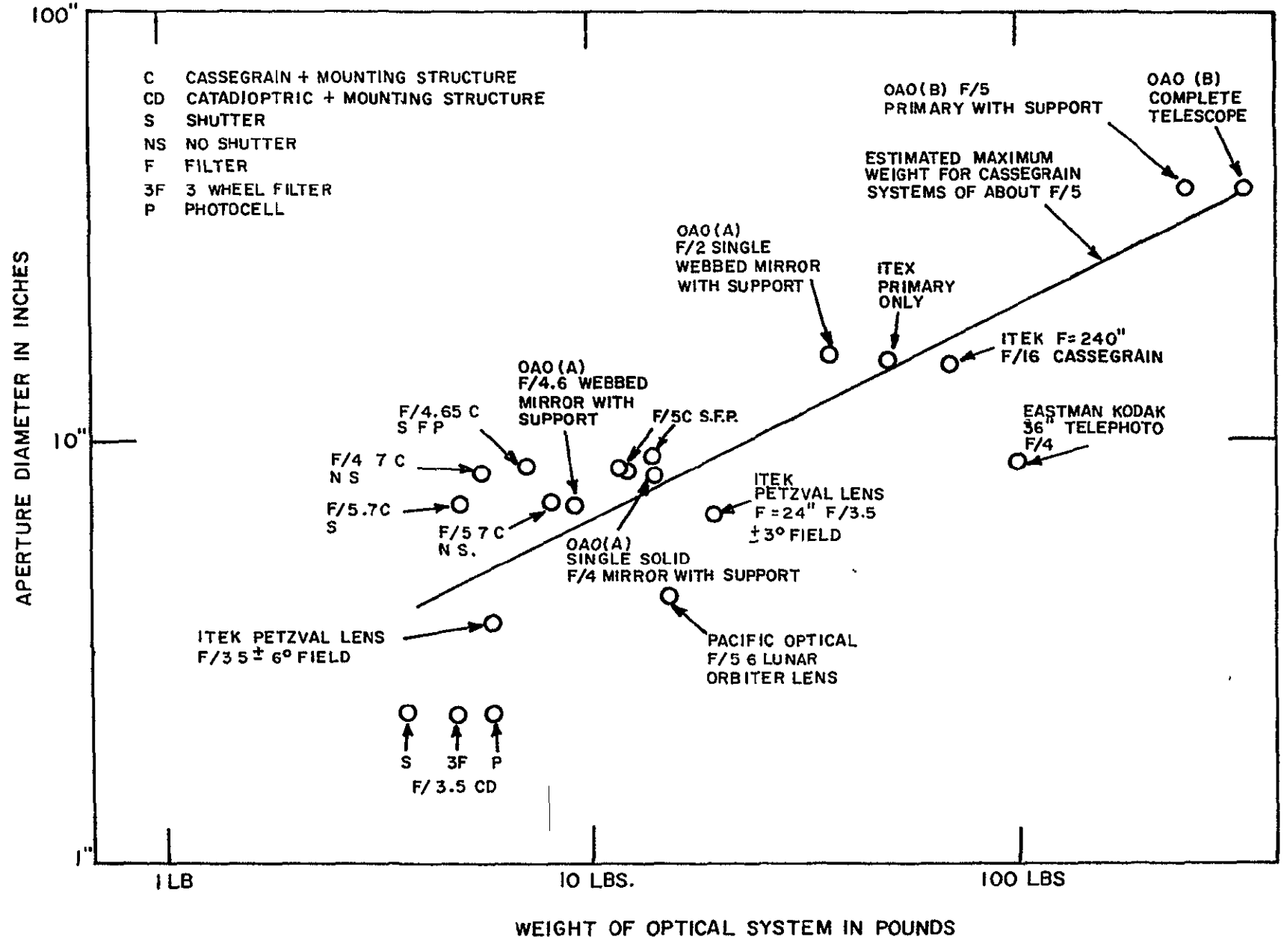

FIGURE 4-11 APERTURE DIAMETER VERSUS WEIGHT FOR A VARIETY OF SPACE OPTICAL SYSTEMS

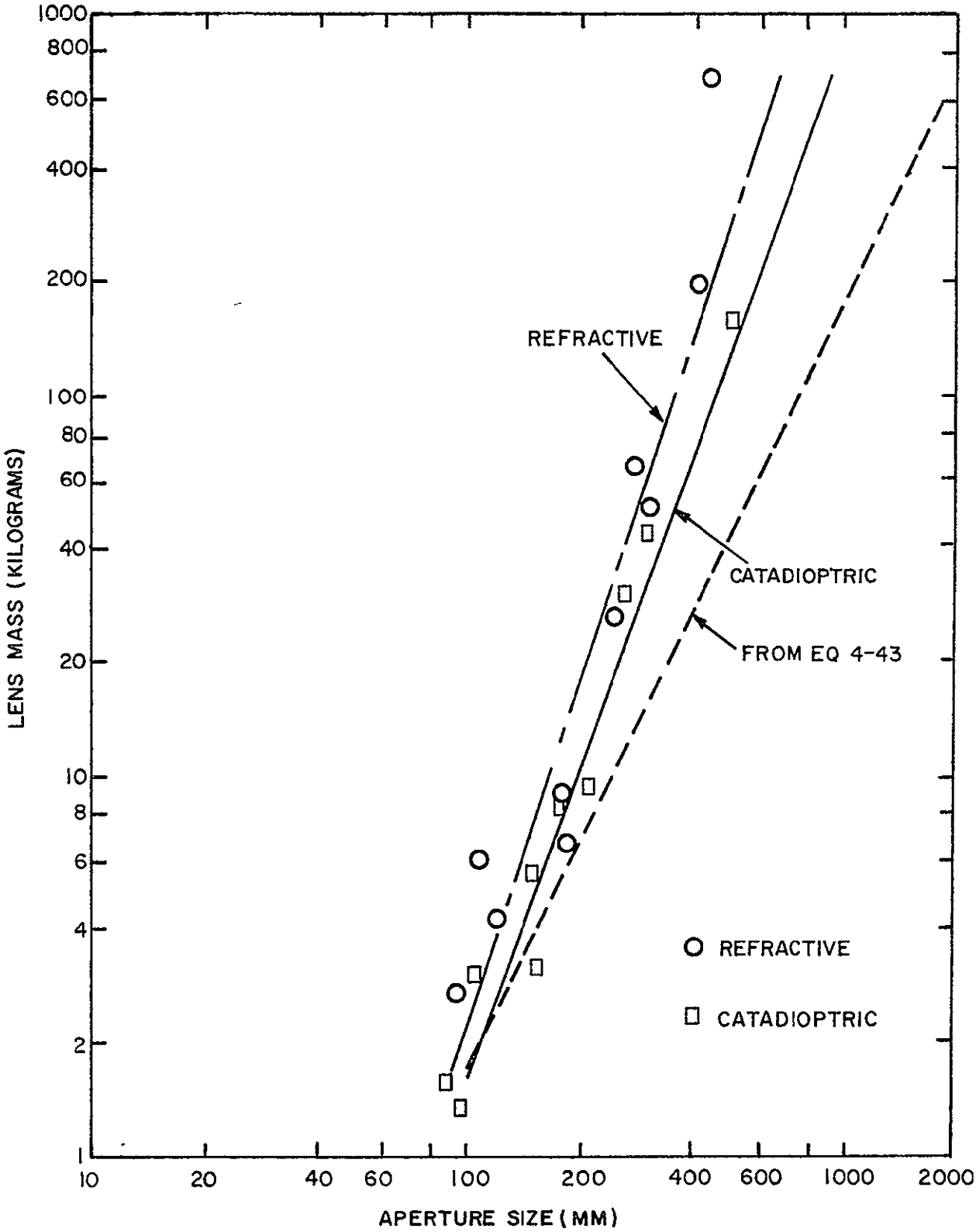

FIGURE 4-12. APERTURE SIZE VS MASS FOR REFRACTIVE AND CATADIOPTRIC OPTICAL SYSTEMS.

modulation transfer function will be degraded according to

$$T = \exp\left[-\left(\frac{2\pi\delta}{\lambda}\right)^2\right] \qquad (4\text{-}44)$$

where T is the modulation transfer function, λ is the wavelength, and δ is the optical surface rms deviation. For convenience, eq. (4-44) is represented in Figure (4-13) as a function of surface deviation. The figure shows that for rms deviations of $\lambda/20$, the modulation transfer due to surface imperfections is about 0.91. The effects of optical surface quality have not been included in the support requirements estimated in this study.

In some cases, it is advantageous to consider camera systems which include variable focal length (zoom) lenses. This is particularly the case when the spacecraft is operating on an elliptical orbit. Since most zoom lenses are three-element systems, it is assumed here that a zoom optical system weighs three times as much as a fixed focal length system. Furthermore, the system optical transmission η, as used in eqs. (4-10), (4-12), and (4-22) should be multiplied by about 0.9 to account for transmission losses in the zoom lens. Zoom lenses may not be practical for optical systems larger than about ten centimeters in diameter. In order that the focal length be properly adjusted with orbit altitude, the operation of the zoom lens must either be pre-programmed or be coupled to an on-board altimeter. Recent design studies[51] indicate that a radar altimeter weighs about 25 pounds and consumes 10 watts of power. Thus for lens diameters of less than ten centimeters, the weight of a zoom camera system is found by adding 25 pounds to the weight estimated from Figure 4-10 plus twice the weight given by eq. (4-43). For lens diameter greater than ten centimeters, three times the weight given by eq. (4-43) should be added.

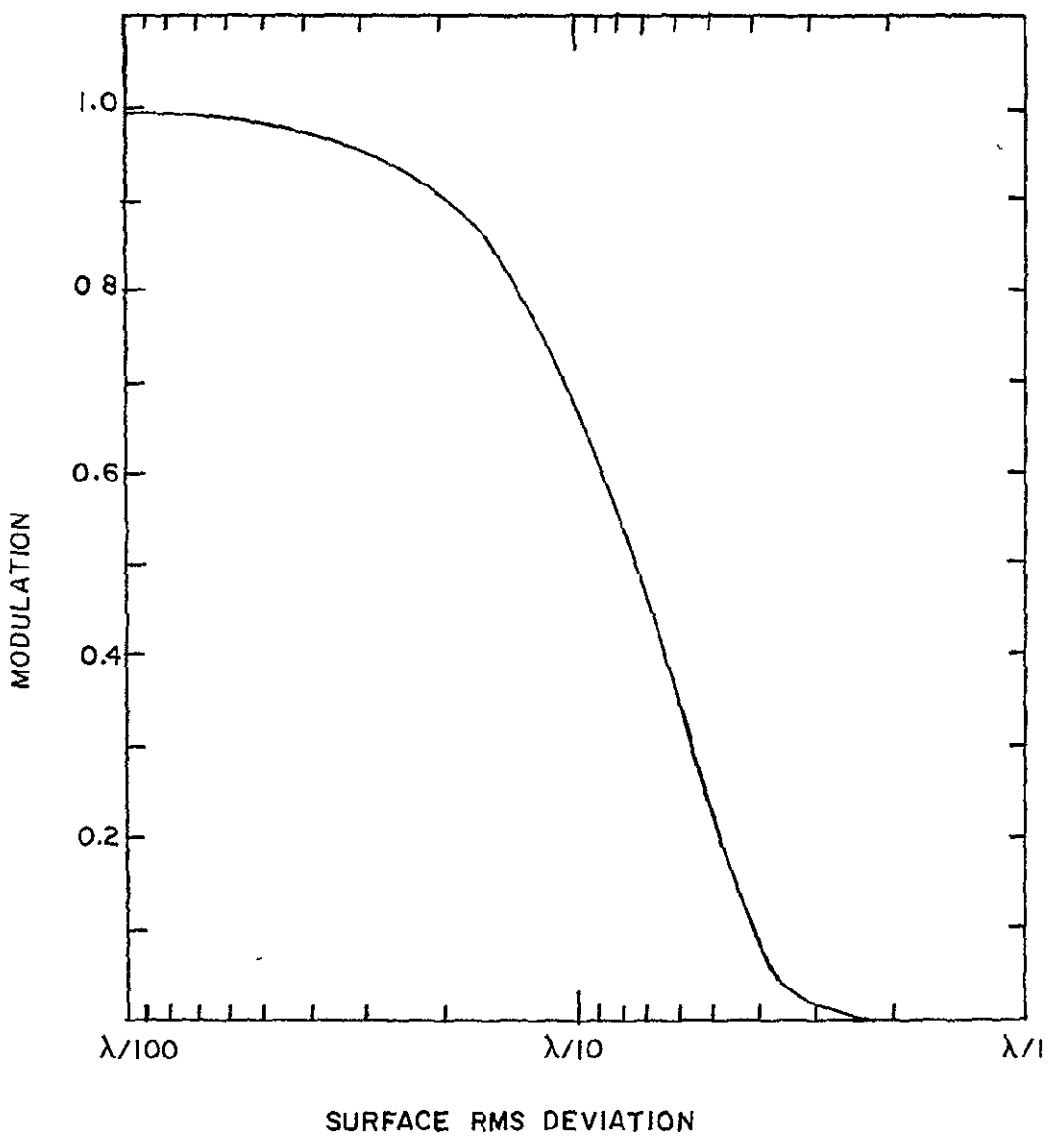

FIGURE 4-13. EFFECT OF OPTICAL SURFACE QUALITY

Only sparse data are available concerning space-qualified IMC systems. The Surveyor mirror assembly[45], which is an IMC-like device, weighed 4.7 pounds, and required ten watts of operating power. The Lunar Orbiter V/H sensor[52] weighed 10.5 pounds, required 10.5 watts of power, and had a volume of 450 cubic inches. Campen[49] has estimated that a unidirectional IMC system weighs twenty pounds. For purposes of support requirement estimation, it is assumed here that a single-direction IMC system, consisting of a nodding mirror and a V/H sensor, weighs fifteen pounds, requires fifteen watts of power, and occupies a volume of 800 cubic inches.

Table 4-8 summarizes the estimation of orbital TV system weights. These estimates are unreliable for tube diameters larger than six inches, or optical system diameters larger than two meters.

4.2.2 System Volume

The data of Tables 4-6 and 4-7 suggest that camera system volume is related to TV tube diameter as shown in Figure 4-14. The implied scaling coefficient is 560 cubic inches per inch of tube diameter. For lens diameters larger than ten centimeters, additional volume is required for the optical subsystem. This may also be the case for long focal length systems. Thus for a lens larger than ten centimeters, or for focal lengths longer than 20 centimeters, an optics volume of approximately

$$V_c = F\, D_c^2 \qquad (4\text{-}45)$$

should be added to the camera system volume. This expression is based on the volume of a right circular cylinder of diameter $1.1\, D_c$ and height $1.1\, F$. The total volume may then be a slight overestimate, since some optics volume is included in the basic camera system volume obtained from Figure 4-14. As mentioned above, approximately 800 cubic inches should also

Table 4-9

TV Camera System Weight Estimation

Type of System	Total System Weight (pounds)	
	$D_c \leq 10$ cm	$D_c > 10$ cm
Basic Camera	$16\ D_t$	$16\ D_t + 0.037\ D_c^2$
Camera + IMC	$15 + 16\ D_t$	$15 + 16\ D_t + 0.037\ D_c^2$
Camera + Zoom	$25 + 16\ D_t + 0.074\ D_c^2$	$25 + 16\ D_t + 0.111\ D_c^2$
Camera + Zoom + IMC	$40 + 16\ D_t + 0.074\ D_c^2$	$40 + 16\ D_t + 0.111\ D_c^2$

D_c = Lens diameter (cm) D_t = TV tube diameter (inches)

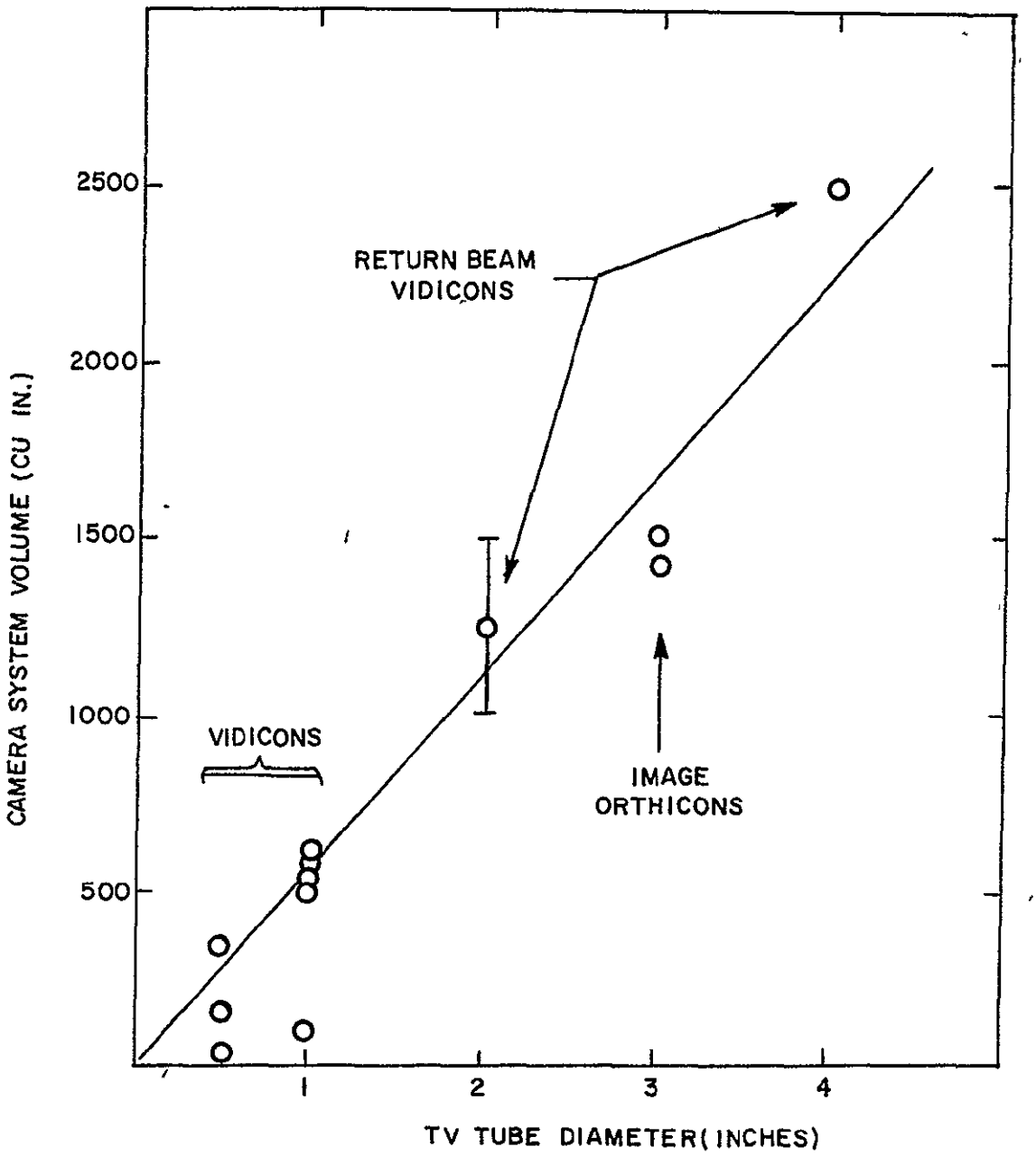

FIGURE 4-14. CAMERA SYSTEM VOLUME

be added if IMC is employed. If an altimeter is used to control a zoom lens, about 1000 cubic inches should be added to the system volume for the altimeter. It may be noted that optical focal lengths may be reduced by folding the optical path length. However, each additional optical element added to the system involves a transmission or reflection factor of about 0.95. Thus, if the focal length is reduced a factor of two by folding the optical path length, the system optical transmission factor should be multiplied by 0.95, etc.

No attempt has been made to estimate camera system shape, as the shape may be tailored to fit specific spacecraft installations. However, the shape must satisfy certain constraints. Two linear dimensions must be large enough to accommodate the TV tube diameter, or the optical subsystem diameter (approximately $1.1D_c$), whichever is larger. The third linear dimension should accommodate the sum of the focal length and the length of the TV tube. Figure 4-15 gives the dependence of tube length upon tube diameter.

4.2.3 System Power

Figure 4-16 shows the dependence of camera-system power upon TV tube diameter, as suggested by the data in Tables 4-6 and 4-7. Each inch of TV tube diameter is associated with about sixteen watts of power. Fortuitously, this is the same numerical scaling coefficient as obtained for camera system weight. Thus, camera system basic weights and powers are estimated rapidly by assuming sixteen pounds and sixteen watts for each inch of tube diameter. Micro-miniaturization may result in basic system power requirements about one-half those implied by the figure. Power requirements estimated in this study are based on the solid line in the figure. As mentioned above, if IMC equipment is included in the system, an additional fifteen watts is required. Yet another ten watts is required for operation of an altimeter, if a zoom lens is included in the system. The system average power requirement estimation is summarized in Table 4-9.

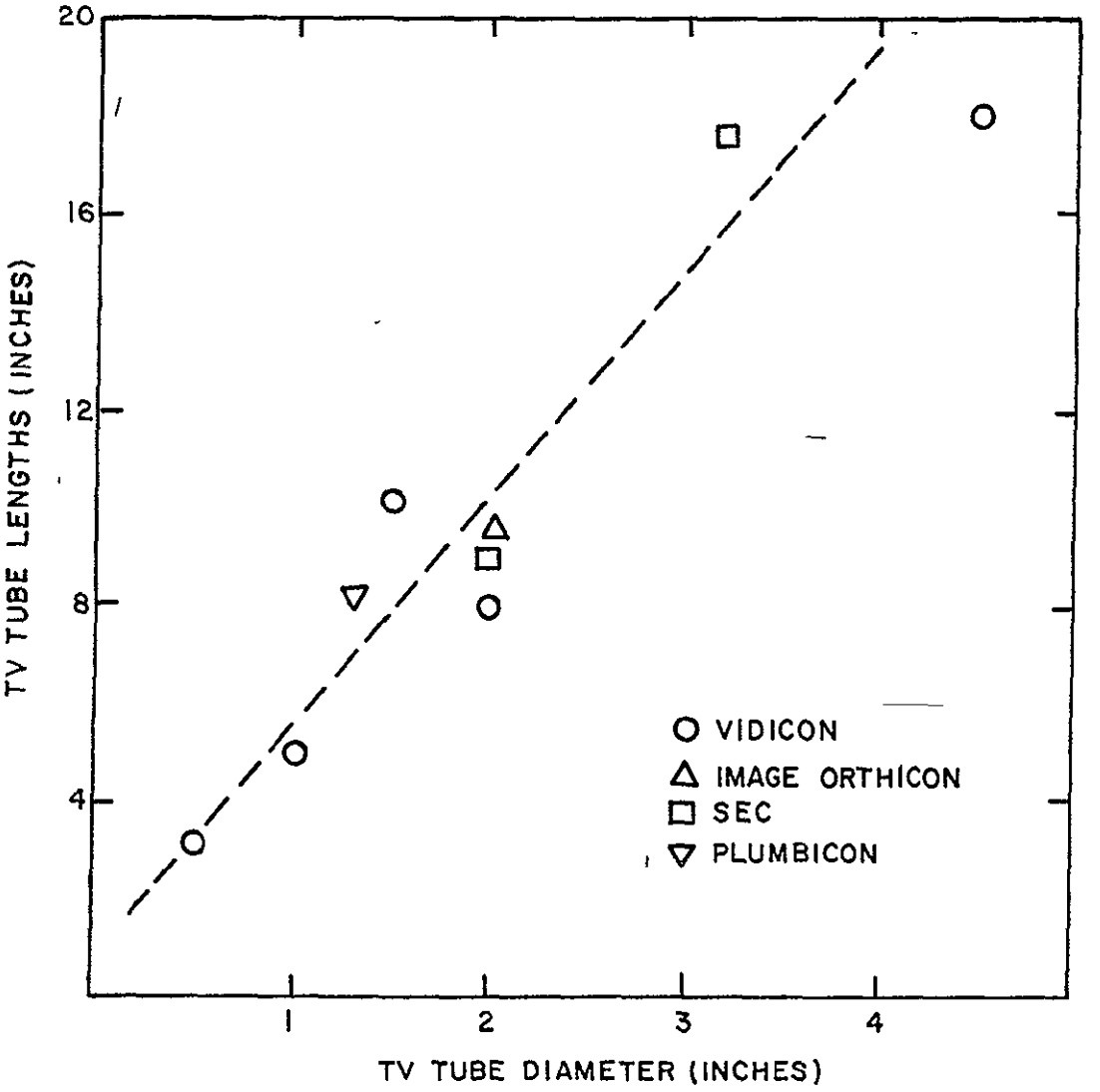

FIGURE 4-15. TV TUBE LENGTHS

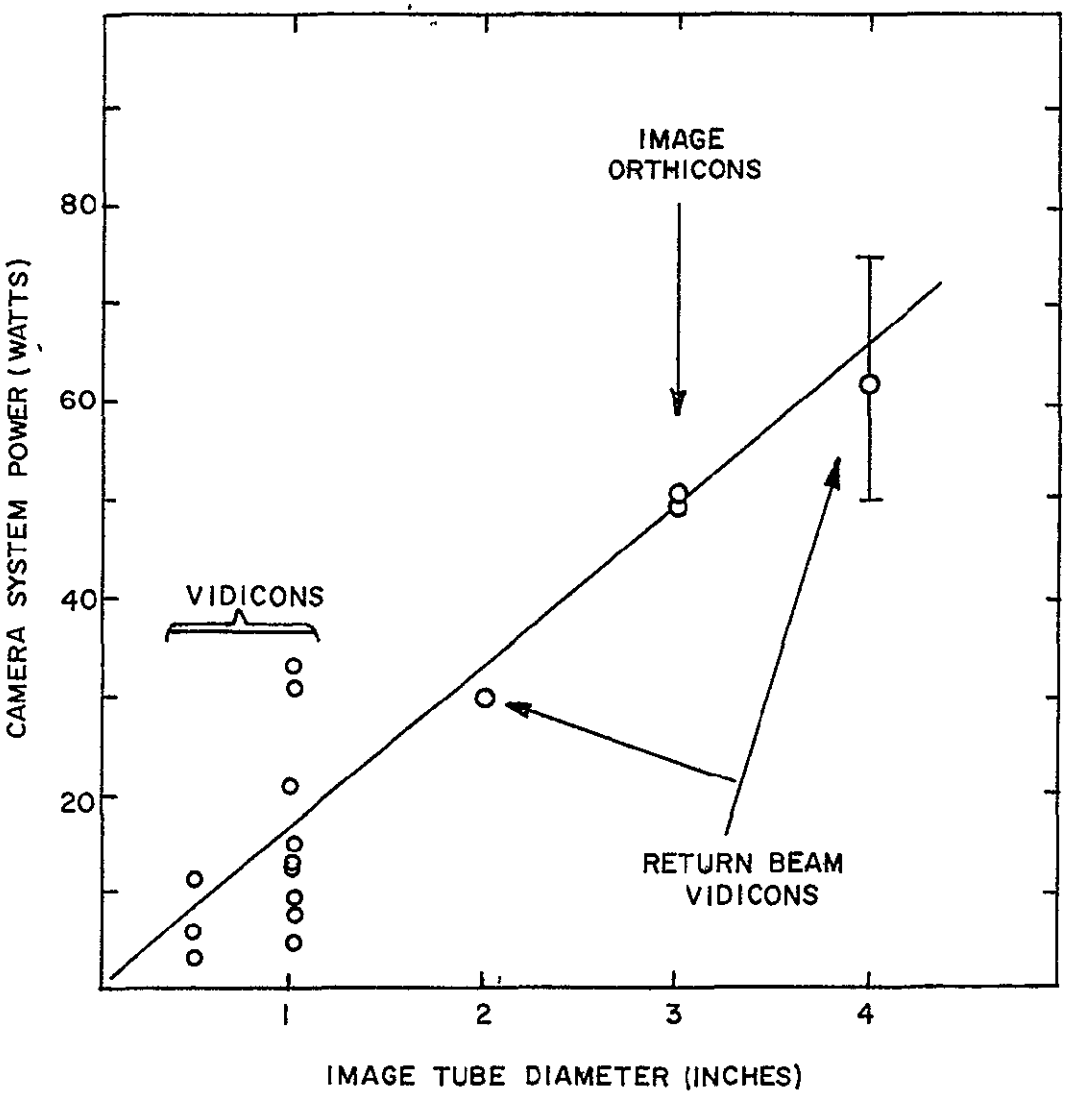

FIGURE 4-16. CAMERA SYSTEM POWER

Peak power requirements are probably twice the average. The scaling laws in the table are unreliable for camera tubes larger than six inches in diameter.

Table 4-10
TV Camera System Power Estimation

Type of System	System Power Requirement (watts)
Basic camera	$16\ D_t$
Camera + IMC	$15 + 16\ D_t$
Camera + zoom	$10 + 16\ D_t$
Camera + zoom + IMC	$25 + 16\ D_t$

D_t = TV tube diameter (inches)

4.2.4 Data Acquisition Rate

The image on the TV tube face consists of approximately L x L picture elements, where L is the number of TV lines. If G binary bits are required to describe each picture element, the total number of data bits required for each image is GL^2. The data rate then depends upon how quickly this information must be transferred from the image tube to the communications and data storage subsystem. If an image is to be acquired every t_c seconds, where t_c is the camera cycle time, a lower limit on the data rate is

$$DR \geq \frac{GL^2}{t_c} \quad \text{bits/sec.} \tag{4-46}$$

The actual data rate may be somewhat higher than this, inasmuch as some small time interval may be required to erase the previous image from the tube face by flooding the face with light. In this study it is assumed that a minimum of 0.1 seconds is required for faceplate preparation. That is, the information must be transferred from the image tube at least 0.1 seconds before acquisition of the next image. Thus the cycle time used

in eq.(4-46) is typically 0.1 seconds less than the image interval time.

The cycle time, or more accurately the image interval time, is the time required for the sensor system to fly to the position where the next image is to be procured. An estimate of this time is given by

$$t_c = \frac{W(1 - g)}{v_h} , \qquad (4\text{-}47)$$

where W is the image ground size, g is the fractional image overlap along the heading line, and v_h is the maximum apparent horizontal speed of the spacecraft. For pseudo-color imagery, in which the scene is viewed alternately through red, green, and blue filters, and the data from the three images are processed to reconstruct a color image, three images must be acquired in the time t_c, and hence the data acquisition rate is three times that given by eq. (4-46).

For long image interval times, the effects of a long storage time on the tube face must be considered. For some types of image tubes, lateral charge leakage along the photoconductor results in a decrease of resolution with increasing tube storage times. This effect is not usually significant for image orthicons and SEC vidicons. A typical slow-scan vidicon having a limiting resolution of about 600 lines after a 10 second storage time will have about 500 line resolution after a storage time of 100 seconds, as shown in Figure (4-17). The limiting resolution appears to be inversely proportional to the logarithm of the storage time. The data rates estimated in this study have assumed a maximum tube storage time of 100 seconds, and the effect of this storage time on resolution has been ignored.

4.2.5 Attitude Control and Platform Stability

If the camera system is to be oriented with sufficient accuracy that the principal point of the image be within Δr

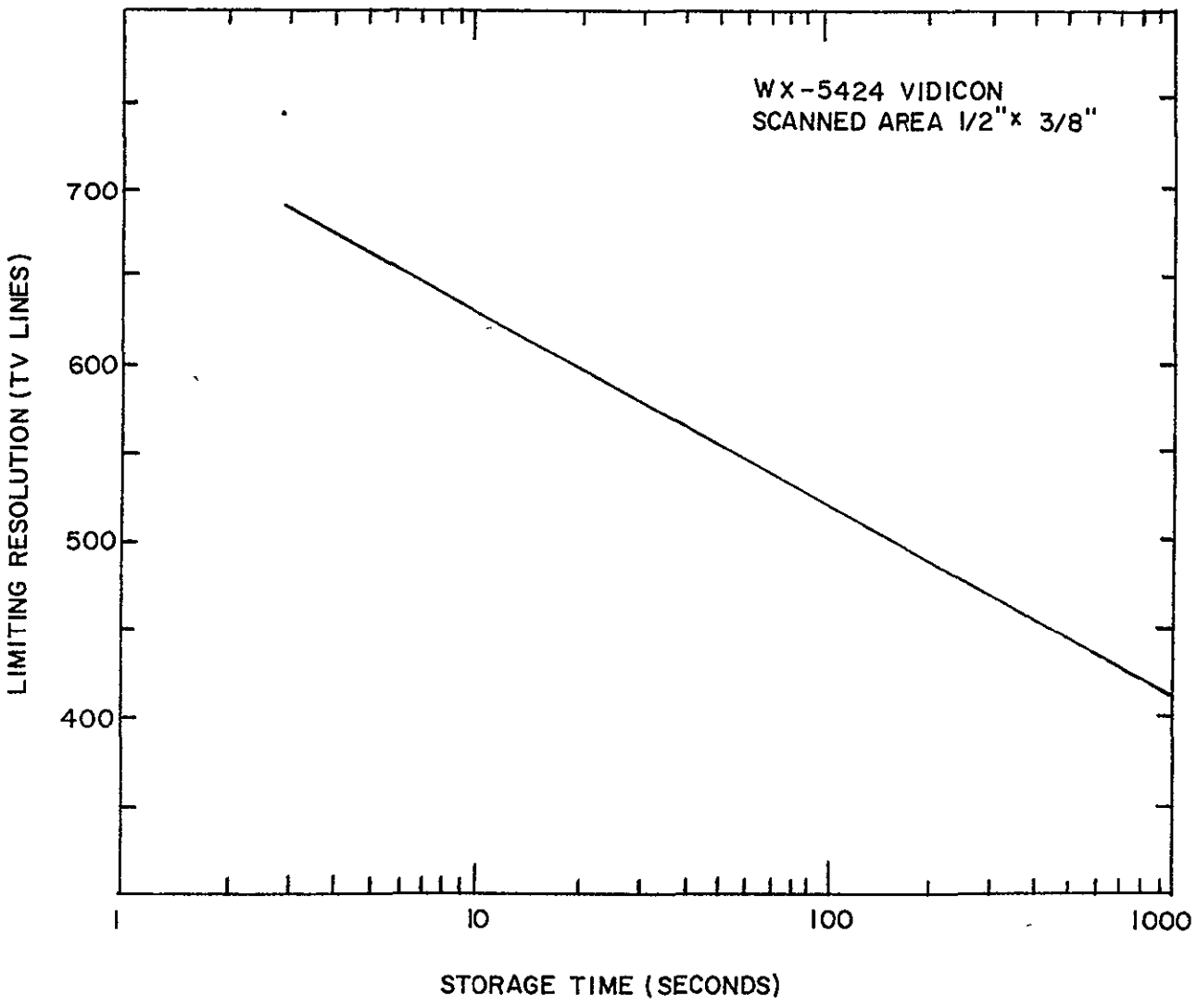

FIGURE 4-17. LOSS OF RESOLUTION WITH STORAGE TIME

ground distance from the sub-satellite point, the required pointing accuracy is

$$\Delta\phi = \frac{\Delta r}{H} \quad \text{radians.} \tag{4-48}$$

For camera rotation about the vertical optical axis (yaw), let x be the apparent motion of a point on the surface during the exposure time t_e, and let S be the horizontal ground distance from the point to the nadir point. If θ is the rotation rate, then

$$x = S\dot{\theta}\, t_e \,. \tag{4-49}$$

If x is permitted to be 1/6 the size of a resolution element, and if S is taken as W/2, then the maximum allowable yaw rate is

$$\dot{\theta} = \frac{r}{3t_e W} \quad \text{rad/sec.} \tag{4-50}$$

It is further assumed that simple IMC cannot relax this requirement

For camera rotation about an axis normal to the optical axis (roll or pitch), the apparent surface movement is approximately

$$x = H\dot{\phi}\, t_e \,, \tag{4-51}$$

where H is the camera altitude and $\dot{\phi}$ the rotation rate. Again if x is permitted to be 1/6 resolution element, the maximum allowable roll or pitch rate is

$$\dot{\phi} = \frac{r}{6t_e H} \quad \text{(w/o IMC).} \tag{4-52}$$

A simple single-direction IMC device is assumed to compensate for 90 percent of the apparent motion, hence

$$\dot{\phi} = \frac{r}{0.6t_e H} \quad \text{(w/IMC).} \tag{4-53}$$

Note that it has been assumed that the camera system does not

rotate about more than one axis simultaneously. That is, an image motion of one-sixth resolution element has been allowed for rotational motion, and each of the above rotation rates has been estimated by assuming a one-sixth resolution element image motion due to rotation about a single axis.

4.2.6 State-of-Art Constraints

The most important limitation on television system capability is the number of lines which can be resolved on the face of the camera tube. The best resolution currently anticipated is provided by the 4½-inch return beam vidicon tube, with a limiting resolution of about 6500 TV lines. As discussed above, in a typical operational situation only about 3400 TV lines can be achieved due to low scene contrast, lens degradation of resolution, and image motion effects. The 4½-inch return beam vidicon is not yet a space-qualified system, but is expected to be so in the near future. Image orthicon television systems can be used for face plate illuminations as low as 2×10^{-6} foot-candle-seconds, but only about 500 TV lines is provided in a typical operational situation. Other television tubes, such as image intensifier tubes, which have been designed explicitly for low-light-level applications have not been considered here.

Optical systems of up to two meters diameter are feasible for space use, particularly in the form of a segmented mirror, but such a system weighs close to 1500 pounds. For small optical systems, zoom lenses provide focal lengths which can be adjusted, by about a factor of five, to suit the operational conditions. Variable focal length devices might be feasible for use with large optical systems, but no extensive design experience is available to provide a basis for scaling laws. Currently available IMC subsystems provide compensation for about ninety percent of the horizontal relative motion between the sensor system and the planetary scene. Some development could result in IMC subsystems which would compensate for ninety-nine percent of the relative motion.

4.3 Experiment Design Procedure

Figure 4-18 presents a suggested design procedure for space-orbital television camera systems. In this study, experiment design proceeds from the image specifications given in Volume I and the orbit selections given in Volume III. The image specifications and orbit parameters which influence television camera design are listed in the two large boxes in the upper left hand corner of the logic diagram (Figure 4-18). The oval boxes in the logic diagram relate to estimation of experiment support requirements, while the rectangular boxes relate to steps in the camera design. The number shown in the lower right hand corner of each box refers to a set of design equations or scaling laws. The design equations and scaling laws are summarized in Figure 4-19. There is a one-to-one correspondence between the boxes in the logic diagram and the blocks in the scaling law chart (Figure 4-19), that is, the two figures are designed for simultaneous use. Their use is summarized here, and a numerical example is provided in Section 6 of Volume I.

Attitude control requirements are relatively independent of specific camera design and can thus be determined at the outset. If vertical height differences are to be deduced from the acquired imagery, a vertical resolution has been given in the image specifications. This desired vertical resolution has certain horizontal resolution implications, and in many cases the ground resolution required in the imagery is controlled by the desired vertical resolution. In particular, if vertical height differences are to be inferred by measurements of stereo parallax differences, the desired vertical resolution will control the required ground resolution for ground image sizes less than $Hr_h/(0.4r_v)$, assuming sixty percent image overlap. Once the required ground resolution is known, the corresponding number of TV lines may be estimated (step #3). This estimate ignores effects of planetary surface curvature, hence the number of TV lines actually required may be somewhat more than the estimate. If the estimated number of lines

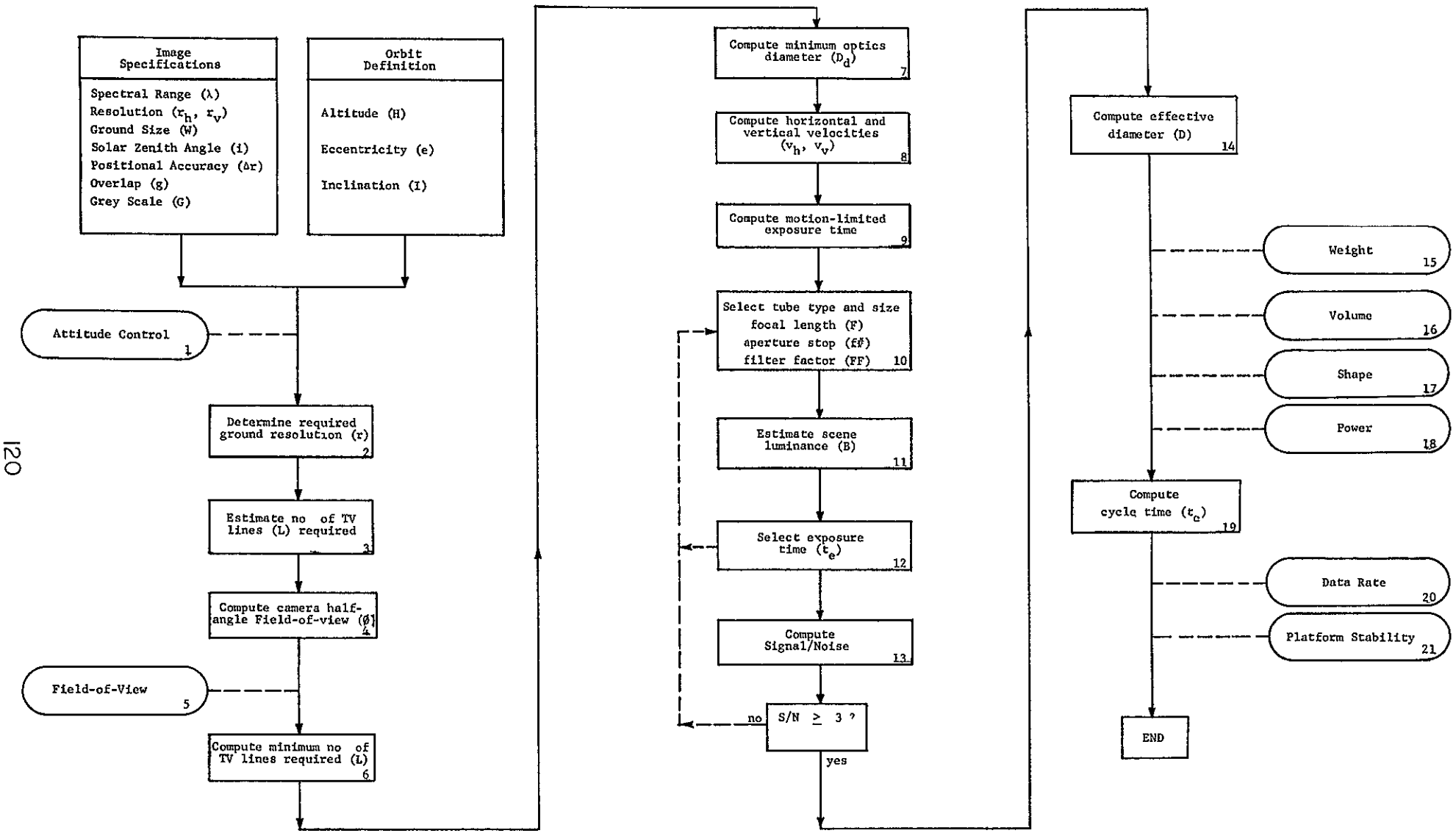

FIGURE 4-18 LOGIC DIAGRAM FOR TELEVISON SYSTEMS

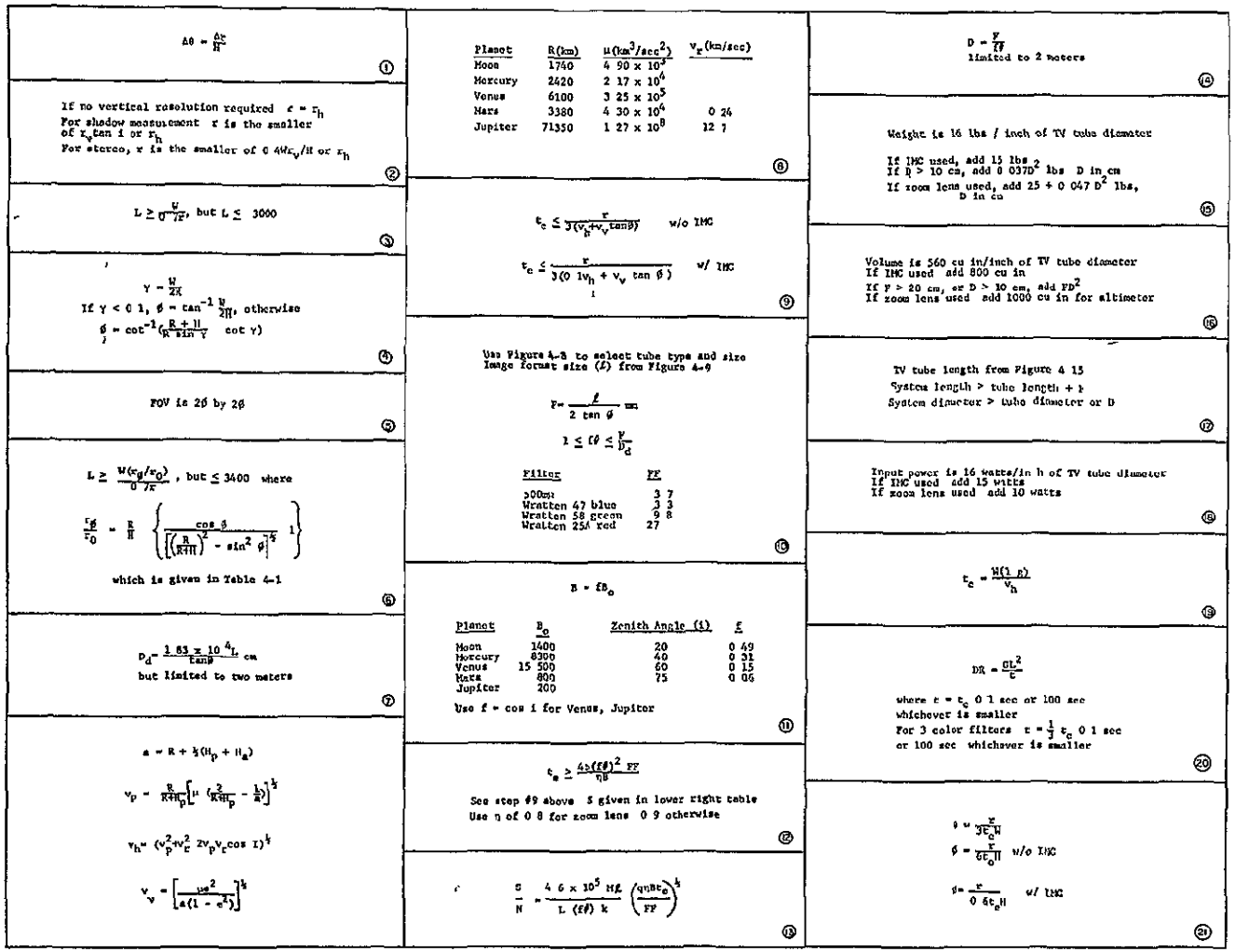

NOMENCLATURE

a orbit semi major axis km
B scene luminance, ft lambert
D optics diameter (F/f#) cm
D_d minimum optics diameter, cm
DR data acquisition rate bits/sec
e orbit eccentricity
f scene photometric function
f# optics aperture stop (f number)
F focal length, cm
FF filter factor
FOV field of view
g=fractional overlap along orbit
G bits per resolution element (normally 6)
H camera altitude km
H_a orbit apoapse altitude km
H_p-orbit periapse altitude,km
i-solar zenith angle
I orbit inclination
k number of grey levels (normally 64)
l-image format size mm
L number of TV lines
M maximum density difference
q quantum efficiency
r desired ground resolution, km
r_h-desired horizontal resolution km
r_v desired vertical resolution, km
R planet radius, km
S min tube illumination ft candle sec
S/N signal to noise ratio
t_c camera cycle time sec
t_e exposure time, sec
v_h apparent horizontal speed km/sec
v_p camera ground speed at periapse, km/sec
v_E planet equatorial rotation speed km/sec
v_v camera vertical speed, km/sec
W image width (length) on ground, km
γ image half angle subtended at planet center
Δr desired image ground positional accuracy km
$\Delta\theta$ allowable camera pointing error, radians
η optical system transmission factor
θ allowable camera yaw rate rad/sec
λ wavelength
μ planet gravitational constant, km^3/sec^2
ϕ camera half angle field of view
ϕ allowable camera pitch or roll rate rad/sec

Tube type	S(ft candle-sec)	M	q
Vidicon	3×10^3	2.0	0.2
Plumbicon	2×10^3	2.3	0.2
RBV	1×10^3	2.0	0.2
SEC	5×10^5	1.8	0.3
Image Orthicon	2×10^6	2.0	0.3

FIGURE 4.19 SCALING LAWS FOR TELEVISION SYSTEMS

exceeds 3000 (corresponding to the operational resolution of a 4.5 inch RBV for a low contrast target), the analysis should be abandoned and a photographic film camera system considered. If the estimated number of lines is less than 3000, the estimate may be refined by computing the camera field-of-view and accounting for the effects of planetary curvature on resolution (step #6). The optical system minimum diameter (step #7) is based on a wavelength of 6000 A and the assumption that the minimum diameter is five times the classical diffraction limit. A two-meter diameter is regarded as the largest diameter permitted by the current state-of-art.

Having determined that the evolving design does not exceed the optical diameter or resolution capability, the apparent horizontal ground speed is computed. For elliptic orbits, the maximum vertical speed of the camera is also computed. As discussed in Section 1.5, the vertical speed encountered during imaging operation may be somewhat less. The maximum available exposure time (step #9) is based on an image motion of one-half resolution element during exposure. Image motion compensation (IMC) permits an exposure time on the order of ten times longer than without IMC. Figure 4-8 is used to facilitate an initial choice of TV tube type and size based on the required number of TV lines. If 550 or more lines are required, an RBV provides the best resolution capability. The effective aperture stop of the optical system should be unity or more and must be consistent with the focal length and maximum optical diameter computed earlier. A large f-number will result in a relatively small optical system, but may require unacceptably long exposure times. The filter factor is normally unity, that is, no filter is used, but at Mars a 500 mμ filter should be used for surface imagery. For pseudo-color imagery, in which alternate blue, green, and red images are procured and are later combined to reconstruct a color image, a filter factor of 27 is appropriate. The scene luminance depends upon the solar zenith angle, for which a preferred range has been given

in the image specifications. In fact, the orbit selections have been made to provide the desired lighting conditions. The scene photometric function should be estimated using the maximum zenith angle (or minimum solar elevation angle, since the zenith angle plus the elevation angle equals ninety degrees). Figure 2-3 in Section 2.1 presents a curve of the surface photometric function as a function of solar zenith angle (which is equivalent to the phase angle for vertical viewing). For those atmospheric imaging experiments which require only daylight conditions, the photometric function may be taken as 0.5, corresponding to a solar zenith angle of sixty degrees. A minimum exposure time, based on the scene luminance and the TV tube sensitivity is computed in step #12. A nominal exposure time, which lies between the minimum exposure time and the maximum exposure time computed in step #9, may then be selected. A small exposure time will reduce the platform stability requirements, but will also reduce the signal-to-noise ratio in the acquired imagery. If the minimum exposure time is not less than the maximum exposure time, the optical system f-number must be decreased, or a more sensitive TV tube selected. Having selected a nominal exposure time, the signal-to-noise ratio may be estimated (step #13). This estimate assumes that the noise is only one shade of grey different from the signal. If the ratio is less than three, some design iteration (as indicated by the dashed lines in the logic diagram) is necessary. The most effective solution is to decrease the f-number, but since this may unnecessarily increase the optical system weight, it is frequently convenient to merely increase the nominal exposure time. The optical system effective diameter (step #14) is state-of-art limited to two meters. The optical diameter may be reduced by increasing the f-number, but this may have a disastrous effect upon the signal-to-noise ratio or the minimum exposure time.

At this stage of the design, the TV system design variables are sufficiently determined that important support requirements may be estimated as shown in steps #15-18. The cycle, or image interval, time (step #19) is based on the linear extent of image ground overlap and the camera system ground speed. The data acquisition rate (step #20) depends on the number of bits in the image and the cycle time, allowing a 0.1 sec interval for blanking of the previous image. For 64 shades of grey in the processed imagery, six binary bits per resolution element are required. For pseudo-color imagery, three color-filtered images must be acquired during the cycle time. In any event, the maximum image tube storage time is taken as 100 seconds. Finally, the maximum permissible camera roll and yaw rates are estimated.

5. FILM CAMERA SYSTEMS

5.1 Design Equations

This section presents the design equations useful in esimating the design parameters of space orbital film camera systems. Section 5.2 presents techniques for relating the design parameters to support requirements, while Section 5.3 summarizes both the design procedure and estimation of support requirements.

5.1.1 Planet-Sensor Geometry

The geometry involved in obtaining vertical frame photography from planetary orbit has been discussed above in Section 1.1, where it was shown that the half-angle camera field-of-view $\emptyset$ is given by

$$\cot \emptyset = \frac{R + H}{R \sin \gamma} - \cot \gamma , \qquad (5\text{-}1)$$

where γ is W/2R, R is the planet radius, H is the camera altitude, and W is the length of one side of the image as projected on the ground. Only when γ is small, does this reduce to the flat planet result:

$$\tan \emptyset = \frac{W}{2H} . \qquad (5\text{-}2)$$

It is assumed here that areas on the planetary surface can be resolved (detected) if their linear dimensions correspond to the width of a resolved line on a standard resolution test target imaged by the system. Thus, an estimate of the total number of lines required to obtain a ground resolution r is given by

$$L \simeq \frac{W}{r} . \qquad (5\text{-}3)$$

However, the resolution r is achieved only at the nadir (principal point of the image). Thus to ensure that the ground

resolution r is achieved throughout the desired imaged area, the number of lines should be increased to

$$L = \frac{W(r_\phi/r_0)}{r} \qquad (5\text{-}4)$$

where the quantity (r_ϕ/r_0) has been given in Table 1-1. By comparison with eq. (4-7), a lesser number of resolved lines is required in a film system, as compared to a TV system, to image the same scene at the same ground resolution. This conclusion is valid only as long as the film scanner spot diameter is significantly smaller than the width of a resolved target line or resolution element. If this is not the case, a Kell factor must be introduced into eq. (5-4) above, just as for TV systems. It should also be noted that the number of lines estimated here is based on one line per scene resolution element and not a line pair (or cycle), as is often assumed in the design of film systems.

5.1.2 Illumination

Computation of scene luminance has been discussed above (Section 4.1.2). Minimum exposure times may be determined from the scene luminance and the aerial exposure index (AEI) of the film. Thus

$$t_e \geq \frac{0.6\ (f\#)^2\ .\ FF}{B\ .\ AEI\ .\ \eta}\ , \qquad (5\text{-}5)$$

where t_e is the exposure time, f# is the relative aperture stop, FF is the filter factor, and η is the lens transmission factor. Maximum exposure times based on image motion considerations are discussed below. Typical film speeds, along with film resolution and weight, are shown in Table 5-1 [30,40]. The resolution shown is from manufacturer's data, and may not be achieved in a typical planetary application, as will be shown later. Also, the number of lines per mm listed in the

table is twice the value usually seen, which refer to line pairs, or cycles, per mm. The lens transmission factor η has been taken in this study as 0.9, which is appropriate for a simple lens. For zoom lenses, η should be taken as about 0.8.

Table 5-1

Aerial Film Characteristics

Film Type	Aerial Exposure Index	Nominal Resolution* (lines/mm) (1.6:1 Contrast)	Film Weight (lbs/ft^2)
SO-243	1.6	410	0.037
3404	1.6	400	0.022
SO-230	6	400	0.022
SO-206	6	224	0.022
SO-226	6	224	0.032
3400	20	130	0.022
SO-136	20	130	0.033
SO-130	20	210	-
SO-102	64	122	-

* Limiting film resolution, not system resolution.

Filter factors have been estimated by using the measured spectral sensitivity of SO-243 film [40], and the measured transmission curves of various filters [35]. If $R(\lambda)$ denotes the film spectral sensitivity, and $T(\lambda)$ is the measured transmission of the filter as a function of wavelength λ, the filter factor is computed from

$$FF = \frac{\int R(\lambda)\, d\lambda}{\int T(\lambda)\, R(\lambda)\, d\lambda} \quad . \qquad (5\text{-}6)$$

In each case the integration was performed from 4000 to 7000 angstrom units, with the results given in Table 5-2. Filter factors for the other films listed in Table 5-1 may be taken as equal to those for SO-243 film, without appreciable error.

Table 5-2

Filter Factors (SO-243 FILM)

Filter Type	Filter Factor
500 mμ	1.8
WRATTEN 47 Blue	14
WRATTEN 58 Green	9.7
WRATTEN 25A Red	3.6

The lens focal length is determined by the image format size (ℓ by ℓ) in the image plane,

$$\text{focal length } F = \frac{\ell}{2 \tan\phi} \tag{5-7}$$

Standard format sizes are 64, 114, 228 mm, corresponding to film sizes of 70 mm, 5 inch, and 9½ inches, respectively. The effective diameter of the lens is F/f#. The lens diameter must be appreciably larger than the diffraction-limited aperture, which is

$$D_d = \frac{1.22 \lambda L F}{\ell} . \tag{5-8}$$

5.1.3 Modulation Transfer

As with television systems, the film camera system modulation transfer function may be computed by multiplying together the transfer functions of the system components. Assuming that the film processing equipment has a transfer function close to unity, the film system MTF is approximated by

$$T_{system} = T_C T_L T_F T_M T_S \tag{5-9}$$

where T_C = apparent scene contrast transfer function,
T_L = lens transfer function,
T_F = film transfer function,
T_M = image motion transfer function,
T_S = film scanner transfer function.

The effects of apparent scene contrast, the optical system, and image motion on the system transfer function were discussed in Section 4.1.5, where it was shown that for an apparent scene contrast of 1.6:1, a lens system of diameter five times the diffraction limit, and an image motion of one-half resolution element, the product $T_C T_L T_M$ is about 0.115. Thus to achieve a system modulation of 0.04, which is required for adequate imagery [39], the film and film scanner modulation must be such that

$$T_F T_S = \frac{0.04}{0.115} = 0.35 \qquad (5\text{-}10)$$

Typical film modulation transfer functions are shown in Figure 5-1, while typical modulation transfer functions for a flying spot scanner are shown in Figure 5-2 as a function of the scanning beam size [53]. A scanning beam of five microns represents the current state-of-art limit. For such a scanning beam size, Figure 5-3 shown the product $T_F T_S$. These results show that the "operational" resolution, that is, that resolution for which the product $T_F T_S$ has a value of 0.35, may be considerably less than the nominal resolution given earlier in Table 5-1. In the case of high definition films having nominal resolutions of about 400 lines/mm, such as SO-243, the modulation transfer of the flying spot scanner at spatial frequencies approaching the film resolution limit is very low, and hence only a small fraction of the film resolution capability can be used effectively. That is, for such systems, the system resolution is determined primarily by the resolution capability of the flying spot scanner. For SO-243 film, the operational

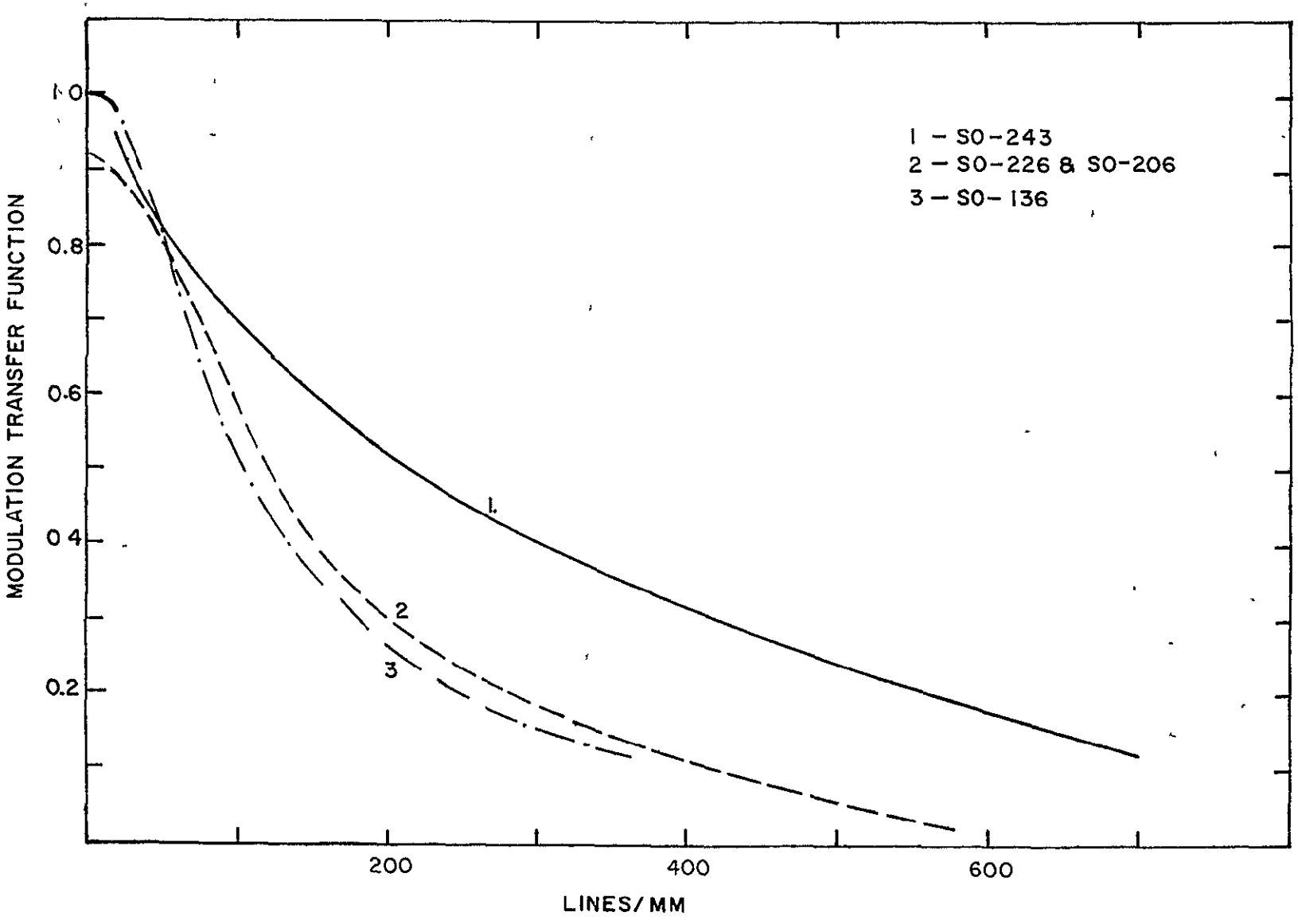

FIGURE 5-1 FILM MODULATION TRANSFER FUNCTION

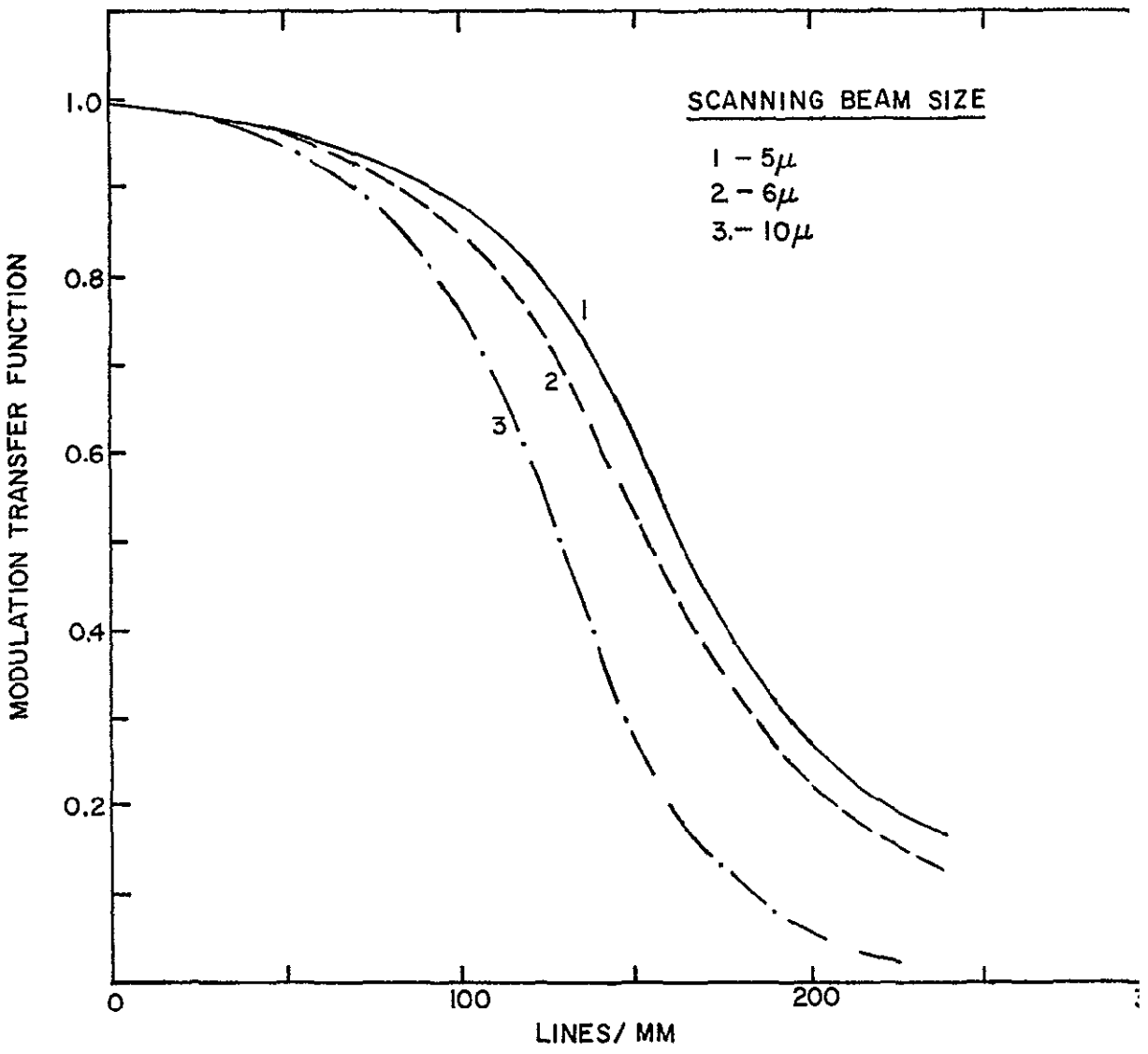

FIGURE 5-2. SCANNER MODULATION TRANSFER FUNCTION

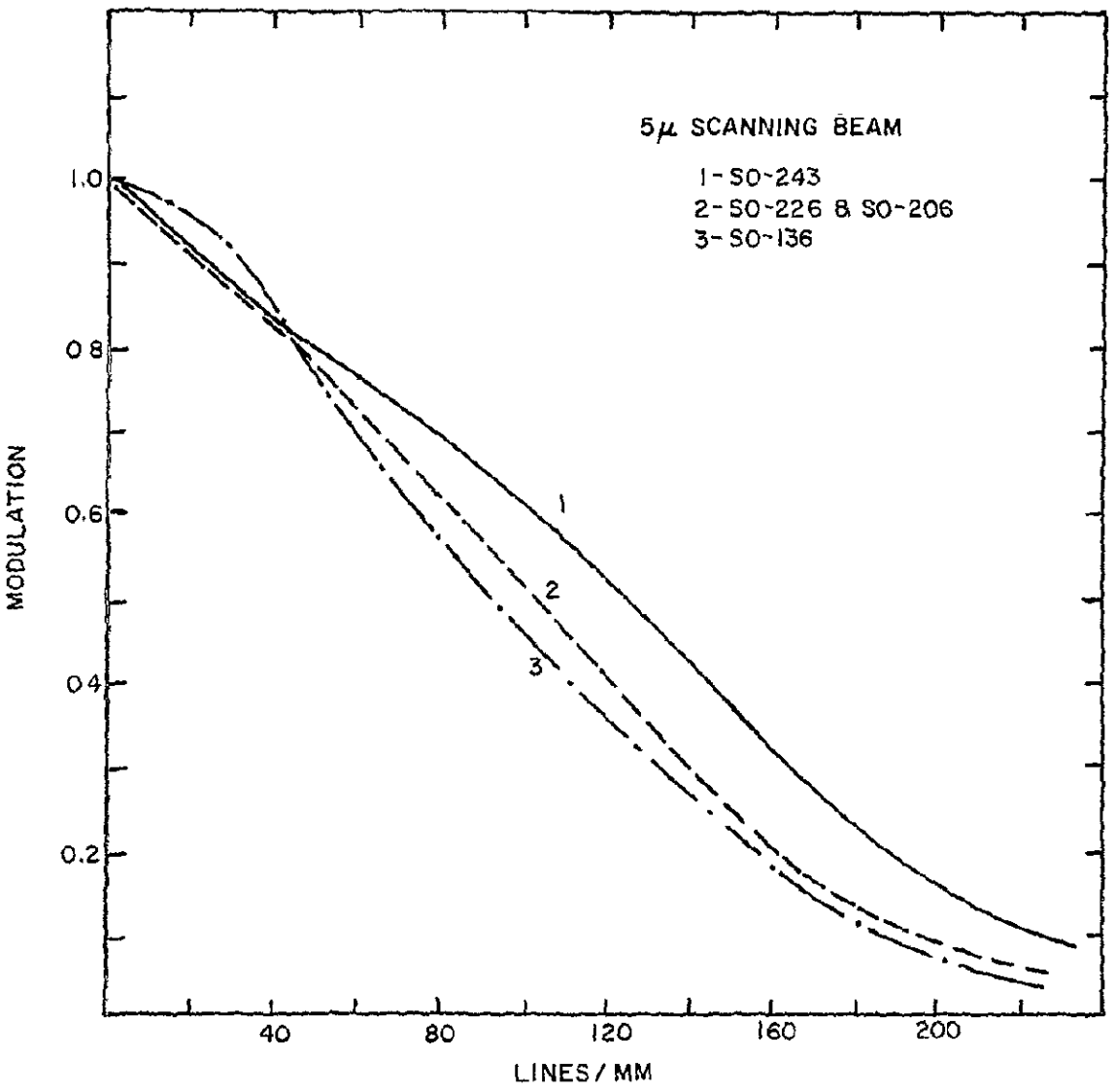

FIGURE 5-3 PRODUCT OF T_F AND T_S

resolution is about 145 lines/mm. At the other extreme, for films having nominal resolutions of about 130 lines/mm, the modulation transfer of the flying spot scanner is nearly unity at the film resolution limit, and the operational resolution capability approaches the film resolution capability. Thus for SO-136 film, the operational resolution is about 120 lines/mm.

An approximate method of analysis is to assume:

a) an apparent scene contrast of 1.6:1,
b) an optical system at least five times larger than the diffraction limit,
c) an apparent image motion of less then one-half resolution element during the exposure time, and
d) a flying spot scanner of five micron spot size.

In this case, the system resolution is given by the "operational" resolution defined above. This technique, although based on the modulation transfer function concept, avoids the complexities of analyzing in detail the modulation transfer of each system component. In some cases, this approximate analysis may result in an overly-conservative sensor system design. Nonetheless, the analysis does lead to an estimate of the system design parameters, and identifies those situations which approach the limitations of film camera sensor systems.

For a specific application, the selection of camera size and film type is controlled by the desired scene resolution and available scene illumination. As with the television systems, the film exposure time which is consistent with an image motion no greater than one-half resolution element is

$$t_e \leq \frac{r}{3(0.1\, v_h + v_v \tan \phi)} \qquad \text{(w/o IMC)} \qquad (5\text{-}11)$$

in the absence of image motion compensation (IMC), and

$$t_e \leq \frac{r}{3(0.1\ v_h + v_v \tan \phi)} \qquad \text{(w/ IMC)} \qquad (5\text{-}12)$$

with image motion compensation. Here r is the desired ground resolution, v_h is the maximum apparent horizontal velocity of the planetary scene as viewed from a fixed sensor system, v_v is the maximum vertical speed of the sensor system during imaging operations, and ϕ is the camera half-angle field-of-view. The calculation of v_h and v_v has been discussed in Section 1.2. In eq. (5-12), it has been assumed that a simple IMC mechanism can compensate for ninety percent of the apparent horizontal velocity. For a given exposure time, the necessary film speed is determined from eq. (5-5) as

$$\text{AEI} \geq \frac{0.6(f\#)^2 \cdot FF}{B\ t_e\ \eta} \qquad (5\text{-}13)$$

where AEI is the film aerial exposure index. The total number of lines required in the film image to achieve the desired ground resolution r has been given by eq. (5-4), that is,

$$L = \frac{W(r_\phi / r_0)}{r}.$$

To facilitate the selection of film type and size, based on the required film speed and total number of lines, Table 5-3 gives film speeds of available aerial films which might be suitable for space-orbital use, and the total number of lines provided per image in standard film sizes (based on the operational resolution defined above).

Table 5-3

Film Lines per Frame

(based on "operational" resolution)

Film Type	AEI	Lines per Frame 70 mm	5-inch	9-½ inch
SO-243	1.6	9300	16500	33000
3404	1.6	9200	16400	32800
SO-230	6	9200	16400	32800
SO-206	6	8300	14700	29400
SO-226	6	8300	14700	29400
SO-130	20	8100	14500	29000
3400	20	7700	13700	27400
SO-136	20	7700	13700	27400
SO-102	64	7600	13600	27100

5.2 Support Requirements

5.2.1 Camera System Weight

The Lunar Orbiter photo subsystem is the only space-qualified film camera system utilizing on-board film processing for which data are readily available. There is, therefore, little reliable data available upon which to base weight and volume scaling laws for space-orbital systems. Here weight and volume scaling laws have been based upon data pertaining to standard aerial reconnaissance cameras [54]. The resulting scaling laws have then been modified to give agreement with the available design data for the few film camera systems which have been suggested for space applications. That is, the functional dependence of the scaling laws has been determined by aerial camera data, while the numerical values of the scaling coefficients have been determined by space camera design data.

The weights of a variety of 70 mm aerial reconnaissance cameras are given in Table 5-4. Some of these tabulate weights may include the weight of the film. The film weight, however, is only a small portion of the camera weight, 100 feet of 70 mm film weighing about three-quarters of a pound, less. Therefore, no attempt has been made to separate out th film weight. There does appear to be a weight dependence upo the IMC capability, cameras without such a capability tending to weigh less than similar cameras with IMC. The camera weights are shown in Figure 5-4 plotted against the effective lens aperture, defined as the focal length divided by the maximum relative lens aperture. In the figure, the circles represent cameras with an IMC capability, the squares without The dashed lines represent analytic fits to the data, i.e.,

$$M = \begin{cases} 11 + 0.2\ D^2 & \text{(w/o IMC)} \\ 16 + 0.2\ D^2 & \text{(w/ IMC)} \end{cases} \qquad (5\text{-}14)$$

where M is the camera weight in pounds, and D is the effectiv lens diameter in centimeters. It appears that the IMC mechanism for a 70 mm camera weighs approximately five pounds This does not include the weight of the V/H sensor.

Camera weights for 5 inch film cameras are given in Table 5-5. Again the IMC capability appears to have an influence on the weight. Figure 5-5 shows camera weight (witho film)as a function of effective lens diameter. As with the previous figure, the circles and squares represent cameras with and without IMC. It seems fruitless to attempt to correlate weight with the amount of IMC provided (film motions o 10.8 to 12 inches per second) because of the scatter in the data. The HR-235 and HR-236 camera weights are somewhat misleading, in that the IMC is provided by a rocking mount and not by a moveable platen. Therefore these camers are represented by squares in the figure. It appears that weights of

Table 5-4

70 mm AERIAL RECONNAISSANCE CAMERAS

Type No.	Camera	Focal Length (mm)	Aperture Stop	Eff. Lens Diameter (mm)	Weight (lbs)	Film Capacity (ft)	IMC
1	CAX-12	38	6.3	6	16.7	100	Yes
2	CAX-12	38	4.5	8.5	16.7	100	Yes
3	CAX-12	76	3.5	22	17.4	100	Yes
4	CAX-12	152	3.5	43	22.3	100	Yes
5	CAX-12	305	4.0	76	26.5	100	Yes
6	KA-26A	76	1.5	51	21	250	Yes
7	TA-7M	70	1.6	44	18	100	Yes
8	TA-10M	150	1.5	100	35	200	Yes
9	X70-7	76	2.0	38	13	50	No
10	X70-7	305	4.0	76	25	50	No
11	KA-75	38	4.5	8.5	12	50	No

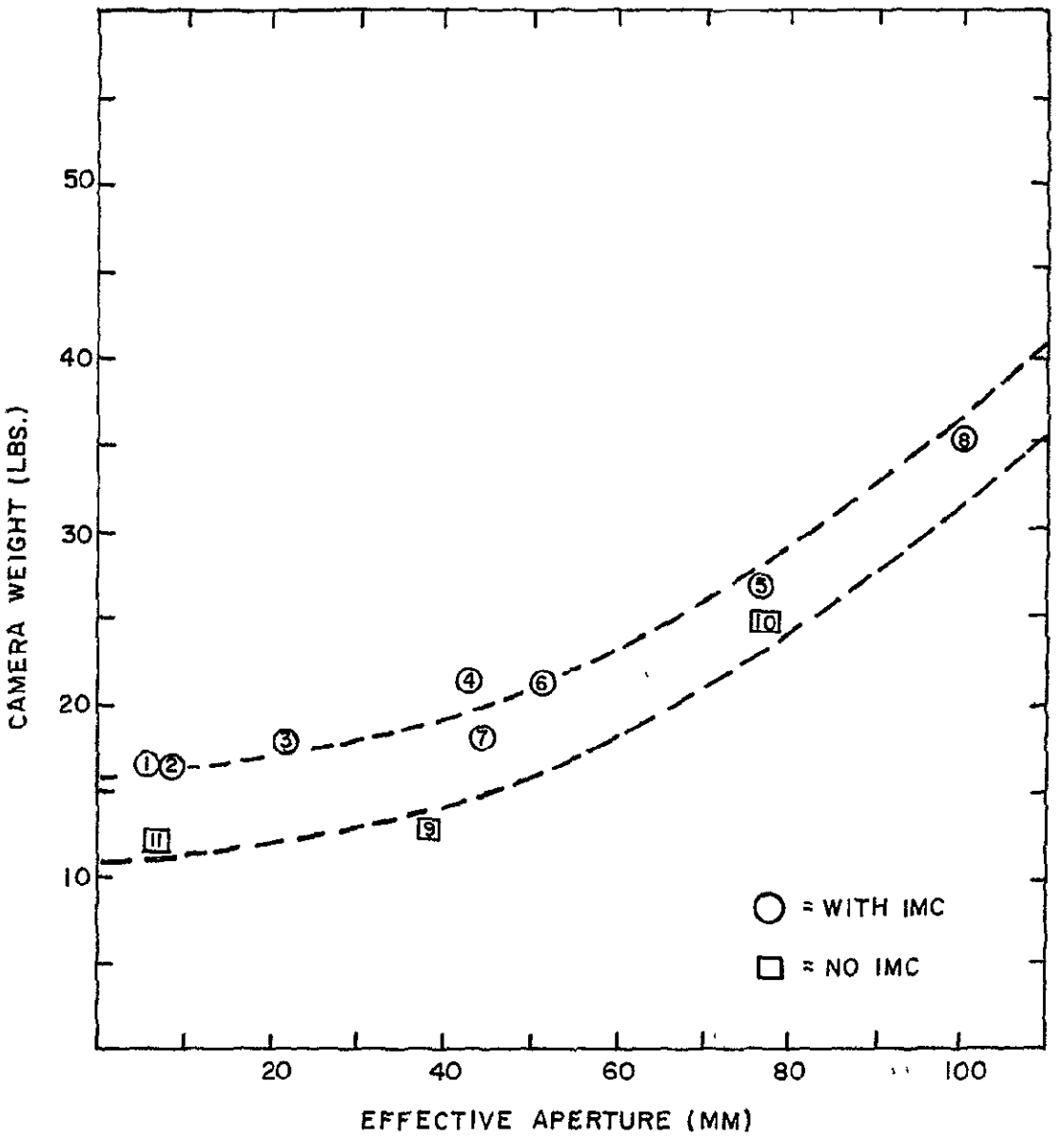

FIGURE 5-4. 70MM FILM CAMERA WEIGHTS

Table 5-5

5 INCH AERIAL RECONNAISSANCE CAMERAS

Type No.	Camera	Focal Length (mm)	Aperture Stop	Eff. Lens Diameter (mm)	Weight (w/o Film) (lbs)	IMC
1	KA-45A	152	2.8	54	39	Yes
2	KA-50A	45	5.6	8	46	Yes
3	KA-51A	152	2.8	54	47	Yes
4	KA-53A	305	3.5	87	61	Yes
5	KA-62A	76	4.5	17	53	Yes
6	KA-76	45	5.6	8	47	Yes
7	KA-76	76	4.5	17	53	Yes
8	KA-76	152	2.8	54	46	Yes
9	KA-76	305	3.5	87	62	Yes
10	KS-87A	76	4.5	17	69	Yes
11	KS-87A	152	2.8	54	68	Yes
12	KS-87A	305	4.0	76	71	Yes
13	KS-87A	457	4.0	114	86	Yes
14	K-24	162	4.5	36	14	No
15	K-24	178	2.5	71	14	No
16	K-24	305	5.0	61	26	No
17	K-24	508	5.6	91	30	No
18	K-25	162	4.5	36	19	No
19	HR-235	305	5.6	54	20	Yes
20	KR-236	152	5.6	27	14	Yes

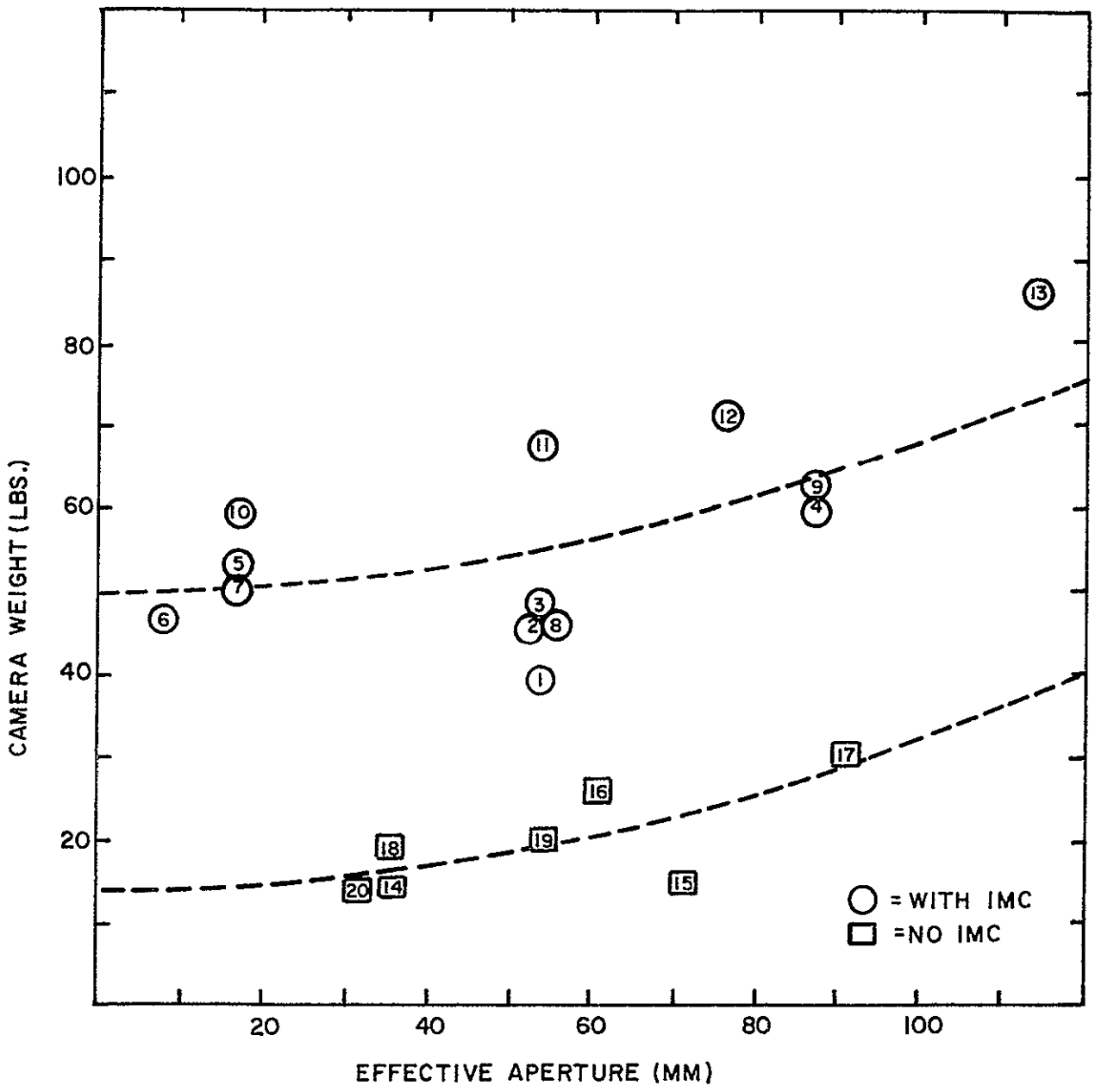

FIGURE 5-5 5 INCH FILM CAMERA WEIGHTS

5 inch cameras may be estimated by

$$M = \begin{cases} 14 + 0.18\ D^2 & \text{(w/o IMC)} \\ 50 + 0.18\ D^2 & \text{(w/ IMC)} \end{cases} \qquad (5\text{-}15)$$

where M is the camera weight in pounds and D is the effective lens diameter in centimeters. Weights estimated by these equations are shown by the dashed lines in the figure. To conclude that IMC mechanisms for 5 inch cameras weigh 36 pounds is probably unjustified. The heavier cameras with an IMC capability tend to be more sophisticated than the lighter cameras without IMC; the heavier cameras incorporating such refinements as automatic exposure controls, etc. Therefore, the difference in weight should not be attributed entirely to IMC.

Weights of various 9-1/2 inch film cameras are given in Table 5-6. IMC capability for 9-1/2 inch cameras is normally provided by the magazine. For example, the K-17D camera has IMC when equipped with an A-18 magazine, but does not have IMC when equipped with an A-9B magazine. Thus the weights given in Table 5-6 do not show a dependence upon IMC capability. Camera weights (excluding film) may be obtained from the table by adding 21 pounds for a non-IMC magazine (A-5B or A-9B), or 57 pounds for an IMC magazine (A-18). The resultant camera weights are shown in Figure 5-6 as a function of lens diameter. There is apparently no IMC-equipped magazine used with the K-22A camera. The dashed lines in the figure show weights estimated according to

$$M = \begin{cases} 51 + 0.15\ D^2 & \text{(w/o IMC)} \\ 86 + 0.15\ D^2 & \text{(w/ IMC)} \end{cases} \qquad (5\text{-}16)$$

where M is the camera weight (without film) in pounds, and D

Table 5-6

9 1/2-INCH AERIAL RECONNAISSANCE CAMERAS

Type No.	Camera	Focal Length (mm)	Aperture Stop	Eff. Lens Diameter (mm)	Weight (w/o Film) (lbs)
1	K-17D	152	6.3	24	30
2	K-17D	305	5.0	61	32
3	K-17D	610	6.0	102	51
4	K-22A	152	6.3	24	26
5	K-22A	305	5.0	61	27
6	K-22A	610	6.0	102	42
7	K-22A	1016	5.0	203	96
8	K-22A	1016	5.6	181	72
9	K-22A	1016	8.0	127	46
10	KA-2	152	6.3	24	32
11	KA-2	305	4.0	76	52
12	KA-2	610	6.0	102	54
13	KA-3A	152	6.3	24	32

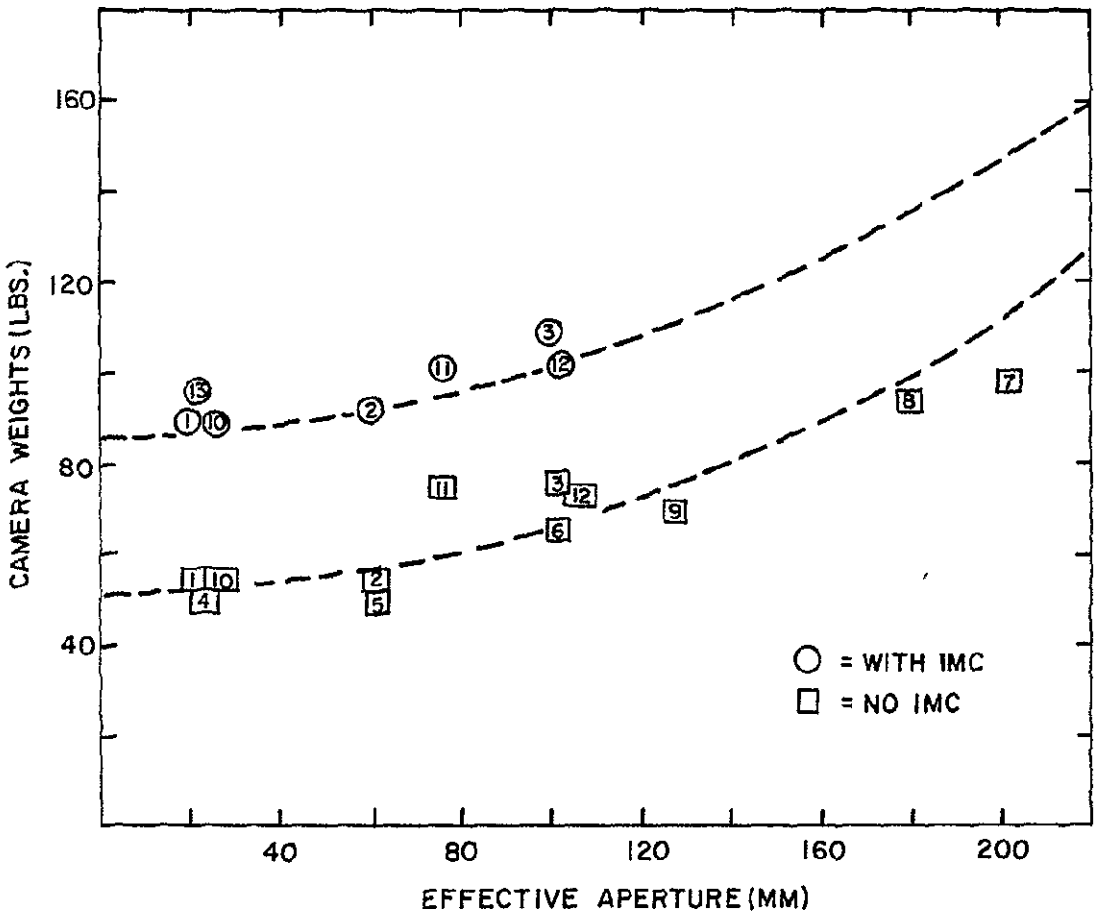

FIGURE 5-6. $9\frac{1}{2}$ INCH FILM CAMERA WEIGHTS (W/ MAGAZINE)

is the effective lens diameter in centimeters. As with the 5 inch film cameras, the 35 pound difference between the two version of eq. (5-16) should probably not be attributed entirely to IMC capability.

These weight scaling laws derived above have the form of a constant, dependent upon camera film size, plus a term dependent upon both film size and lens diameter. They may be summarized approximately by

$$M = 8 + a\ S^2 + (0.22 - 0.0076\ S)\ D^2 \qquad (5\text{-}17)$$

where M is the camera weight in pounds, S is the film size in inches, D is the lens diameter in centimeters, and a is 0.54 for non-IMC cameras, and 0.95 for cameras with IMC. Perusal of Figures 5-4, 5-5, and 5-6 indicates that the weight scaling laws will estimate weights of aerial reconnaissance cameras to within fifty percent, provided the lens diameter is not much greater than ten centimeters (actually twenty centimeters for 9-1/2 inch film cameras). For larger optical systems, additional weight must be added to the camera system. Section 4.2.1 has discussed the weights of large optical systems, and it was concluded that the optical system weight is approximately

$$M = 0.037\ D^2\ , \qquad (5\text{-}18)$$

using the same units as above.

The camera systems weights estimated above have not included the weight of the V/H sensor, film, processing material, scanning equipment, or radiation shielding. A typical V/H sensor [52] weighs about ten pounds, while typical film weights have been given in Table 5-1. The solution content of PoroMat processing [30] weighs about 0.034 lbs/sq ft, and has at least a two year storage life. In this study, the processing material has been assumed to weigh 0.04 pounds per square foot

of processed film. Bimat processing is about one-third the weight of PoroMat processing, but has a much shorter useful life. Finally, a flying spot scanner is estimated to weigh about ten pounds.

The amount of radiation shielding required is a function of the type and amount of film, and the radiation to which the film is exposed. Bashe and Kennedy[30] have estimated the shielding requirements for a Martian orbiter by examining the calculations of Hill, Ritchie, and Simpson[55], and conclude that the most important source of film damage arises from exposure to 100 MeV solar flare protons and that ten gm/cm^2 of aluminum will provide adequate shielding for SO-243 film on an eleven month mission to Mars. On the other hand, Slater[29] has stated that solar X-rays appear to present the greatest radiation hazard. Watts and Lewis[56] have exposed different types of aerial photographic film to electron, proton, X-ray, γ-ray, and bremsstrahlung radiation. Their results indicate clearly that film is most sensitive (per roentgen exposure) to keV X-rays and bremsstrahlung. Watts and Lewis also point out that the equivalent of about three gm/cm^2 of aluminum shielding is provided by the camera body and film magazine, and that the sensitivity of film to radiation of any given type is approximately proportional to the aerial exposure index of the film.

For purposes of shielding weight estimation, it is assumed here that seven gm/cm^2 of aluminum is required to shield SO-243 film on a 330 day mission to Mars. For other missions, the shielding weight required is taken to be proportional to the mission duration, and inversely proportional to the square of the target planet's distance from the Sun.

To estimate the amount of shielding required, the film is considered to be wound on a spool of inner radius 0.4 inches and outer radius

$$R_S = (R_o^2 + \frac{tL}{\pi})^{\frac{1}{2}} , \qquad (5\text{-}19)$$

where R_o is the inner radius, t is the film thickness (5.2 mils for SO-243), and L is the film length. The surface area of the film spool which must be shielded is then, approximately,

$$A = 2 \pi R_S (R_S + S) \qquad (5\text{-}20)$$

where S is the film size. Covering this area with seven gm/cm^2 of shielding leads to the estimates of shielding weight shown in Figure 5-7, for different film sizes as a function of film length. For comparison, Bashe and Kennedy estimate about 6.5 pounds of shielding for 100 meters of 70 mm SO-243 film, while Figure 5-7 yields about nine pounds of shielding. The estimates in the figure are for use of SO-243 film on a 330 day mission to Mars. Estimates for other missions are obtained by assuming the required shielding weight is proportional to the film aerial exposure index, the time duration of the mission, and inversely proportional to the square of the target planet's distance from the Sun.

The total number of photos required to complete the desired planetary coverage may be estimated according to

$$\text{no. of photos} = \frac{C \cdot 4\pi R^2}{(1 - g)(1 - s) W^2} \qquad (5\text{-}21)$$

where C is the fractional planetary coverage, R is the planetary radius, g is the fractional forward overlap, and s is the fractional side overlap. The film length is obtained by multiplying by S, the camera film size, hence

$$\text{film length } L^* = \frac{4\pi CSR^2}{(1 - g)(1 - s) W^2} \qquad (5\text{-}22)$$

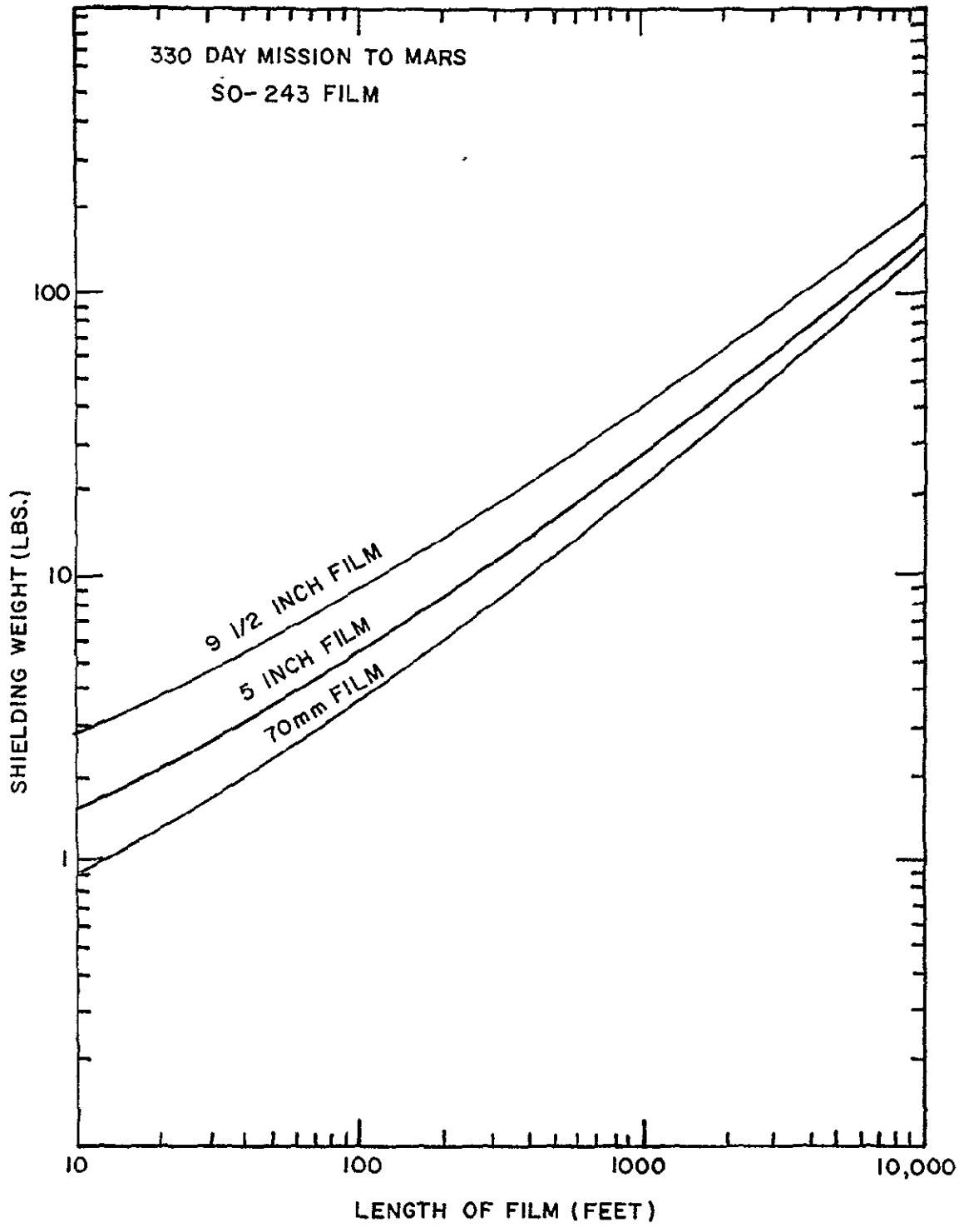

FIGURE 5-7 RADIATION SHIELDING WEIGHT

Estimates using the weight scaling laws derived above will now be compared to design data for some space-qualified systems. The Lunar Orbiter photo subsystem[57] utilizes Bimat-processed 70 mm film with both a 24 inch f/5.6 lens and an 80 mm f/5.6 lens. Using eq. (5-14) for an IMC-equipped system, the basic camera weight is estimated as 40 pounds, using the 24 inch lens. The weight of the additional 80 mm lens is estimated as less than one pound. The film weight, for 260 feet of SO-243 film, is estimated as a little over two pounds, using the areal density from Table 5-1. The weight of the Bimat processing is estimated as a trifle less than one pound. As mentioned above, the V/H sensor and flying spot scanner are estimated to weigh ten pounds each. The shielding weight is neglected here. Thus the weight of the Lunar Orbiter camera system is estimated as:

basic camera (w/24" lens)	40 lbs
80 mm lens	1
film and processing	3
V/H sensor	10
flying spot scanner	10
total weight	64 lbs.

For comparison, the actual system weight is about 130 pounds.

Bashe and Kennedy[30] have estimated that a 70 mm film camera system (with IMC) should weigh about 46 pounds, excluding lens, film, processing, and shielding weight. By setting D equal to zero in eq. (5-14), the camera weight is estimated as 16 pounds, without lens. Adding ten pounds each for the V/H sensor and flying spot scanner, yields a system weight of 36 pounds, as compared to 46 pounds.

In a recent study[52], it has been estimated that a 70 mm film system with a 24 inch f/4 lens should weigh about 74 pounds, including 100 feet of PoroMat-processed film. Eq. (5-14) yields 63 pounds; adding 20 pounds for the V/H sensor and flying spot scanner, and two pounds for the film and processing gives an estimated system weight of 85 pounds. It is

not apparent if the reported estimate includes shielding weight or not. The shielding weight for 100 feet of 70 mm film should be small when compared to the total system weight.

The above comparisons indicate that the weight scaling laws derived here for 70 mm cameras yield estimates which are accurate to within a factor of two. As far as larger film sizes are concerned, unpublished data for suggested Apollo Applications experiments estimate the weight of a metric camera package consisting of two 9 x 14 inch film metric cameras (each having a 24 inch focal length) and two 70 mm stellar cameras at about 300 pounds. Using the scaling law for a 9½ inch IMC-equipped camera, each large camera is estimated as weighing about 100 pounds (assuming an f/5.6 lens). Adding 30 pounds for both 70 mm cameras, and 10 pounds for a single V/H sensor, the total package is estimated at 240 pounds.

In summary, the weight scaling laws can be used to estimate, within a factor of two, the weights of space film systems consisting of cameras using 70 mm to 9½ inch film and lens apertures less than twenty centimeters.

5.2.2 Camera Dimensions

The dimensions of 70 mm aerial reconnaissance cameras with a film carrying capacity of 100 feet may be approximately expressed by (8+F) x 7 x 10 inches, where F is the focal length in inches. This expression fits the dimensions of the cameras listed in Table 5-4 to within two inches in length (the term involving the focal length) and to within one inch in the other dimensions. This approximation provides no allowance for the volumes occupied by the scanning equipment, processing mechanisms, dessicants, shielding, etc. The Fairchild planetary camera design[30] suggests a 70 mm camera of 24 x 6 x 18 inches, including all necessary auxiliary equipment except the V/H sensor. It is therefore suggested that sizes of 70 mm space cameras be approximated by

$$\text{70 mm camera} : (16 + F) \times 8 \times 20 \text{ inches} \qquad (5\text{-}23)$$

for 100 foot film capacity, not including the V/H sensor. This equation has been obtained from the aerial reconnaissance camera size by doubling the width, and the constant term in the length, to force near agreement with the Fairchild design. Eq. (5-19) implies that the diameter of the film supply and take-up spools are approximately proportional to the square root of the film length. Assuming that half the camera width and half the camera length (excluding the lens) is required for film and processing storage on a 100 foot capacity camera, the dimensions become

$$\text{70 mm camera} : (8 + F + 0.8\ L^{\frac{1}{2}}) \times 7 \times (10 + L^{\frac{1}{2}}) \qquad (5\text{-}24)$$

for arbitrary film length L in feet.

Dimensions for 100 foot capacity 5 inch and 9½ inch film aerial reconnaissance cameras are approximately (6 + F) x 10 x 14 and (2 + F) x 16 x 15 inches, respectively. These width and depth estimates are accurate to within two inches, but the length estimate is only accurate to within three inches for the 9½ inch film cameras and to within six inches for the 5 inch film cameras. Using an analogous argument as above, the dimensions of space camera systems are taken as

$$\text{5 inch camera} : (4 + F + 0.8\ L^{\frac{1}{2}}) \times 10 \times (18 + L^{\frac{1}{2}}) \qquad (5\text{-}25)$$

$$9\tfrac{1}{2} \text{ inch camera} : (F + 0.8\ L^{\frac{1}{2}}) \times 16 \times (20 + L^{\frac{1}{2}}) \qquad (5\text{-}26)$$

For long focal length systems, the camera system length may be decreased by using a folded optical path. However, the lens transmission factor must then be multiplied by the mirror reflectivity (typically 0.95) for each path reflection.

The V/H sensor, if IMC is required, is not included in the above dimension estimates. The sensor volume should be independent of film size and length. The Lunar Orbiter V/H mechanism has dimensions of approximately 6 x 6 x 6 inches, while the V/H electronics has dimensions of about 3 x 6 x 11 inches[58]. These packages may be placed more or less at random near the camera system.

5.2.3 Power Requirements

The average power requirements of aerial photographic systems are given in Table 5-7. These requirements are relatively high, since aircraft power sources are capable of providing large amounts of power. The data[54] from which these power requirements were derived show occassional deviations of nearly a factor of ten from the average values presented in Table 5-7. No particular reason for these variations was discovered. The starting power requirements appear to be approximately two to three times the average power requirements. The average power requirements given in the table can be approximated by

$$\text{average power (watts)} = \begin{cases} 80 + 2.4\ S^2 & \text{(w/o IMC)} \\ 130 + 7.3\ S^2 & \text{(w/ IMC)} \end{cases} \qquad (5\text{-}27)$$

where S is the film size in inches. It may be noted that, because of the S^2 dependence, the power is proportional to the film mass per frame, aside from a constant. That is, the power depends upon the weight of the film advanced per image. Eq. (5-27) is, of course, only valid for aerial reconnaissance systems.

Table 5-7

Reconnaissance Camera Power Requirements

Camera Size	Average Power (watts) w/o IMC	w/ IMC
70 mm	110	200
5 inch	125	300
9½ inch	300	800

A recent planetary film system design[52] envisions an image format of 4.5 x 2.25 inches. The system power requirements are 20 watts for photography, 40 watts for processing, and 12 watts for film scanning. The film area required for each photo must be about 5 x 2.75 inches, and therefore the power requirement estimated from eq. (5-27), assuming an IMC capability, is about 230 watts. Thus it is assumed here that photography power requirements for space film systems are one-tenth those of aerial reconnaissance systems. The processing power requirement is taken as twice the camera power, and the scanning power as 0.6 times the camera power. Thus the total system average power for space film systems is approximately

$$P = \begin{cases} 29 + 0.86\ S^2 & \text{(w/o IMC)} \\ 47 + 2.6\ \ S^2 & \text{(w/ IMC)} \end{cases} \qquad (5\text{-}28)$$

where P is the average system power in watts, and S is the film size in inches (for a square format).

For Lunar Orbiter, the film area required for a single exposure is about 2.75 x 12 inches, and eq. (5-28) yields a power estimate of about 130 watts. Since the Lunar

Orbiter photo subsystem requires about 80 watts[52], the estimates afforded by eq. (5-28) may be unduly conservative.

5.2.4 Data Acquisition Rate

As with the television systems, an estimate of the system data acquisition rate is given by

$$DR = \frac{GL^2}{t_c} \text{ bits/sec} , \tag{5-29}$$

where t_c is the cycle time, and G is the number of binary bits used to describe a resolution element. In this study, G has been taken as six, implying 64 shades of grey in the acquired imagery. The cycle time is approximately

$$t_c = \frac{W(1-g)}{v_h} , \tag{5-30}$$

where W is the image ground size, g is the fractional image overlap along the heading line, and v_h is the maximum apparent horizontal speed of the spacecraft.

5.2.5 Attitude Control and Platform Stability

The required pointing accuracy is

$$\Delta\theta = \frac{\Delta r}{H} \text{ radians}, \tag{5-31}$$

where Δr is the allowable error in location of the principal point of the image as projected on the planetary scene. Maximum allowable sensor system rotation rates were discussed in Section 4.2.5. It was shown that the maximum allowable yaw rate is

$$\dot{\theta} = \frac{r}{3\ t_e\ W} \text{ rad/sec.} \tag{5-32}$$

Similarly, the maximum allowable roll or pitch rate is

$$\dot{\phi} = \frac{r}{6\ t_e\ H} \qquad \text{(w/o IMC)} \qquad (5\text{-}33)$$

without image motion compensation, and

$$\dot{\phi} = \frac{r}{0.6\ t_e\ H} \qquad \text{(w/ IMC)} \qquad (5\text{-}34)$$

with image motion compensation.

5.3 Experiment Design Procedure

Figure 5-8 shows a logic schematic for the design of a planetary orbital photographic film camera system. The procedure is very similar to that described in Section 4.3 for television camera systems. The major differences are that film, processing, and shielding weights must be determined for photographic film systems and that photographic films are sufficiently sensitive to provide adequate signal-to-noise ratios without special attention in the design of the system. Experiment design is predicated upon the image specifications given in Volume I and the orbit selections given in Volume III. From this point in the logic diagram (Figure 5-8), the oval boxes represent estimation of experiment support requirements, while the rectangular boxes represent steps in the design procedure. The scaling laws and design equations associated with the design analysis are summarized in Figure 5-9. The numbers in the lower right hand corner of the boxes in both figures relate each figure to the other. The suggested design procedure is summarized here, and a numerical example is given in Section 6 of Volume I.

The required camera pointing accuracy is independent of specific design details and can be estimated immediately (step #1). The ground resolution which must be achieved by the camera system is determined by the horizontal and vertical

resolution given in the image specifications. The ground resolution may be controlled by the vertical height differences which must be detected. Assuming an image overlap of sixty percent for stereo coverage, the required ground resolution in the imagery is controlled by the desired vertical resolution whenever the image ground size is less than $Hr_h/(0.4r_v)$. The total number of lines required in the image may be estimated (step #3) ignoring effects of planetary curvature. Approximately 33,000 lines per image are provided under low contrast conditions by 9.5 inch So-243 film. Thus if the estimated number of lines required exceeds this value, no currently available film can provide the required resolution over the necessary ground area. An accurate computation of the required number of lines (step #6) follows calculation of the camera field-of-view and an evaluation of effects of planetary curvature on ground resolution. The minimum useful optical system diameter (step #7) is taken as five times the classical diffraction limit based on a wavelength of 6000 Å, and is state-of-art limited to smaller than two meters.

The maximum apparent ground speed is determined by the orbit parameters (step #8). As with the TV system scaling law chart, the vertical camera speed shown is the maximum value experienced at any point along the orbit. The maximum value encountered during imaging operations may be computed as discussed in Section 1.5 above. Exposure times (step #9) are constrained by permitting image motion smear of one-half resolution element. With image motion compensation (IMC), the exposure time can be increased nearly a factor of ten. An initial choice of the film type and size may be made from Table 5-3 based on the required number of lines. Unless need of a fast film is anticipated, SO-243 film should be chosen in the smallest useful film size. The focal length is computed and a reasonable f-number selected. No filter is required except for Mars surface imagery (500 mμ filter) and pseudo-color imagery (filter factor of about 14). The scene luminance (step #11) is estimated

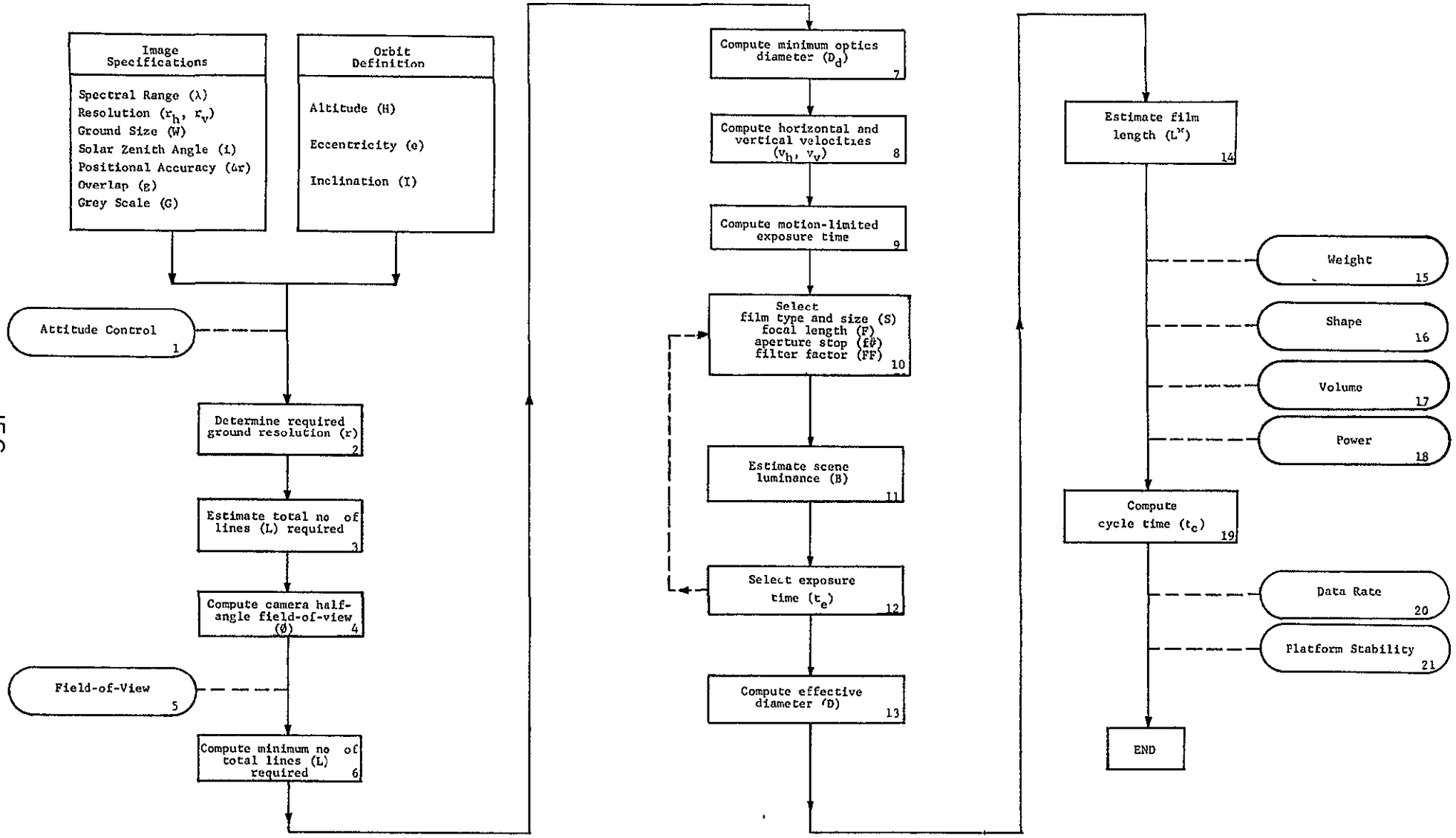

FIGURE 5-8 LOGIC DIAGRAM FOR PHOTOGRAPHIC FILM SYSTEMS

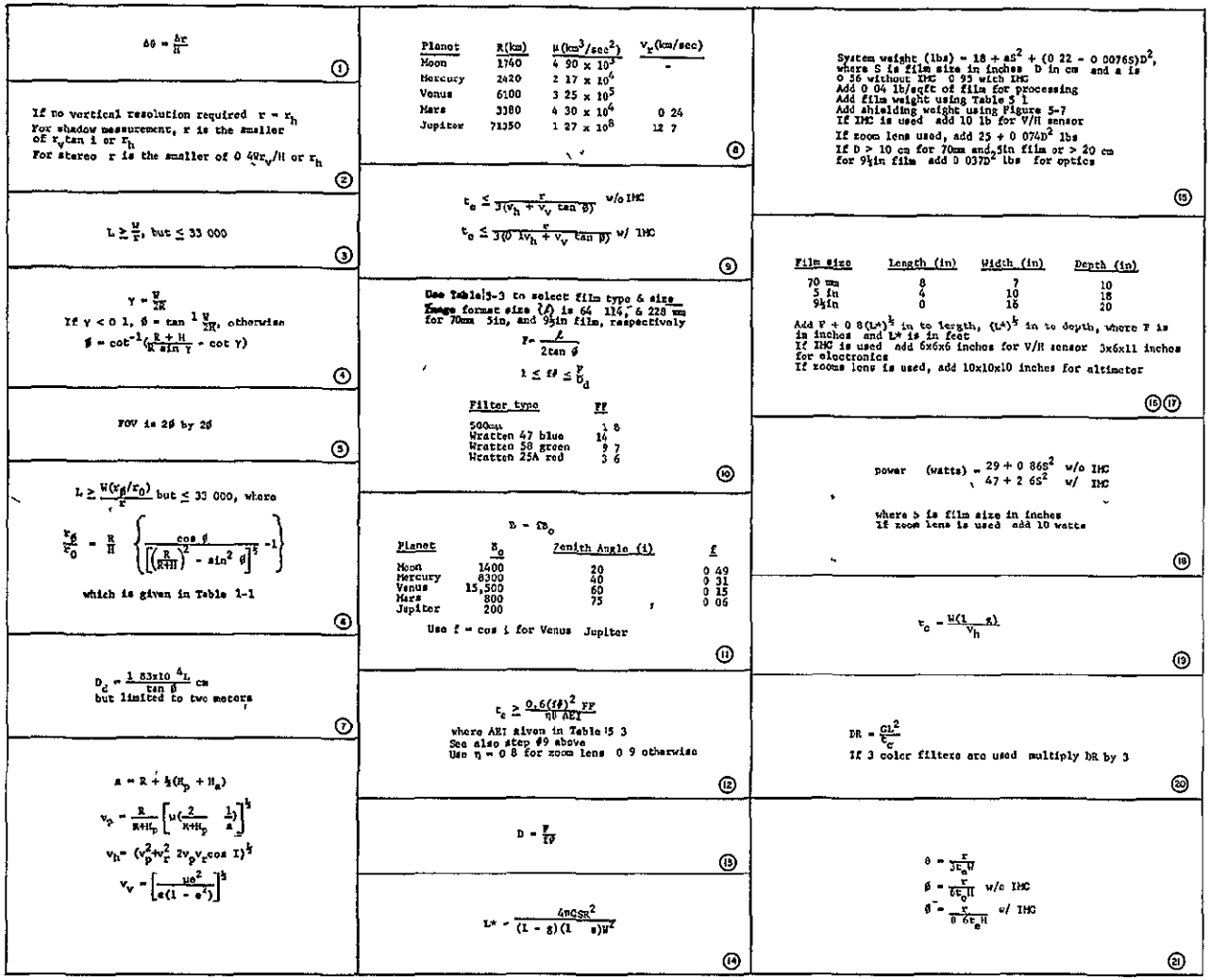

NOMENCLATURE

a orbit semi major axis, km
AEI film aerial exposure index
B scene luminance ft-lambert
C planetary fractional coverage
D optics diameter (F/f#), cm
D_d minimum optics diameter cm
DR data acquisition rate bits/sec
e orbit eccentricity
f scene photometric function
f# optics aperture stop (f number)
F focal length cm
FF filter factor
FOV field of view
g fractional overlap along orbit
G bits per resolution element (normally 6)
H camera altitude, km
H_a-orbit apoapse altitude, km
H_p orbit periapse altitude km
i solar zenith angle
I orbit inclination
f image format size
L-total no of lines per frame
L^* total length of film feet
r desired ground resolution, km
r_h desired horizontal resolution km
r_v desired vertical resolution km
R planet radius, km
s fractional side overlap
S film width inches
t_c cycle time, sec
t_e exposure time, sec
v_h apparent horizontal speed km/sec
v_p camera ground speed at periapse km/sec
v_r-planet equatorial rotation speed, km/sec
v_v camera vertical speed, km/sec
W image width (length) on ground km
γ image half angle subtended at planet center
δr desired image ground positional accuracy km
δf allowable camera pointing error radians
η optical system transmission factor
θ allowable camera yaw rate rad/sec
λ wavelength
μ planet gravitational constant, km^3/sec^2
φ camera half angle field of view
$\dot\beta$ allowable camera pitch or roll rate rad/sec

FIGURE 5-9 SCALING LAWS FOR PHOTOGRAPHIC FILM SYSTEMS

exactly as for TV systems. The minimum exposure time (step #12) is proportional to the square of the f-number and inversely proportional to the film aerial exposure index (AEI). If the minimum exposure time is not less than the maximum, the minimum may be reduced by decreasing the f-number, which will increase the optical system size, or by selecting a faster film, which may require a larger film size to retain the necessary number of lines per image. Selection of a short exposure time will reduce the platform stability requirements. The optical system effective diameter (step #13) is simply the focal length divided by the f-number, and is state-of-art limited to about two meters. For large optical systems, the weight is proportional to the diameter squared, hence the diameter should be kept less than ten or twenty centimeters, if possible. The optical diameter may be reduced by increasing the f-number, but this may have an adverse effect on the minimum exposure time. The required length of film (step #14) depends upon the amount of planetary coverage. The maximum fractional coverage attainable is specified on each orbit data sheet of Volume III. The film length estimate shown assumes only one acquired image per image ground area. Thus for pseudo-color operation, the actual film length required is three times the estimate shown. Similarly, if two planetary coverages are required, the film length must be doubled.

Having determined the basic camera system variables, the remaining support requirements may be estimated. The film weight is estimated using the film weight per square foot listed in Table 5-1. Figure 5-7 gives the shielding weight for SO-243 film on a 330 day mission to Mars as a function of film length. The value obtained from the figure should be multiplied by the ratio of the interplanetary trajectory flight time plus the time required in orbit to 330 days, by the square of the ratio of Mars heliocentric distance (1.52 AU) to the target planet's heliocentric distance, and by the ratio of the film AEI to that

of SO-243 (1.6). The camera system shape is estimated (step #16) as shown by using the focal length and film length. The volume is simply obtained by multiplying together the camera system length, width, and depth. Additional volume may be required for IMC equipment or an altimeter. The system average power requirement depends upon the film size as shown in step #18. Finally, the cycle time, data acquisition rate, and maximum permissible camera roll and yaw rates are estimated in a manner virtually identical to that for TV systems.

6. INFRARED SCANNING SYSTEMS

6.1 Design Equations

The following paragraphs deal with the sensor design variables of space-orbital optical-mechanical scanning systems for obtaining imagery in the infrared portion of the spectrum. Section 6.2 presents empirical data pertinent to estimating sensor system support requirements, while Section 6.3 summarizes a suggested procedure for the logical design of infrared scanning systems.

6.1.1 Scanning Operation

The relations between sensor system field-of-view and imaged area on the planetary surface, and between sensor system angular resolution and ground resolution both parallel and normal to the heading line, have been discussed in Section 1.2. It was shown that if a great-circle arc-length W on the planetary surface is to be scanned, the total angle through which the scanning beam must rotate is 2ϕ, where

$$\phi = \cot^{-1} \left(\frac{R + H}{R \sin \gamma} - \cot \gamma \right) . \qquad (6\text{-}1)$$

Here R is the radius of the planet, H is the altitude of the sensor system, and γ is W/2R radians. For small values of W/R, in particular, for γ less than about 0.1, eq. (6-1) reduces to the flat planet result,

$$\phi = \tan^{-1} \left(\frac{W}{2H} \right) . \qquad (6\text{-}2)$$

The ground resolution r_x normal to the heading line is

$$r_x = \Delta\phi \cdot R \left\{ \frac{\cos \phi}{\left[\left(\frac{R}{R+H} \right)^2 - \sin^2 \phi \right]^{\frac{1}{2}}} - 1 \right\} , \qquad (6\text{-}3)$$

while the ground resolution r_y parallel to the heading line is

$$r_y = \Delta\phi \cdot R_s = \frac{\Delta\phi \cdot R \sin\gamma}{\sin\phi} , \qquad (6\text{-}4)$$

where $\Delta\phi$ is the angular resolution of the sensor system, and R_s is the slant range. If $\Delta\phi$ is independent of ϕ, as has been assumed in this study, it is seen that both r_x and r_y increase with ϕ. That is, the ground resolution degrades as one moves away from the subsatellite point. If r is the ground resolution which must be achieved throughout the entire scan, the angular resolution is constrained by

$$\Delta\phi \leq \frac{r}{H(r_\phi/r_0)} , \qquad (6\text{-}5)$$

where r_ϕ/r_0 has been given in Table 1-1 as a function of ϕ and H/R.

The scanning beam, of angular size $\Delta\phi$ by $\Delta\phi$, is swept across the planetary surface by the rotation of a multi-faced scanning mirror, schematically shown in Figure 6-1. To avoid gaps between successive scan lines on the planetary surface, the distance traveled along the heading line by the sensor in the time taken to scan a single line must be less than the width of the scan line. Thus, if t is the time required to scan the great-circle arc-length W, then

$$v_h t \leq H \cdot \Delta\phi , \qquad (6\text{-}6)$$

where v_h is the apparent speed of the sensor along the heading line. The computation of v_h has been discussed in Section 1.5. If the scanning mirror has m faces,

$$t = \frac{2\pi}{m\omega} , \qquad (6\text{-}7)$$

where ω is the angular rotation rate (in radians per second)

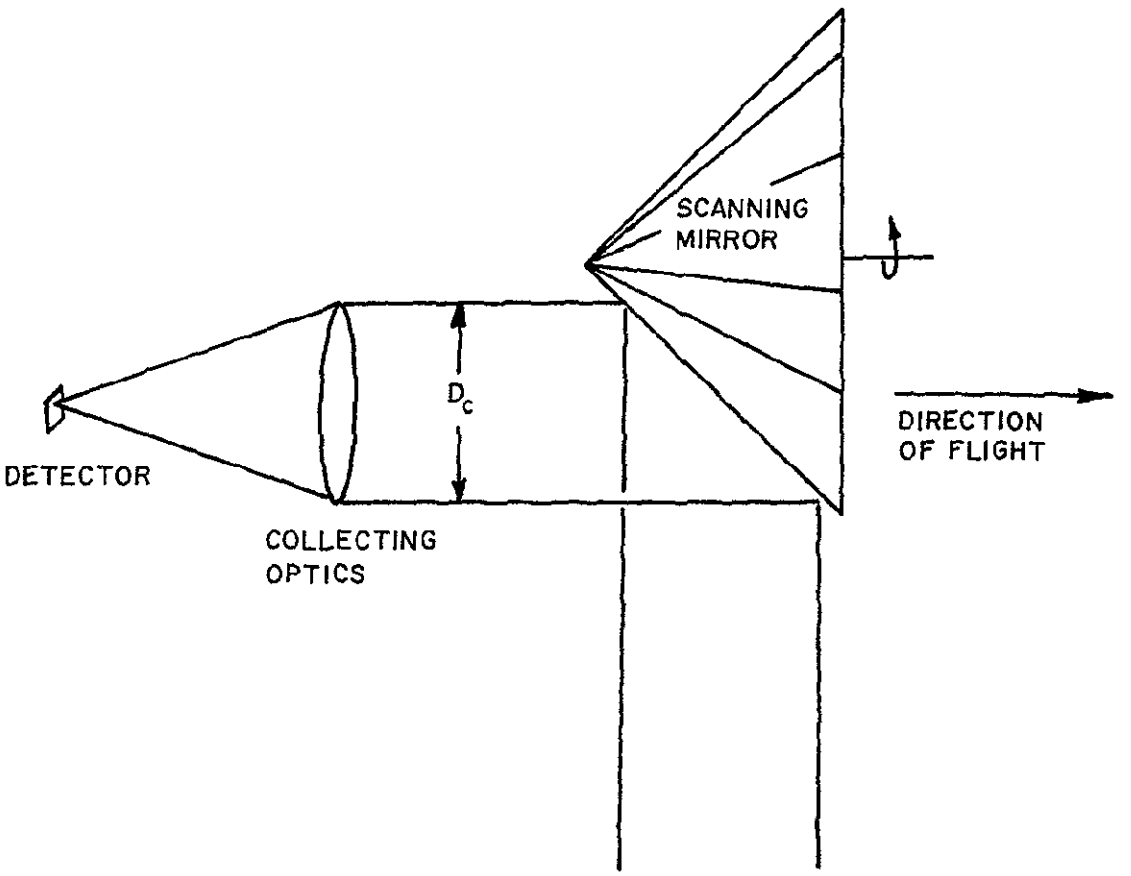

FIGURE 6-1. OBJECT PLANE SCANNING

of the scanning mirror. It should be noted that each face of the scanning mirror observes the planetary scene through a rotation angle of $2\pi/m$ radians, centered on the vertical. If each face is to observe the great-circle arc-length W by rotating through an angle $2\emptyset$, then m must be less than $\pi/\emptyset$. Substituting eq. (6-7) into eq. (6-6), and rearranging, the scanning mirror rotation rate is constrained by

$$\omega \geq \frac{2\pi\, v_h}{m\, H \cdot \Delta\emptyset} , \tag{6-8}$$

if gaps are not to appear between the scan lines. A rotation rate larger than the required minimum value will result in some overlap of scan lines. By using more than one detector, multiple scan lines can be swept out simultaneously. For a linear array of p detectors[19],

$$\omega \geq \frac{2\pi\, v_h}{p\, m\, H \cdot \Delta\emptyset} , \tag{6-9}$$

and the scan rate may be reduced from the single detector case.

For some orbital imaging experiments, such as those designed to obtain images of cloud formation, the image specifications given in Volume I indicate that data from all the resolution elements within the scene area (W by W) should be procured in some time interval less than the maximum allowable image acquisition time t_a. Except for exceedingly small values of t_a, the condition expressed by eq. (6-6) suggests that data from a single scan line will be procured in a time interval much less than t_a. However, it is also necessary to procure data from all the scan lines in the scene dimension W along the heading line in a time interval less than t_a. This implies that

$$v_h t_a \geq W . \tag{6-10}$$

The scanning rate is also constrained by the response time of the detector. That is, if the detector response time is τ, the scanning beam must observe each resolution element on the planetary surface for a length of time longer than τ. It is assumed here that 2τ is a sufficient time, hence

$$\omega \leq \frac{\Delta\phi}{2\tau} . \qquad (6\text{-}11)$$

The rotation rate of the scanning mirror is also limited by distortion of the optically flat surfaces. Chase and Kaisler[20] have studied such mechanical problems, and have shown that the bursting speed of a thin-walled cylinder is

$$\omega = \frac{6.26}{D_s} \left(\frac{S}{\rho}\right)^{\frac{1}{2}} , \qquad (6\text{-}12)$$

where D_s is the cylinder diameter in meters, S is the yield stress in kg/m^2, and ρ is the wall density in kg/m^3. Representative values of S/ρ are 1.78×10^4 meters for aluminum, 1.52×10^4 meters for beryllium, and 6.35×10^3 meters for stainless steel. Assuming that the scanning mirror may be treated as a thin-walled cylinder, and that significant optical distortion will occur at rotational speeds of one-fourth the bursting speed, the scanning mirror rotation rate is limited by

$$\omega \leq \frac{193}{D_s} \text{ radians/sec}, \qquad (6\text{-}13)$$

for a beryllium mirror.

These operational and mechanical constraints confine the scanning mirror rotation rate to the range

$$\frac{2\pi v_h}{pm\ H \cdot \Delta\phi} \leq \omega \leq \begin{matrix} \Delta\phi/2\tau \\ \text{or} \\ 193/D_s \end{matrix}$$

For high resolution (small $\Delta\phi$ systems), it is evident that simultaneous scans may be required. This can best be accompli by an array of detectors, although the current state-of-art probably limits p to 50 or less[59,60]. Since only the produc pm occurs, it is equally effective to increase the number of faces on the scanning mirror. Aside from the necessity of $m < \pi/\phi$, increasing m much beyond four may result in unreasona large scanning mirrors, since it is evident from Figure 6-1 that each face must be at least as large as the collecting aperture. Rotating scanning mirrors of base diameters larger than one or two meters are impractical. Finally, although eq. (6-13) implies that rotation rates for very small scanning mirrors are limitless, a reasonable upper limit is probably 200,000 rpm, or about 2×10^6 radians per second.

6.1.2 Detector Sensitivity

The sensitivity of infrared detectors is commonly represented[17] by the quantity D^*, defined as

$$D^* = \frac{(A\ \Delta f)^{\frac{1}{2}}}{NEP} , \qquad (6\text{-}14)$$

where A is the area of the detector, Δf is the noise bandwidth and NEP is the noise equivalent power. For photon detectors, the response is proportional to the rate at which photons are detected. No photons are detected, however, unless the photon energy is greater than some threshold value. Since photon energy is inversely proportional to wavelength, the response of an idealized photon detector per unit photon energy increases with wavelength, and suddenly vanishes at a wavelength corresponding to the threshold energy. Thus the wavelength dependence of D^* for an infrared photon detector is often approximated by

$$D^*(\lambda) = \frac{\lambda}{\lambda_p} D^*_p , \qquad (6\text{-}15)$$

where λ_p is the wavelength of peak response, and D^*_p is the value of $D^*(\lambda)$ at λ_p. On the other hand, thermal detectors, such as thermistors and thermocouples, are essentially energy detectors and hence have a flat response per unit incident energy. Characteristics of typical infrared detectors, both photon and thermal, are shown in Table 6-1. It should be noted that the detectivities are given in units of meters - $Hz^{\frac{1}{2}}$/watt, rather than cm-$Hz^{\frac{1}{2}}$/watt, as is usually done. Typica spectral response curves are shown in Figure 6-2.

Solving eq. (6-14) for the noise equivalent power, and using eq. (6-15),

$$NEP = \frac{\lambda_p (A\Delta f)^{\frac{1}{2}}}{\lambda D^*_p} \quad . \tag{6-16}$$

If $M(\lambda)$ is defined as the spectral power incident upon the detector, the signal-to-noise ratio is

$$\frac{S}{N} = \frac{D^*_p}{\lambda_p} \left(\frac{\Delta\phi}{A\omega}\right)^{\frac{1}{2}} \int \lambda M(\lambda) d\lambda \quad , \tag{6-17}$$

where Δf has been taken as $\omega/\Delta\phi$, and the integration is performed over the wavelength passband of the sensor system or detector. This derivation has been somewhat less than rigorou but essentially the same result has been obtained by Jamieson[and by Hawkins[27]. Jamieson also suggested that for chopped systems, eq. (6-17) should be multiplied by $2^{\frac{1}{2}}/\pi$ to obtain an effective rms signal-to-noise ratio, since the rms value of the fundamental harmonic of a square wave form is $2^{\frac{1}{2}}/\pi$ of t peak-to-peak value of the modulation. With this correction,

$$\frac{S}{N} = \frac{D^*_p}{\pi\lambda_p} \left(\frac{2\Delta\phi}{A\ \omega}\right)^{\frac{1}{2}} \int \lambda M(\lambda) d\lambda \quad , \tag{6-18}$$

Table 6-1

Infrared Detector Characteristics

Wavelength of Peak Response $\lambda_p(\mu)$	Detector	Photon or Thermal	Operating Temperature (deg K)	Response Time (μsec)	Peak Detectivity D_p^*(m-Hz$^{\frac{1}{2}}$/watt)	Reference
2.3	PbS	P	295	0.1	1.1×10^9	25
2.6	PbS	P	195	3.5	5.5×10^9	25
3.0	InAs	P	77	2	2.5×10^9	25
3.3	PbS	P	77	3	1.4×10^9	25
3.5	PbSe	P	295	2	2.5×10^7	25
4.2	PbSe	P	195	30	2.5×10^8	25
5.1	InSb	P	77	2	7×10^8	25
6	Ge:Au	P	77	1	4.5×10^7	25
11	Ge:Hg	P	23	1	2.3×10^8	25
12	HgCdTe	P	77	0.01	8×10^7	61
18	Si:Al*	P	23	0.00005	4×10^8	62
23	Ge:Cu	P	4	0.003	3×10^8	25
30	Si:B*	P	23	0.0002	5×10^8	62
34	Ge:Zn	P	4	1	2×10^8	25
-	Thermistor	T	295	> 500	$8 \times 10^4 \times [\tau(\mu\text{sec})]^{\frac{1}{2}}$	18

*in developmental stages

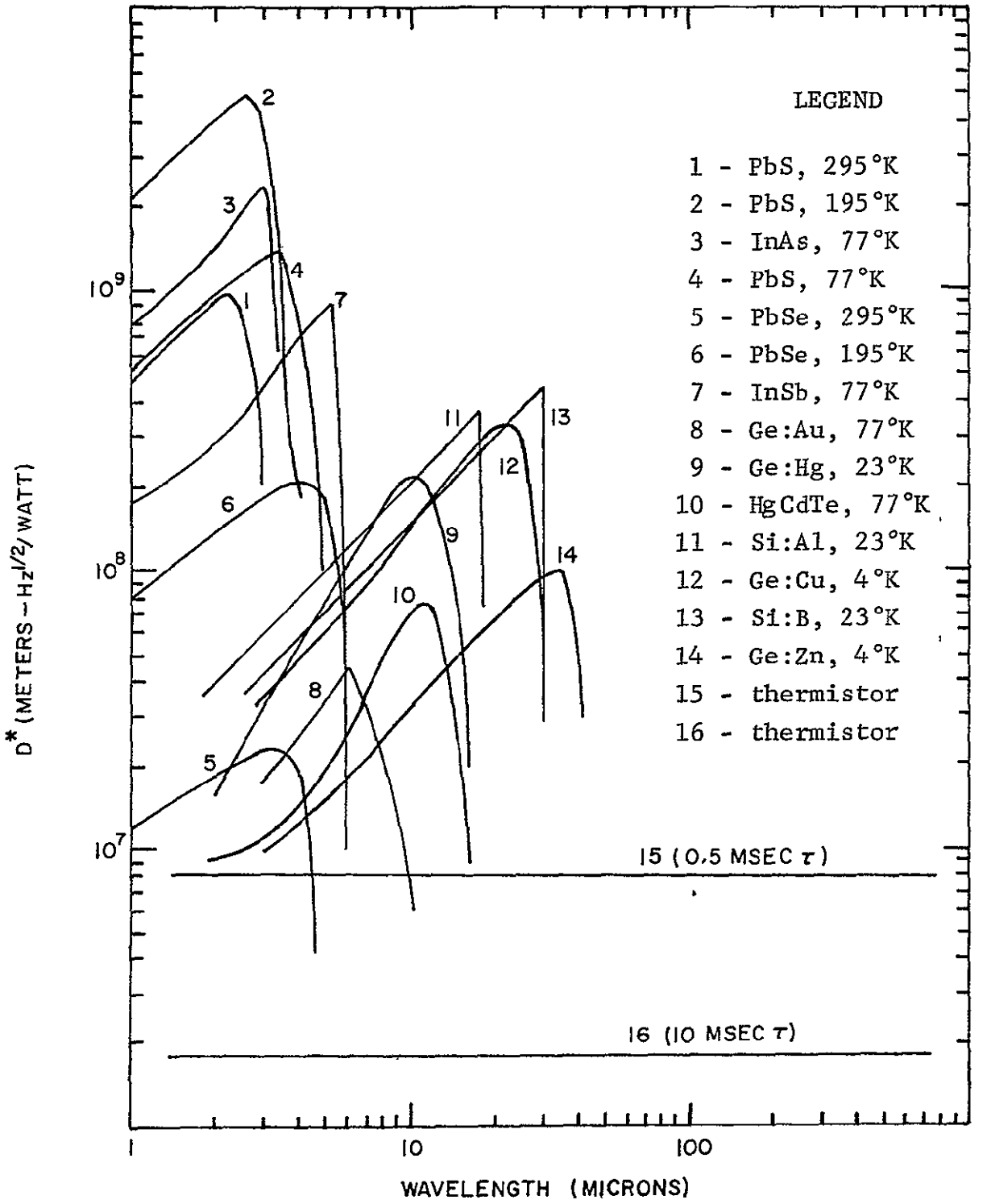

FIGURE 6-2. INFRARED SPECIFIC DETECTIVITIES

for infrared scanning systems using photon detectors, and

$$\frac{S}{N} = \frac{D^*_p}{\pi} \left(\frac{2\Delta\phi}{A\,\omega}\right)^{\frac{1}{2}} \int M(\lambda)\,d\lambda \qquad (6\text{-}19$$

for infrared scanning systems using thermal detectors.

6.1.3 Collecting Optics

Eqs. (6-18) and (6-19) show that the sensor system signal-to-noise ratio is linearly proportional to the total power incident upon the detector, but weighted by the spectral responsivity of the detector. Conversely, if a specific value of the signal-to-noise ratio is required for high quality imagery, the amount of power focused upon the detector by the collecting optics must exceed some minimum value, which is linearly related to the minimum acceptable signal-to-noise rat It is convenient to discuss separately the imaging of solar infrared energy reflected by the planetary scene and the imagi of thermal infrared energy emitted by the planetary scene. Th near infrared portion of the spectrum, from 0.8 microns to abc 2.5 microns, is useful for detection of reflected solar energy while the mid and far infrared, above 2.5 microns, is useful for detection of thermally emitted energy.

a. Reflected Solar Energy

If $H(\lambda)$ is the solar spectral irradiance at the heliocentric radius of the planet, $a(\lambda)$ is the planetary scer albedo, and f is the scene photometric function, then it has been shown in Section 2.1 that

$$I(\lambda) = \frac{1}{\pi} H(\lambda)\, a(\lambda)\, f \cos \epsilon \qquad (6\text{-}2$$

where $I(\lambda)$ is the spectral radiance, and ϵ is the angle of reflection. The spectral radiance is the amount of solar powe reflected into a unit solid angle by a unit area of the observ scene. It was also shown earlier that for the imaging

operations pertinent to this study, the photometric function f is dependent only upon the nature of the scene (surface or clouds) and the angle of incidence at the scene. Preferred forms for the photometric function were indicated in Table 2-1. The spectral power incident upon the detector, $M(\lambda)$, is then

$$M(\lambda) = \frac{D_c^2 \, r_x r_y f \, H(\lambda) \, \eta(\lambda) \, a(\lambda) \cos \epsilon}{4 \, R_s^2} . \qquad (6\text{-}21)$$

Here $\pi D_c^2/4 \, R_s^2$ is the solid angle subtended by the collecting optics of diameter D_c at the range R_s, $r_x r_y$ is the area of a scene resolution element, and $\eta(\lambda)$ is the optical efficiency of the sensor system. By using the geometrical relations developed in Section 1, it can be shown that

$$\frac{r_x r_y \cos \epsilon}{R_s^2} = (\Delta\phi)^2 , \qquad (6\text{-}22)$$

where $\Delta\phi$ is the angular resolution of the sensor system. Substitution of eq. (6-22) into eq. (6-21) yields

$$M(\lambda) = \frac{1}{4} (\Delta\phi)^2 \, D_c^2 \, f \, \eta(\lambda) \, H(\lambda) \, a(\lambda) . \qquad (6\text{-}23)$$

An expression for the diameter of the collecting optics may be obtained by using eq. (6-23) with eqs. (6-19) or (6-20). For a photon detector system,

$$D_c = \frac{1}{\Delta\phi} \cdot \left(\frac{\omega}{\Delta\phi}\right)^{\frac{1}{4}} \left(\frac{2 \cdot 2^{\frac{1}{2}} \pi \ell \lambda_p \cdot S/N}{D_p^* \, f \, \eta} \right)^{\frac{1}{2}} \left(\int \lambda H a d\lambda \right)^{-\frac{1}{2}} , \quad (6$$

and for a thermal detector system

$$D_c = \frac{1}{\Delta\phi} \cdot \left(\frac{\omega}{\Delta\phi}\right)^{\frac{1}{4}} \left(\frac{2 \cdot 2^{\frac{1}{2}} \pi \ell \cdot S/N}{D_p^* f \eta}\right)^{\frac{1}{2}} \cdot \left(\int \mathrm{Had}\lambda\right)^{-\frac{1}{2}}, \quad (6$$

where ℓ has been introduced as the linear size (i.e., the squa root of the area) of the detector, and η has been removed fron under the integral sign as an average value of the system transmission factor. Detector sizes ranging from 0.1 to three millimeters are reasonable for the detectors listed in Table 6-1, while optical transmission factors of about 0.85 are comm in the near infrared spectral region.

Eqs. (6-24) and (6-25) both have the form

$$D_c = \frac{1}{B \cdot \Delta\phi} \left(\frac{\omega}{\Delta\phi}\right)^{\frac{1}{4}} \left(\frac{J \cdot S/N}{D_p^* \eta}\right)^{\frac{1}{2}}, \qquad (6\text{-}26)$$

where the parameter B is defined by

$$B^2 = \frac{f}{2 \cdot 2^{\frac{1}{2}} \pi \lambda_p} \int_{\lambda_1}^{\lambda_2} \lambda \, H(\lambda) \, a(\lambda) \, d\lambda \qquad (6\text{-}27)$$

for <u>photon</u> detectors, and

$$B^2 = \frac{f}{2 \cdot 2^{\frac{1}{2}} \pi} \int_{\lambda_1}^{\lambda_2} H(\lambda) \, a(\lambda) \, d\lambda \qquad (6\text{-}28)$$

for <u>thermal</u> detectors. The integration is performed over the spectral passband (from λ_1 to λ_2) of the sensor system. For photon detectors, λ_2 should be set equal to λ_p. However, for near infrared sensor systems, where λ_2 is in the range 2-3 microns, little error is introduced by integrating from λ_1 to λ_2, since $H(\lambda)$ is small near λ_2, and the value of the integra is insensitive to the precise value of the upper limit of

integration. The integrals shown in eq. (6-27) and (6-28) have been evaluated over the spectral interval from 0.8 to 2.0 microns in the case of Mercury, and from 0.8 to 2.5 microns in the case of the other planets, using the data presented in Section 2. The results are shown in Table 6-2 in terms of the constants C_p and C_t defined by the integrals shown above. That is, C_p denotes the integral in eq. (6-27), while C_t denotes the integral in eq. (6-28).

Table 6-2

Values of C_p and C_t

Planet	Spectral Interval (microns)	Photon Detectors C_p (watts/m)	Thermal Detectors C_t (watts/m^2)
Moon	0.8-2.5	2.22×10^{-4}	143
Mercury	0.8-2.0	1.26×10^{-3}	852
Venus	0.8-2.5	6.38×10^{-4}	525
Mars	0.8-2.5	1.00×10^{-4}	77.3
Jupiter	0.8-2.5	3.71×10^{-6}	3.55

The signal-to-noise ratio required of the sensor system clearly influences the optical design. Smith and Wood[28], along with other workers, have reviewed this problem, and it appears that for visual imagery an S/N of about three is required to resolve a standard three-bar pattern. That is, for a high contrast target, an S/N of about three is required for good imagery. Presumably, similar results would be obtained in the infrared portions of the spectrum. For a low contrast target, the signal must be increased to afford the same probability of detection, or image quality. Suppose that the target or scene consists of small areas whose reflectivities

differ by five percent. This corresponds roughly to a scene contrast of 1.05:1 and the modulation transfer function for this contrast is about 0.025. If a signal-to-noise ratio of three is required for a scene of high contrast, then a signal-to-noise ratio of 3/0.025, or 120, is required for reliable detection of reflectivity differences of five percent. Althou for some applications, such as study of lithologic contacts, it may be argued that detection of reflectivity differences on the order of one percent are desirable, such highly precise measurements are probably best performed by spectroscopic, rather than imaging, experiments.

b. Thermally Emitted Energy

In imaging thermally emitted radiation, the quantity of interest is the difference in radiance between two adjacent scene resolution elements whose equivalent brightness temperatures differ by the amount ΔT. This computation has been discussed in Section 2.2. By an analogous development to that presented above for reflected sunlight, the required diameter of the collecting optics is

$$D_c = \frac{1}{B \cdot \Delta\emptyset} \left(\frac{\omega}{\Delta\emptyset}\right)^{\frac{1}{4}} \left(\frac{\ell \cdot S/N}{D_p^* \eta}\right)^{\frac{1}{2}}, \qquad (6\text{-}29)$$

which is formally identical to eq. (6-26). However, now the parameter B is defined by

$$B^2 = \frac{\Delta T}{2 \cdot 2^{\frac{1}{2}} \pi \lambda_p} \int_{\lambda_1}^{\lambda_p} \lambda \frac{\partial R}{\partial T} \, d\lambda \qquad (6\text{-}30)$$

for photon detectors, and

$$B^2 = \frac{\Delta T}{2 \cdot 2^{\frac{1}{2}} \pi} \int_{\lambda_1}^{\lambda_2} \frac{\partial R}{\partial T} \, d\lambda \, , \qquad (6\text{-}31)$$

for thermal detectors. Here R is the black body spectral radiant emittance, and T is the equivalent black body temperature of the emitting surface. The evaluation of these integrals was discussed in Section 2.2, where it was shown that the Rayleigh-Jeans approximation for R may be used if λT is greater than 0.014 meters-deg K, and the Wien approximation may be used if λT is less than 0.014 meters-deg K.

Thus for photon detectors,

$$B^2 = \frac{ck(\Delta T)}{2 \cdot 2^{\frac{1}{2}} \lambda_p} \left(\frac{1}{\lambda_1^2} - \frac{1}{\lambda_p^2} \right) \qquad (6\text{-}32)$$

using the Rayleigh-Jeans approximation, and

$$B^2 = \frac{ck(\Delta T)}{2^{\frac{1}{2}} \lambda_p} \left(\frac{kT}{hc} \right)^2 \left[e^{-x}(x^3 + 3x^2 + 6x + 6) \right]_{x_1}^{x_2} \qquad (6\text{-}33)$$

using the Wien approximation. Here c is the speed of light (3×10^8 meters/sec), k is Boltzmann's constant ($1{,}381 \times 10^{-23}$ joules/deg K), h is Planck's constant (6.626×10^{-34} joule-sec), and x_i is defined by

$$x_i = \frac{hc}{\lambda_i kT} = \frac{0.0144 \text{ meters-deg K}}{\lambda_i T} \, . \qquad (6\text{-}34)$$

Similarly, for thermal detectors,

$$B^2 = \frac{ck(\Delta T)}{3 \cdot 2^{\frac{1}{2}}} \left(\frac{1}{\lambda_1^3} - \frac{1}{\lambda_2^3} \right) \qquad (6\text{-}35)$$

using the Rayleigh-Jeans approximation, and

$$B^2 = \frac{ck(\Delta T)}{2^{\frac{1}{2}}} \left(\frac{kT}{hc}\right)^3 \left[e^{-x}(x^4 + 4x^3 + 12x^2 + 24x + 24) \right]_{x_1}^{x_2}$$

(6-36)

using the Wien approximation, where x_i is defined above.

For any given experiment, the computation of the required collector diameter depends upon the apparent black body temperature T and the temperature difference ΔT which is to be detected. Volumes I and II of this report have presented estimates of these parameters; they are summarized here in Table 6-3 for convenience. The black body temperature depends upon whether atmospheric or surface phenomena are to be observed in daytime or in darkness. The temperatures given in the table are estimates of the minimum temperatures expected.

Table 6-3

Estimates of Planetary Temperatures

Planet	Temp. Resolution (deg K)	Atmospheric Temperature (deg K)	Surface Temperature (deg K)
Moon	1	-	120
Mercury	5	-	100
Venus	5	200	550
Mars	2	150	200
Jupiter	2	100	150

For reflected solar energy, it was appropriate to modify the signal-to-noise ratio to account for a low contrast target. The signal, however, was regarded as the power reflected by the scene, and not as a "difference signal" as is appropriate here. In the case of thermally emitted radiation, where the signal is regarded as the difference in received power from two different resolution elements, a signal-to-noise ratio of three should be adequate for good imagery. In principle, one would expect that this should give essentially the same results as computing the total power received, and then modifying the required signal-to-noise ratio to account for detection of low contrast targets.

To summarize, the minimum diameter required for the collecting optics is given by eq. (6-26), which is repeated here for convenience:

$$D_c = \frac{1}{B \cdot \Delta\phi} \left(\frac{w}{\Delta\phi}\right)^{\frac{1}{4}} \left(\frac{\ell \cdot S/N}{D_p^* \eta}\right)^{\frac{1}{2}}$$

The appropriate form of B depends upon both the energy source and the type of detector. Table 6-4 summarizes the computation of B. For imagery of reflected sunlight, a value of 120 should be used for S/N, while for imagery of thermally emitted radiation, a value of 3 should be used for S/N. Similarly, the optical transmission η should be about 0.85 for reflected sunlight, and about 0.8 for thermal emission.

For either thermally emitted or reflected energy, the minimum acceptable diameter of the collecting optics may be controlled by image plane resolution. That is, in either case, the diameter of the collecting optics must be larger than that implied by the diffraction limit:

$$D_c \geq D_d = \frac{1.22\lambda}{\Delta\phi} \qquad (6\text{-}37)$$

Table 6-4

Computation of B

Detector Type	Energy Source	λT (meters-deg K)	B^2
Photon	Sunlight	any value	$\frac{0.113\ fC_p}{\lambda_p}$
	Thermal Emission	≥ 0.014	$\frac{1.46\times10^{-15}\Delta T}{\lambda_p}\left(\frac{1}{\lambda_1^2}-\frac{1}{\lambda_2^2}\right)$
		≤ 0.014	$\frac{1.41\times10^{-11}T^2\Delta T}{\lambda_p}\left[e^{-x}(x^3+3x^2+6x+6)\right]_{x_1}^{x_2}$
Thermal	Sunlight	any value	$0.113\ fC_t$
	Thermal Emission	≥ 0.014	$9.77\times10^{-16}\Delta T\left(\frac{1}{\lambda_1^3}-\frac{1}{\lambda_2^3}\right)$
		≤ 0.014	$9.82\times10^{-10}T^3\Delta T\left[e^{-x}(x^4+4x^3+12x^2+24x+24)\right]_{x_1}^{x_2}$

Note x_1 is (0.0144 meters-deg K)/$\lambda_i T$; C_p and C_t are given in Table 6-2

The focal length of a simple optical system is

$$F = \frac{\ell}{\Delta\phi} \quad , \tag{6-38}$$

where ℓ is the linear size of a single detector. The effectiv f-number of the system is then

$$f\# = \frac{F}{D_c} = \frac{\ell}{D_c \Delta\phi} \cdot \tag{6-39}$$

For reasonable optical systems, the f-number should be unity or larger. However, use of an immersion lens[18] reduces the effective detector size by a factor of n, the index of refraction of the immersion lens. That is, f-numbers of about 0.3 are possible if immersion lenses are used. However, such lenses will reduce the optical efficiency of the sensor system, and complicate the construction of linear arrays of detectors.

6.1.3 Atmospheric Absorption

Infrared absorption of planetary atmospheres has been neglected in the development above. Such absorption is expected to significantly influence the imaging sensor system design only in the case of infrared imagery of planetary surfaces. The analysis of scientific objectives presented in Volume II indicates that infrared imagery of planetary surface plays a useful role in the exploration of the Moon, Mercury, and Mars. Since the Moon and Mercury have no atmospheres, atmospheric absorption does not affect the design of imaging experiments performed from orbit about the Moon or Mercury. At Mars, however, there is appreciable atmospheric absorption, due primarily to carbon dioxide absorption bands. An estimate of the atmospheric transmission for Mars is given in Figure 6-3. The transmission above 20 microns is not well known, as indicat by the dashed line in the figure. However, no absorption is expected, since CO_2 does not absorb above 20 microns. The

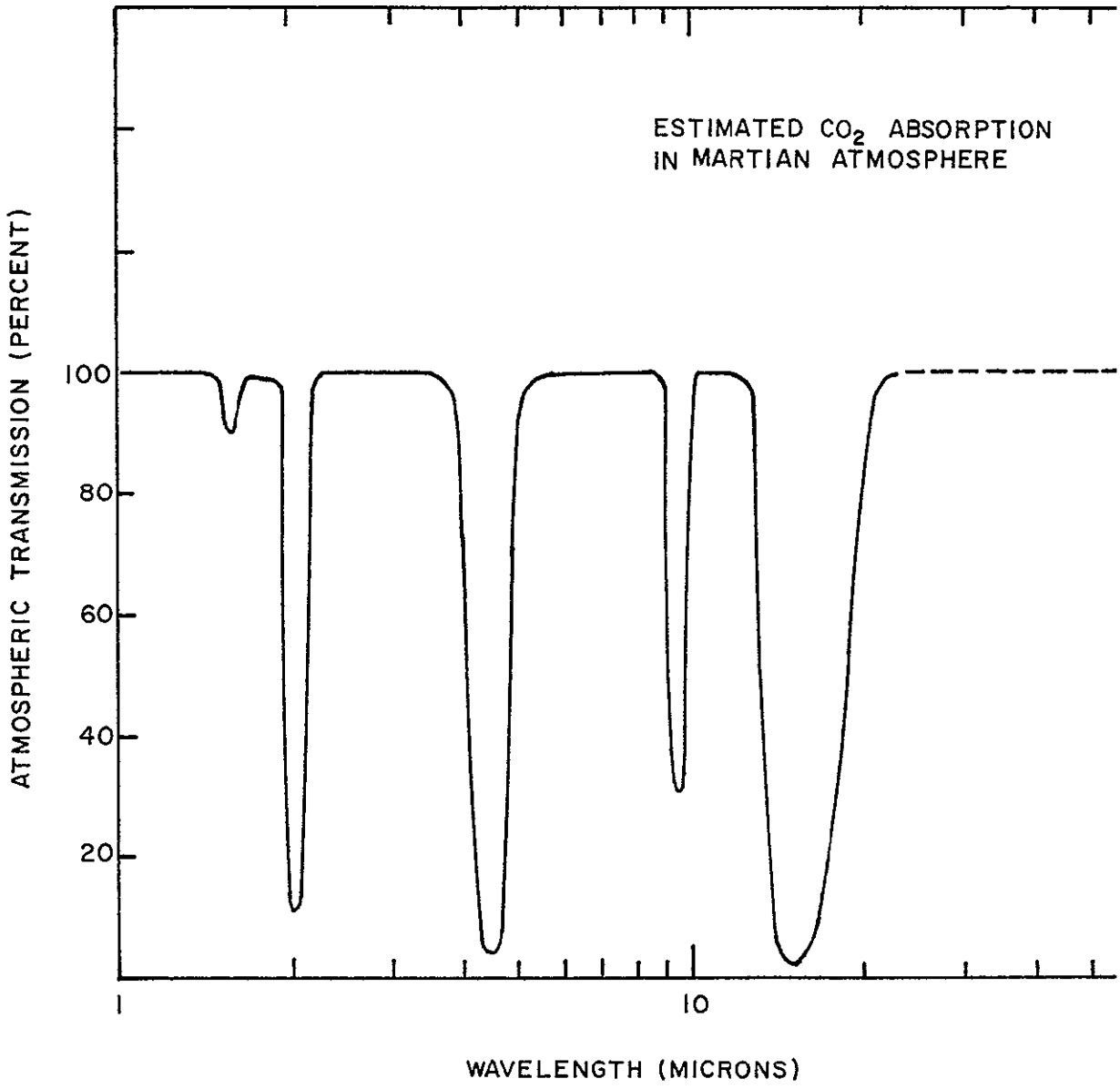

FIGURE 6-3 MARTIAN ATMOSPHERE ABSORPTION

useful infrared surface imaging experiments at Mars are for study of lithologic contacts and surface thermal anomalies. The desired infrared imagery of contacts consists of imaging reflected solar energy in the spectral region from 0.8 to 2.5 microns. Figure 6-3 shows a deep CO_2 absorption band at 2 microns. However, since the amount of solar energy reflected at 2 microns or greater is very much less than the amount of solar energy reflected at wavelengths from 0.8 to 2 microns (as shown in Figure 2-1), little error will be introduced by neglecting the 2 micron absorption band. For infrared imagery of surface thermal anomalies, the spectral region from 3 to 100 microns is of interest. Ignoring absorption in the 9.5 micron CO_2 band, the effect of atmospheric absorption may be approximated by omitting the spectral region from 4 to 5 microns and from 12 to 20 microns in computing the power incident upon the collecting optics.

6.2 Support Requirements

6.2.1 System Weight

Some of the characteristics of infrared scanning systems which have been flown in space, or have been designed in some detail for space use, are shown in Table 6-5. No satisfactory scaling laws have been derived from these data, with the exception of the system power requirement discussed in Section 6.2.3 below. As with the UV scanning systems, the system weight may be estimated by estimating the weights of system components.

By assuming that the weights of infrared optical systems are not radically different from the weights of similarly sized optical systems designed for use in the visibl portion of the spectrum, the weight of the collecting optics is approximately

$$M_c = 168\ D_c^2 \ . \qquad (6\text{-}40)$$

Table 6-5

Infrared Scanning Systems

System	Detector	Operating Temperature (°K)	Collecting Aperture Diameter (inches)	System Weight (lbs)	System Power per channel	Reference
Nimbus 5-Channel	bolometer	295	2	8	1.5	63
Mariner II	thermistor	295	1.3	3	1.2	64
Dual-Channel Radiometer	PbS	295	3	9	7	65
Venus Horizon Scanner	Ge	295	3	12	5	66
Spectro-photometer	PbSe	220	4	16	5	67
Nimbus NRIR	PbSe	220	4	11	4	68
Mariner 6 & 7	thermopile	295	1(two)*	8	1.5	69

* two sets of collecting optics are used

Here M_c is the mass of the optical system in kilograms, and D_c is the diameter of the collecting optics in meters. Optical system weights have been estimated for the sensor systems listed in Table 6-5 by using this equation, and the results are consistent with the tabulated sensor system weights. Eq. (6-40) is of questionable validity for collector diameters larger than two meters. This is not a serious deficiency, since such large optical systems are near the limit of the current and near-future state-of-art.

The size of the scanning mirror is related to the diameter of the collecting optics. Each face of the scanning mirror must have an area at least as large as the area of the collecting optics. If D_s is the diamter of the scanning mirror base, some simple analysis will show that

$$\frac{D_s}{D_c} = \begin{cases} 2^{\frac{1}{2}} & \text{for } m = 1, \\ 1 + \sec \phi & \text{for } m = 2, \\ [1 + \csc (\frac{\pi}{m} - \phi)] \sec \phi & \text{for } m \geq 3. \end{cases} \qquad (6\text{-}41)$$

By assuming that the thickness of the scanning mirror assembly is $D_s/10$ for m equal to one, $D_s/15$ for m equal to two, $D_s/20$ for m greater than two, and that the mass of the scanner shaft and bearings, the drive motor, and the scanner housing is 0.1, 0.1, and 0.5 times the mirror mass, respectively, the total mass of the scanning assembly is estimated as

$$M_s = \begin{cases} 0.13\rho \, D_s^{\,3} & \text{for } m = 1, \\ 0.22\rho \, D_s^{\,3} & \text{for } m = 2, \\ 0.015 \, \rho m \, D_s^{\,3} \sin \frac{2\pi}{m} & \text{for } m \geq 3. \end{cases} \qquad (6\text{-}42)$$

Here ρ is the density of the construction material. Suggested values are 1.85×10^3 kg/m^3 for beryllium, 2.7×10^3 kg/m^3 for

aluminum, and 7.9×10^3 kg/m^3 for stainless steel. Beryllium assemblies have been assumed for all support requirements estimated in this study.

A single detector and its associated electronics is assumed to have a mass of about one kilogram. It is unlikely that the electronics weight increases linearly with the number of detectors, particularly for p greater than ten or so. It is assumed here that the mass of the detectors and electronics is approximately

$$M_d = p^{\frac{1}{2}} \text{ kilograms.} \qquad (6\text{-}43)$$

This estimate should be accurate, to within a factor of three, for p not greater than fifty. The development and use of discrete circuit components may reduce this by a factor of two or three. Since, in most cases, the detector and electronics mass is either small in an absolute sense, or small compared to the weight of the optics and scanning mechanism, uncertainties in the unit weight of a detector do not lead to large errors in the sensor system weight. For very small scanning assemblies and collecting optics, the weight of structural material and packaging becomes significant. Thus the minimum sensor system mass is taken as one kilogram.

A remaining sensor system component which may contribute heavily to the total sensor system weight is the detector coolant system. For detectors operating at 295 deg K, no special cooling system is required, other than the spacecraft thermal control system. A radiative cooling system should be adequate for detectors operating at 195 deg K. For 77 deg K operation, cyrogenic cooling systems are probably required, although such operating temperatures might be achieved by two-stage radiant coolers currently under development[70]. Detector operation at 23 deg K requires a cyrogenic cooling system, while operation at 4 deg K is probably not even feasible (for the current state-of-art).

A single-stage radiant cooler should provide detector operating temperatures down to about 135 deg K. A Nimbus design[71] contemplates radiative cooling to such temperatures by use of a one-half pound radiative horn dissipating 20 milliwatts. The horn size is 6 x 6 x 6 inches. Thus the radiator area required for single-stage radiant cooling is approximately

$$A_r = 5P_d \text{ square meters,} \qquad (6\text{-}44)$$

where P_d is the power (watts) which must be dissipated. Similarly, the radiator mass is approximately

$$W_r = 10P_d \text{ kilograms,} \qquad (6\text{-}45)$$

where again P_d is the required power dissipation in watts.

Gross and Weinstein[72] have studied the feasibility of solidified gas cooling, and have constructed various laboratory models. For one year operation, a detector heat load of 0.1 watts, and an outer container temperature of 300 deg K, their studies show that a solid methane system could provide cooling to about 77 deg K, a neon system to about 23 deg K, and a solid hydrogen system to about 13 deg K. The required coolant and insulation weights are 26.3, 119, and 65.8 pounds, respectively; the measured solidified gas densities are 0.52, 1.35, and 0.103 g/cc, respectively. The total coolant system weight for a solid methane system, operating under the conditions stated above, is approximately 35 pounds. It is assumed here that the coolant system weight is proportional to the weight of the coolant and insulation, and that the coolant and insulation weight is proportional to the operating time and the power to be dissipated. It is also assumed that the coolant system volume can be approximated by dividing the system weight by the density of the solidified gas. Thus the coolant system mass is

$$M_g = aP_d\ t_{op}\ , \qquad (6\text{-}46)$$

and the cooling system volume is

$$V_g = bP_d\ t_{op}\ , \qquad (6\text{-}47)$$

where a and b are scaling coefficients given in Table 6-6, P_d is the power which must be dissipated, and t_{op} is the operating time. The operating time may be approximated by the mission duration, which is given on the orbit data sheets in Volume III, although this neglects any coolant loss during the flight time from Earth to the planet. No attempt has been made here to account for coolant system outer skin temperatures different from 300 deg K. The studies done by Gross and Weinstein seem to imply that the amount of coolant required is roughly proportional to the square root of the outer skin temperature. No data is available which implies limits to the validity of the coolant system scaling laws presented here.

Table 6-6

Coolant Scaling Coefficients

Coolant	Operating Temperature (deg K)	a (kg/watt-day)	b (cm^3/watt-day)
Methane	77	0.44	850
Neon	23	2.0	1500
Hydrogen	13	1.1	11000

For both radiative and cyrogenic cooling systems, the coolant system mass and size is assumed proportional to the amount of power which must be dissipated. As a minimum, the power which is focused on the detector by the optical system must be dissipated. Using eq. (6-23), the amount of solar power reflected by the planet upon the collecting optics, and focused on each detector is

$$0.25\ (\Delta\phi)^2\ D_c^{\,2}\ \eta \int_j H(\lambda)\ a(\lambda)\ d\lambda\ ,$$

where the photometric function f has been taken as unity, and the integration is to be performed over the transmission pass band of the collecting optics. If this is taken as the spectral interval from 0.8 to 2.5 microns (or 2.0 microns in the case of Mercury), then the value of the integral is given by the constant C_t in Table 6-2. In Section 2.2, it was shown that the total amount of thermal power emitted per unit area of surface into a unit solid angle is

$$\int_0^\infty \frac{R(\lambda,T)}{\pi}\ \cos\epsilon\ d\lambda = \frac{\sigma\ T^4\ \cos\epsilon}{\pi}\ ,$$

where σ is the Stefan-Boltzmann constant, T is the equivalent black body temperature, and ϵ is the angle of emission. Multiplying by the area of a resolution element, the solid angle subtended by the collecting optics, an assumed optical system efficiency of 0.8, and adding the result to the reflected solar power incident upon the detector, the total power focused on an array of detectors is approximately

$$P_d = 0.2p(\Delta\phi)^2\ D_c^{\,2}\ (C_t + \sigma\ T^4)\ . \qquad (6\text{-}48)$$

Here p is the number of detectors, and σ has the value

5.67×10^{-8} watts/(m^2-deg K^4). An upper limit to the temperature T is the observed blackbody temperature on the sunlit side of the planet as given in Table 6-7. Eq. (6-48) gives only the maximum power focused on the detector by the collecting optics. In addition, heat is transferred to the detector from the spacecraft by both conduction and radiation. If the detector temperature is small compared to the ambient temperature, the power transferred to the detector by radiation is approximately $\ell^2 \sigma T^4$, or on the order of 500 watts per square meter of detector area. Assuming that something on the order of 20 milliwatts per detector is transferred by conduction, the total power to be dissipated is rather crudely estimated to be

$$P_d = p[0.02 + 500 \ell^2 + 0.2(\Delta\emptyset)^2 D_c^2 (C_t + \sigma T^4)]. \quad (6\text{-}49)$$

The use of appropriate filters could eliminate either the reflected sunlight term or the planetary thermal radiation term.

Table 6-7

Planetary Maximum Temperatures

Planet	Maximum Temperatures (deg K)
Moon	400
Mercury	600
Venus	700
Mars	300
Jupiter	200 (?)

6.2.2 System Volumes

In addition to the cooling system volume discussed above, the sensor system volume must include the volume of the collecting optics and scanning mechanism. The volume of the scanning assembly may be approximated by a right circular cylinder of diameter 1.1 D_s and height 0.6 D_s. Similarly, the volume of the collecting optics may be approximated by a right circular cylinder of diameter 1.1 D_c and height 1.1 F. Thus the sensor system volume, exclusive of the coolant subsystem, is approximately

$$V = \frac{\pi}{4} (0.73\ D_s^3 + 1.3\ F\ D_c^2) . \qquad (6\text{-}50)$$

Unless the scanning and optical systems are very small, this estimate should be generous enough that it includes the detector and electronics volume and the scanning assembly drive mechanism. The minimum sensor system volume is taken as 10^{-3} cubic meters (or about 0.04 cubic feet). For long focal lengths, it may be convenient to fold the optical path length by reflection. However, for each reflection in the optical path, the optical efficiency of the sensor system decreases by about ten percent. The folded path length should then be used in eq. (6-50), and the diameter of the collecting optics as computed by eq. (6-26), for example, should be divided by 0.95 for each reflection.

6.2.3 System Power Requirements

The data presented in Table 6-5 indicate that infrared scanning systems using thermal detectors require about 1.5 watts per detector, while infrared scanning systems using photon detectors require about 5 watts per detector. For arrays containing large numbers of detectors, greater than ten, it is likely that the system power does not increase linearly with the number of detectors. A reasonable assumption appears to be that the total system power requirement in watts is

$$P = \begin{cases} 1.5\ p^{\frac{1}{2}} & \text{for thermal detectors} \\ 4\ p^{\frac{1}{2}} & \text{for photon detectors} \end{cases} \qquad (6\text{-}51)$$

where some minor allowance for improvement in the state-of-art represented by Table 6-5 has been made for photon detectors. Eq. (6-51) is expected to be accurate within a factor of two or three for p up to 50, which is the current state-of-art limitation.

6.2.4 Data Acquisition Rate

The system data acquisition rate is very simply

$$DR = \frac{p\ G\ \omega}{\Delta\ \emptyset} \text{ bits/sec,} \qquad (6\text{-}52)$$

where p is the number of detectors, G is the number of binary bits required for each resolution element, and $\omega/\Delta\emptyset$ is the number of resolution elements scanned per second. For high quality imagery, 64 shades of gray are required; G has been taken as six in this study.

6.2.5 Pointing and Platform Stability

If Δr is the desired positional accuracy of the image, that is, if the planetary location of the resolution element at the center of the scan line is to be known with an accuracy of Δr unit lengths, then the required pointing accuracy is

$$\Delta\emptyset = \frac{\Delta r}{H} \text{ radians.} \qquad (6\text{-}53)$$

An estimate of the permissible angular rotation rates of the scanning beam is afforded by noting that the dwell time on each resolution element is $\Delta\emptyset/\omega$. Limiting the sensor system roll, yaw, and pitch rates to those resulting in apparent image movements of one-half resolution element gives

$$\therefore \dot{\theta} = \frac{\omega}{2} \text{ rad/sec}, \qquad (6\text{-}54)$$

where $\dot{\theta}$ is the maximum allowable roll, yaw, or pitch rate.

6.2.6 State-of-Art Constraints

Throughout the above development of scaling laws for infrared optical-mechanical scanning systems, operational and mechanical constraints due to current state-of-art limitations have been pointed out, where appropriate. The major constraints deal with the optical system and the detector system. As far as the detectors are concerned, Table 6-1 has summarized the current performance capabilities. Detector sizes as small as 0.1 x 0.1 mm are available. Although arrays of up to 50 detectors are now feasible, many laboratories are working with small (10 x 10) two-dimensional arrays in an effort to increase this to upwards of 100 x 100.

Scanning mechanisms other than the type discussed here are feasible. For example, split-field scanning optics may be more suitable when large collecting optics are required. For the imaging experiments considered in this study, each scan line must include a minimum of one hundred resolution elements. To do away with the rotating scanning mechanism entirely and employ some sort of "push-broom" technique, would require a band of more than 100 detectors scanning forward along the heading line by virtue of spacecraft motion along the orbit. This technique is beyond current technological capabilities, and little experience in the design of such systems is available. Despite the likelihood of achieving such a capability in the next decade, the support requirements estimated in this study have been based on mechanical scanning.

The scanning mechanism appears to be limited to angular rotation rates of 10^6 radians/second, although this estimate is based on currently operating aircraft systems and it is not clear how much this constraint can be relaxed in the

vacuum of space. Although reflective infrared optical systems of greater than one meter in diameter appear feasible, this would imply scanning mirrors greater than two meters or so in diameter. Such mirrors are so far beyond the range of current operating experience that two meter scanning mirrors and one meter collecting optics are a prudent practical limit. There appears to be no fundamental limitations to the use of one or two meter diameter optical systems. In fact, much larger (200-inch) systems might be employed, but at great expense in weight. The scaling law given above for the weights of optical systems is unreliable for diameters much larger than two meters. Optical surfaces must be accurate to within about 1000 Å, and this is clearly a problem for large surfaces.

6.3 Design Procedures

Figure 6-4 is a logic diagram which summarizes the design procedures developed above for infrared scanning systems. Given a set of image specifications and a set of orbit parameters, the logic diagram indicates each step in the estimation of the support requirements implied by any specific infrared experiment. The square boxes in the figure represent steps in the design procedure, while the oval boxes represent estimation of specific support requirements. In this study, image specifications have been given in Volume I, and orbit parameters in Volume III. The design procedure and scaling laws are, of course, applicable to many situations beyond the scope of this study. The scaling laws are summarized in Figure 6-5, which is intended for use with Figure 6-4. Unless specified otherwise, the use of MKS units is implied. A numerical example is provided in Section 6 of Volume I.

The image specifications required for effective system design are shown in the upper left hand corner of the logic diagram. The solar zenith angle is required for imaging of reflected sunlight, the desired temperature resolution is required for imaging of thermal radiation. The attitude control

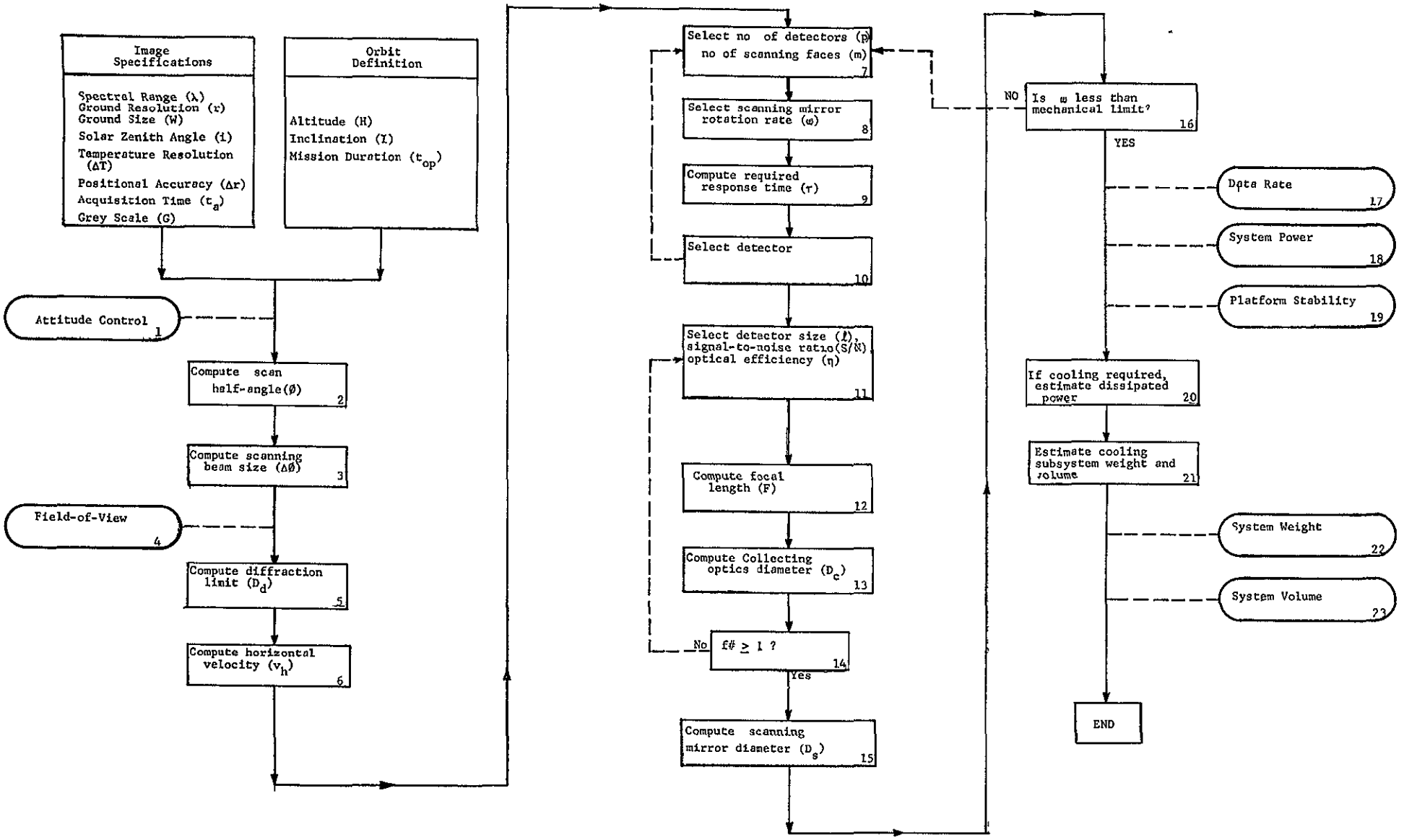

FIGURE 6-4 , LOGIC DIAGRAM FOR INFRARED SCANNING SYSTEMS

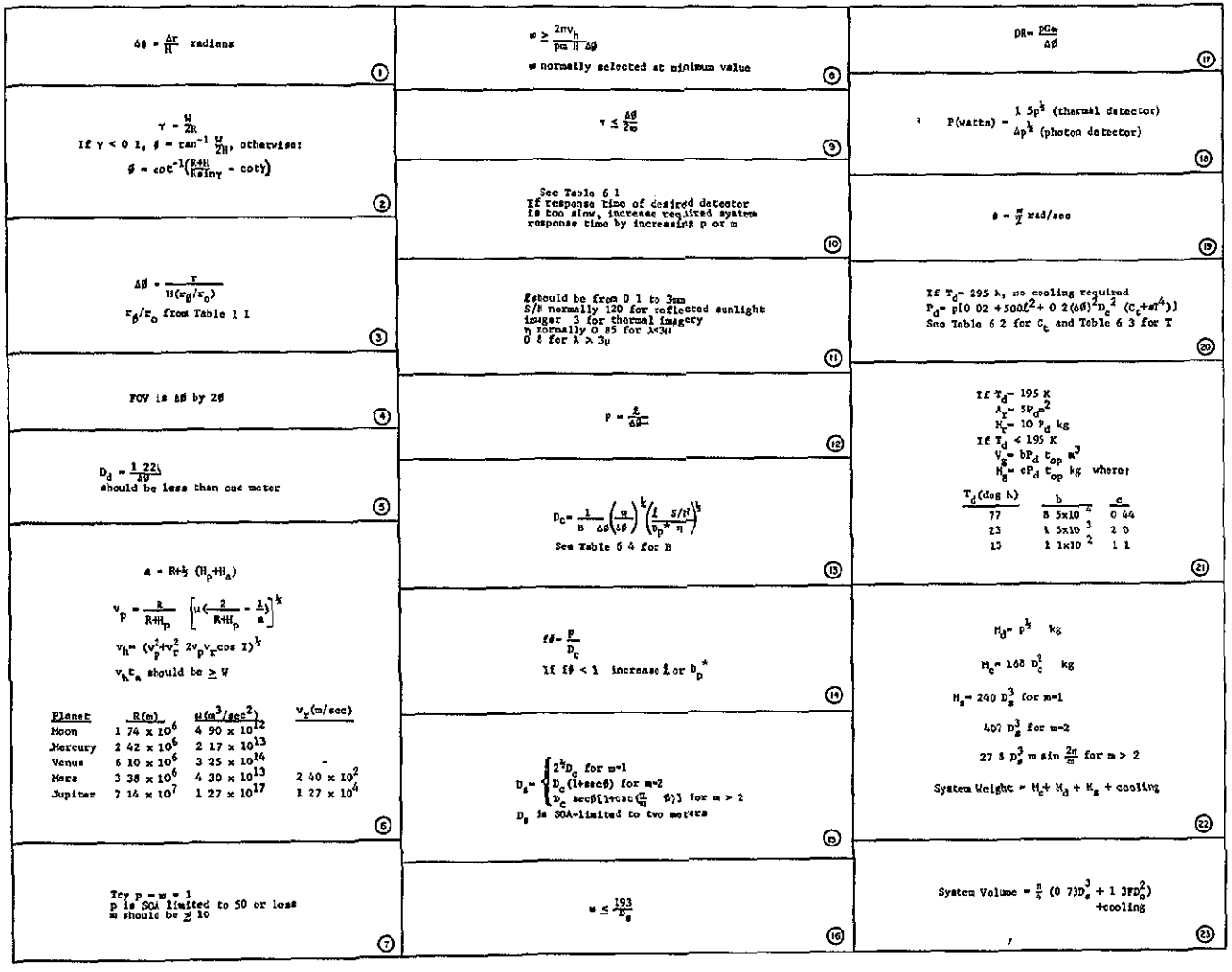

FIGURE 6.5 SCALING LAWS FOR INFRARED SCANNING SYSTEMS

NOMENCLATURE
(MKS units implied unless stated otherwise)

a orbit semi major axis
A_r radiator area
B constant from Table 6.4
C_c constant from Table 6.2
D_c diameter of collecting optics
D_d collecting optics diffraction limit
D_p^* detectivity see Table 6.1
D_s diameter of scanning mirror
DR data acquisition rate
f# optics aperture stop (f number)
F focal length
FOV-field of-view
G bits per resolution element (normally 6)
H sensor system altitude
H_a orbit apoapse altitude
H_p orbit periapse altitude
I solar zenith angle
I orbit inclination
ℓ detector size
m no of faces on scanning mirror
M_c mass of collecting optics
M_d mass of detector and electronics
M_g mass of solid gas cooling system
M_r mass of radiative cooling system
M_s mass of scanning system
p number of detectors
P system power requirement
P_d power dissipated by cooling
r desired ground resolution
R planet radius
SOA state of art
S/N signal to noise ratio
t_a maximum acquisition time
t_{op} mission duration (must be in days)
T planetary temperature (deg K)
T_d detector temperature, see Table 6.1
v_h apparent horizontal speed
v_p sensor ground speed at periapse
v_r planet equatorial rotation speed
V_g volume of solid gas cooling system
W ground length of scan
γ-scan half-angle subtended at planet center
Δr desired image ground positional accuracy
ΔT desired temperature resolution (deg K)
$\Delta\theta$ allowable sensor pointing error
$\Delta\phi$ angular width of scanning beam
η optical system transmission factor
λ wavelength
μ planet gravitational constant
σ Stefan Boltzmann constant (5.67×10^{-8})
τ response time
$\dot{\theta}$-allowable sensor rotation rate
ϕ scan half angle
w scanning mirror rotation rate

and field-of-view requirements are computed in a straightforward manner. The size of a diffraction-limited optical system (step #5) is computed early in the design procedure to quickly identify those situations requiring optical systems beyond the current state-of-art. The size of the optical system is also influenced by the amount of energy which must be collected (step #13).

If the diffraction-limited optics is of feasible size (one meter diameter or less), the apparent ground speed is estimated (step #6), and a preliminary choice is made for the number of detectors and the number of scanning mirror faces (step #7). Minimum system weight and power requirements usually, but not always, increase with the number of detectors (p) and the number of mirror faces (m). It is therefore usually best to choose p and m equal to one and increase them only as required. Having chosen p and m, the minimum rotation rate of the mirror may be determined (step #8). A design rotation rate should be selected which is consistent with the minimum rate. Although the platform stability requirements are eased by choosing a high rotation rate, the necessary optical system diameter increases slowly with the rotation rate. Therefore the design rotation rate is usually chosen to be the minimum rotation rate. The rotation rate also influences the choice of a detector, since the detector must possess a response time (step #9) consistent with the rotation rate. That is, fast rotation rates require detectors with short response times.

The type of detector chosen (step #10) from Table 6-1 depends upon the desired response time and spectral range. For imagery of reflected sunlight, the PbS and InAs detectors provide good sensitivity, but their response times are relatively long. Detectors which operate at 295 deg K will require no weight for cooling. In selecting detectors for imagery of thermally emitted radiation, it is useful to note that the wavelength (in microns) at which thermal radiation per unit wavelength is a maximum is approximately 3000 divided by the temperature (in deg K). For example, for a surface at 300 deg K,

the peak of the spectral emission curve occurs at about 10 microns. If a long response time can be used, a thermistor detector is attractive, since no detector cooling is required. The response time required of the detector may be increased by increasing p or m and thus reducing the mirror rotation rate. Increasing m beyond three or four will increase rapidly the required size of the scanning mirror. The system power requirements increase with p, and values of p larger than 50 are not feasible at the current state-of-art. In most cases, p should be increased to 50 before m should be increased past four. Achieving a sensor system design which is optimum, in any sense, is clearly an iterative procedure.

Proper choice of the signal-to-noise ratio and optical efficiency is shown on the scaling law chart (step #11). The detector size may be chosen initially as one millimeter. The focal length and optics diameter are computed as shown (steps #12 and #13). For a single detector system, f-numbers (step #14) of about 0.3 are feasible by use of an immersion lens. For linear arrays of detectors, the f-number should be at least one. If a shrewd detector choice has been made earlier, it will not be possible to increase the aperture stop by choosing a more sensitive detector. The detector size may be increased by noting that the f-number increases with the square root of the detector size. For example, if the initial system design results in an f-number of 0.5, the detector size must be increased by a factor of four to achieve an f-number of one. The f-number can also be increased by decreasing the mirror rotation rate, but this is a relatively inefficient procedure since the optics diameter goes as the fourth root of the rotation rate.

Once the optics diameter has been determined, satisfying both the spatial resolution requirements (step #5) and the energy collection requirements (step #13), the diameter of the scanning mirror may be estimated (step #15). Large mirrors are subject to optical distortion of the mirror surfaces at even moderate rotation rates (1000 rpm), and it may be necessary

to reduce the rotation rate (step #16). This may, of course, require a selection of a detector with a shorter response time than that originally selected. The data acquisition rate, power requirement, and platform stability constraints may now be estimated. If the detector chosen from Table 6-1 operates at 195,77, or 23 deg K, the power which must be dissipated is estimated as shown in step #20. Detector operation at 4 deg K is beyond the current state-of-art. If appropriate optical filtering is employed, the C_t term may be omitted for thermal imagery and the T^4 term for sunlight imagery. The cooling system weight and size may be estimated (step #21), based on the required power dissipation. It may be noted that solid hydrogen cooling systems (13 deg K) tend to be half as heavy as solid neon systems (23 deg K), but occupy nearly eight times the volume. Finally, the sensor system weight and volume may be estimated as shown.

7. PASSIVE MICROWAVE SYSTEMS

7.1 Design Equations

This section presents mathematical and physical relationships for estimating the design variables of passive microwave imaging systems. Section 7.2 provides a collection of semi-empirical scaling laws, which relate the sensor system support requirements to the sensor design variables. Section 7.3 summarizes a suggested logical procedure for sensor system design and estimation of experiment support requirements.

7.1.1 Scanning Operation

In Section 1.2 it was shown that to achieve full coverage along the length W of a scan line as projected on the planetary surface, the half-angle field-of-view (or scan angle) is given by

$$\phi = \cot^{-1}\left(\frac{R + H}{R \sin \gamma} - \cot \gamma\right) , \qquad (7\text{-}1)$$

where R is the planet radius, H is the sensor altitude, and γ is W/2R radians. For small values of γ, less than about 0.1 radians, eq. (7-1) reduces to

$$\phi = \tan^{-1} \frac{W}{2H} . \qquad (7\text{-}2)$$

To prevent gaps in the ground coverage between successive scan lines, the antenna must scan each line rapidly enough that the edges of successive scan lines touch or overlap directly beneath the spacecraft. If $\Delta\phi$ is the angular width of the scanning beam, then the time available for observing an entire scan line is

$$t_s \leq \frac{H \cdot \Delta\phi}{v_h} , \qquad (7\text{-}3)$$

where v_h is the apparent horizontal velocity of the planet surface, and the antenna fly-back time has been neglected. The computation of v_h has been discussed in Section 1.5. If r is the required ground resolution, $\Delta\emptyset$ is approximately r/H, and thus the available scan time is on the order of r/v_h. Perusal of the image specifications given in Volume I, along with estimated values of v_h, suggests that for detailed scale measurements (when r is small) the available scan time may be on the order of one millisecond. However, the required fields-of-view are sufficiently narrow that antenna scanning rates on the order of 0.1 radians per second appear to be adequate. Such modest scanning rates imply that either mechanically-scanned or electrically-scanned antennas could be used.

For mechanically-scanned antennas, the scanning time is limited to

$$t_s \leq \frac{H \cdot \Delta\emptyset}{v_h} - t_f \ , \qquad (7\text{-}4)$$

where t_f is the fly-back time, that is, the time required to slew the antenna from the end of one scan line to the beginning of the next scan line. The number of resolution elements encompassed by a single scan line is $2\emptyset/\Delta\emptyset$, and therefore the antenna dwell time per resolution element is limited by

$$t_d \leq \frac{\Delta\emptyset}{2\emptyset} \left(\frac{H \cdot \Delta\emptyset}{v_h} - t_f\right) . \qquad (7\text{-}5)$$

In principle, the data from a single resolution element may be integrated over the entire dwell time, in an effort to reduce statistical deviations in the data. However, since the antenna is in continuous motion along the scan line, the data tends to become "smeared" spatially when the integration time approaches the dwell time. It is assumed here that the maximum useful integration time is approximately one-half the dwell time. That is,

$$\tau \leq \frac{\Delta\phi}{4\phi} \left(\frac{H \cdot \Delta\phi}{v_h} - t_f\right) , \qquad (7\text{-}6)$$

where τ is the integration time.

The fly-back time may be used for calibration. Because of gain changes in the amplifier sections of microwave radiometers, it has become a general practice to calibrate the receiver one or more times per scan line. If the fly-back time is used for calibration, and if the fly-back time is set equal to the dwell time per resolution element, then there must be $(2\phi/\Delta\phi) + 1$ equal time intervals in $t_s + t_f$. Neglecting unity in comparison with $2\phi/\Delta\phi$,

$$t_f \simeq \frac{H(\Delta\phi)^2}{2\phi\, v_h} , \qquad (7\text{-}7)$$

and

$$\tau \leq \frac{H(\Delta\phi)^2}{4\phi\, v_h} . \qquad (7\text{-}8)$$

However, if the fly-back time is used for calibration, t_f must be long enough to allow the detector to be switched to and from the reference temperature source. Currently available switches for this purpose have switching times on the order of 0.1 milliseconds[73]. Thus the minimum fly-back time is taken in this study as 0.2 milliseconds.

For electrically-scanned antennas, the integration time may be set equal to the dwell time, since the antenna does not move continuously across a scene resolution element. However, some switching time is required for the antenna beamwidth to move from one resolution element to the next. Currently available antennas have a beam-switching time of 1.5 milliseconds[73], which is apparently controlled by inductance in the ferrite phase-shifters. It is assumed here

that, with some technological development, this time could be reduced to about 0.1 milliseconds. Finally, assuming a calibration time of 0.2 milliseconds per scan, the integration time permitted by an electrically-scanned antenna is

$$\tau \leq \frac{\Delta\phi}{2\phi}\left(\frac{H\cdot\Delta\phi}{v_h} - 2 \times 10^{-4}\right) - 1 \times 10^{-4} \text{ sec.} \qquad (7\text{-}9)$$

Clearly, it is not feasible to use an electrically-scanned antenna unless

$$t_f \simeq \frac{H(\Delta\phi)^2}{2\phi\, v_h} > 10^{-4} \text{ sec.} \qquad (7\text{-}10)$$

As with all scanning systems, if data is to be acquired from a planetary scene of area W by W in some time interval less than a specified maximum acquisition time, then

$$v_h t_a \geq W, \qquad (7\text{-}11)$$

where t_a is the maximum acquisition time.

7.1.2 Spatial Resolution

To achieve the ground resolution r throughout the scan length W, the sensor system angular resolution $\Delta\phi$ must satisfy

$$\Delta\phi \leq \frac{r}{(r_\phi/r_0)H}, \qquad (7\text{-}12)$$

where r_ϕ/r_0 has been given in Table 1-1, and H is the sensor system altitude. The quantity r_ϕ/r_0 accounts for the increased slant range and the curvature of the planetary surface at the extremities of the scan line. For a microwave imaging system, $\Delta\phi$ may be identified with the antenna half-power beamwidth.

The diameter of a parabolic dish receiving antenna, whose half-power beamwidth is $\Delta\phi$, is[74]

$$D = \frac{1.2\lambda}{\Delta\phi} , \qquad (7\text{-}13)$$

where λ is the operating wavelength. If small beamwidths are required, it may be necessary to use small wavelengths or large antennas.

Hiatt and Larson[75] have assessed the maximum antenna sizes expected to be feasible in 1970, with the results shown in Figure 7-1. The antenna sizes shown are constrained by the surface tolerances which can be maintained. A more recent survey by Rider and Sung[76] states that, at the present level of technology, a fifty-foot parabolic dish antenna is within reach of a short development effort. This size antenna is in very close agreement with the Hiatt and Larson evaluation, and implies that the antenna sizes shown in Figure 7-1 are not currently achievable, but rather represent a minor advancement in the state-of-art. The support requirements estimated in this study are based on the attainable antenna sizes shown in the figure.

By using eq. (7-13) with the maximum antenna sizes shown in Figure 7-1, the attainable angular resolution may be computed as a function of antenna size and wavelength. The results are shown in Figure 7-2. These data show that to achieve angular resolutions of less than two milliradians, it is necessary to operate at about eight millimeter wavelengths or less (operating frequencies of 38 GHz or higher). Since the image specifications given in Volume I, and the orbit selections given in Volume III, imply that angular resolutions of one milliradian or less may be required for adequate microwave imagery from orbit, it appears that either significant advances must be made in antenna technology or the only microwave imaging systems of interest are those which operate in the vicinity of 100 GHz, or higher.

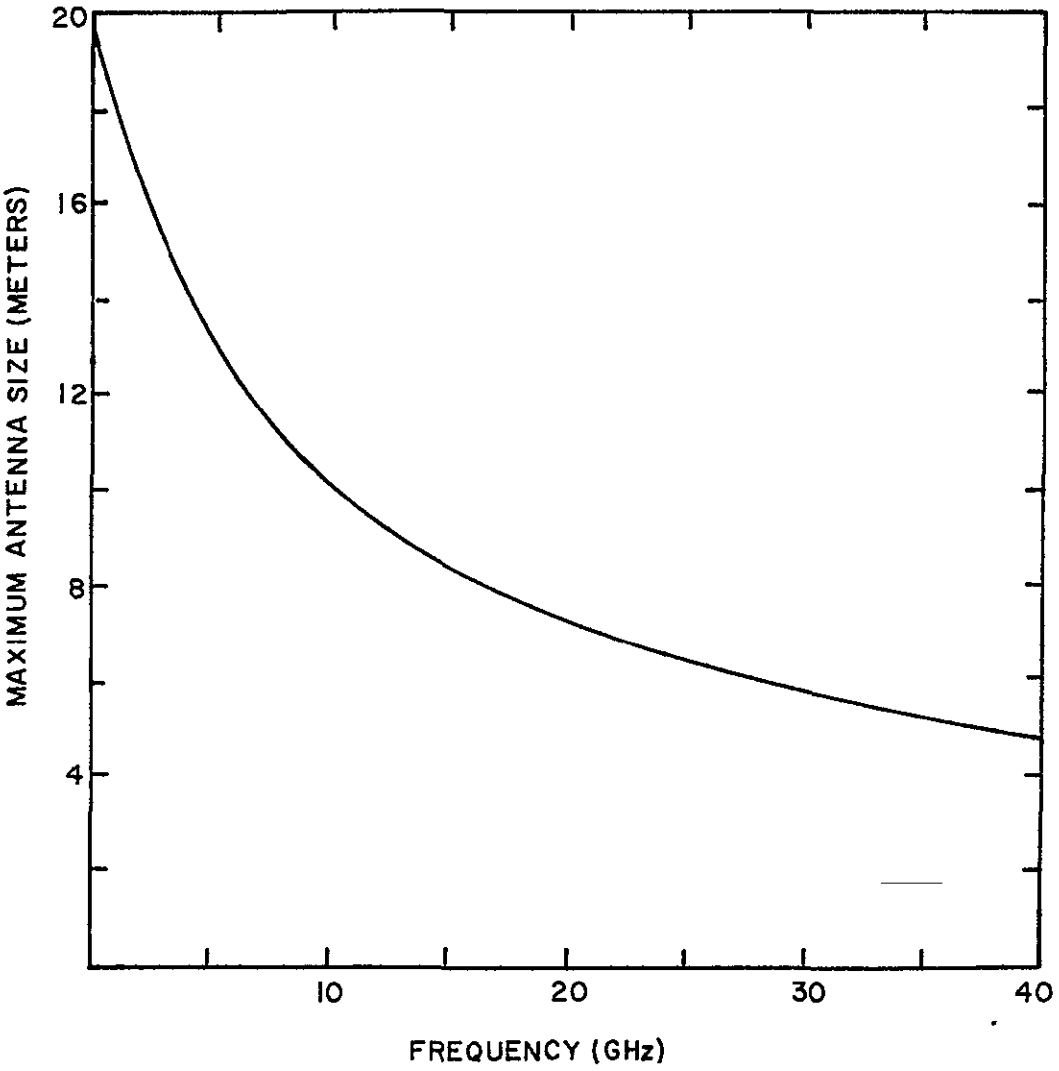

FIGURE 7-1. MAXIMUM ANTENNA SIZE

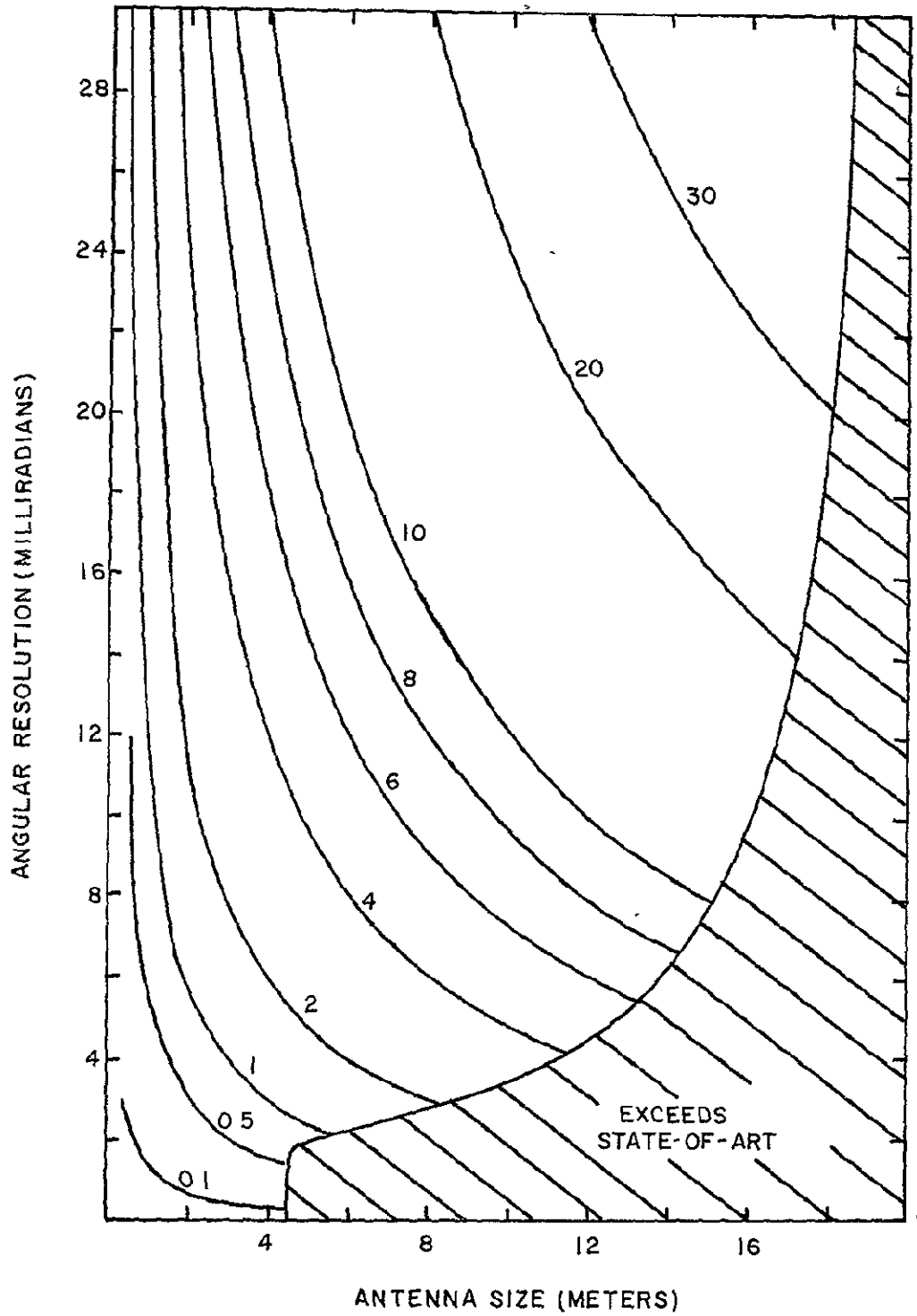

FIGURE 7-2 ATTAINABLE ANGULAR RESOLUTION
(PARAMETRIC VALUES GIVE WAVELENGTH IN CM)

A somewhat different formulation is required in the case of electrically-scanned antennas. The antenna array length required to achieve the beamwidth $\Delta\phi$ is[77]

$$L = \frac{A\,\lambda}{\Delta\phi \cos \phi} , \qquad (7\text{-}14)$$

where ϕ is the maximum scan angle, and A is related to the sidelobe level as shown in Figure 7-3. The general practice is to design the antenna for a sidelobe level of about -35 dB, in which case,

$$L = \frac{1.13\lambda}{\Delta\phi \cos \phi} , \qquad (7\text{-}15)$$

For small values of ϕ, eq. (7-15) gives similar results to eq. (7-13). Thus Figure 7-2 also applies to electrically-scanned antennas, at least approximately, if the array length L is identified with D.

7.1.3 Temperature Resolution

Johnson[78] has recently provided a fairly rigorous statistical analysis of a typical microwave radiometer. The model used consists of a resistive load, a square-law detector, a low-pass filter, and an integrator, as shown in Figure 7-4. The resistive load R_s represents those system components forward of the square-law detector, such as the antenna and RF amplifier. The output x(t) of the resistive load is limited to some pre-detection bandwidth B. The resistive load is represented by a composite system temperature T_s, which includes the antenna noise temperature T_A, any noise temperature addition T_L due to resistive losses, and the equivalent noise temperature of the RF amplifier section. Thus,

$$T_s = T_A + T_L + (F-1)\,T_o , \qquad (7\text{-}16)$$

where F is the system noise figure, and T_o is 290 deg K.

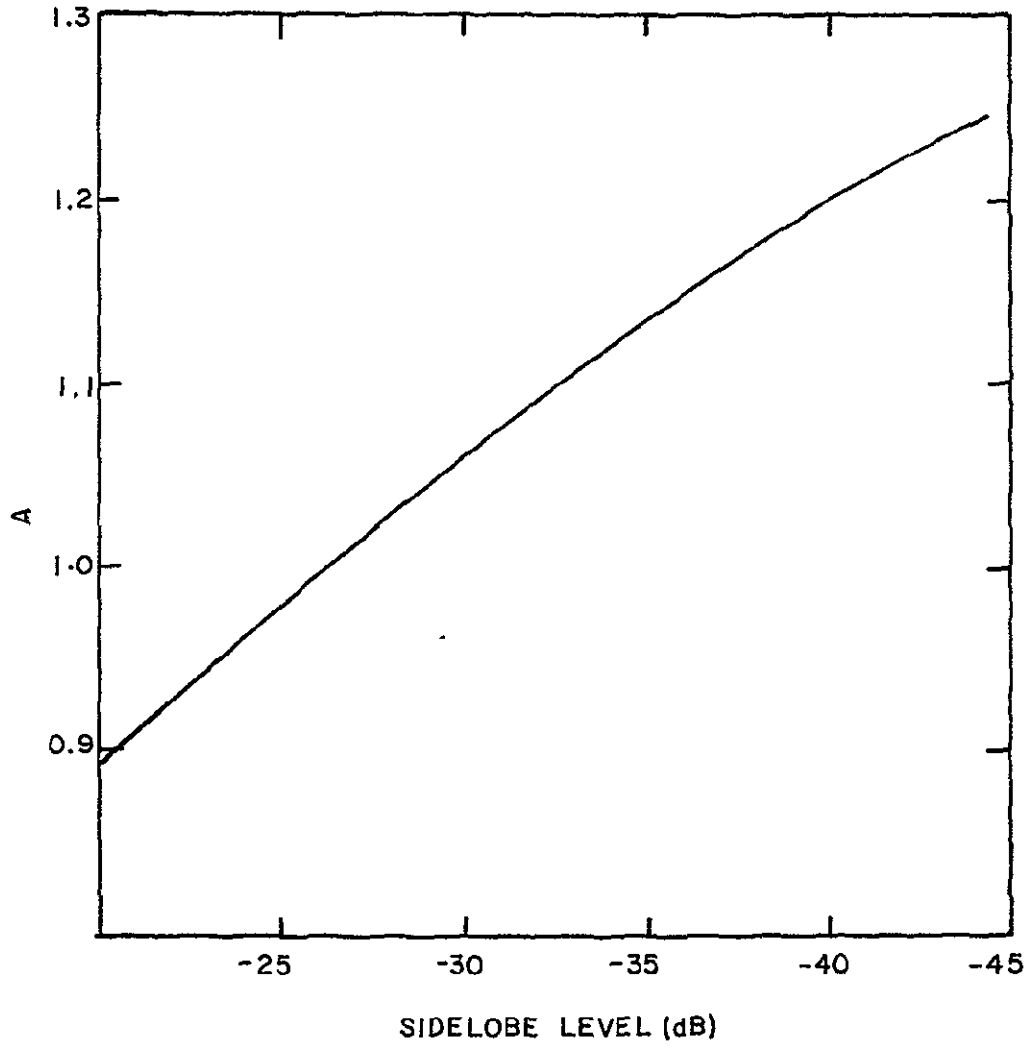

FIGURE 7-3. ANTENNA CONSTANT A

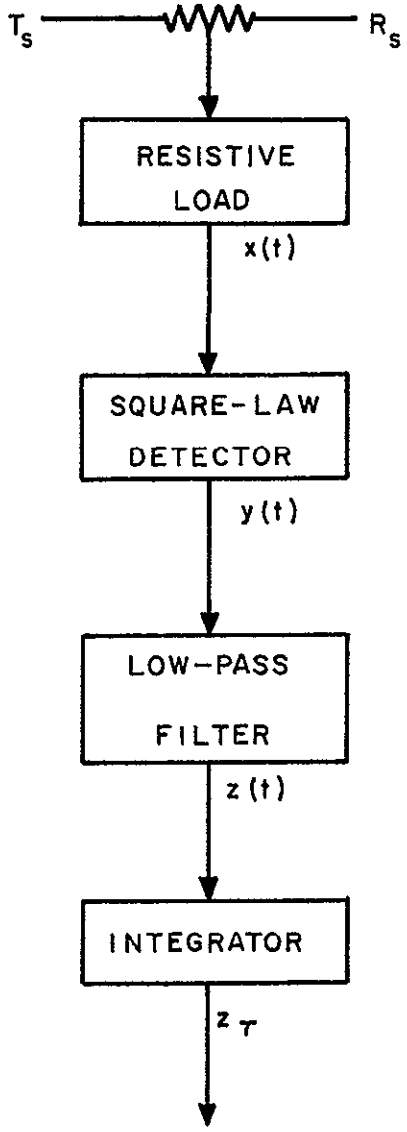

FIGURE 7-4. BLOCK DIAGRAM OF RADIOMETER

The time-averaged value of the resistive load voltage output $x(t)$ vanishes, but the time-averaged value of $x^2(t)$ does not. For this reason, a square-law detector is used whose voltage output, as a function of time, is

$$y(t) = a\, x^2(t) , \tag{7-17}$$

where a is a detector constant. Thus the mean value of $y(t)$ is related to the average input power. A considerable portion of the power in $y(t)$ lies in the vicinity of $2f_o$, where f_o is the center frequency of the input power spectrum, that is, the system operating frequency. This second harmonic power contributes only noise, therefore a low-pass filter that passes frequency components below the predetection bandwidth B, but rejects frequency components above, is normally included in the system. The voltage output of the low-pass filter is represented by $z(t)$. The integrator reduces the noise components of the filter output by sampling over a certain time period, and delivering a smoothed output that is a function of the average of these samples over the integration time τ. That is,

$$z_\tau = \int_\tau z(t)\, dt . \tag{7-18}$$

Johnson shows that if the input temperature T_s is changed by an amount ΔT_s, the output average signal-to-noise ratio is

$$\frac{S}{N} = \frac{\Delta T_s}{K T_s} (B\tau)^{\frac{1}{2}} , \tag{7-19}$$

where the signal is regarded as the change in the average value of z_τ resulting from a change in T_s, and K is a constant (usually a factor of 2 or 3) associated with the detailed design of the radiometer. Solving for the integration time required to detect the temperature difference ΔT_s,

$$\tau = \frac{1}{B}\left(\frac{K\,T_s \cdot S/N}{\Delta\,T_s}\right)^2 \qquad (7\text{-}20)$$

The predetection bandwidth B can be related to the operating frequency. The current state-of-art[74,79] restricts the maximum obtainable bandwidths to approximately ten percent of the operating frequency. Thus, in order to achieve a temperature resolution ΔT, the integration time must satisfy

$$\tau \geq \frac{40}{f}\left(\frac{T_s \cdot S/N}{\Delta T}\right)^2, \qquad (7\text{-}21)$$

where f is the system operating frequency, and K has been taken as 2 (which is appropriate for a Dicke radiometer). However, the available integration time is determined by the scanning operation, as shown in eqs. (7-6) and (7-9). To evaluate eq. (7-21), the system temperature T_s must be calculated, and a value must be selected for the signal-to-noise ratio.

Johnson[78] has shown that the average signal-to-noise ratio in the integrator output is $\Delta\bar{z}_\tau/\sigma(z_\tau)$, where $\Delta\bar{z}_\tau$ is the change in the average integrator output due to a change in the system temperature T_s, and $\sigma(z_\tau)$ is the standard deviation of the integrator output. The general practice is to compare an observed $\Delta\bar{z}_\tau$ to some multiple of the noise, say H times $\sigma(z_\tau)$. If $\Delta\bar{z}_\tau$ exceeds $H\sigma(z_\tau)$, then the detected $\Delta\bar{z}_\tau$ is regarded as a bona fide signal; if $\Delta\bar{z}_\tau$ does not exceed $H\sigma(z_\tau)$, then the $\Delta\bar{z}_\tau$ is regarded as noise-generated. If a large value is selected for H, many true signals will be undetected; if a low value is selected for H, many random deviations will be "detected" as signals. Johnson relates the value of H both to a detection probability P_D, and a false alarm probability P_{FA}. That is, P_D is the probability that a true signal ΔT_s will result in a $\Delta\bar{z}_\tau$ which is classified as a signal, and P_{FA}

is the probability that a noise-generated $\Delta\bar{z}_\tau$ will be classified wrongly as a signal. Table 7-1 presents the false alarm probability P_{FA} as a function of threshold level H. For example, if $\Delta\bar{z}_\tau$ is three times $\sigma(z_\tau)$, there is only a 3.4 percent probability that Δz_τ is noise-generated. Table 7-2 presents the detection probability P_D as a function of $\Delta\bar{z}_\tau/\sigma(z_\tau)$. Thus if the threshold level is three, and if $\Delta\bar{z}_\tau/\sigma(z_\tau)$ is six, there is a 98.3 percent probability that such a signal will be detected.

Table 7-1

False Alarm Probability

H	P_{FA}
0	1.000
0.5	0.723
1.0	0.480
1.5	0.289
2.0	0.157
2.5	0.077
3.0	0.034
3.5	0.013
4.0	0.005

Table 7-2

Detection Probability

$\Delta\bar{z}_T/\sigma(z_T)$	P_D
H-2.0	0.079
H-1.5	0.144
H-1.0	0.240
H-0.5	0.362
H	0.500
H + 0.5	0.638
H + 1.0	0.760
H + 1.5	0.856
H + 2.0	0.921
H + 2.5	0.961
H + 3.0	0.983

In this study, it is assumed that a false alarm probability of five percent is acceptable. From Table 7-1, the threshold level corresponding to this false alarm probabil is 2.8. If the probability of detection is to be ninety percent, then from Table 7-2, $\Delta\bar{z}_T/\sigma(z_T)$ must be about H + 1.8, or 4.6. This value may now be substituted into eq. (7-21) for the signal-to-noise ratio to yield

$$\tau \geq \frac{850}{f}\left(\frac{T_s}{\Delta T}\right)^2. \qquad (7\text{-}22)$$

For a specific operating frequency and desired temperature resolution ΔT, the minimum required integration time may now be determined once the system temperature T_s is evaluated.

7.1.4 Effective System Temperature

The effective system temperature T_s consists of the antenna noise temperature T_A, a resistive loss temperature T_L, and an amplifier noise temperature T_N. That is,

$$T_s = T_A + T_L + T_N \, . \tag{7-23}$$

Each of the contributing terms will be discussed separately.

The antenna temperature T_A is merely a useful way of describing the amount of available power received by the antenna. If the antenna is conceptually replaced by a resistive component, the antenna temperature is defined such that the Johnson noise power of the resistive component is equal to the available power collected by the antenna. That is,

$$\text{Available power} = k \, T_A \, B \, , \tag{7-24}$$

where k is Boltzmann's constant (1.381×10^{-23} joules/deg K) and B is the predetection bandwidth. The available, or collected, power may be related to the thermal power emitted by the planetary surface or scene.

In Section 2.2 it was shown that the spectral radiance (the power per unit wavelength per unit solid angle emitted by a unit area of surface) of a black body is

$$N(\lambda,T) = \frac{1}{\pi} R(\lambda,T) \cos \epsilon \, , \tag{7-25}$$

where $R(\lambda,T)$ is the black body spectral radiant emittance, and ϵ is the angle of emission as measured from the normal to the surface. T is the equivalent black body temperature of the emitting source. Using the Rayleigh-Jeans approximation to $R(\lambda,T)$, and transforming from power per unit wavelength to power per unit frequency,

$$N(f,T) = \frac{2\,k\,T\,f^2}{c^2} \cos\epsilon \ . \qquad (7\text{-}26)$$

The Rayleigh-Jeans approximation is valid to within ten percent for λT greater than about 27 cm-deg K. Thus for equivalent blackbody temperatures of 100 deg K or more, the Rayleigh-Jeans approximation is accurate to within ten percent for frequencies of 110 GHz or less. Using eq. (7-26), the power per unit frequency collected by an effective antenna area A from an emitting source of area $r_x r_y$ at the slant range R_s is

$$p(f) = \frac{r_x r_y\, kT\, f^2\, A \cos\epsilon}{c\, R_s^2} \ , \qquad (7\text{-}27)$$

where a factor of one-half has been included since the maximum amount of energy accepted by an antenna, from a randomly polarized wave, is one-half the total energy content of the wave. Noting that

$$\frac{r_x r_y \cos\epsilon}{R_s^2} = (\Delta\phi)^2 \ , \qquad (7\text{-}28)$$

where $\Delta\phi$ is the angular resolution of the system, eq. (7-27) may be integrated over the predetection bandwidth, from f_1 to f_2, to find the total power collected by the antenna:

$$P = \int_{f_1}^{f_2} p(f)\,df = \frac{A\,kT(\Delta\phi)^2}{3\,c^2}\,(f_2^3 - f_1^3) \ . \qquad (7\text{-}29)$$

If f_o is the operating frequency, then f_2 is $f_o + \frac{1}{2}B$ and f_1 is $f_o - \frac{1}{2}B$, where B is the bandwidth. Since B is at most about one-tenth f_o, the frequency cubed term in eq. (7-29) is well-approximated by $3B\,f_o^2$, in which case,

$$P = \frac{A\ k\ T\ B(\Delta\phi)^2\ f^2}{c^2} , \qquad (7\text{-}30)$$

where the subscript on f_o has been omitted for simplicity. Equating this result to eq. (7-24), and solving for the antenna temperature,

$$T_A = A\left(\frac{f\cdot\Delta\phi}{c}\right)^2 T . \qquad (7\text{-}31)$$

Assuming that the angular resolution is related to antenna size by eq. (7-13), and that the antenna efficiency is about eighty percent, that is, the effective antenna area is eighty percent of the physical area, then

$$T_A \simeq T . \qquad (7\text{-}32)$$

The support requirements estimated in this study are based on an equality here, that is, the antenna noise temperature is taken equal to the equivalent blackbody temperature of the emitting planetary scene.

It has been shown, in eq. (7-22), that the required integration time increases with the square of the effective system temperature. A conservative design procedure is to assume the maximum observed planetary blackbody temperature. For Venus, the observed temperature depends upon whether the atmosphere or the surface is being observed. A similar situation exists for Jupiter, but it is unlikely that the atmosphere can be penetrated to any significant depth at microwave frequencies. Table 7-3 summarizes the maximum observed temperatures for the planets.

Table 7-3

Maximum Planetary Temperatures (deg K)

Planet	Temperature
Moon	400
Mercury	600
Venus	700
Mars	300
Jupiter	150 (?)

The development above has ignored any atmospheric attenuation between the emitting scene and the receiving antenna. It is assumed here that there is no appreciable atmospheric attenuation at microwave frequencies in the case of the Moon, Mercury, and Mars. The situation at Venus and Jupiter is quite different, and is discussed in detail in Section 8.1.8. Thermal radiation emanating from the surface of Venus and passing vertically upward through the entire atmosphere is attenuated by the approximate factor $\exp(-3.3/\lambda^2)$, where λ is the wavelength in centimeters. Thus the Venus surface temperature given in Table 7-3 should be multiplied by $\exp(-3.6 \times 10^{-3} f^2)$, as should the desired surface temperature resolution, where f is the frequency in GHz. For microwave imagery of the Venusian surface, frequencies of less than about 15 GHz should be used.

Amplifier noise temperatures have been investigated by Matthei[80], who has assessed the current technological capabilities of microwave amplifiers. His evaluation is shown by the solid line in Figure 7-5, which applies specifically to tunnel diode amplifiers. The dashed line in the figure is based on informal discussions with microwave receiver manufacturers[81,82]. Lower noise temperatures can be obtained by

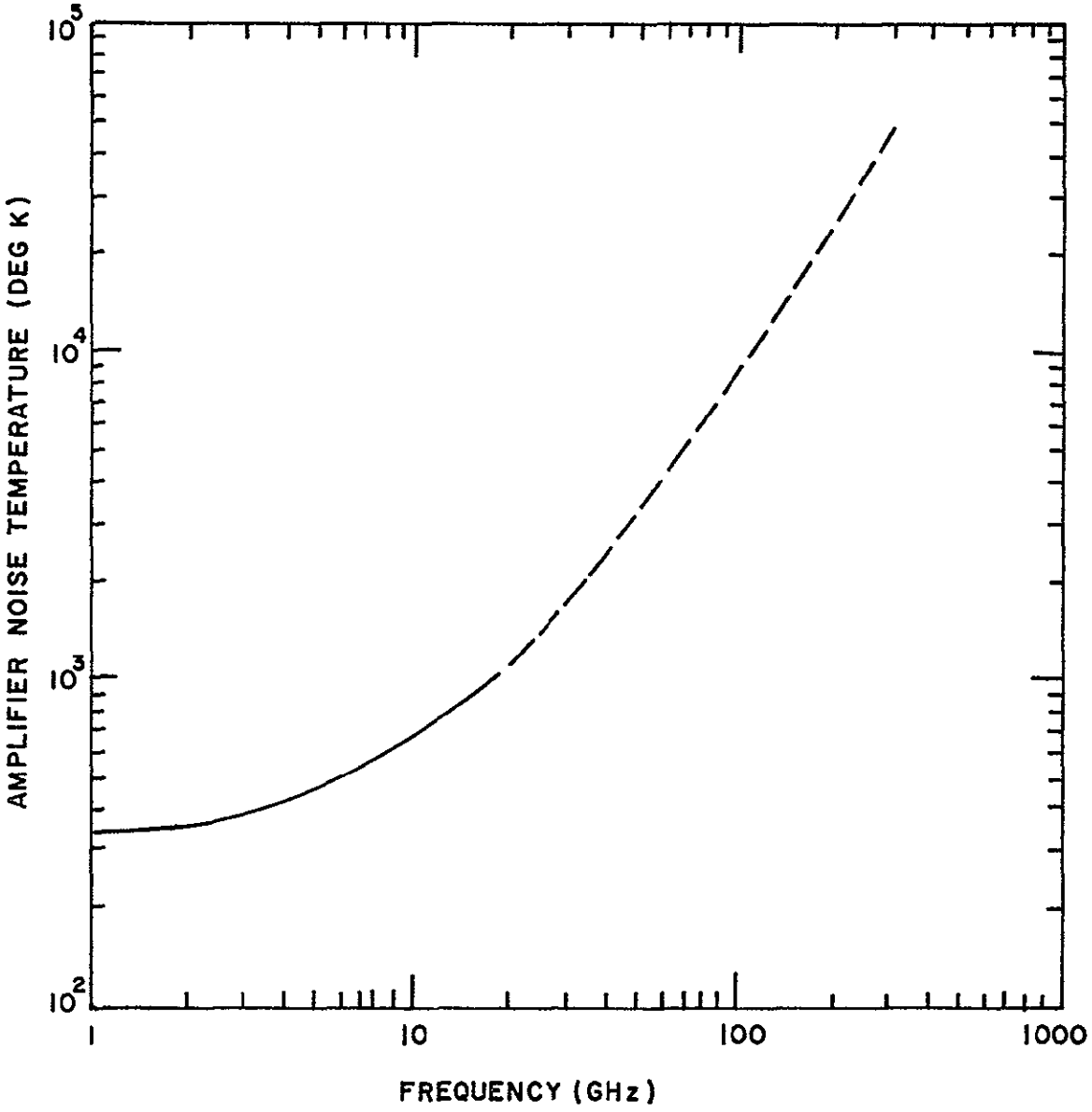

FIGURE 7-5. AMPLIFIER NOISE TEMPERATURE

using advanced equipment, such as parametric amplifiers or traveling-wave maser amplifiers, but these components are still in the development stages and cannot be regarded as even approaching a space-qualified status. Figure 7-5 suggests that for frequencies higher than ten GHz, microwave imagers for space-orbital use will be internal-noise-limited.

Finally, the effective system noise temperature is taken in this study as

$$T_s = T_A + T_N + 100°K \ , \qquad (7\text{-}33)$$

where miscellaneous signal losses have been assigned a noise temperature of 100 deg K. The amplifier noise temperature T_N is given by Figure 7-5 as a function of frequency, and T_A is given by Table 7-3. For Venus, the values given in the table should be modified to account for atmospheric absorption as noted above.

The dilemma of the passive microwave system designer is to satisfy eqs.(7-6) or (7-9) and (7-22) simultaneously. That is, the integration time must be short enough to permit scanning across the entire field-of-view before the next resolution element comes into view, yet it must be long enough that the desired temperature resolution can be achieved. Eq.(7-22) seems to suggest that by increasing the operating frequency, the integration time required to attain a specific temperature resolution may be made as small as desired. But Figure 7-5 has shown that the amplifier noise increases with frequency, thus increasing the required integration time. Although increasing the frequency (and hence decreasing the wavelength) decreases the antenna size for a given angular resolution, the receiver weight and power increase, as will be shown below.

To facilitate an intelligent choice of operating frequency, beyond that implied by the required angular resolution and antenna size limitations as shown in Figure 7-2,

values of minimum integration times as a function of frequency are shown for the different planets in Figure 7-6. The image specifications given in Volume I indicate that the required temperature resolution is one deg K for the Moon, two deg K for Mars and Jupiter, and five deg K for Mercury and Venus. For these temperature resolutions, eq.(7-22) was used to compute minimum integration times. Eq.(7-33) was used for the system noise temperature, with amplifier noise temperature from Figure 7-5, and antenna noise temperature from Table 7-3. However, for Venus, the brightness temperature was taken as

$$T_A = 700\ \alpha + 250\ (1-\alpha)\ \text{deg K} \qquad (7\text{-}34)$$

where α is the atmospheric attenuation factor, $\exp(-3.6\times10^{3}f^{2})$, while the required temperature resolution was taken as 5α deg K for surface imaging and $5(1-\alpha)$ deg K for atmospheric attenuation. That is, the surface temperature is taken as 700 deg K, the atmospheric temperature as 250 deg K. Figure 7-6 shows that at high frequencies, the minimum integration time tends to be independent of planetary temperature, because the system becomes internally-noise limited. Thus for two deg K resolution, the minimum integration time at Mars (300 deg K) is nearly the same as for Jupiter (150 deg K) above 50 GHz.

The Venus curves in the figure suggest that frequencies of about 10 GHz should be used for surface imaging, and frequencies of about 30 GHz should be used for atmospheric imaging. The crossover point at about 15 GHz indicates that below 15 GHz a five deg K temperature difference on the surface is more readily detected than a five deg K temperature difference in the atmosphere, while above 15 GHz the reverse is true. A simple microwave imaging system cannot, of course, indicate whether an observed temperature difference is due to surface or to atmospheric temperature differences.

Since the minimum integration time is inversely proportional to the square of the required temperature reso-

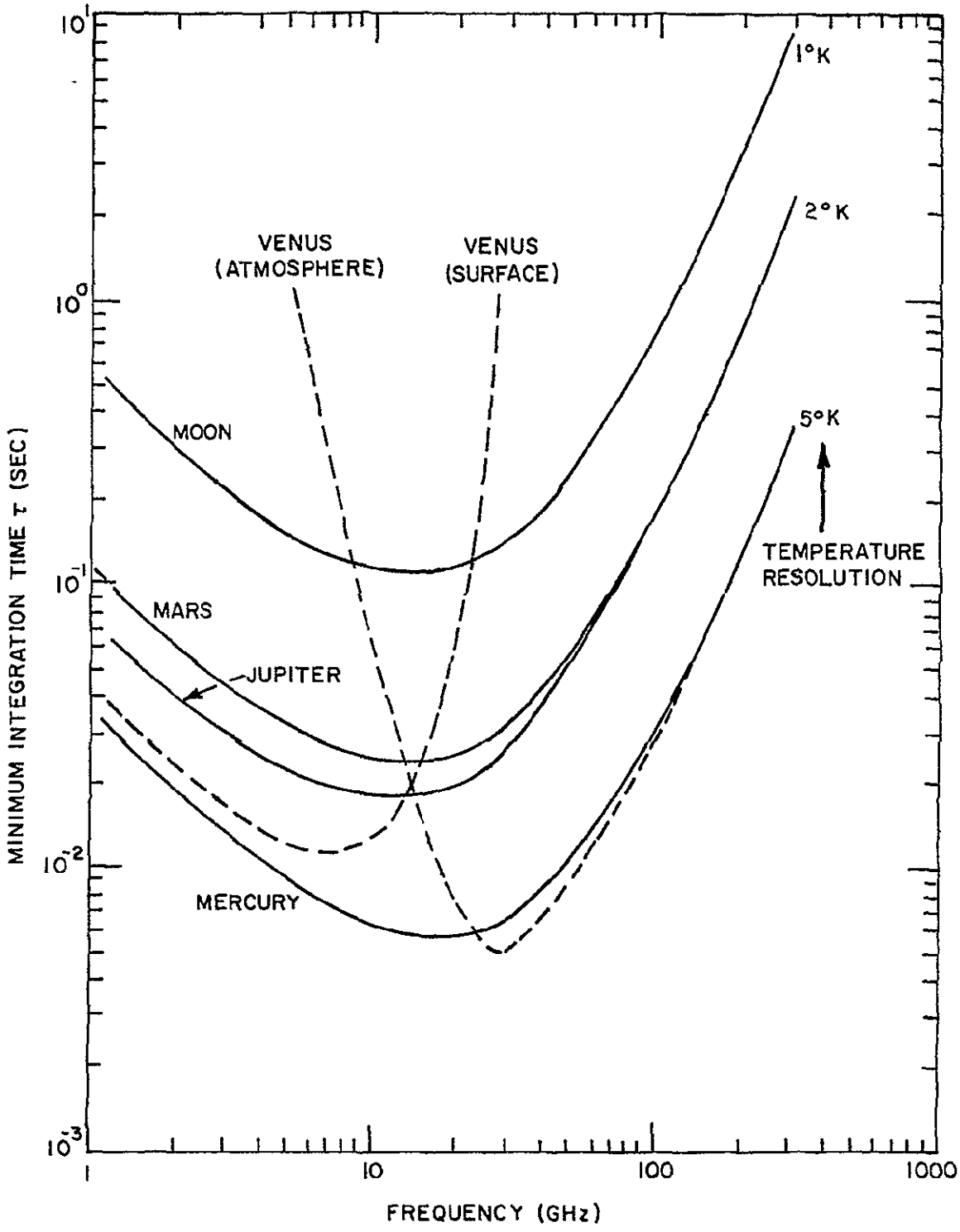

FIGURE 7-6 MINIMUM INTEGRATION TIME

lution, the data given in Figure 7-6 can easily be modified to account for different values of temperature resolution. For example, the figure shows that at Mars an integration time of 0.024 sec is required for a temperature resolution of two deg K at 13 GHz. If a temperature resolution of one deg K is required, the necessary integration time is then $0.024 \times (2)^2/(1)^2$ or 0.096 sec, at 13 GHz.

7.2 Support Requirements

7.2.1 System Weight

The weight of a microwave imaging sensor system may be estimated by estimating the weights of the antenna subsystem and the receiver and adding the results. The antenna weight is estimated differently for mechanically-scanned and electrically-scanned antennas.

Aircraft-borne mechanically-scanned microwave receiving antennas have weights per unit area as high as fifteen pounds per square foot[83]. It is expected that spacecraft-borne antennas can be fabricated at appreciably lighter weights, since aircraft vibration and atmospheric turbulence problems need not be contended with. Titus[84] has constructed a feasibility demonstration model of a deployable mechanically-scanned active microwave antenna weighing about 0.85 pounds per square foot. This antenna operates at relatively long wavelengths, about twenty centimeters, and antennas designed for shorter wavelengths probably weigh somewhat more per unit area. The support requirements in this study are based on mechanically-scanned antenna weights of 1.5 pounds per square foot, including the drive mechanism. This scaling coefficient is felt to be accurate, well within a factor of three, for frequencies of about 1-100 GHz and antenna diameters indicated as feasible in Figure 7-1. Thus for mechanically-scanned antennas,

$$M_A = 5.8D^2 , \qquad (7\text{-}35)$$

where M_A is the mass of the antenna in kilograms, and D^2 is the antenna diameter in meters.

For electrically-scanned antennas, the length L of each element is determined by eq. (7-15), but the interelement spacing d is fixed by the requirement to avoid grating side-lobes[77]. Falco and Oister[73] have shown that this implies that

$$d^2 + Ld - \frac{L\lambda}{1 + \sin \phi} = 0, \tag{7-36}$$

where ϕ is the scan half-angle. Solving for d,

$$d = -\frac{L}{2} + \tfrac{1}{2}\left(L^2 + \frac{4 L \lambda}{1 + \sin \phi}\right)^{\frac{1}{2}} . \tag{7-37}$$

Unless the antenna is very small, λ is much less than L/4, in which case eq. (7-37) reduces to

$$d \simeq \frac{\lambda}{1 + \sin \phi} \tag{7-38}$$

The total number of elements is

$$N = \frac{L}{d} + 1. \tag{7-39}$$

The antenna weight is estimated by multiplying the weight per element by the total number of elements. The aerojet-General electrically-scanned antenna[73,77] consists of 49 elements and weighs about seven pounds, including about five pounds for the 49 ferrite phase-shifters. Thus each phase-shifter has a mass of about 46 grams, and each element about 19 grams.

The active length of each element is about 16.35 inches, while the total length is about 18 inches to allow for end termination. Each element has a mass of about 0.42 grams per cm of length, where the total length is approximately 1.1L. The operating wavelength is 1.55 cm, and it may be assumed that the waveguide mass per unit length increases linearly with wavelength Thus the mass of an electrically-scanned antenna is taken as

$$M_A = N(0.046 + \frac{0.89\ L}{f}) , \qquad (7\text{-}40)$$

where M_A is the antenna mass in kilograms, N is the number of elements, L is the active length in meters, and f is the operating frequency in GHz. Use of electrically-scanned antennas at frequencies lower than 5 GHz, or higher than 35 GHz, presupposes a minor advancement in the current state-of-art.

Microwave receiver weights are assumed to be independent of the antenna scan mode (mechanical or electrical). Estimated receiver weights, based on informal discussions with manufacturers[81,82] of microwave imaging systems designed for space use, are shown in Figure 7-7 as a function of operating frequency. The estimates shown are consistent with the 12-pound Aerojet-General receiver[85] operating at 19.35 GHz, a three-pound receiver[86] operating at nine different frequencies between 0.4 and 10 MHz, and laboratory demonstration models[82] operating at one and at ten GHz.

The sensor system weight scaling laws presented here are expected to be accurate, within a factor of two to three, for all antenna sizes indicated as feasible in Figure 7-1, and for operating frequencies in the range from about one MHz to a few hundred GHz. The receiver weights are consistent with the amplifier noise temperatures shown in Figure 7-5.

Use of the weight scaling laws may be illustrated by considering the Mariner II microwave radiometer. This two-channel system operated at wavelengths of 13.5 and 19

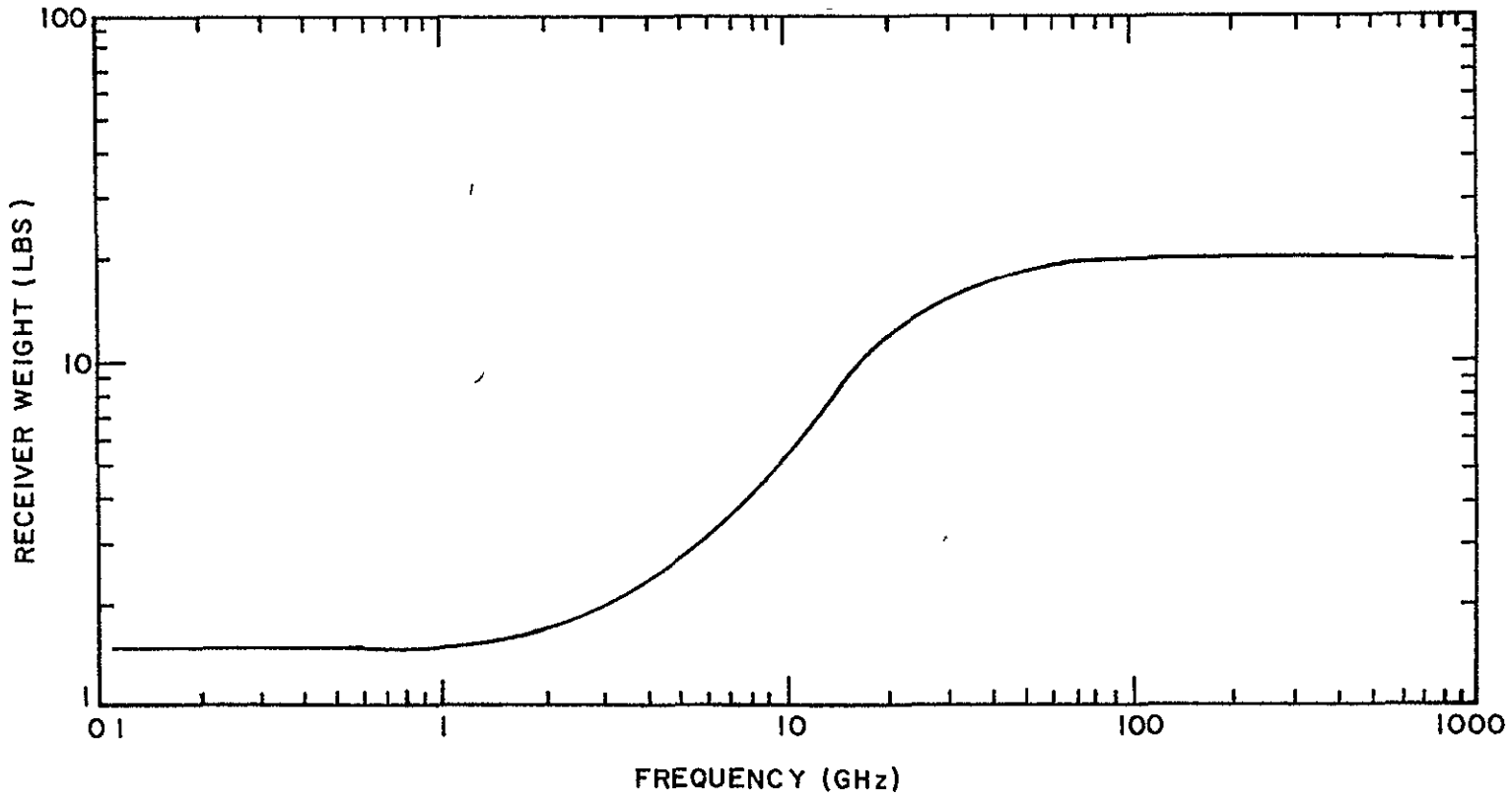

FIGURE 7-7. MICROWAVE RECEIVER WEIGHT

millimeters with antenna 3 dB beamwidths of 2.2 and 2.64 degrees, respectively[87]. Use of eq. (7-13) implies an antenna diameter of about 45 centimeters, and therefore eq. (7-35) predicts an antenna mass of 1.2 kilograms, or about 2.6 pounds. For an operating frequency of 22 GHz, corresponding to a wavelength of 13.5 millimeters, Figure 7-7 predicts a receiver weight of 13 pounds. The estimated system weight of nearly 16 pounds compares favorably with an actual system weight of about 20 pounds[88].

7.2.2 System Volume

Antenna areas are estimated to be about D^2 square meters for mechanically-scanned antennas, and about 1.2 L^2 for electrically-scanned antennas. The Aerojet-General microwave receiver[77] was originally designed to fit inside a standard Nimbus module of about 130 cubic inches, but the receiver size grew somewhat larger during actual construction. A 60 GHz receiver has been designed[88] to occupy 312 cubic inches. The conclusion that receiver volume is linearly proportional to operating frequency is probably unwarranted. The support requirements generated in this study have assumed receiver volumes of 100 cubic inches for frequencies lower than one GHz, 200 cubic inches from 1 to 30 GHz, 300 cubic inches from 30 to 100 GHz, and 500 cubic inches above 100 GHz. These receiver volume estimates are probably accurate within a factor of three and presume use of solid-state circuitry as employed in the Aerojet-General receiver.

7.2.3 System Operating Power

As with the system weight, the system average power requirement may be regarded as the sum of two components: the power required for antenna scanning, and the power required by the microwave receiver.

An estimate of the power required to drive a mechanically-scanned antenna may be based upon the torque required to slew the antenna from the end of one scan line

to the beginning of the next. It is assumed here that during the first half of the fly-back time, the antenna rotates at constant angular acceleration α through the scan half-angle $\emptyset$. During the second half of the fly-back time, the antenna decelerates at the constant rate $-\alpha$ through the scan half-angle. If the antenna is initially at rest, the angular acceleration required to rotate the antenna through the angle $\emptyset$ in time $\frac{1}{2}t_f$ is

$$\alpha = \frac{8\emptyset}{t_f^2} , \tag{7-41}$$

and the corresponding torque is

$$T = I\alpha = \frac{8\emptyset I}{t_f^2} , \tag{7-42}$$

where I is the antenna moment of inertia. Regarding the antenna as a disk of diameter D, the moment of inertia about an axis lying in the plane of the disk and passing through the center of mass is $M_A D^2/16$, where M_A is the antenna mass. Assuming that the antenna rotates about an axis parallel to the plane of the antenna disk, but displaced a distance of D/2 from the center of the disk, the moment is $M_A D^2/16 + M_A D^2/4$, and then the torque is

$$T = \frac{5\ M_A D^2\ \emptyset}{2\ t_f^2} . \tag{7-43}$$

The amount of work done upon the antenna is

$$W = T\emptyset = \frac{5\ M_A D^2\ \emptyset^2}{2\ t_f^2} , \tag{7-44}$$

and hence the power required to rotate the antenna through

the angle $\emptyset$ in the time $t_f/2$ is

$$P = \frac{2W}{t_f} = \frac{5\ M_A (D\emptyset)^2}{t_f^3} . \qquad (7\text{-}45)$$

Since an equal amount of power is required to decelerate the antenna during the second half of the fly-back time, the antenna power requirement is taken as

$$P_A = \frac{40\ M_A\ (D\emptyset)^2}{t_f^3} , \qquad (7\text{-}46)$$

where the antenna drive motor is assumed to have an efficiency of 25 percent.

As an example, consider the power requirement for a Mariner II-type scanning experiment. In the search mode, the Mariner II scan rate was one deg/sec[87], corresponding to a dwell time of about 2.6 seconds per resolution element. Taking the scan half-angle as 30 degrees, the fly-back time as 2.6 seconds, the antenna diameter as 45 centimeters, and the antenna mass as 1.2 kilograms, eq. (7-46) yields an antenna power requirement of 0.15 watts.

For electrically-scanned antennas, the power requirement is taken as proportional to the number of phase-shifters, which is equal to the number of elements as given by eq. (7-39). Since the Aerojet-General antenna required about 9.5 watts of power for 49 phase-shifters[73], the antenna power requirement for electrically-scanned antennas is

$$P_A = 0.194\ N \text{ watts} , \qquad (7\text{-}47)$$

where N is determined from eq. (7-39).

An estimate of the receiver average power requirement is shown in Figure 7-8, as a function of operating frequency. The curve given in the figure is based on a power requirement of 0.9 watts at 0.4-10 MHz[86], 5 watts at 19.35 GHz (obtained by subtracting an antenna power of 9.5 watts from a system power requirement of 14.8 watts[85]), 4.85 watts at 22 GHz (obtained by subtracting an estimated antenna power of 0.15 watts from the Mariner II radiometer system power of five watts[88]), and about 40 watts at 60 GHz[88]. The large average power requirement at high frequencies is presumably due to local oscillator power consumption. The dashed line indicates that the power estimate at frequencies higher than 60 GHz is somewhat speculative. Based on Mariner II experience, the peak power requirement is estimated as twice the average power requirement.

The power scaling laws presented here are expected to be accurate, within a factor of two, or possibly three, for frequencies between 1 and 40 GHz. Ferrite phase-shifters can be used on electrically-scanned antennas at frequencies from 5 to 35 GHz. In this range, eq. (7-47) is felt to be accurate within a factor of two. No design data is available for electrically-scanned antennas operating out of this frequency range, and less confidence can be placed in the validity of eq. (7-47). The heuristic argument leading to the power scaling law for mechanically-scanned antennas, eq. (7-46), is applicable at all frequencies. The power estimates obtained by use of eq. (7-46) are most useful in identifying operational situations which potentially result in a large antenna power drain. The reliability of the receiver power estimates shown in Figure 7-8 decreases with increasing operating frequency above 30 GHz. The dashed line is felt to be accurate within a factor of five.

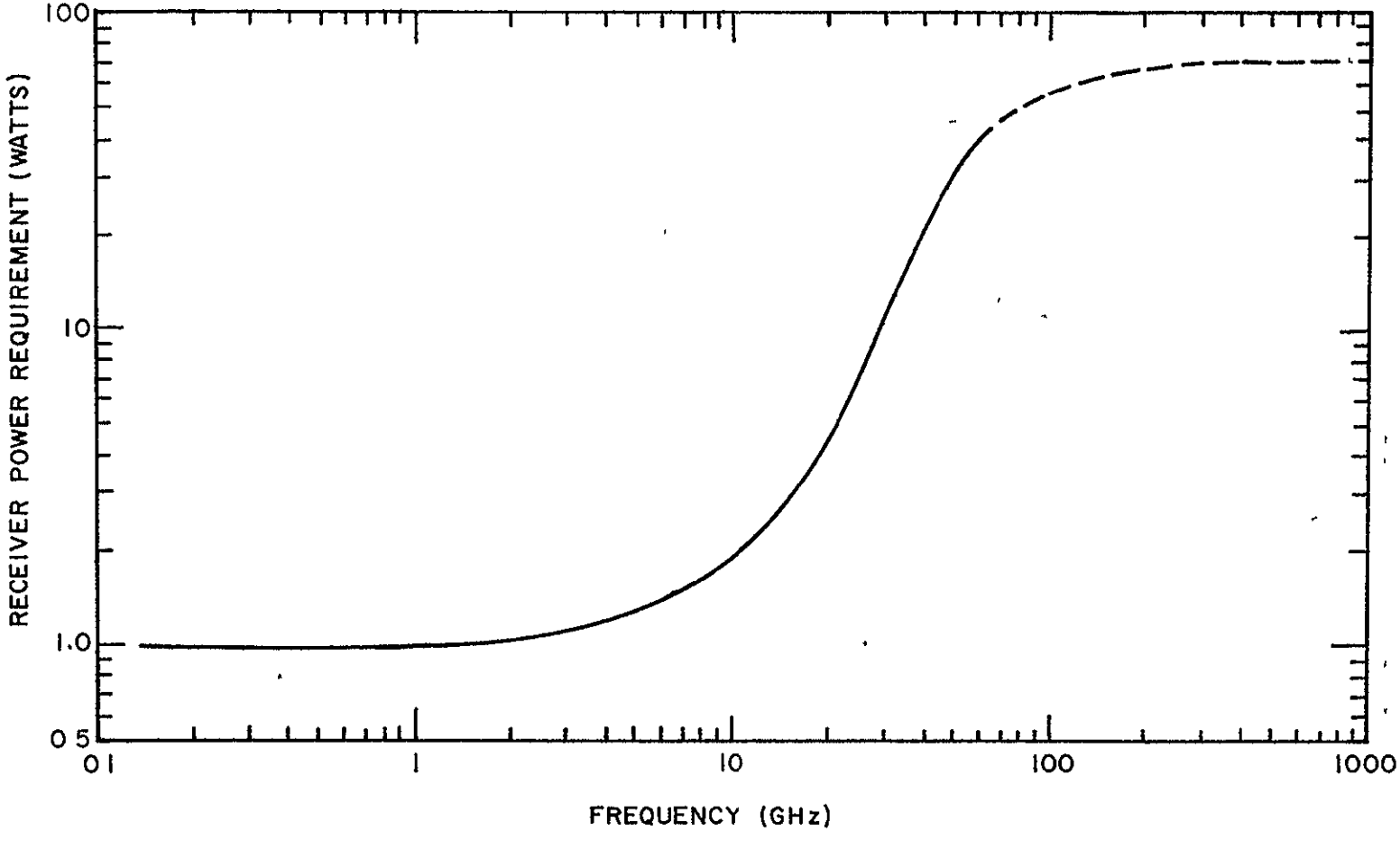

FIGURE 7-8. MICROWAVE RECEIVER POWER

7.2.4 Data Acquisition Rate

If the antenna fly-back time is much smaller than the line scan time t_s, then

$$t_s \simeq \frac{H \cdot \Delta\phi}{v_h} . \qquad (7\text{-}48)$$

During this time, the number of ground resolution elements from which data is collected is $2\phi/\Delta\phi$, where ϕ is the scan half-angle, and $\Delta\phi$ is the system angular resolution. Assuming that G binary bits are used to describe the data acquired from each resolution element, the sensor system data acquisition rate is

$$DR = \frac{2G\, v_h\, \phi}{H(\Delta\phi)^2} . \qquad (7\text{-}49)$$

This estimate does not include calibration data, which should not alter the data rate significantly. Also, G has been taken as six throughout this study. If the antenna fly-back time is long, such as might occur in an attempt to reduce the power requirement of a mechanically-scanned antenna, the data acquisition rate is

$$DR = \frac{2\, G\, v_h\, \phi}{\Delta\phi(H \cdot \Delta\phi - t_f\, v_h)} , \qquad (7\text{-}50)$$

where t_f is the fly-back time. If t_f is small, eq. (7-50) reduces to eq. (7-49).

8.2.5 Pointing and Platform Stability

If Δr is the desired positional accuracy of the image, that is, if the planetary location of the resolution element at the center of the scan line is to be known with an accuracy of Δr unit lengths, then the required sensor system pointing accuracy is

$$\Delta\theta = \frac{\Delta r}{H} \text{ radians.} \qquad (7\text{-}51)$$

An estimate of the permissible antenna angular rotation rates may be based upon limiting the apparent image motion to one-half the length of a resolution element in a time interval equal to the antenna dwell time on that resolution element. Proceeding as in the estimation of the data acquisition rate above, the maximum allowable roll, yaw, or pitch rate is

$$\dot{\theta} = \frac{v_h \, \emptyset}{H \cdot \Delta\emptyset} \text{ rad/sec} , \qquad (7\text{-}52)$$

neglecting the antenna fly-back time. If the fly-back time appreciably affects the dwell time,

$$\dot{\theta} = \frac{v_h \, \emptyset}{H \cdot \Delta\emptyset - t_f \, v_h} \text{ rad/sec} . \qquad (7\text{-}53)$$

7.2.6 State-of-Art Constraints

The most significant limitations upon passive microwave imaging systems arising from current technological capabilities are limitations upon antenna size and receiver noise temperatures. Figure 7-1 has shown antenna sizes which are expected to be feasible in the early 1970's. The influence these sizes have upon attainable system angular resolution has been shown in Figure 7-2. These results imply that successful performance of many of the orbital microwave imaging experiments of interest to this study will require operating frequencies in the neighborhood of 100 GHz, or higher, or that significant advances are required in passive microwave antenna technology. Figure 7-5 has shown noise temperatures of microwave amplifiers (specifically tunnel diode) thought to be feasible for space-orbital use. Although a

variety of low-noise amplifiers are finding increasing use in Earth-based microwave equipment, an extensive development program would be required to space-qualify low-noise amplifiers. An additional constraint is the limitation on switching time at about 0.1 milliseconds. This applies both to the Dicke switch and the phase-shifters in an electrically-scanned antenna. In most cases, this is not a serious limitation, compared to the much longer integration times required by an internal-noise-limited system. Finally, it should be emphasized that electrically-scanned antennas have been designed only for the frequency range 5-35 GHz. Operation at the much higher frequencies required for many of the experiments considered in this study will require advancement of the current state-of-art.

7.3 Experiment Design Procedure

A suggested design procedure, based upon the preceding development, is summarized in Figure 7-9. The design equations and scaling laws are condensed in Figure 7-10. The items in both figures are numbered for simultaneous use. Aside from the image specifications and orbit definition in the logic diagram (Figure 7-9), the oval boxes portray estimation of support requirements while the rectangular boxes represent phases in the sensor system design procedure. The procedure is summarized here, and a numerical example is given in Section 6 of Volume I.

The first five steps in the design procedure are identical to those employed in the design of infrared scanning systems. The cycle time (step #6) is the time available for the antenna to sweep across the entire scan line and return to the start of the next scan line. This time includes the actual scanning time and the fly-back and calibration time. Next the maximum available integration time per ground resolution element is computed for both mechanically and electrically scanned antennas (step #7). The maximum integration time available for mechanically-scanned antennas is on the order of one-half that

for electrically-scanned antennas, even neglecting the fly-back time. The required integration time depends upon the observed planet, the required temperature resolution, and the operating frequency as shown in Figure 7-6. By comparing the available time with the required time, the amount of design flexibility (if any) can be determined (step #8). If the available time exceeds the required time, the operating frequency may be chosen (step #9). The larger the chosen operating frequency, the smaller the required antenna. However, for mechanically-scanned antennas, the design integration time chosen should be appreciably less than the maximum available time, to allow for fly-back time. The fly-back time should be very roughly one-half the cycle time or an excessive antenna power requirement will result. The operating frequency determines the operating wavelength (step #10), and the antenna size is based on wavelength and required angular resolution (step #11). It may be noted that large scan angles may result in large electrically-scanned antennas. The antenna sizes permissible with the near-future state-of-art have been shown in Figure 7-1. Some iteration between antenna size and operating frequency, as indicated by the dashed line in the logic diagram, may be necessary. Once the antenna type and size and the operating frequency have been fixed, the system weight, size, power requirement, data acquisition rate, and platform stability requirements may be estimated as shown.

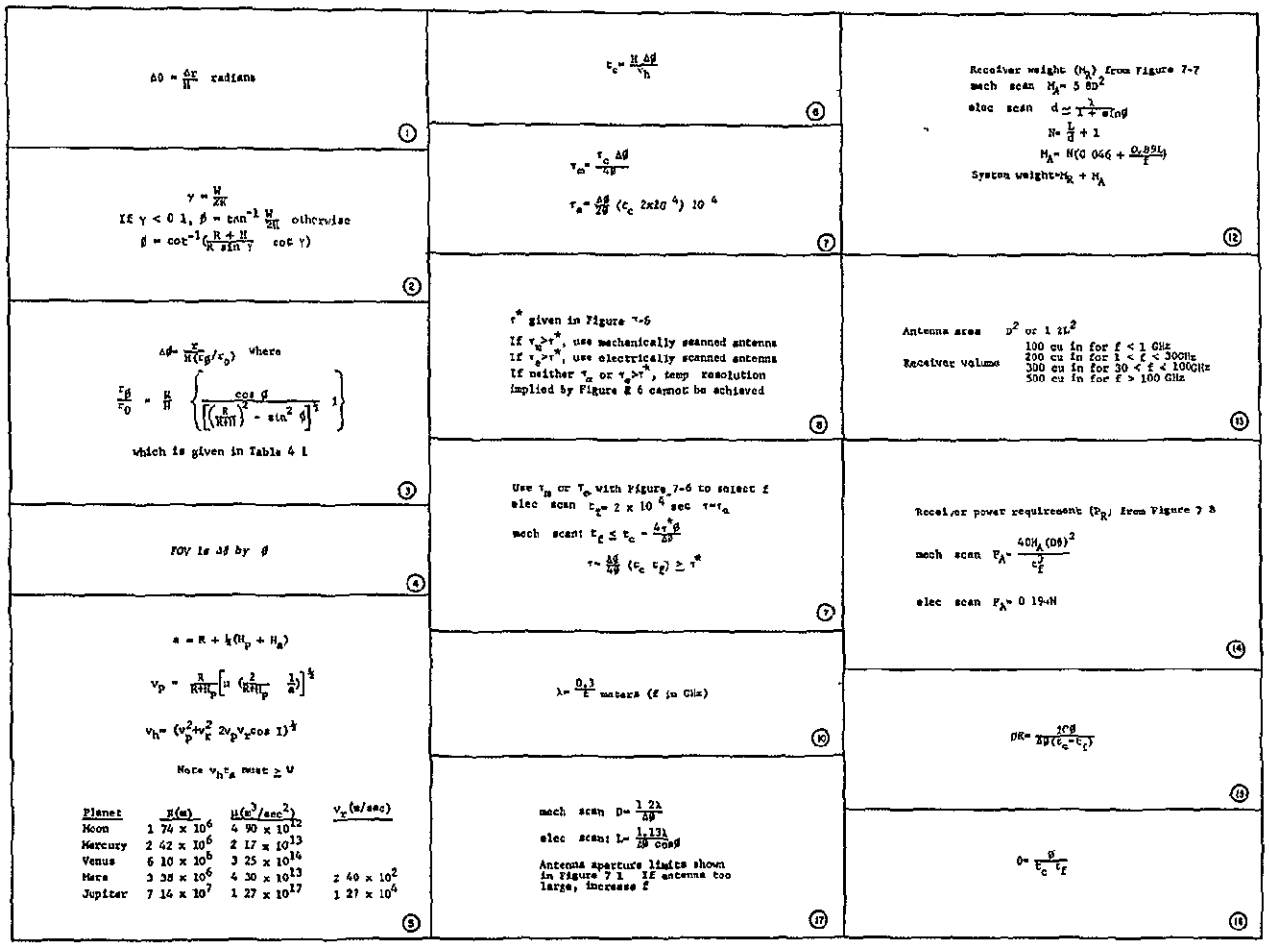

FIGURE 7-11 SCALING LAWS FOR PASSIVE MICROWAVE SYSTEMS

NOMENCLATURE

(MKS units throughout unless specified otherwise)

a orbit semi major axis
c speed of light
d antenna element spacing
D parabolic antenna diameter
DR data acquisition rate
f operating frequency (in GHz)
FOV-field of view
G binary bits per resolution element (normally 6)
H antenna altitude
H_a *orbit apogee* altitude
H_p orbit periapse altitude
I orbit inclination
L antenna active length
M_A antenna weight
M_R receiver weight
N=number of antenna elements
P_A antenna power requirement
P_R receiver power requirement
r-desired ground resolution
R planet radius
t_a-*maximum permitted a quisition time*
t_c-antenna cycle time
V_h apparent horizontal ground speed
V_p ground speed of antenna at periapse
V_r planet equatorial rotation speed
W ground length of scan line
γ half angle subtended by W at planet center
Δr desired ground positional accuracy
$\Delta\theta$ required antenna pointing accuracy
$\Delta\beta$ angular size of scanning beam
$\dot{\beta}$ maximum permissible platform rotation rate
λ *operating wavelength*
μ-planet gravitational constant
τ-integration time actually used
τ^* integration time required
τ_a-integration time afforded by electrical scan
τ_m integration time afforded by mechanical scan
β scan half angle

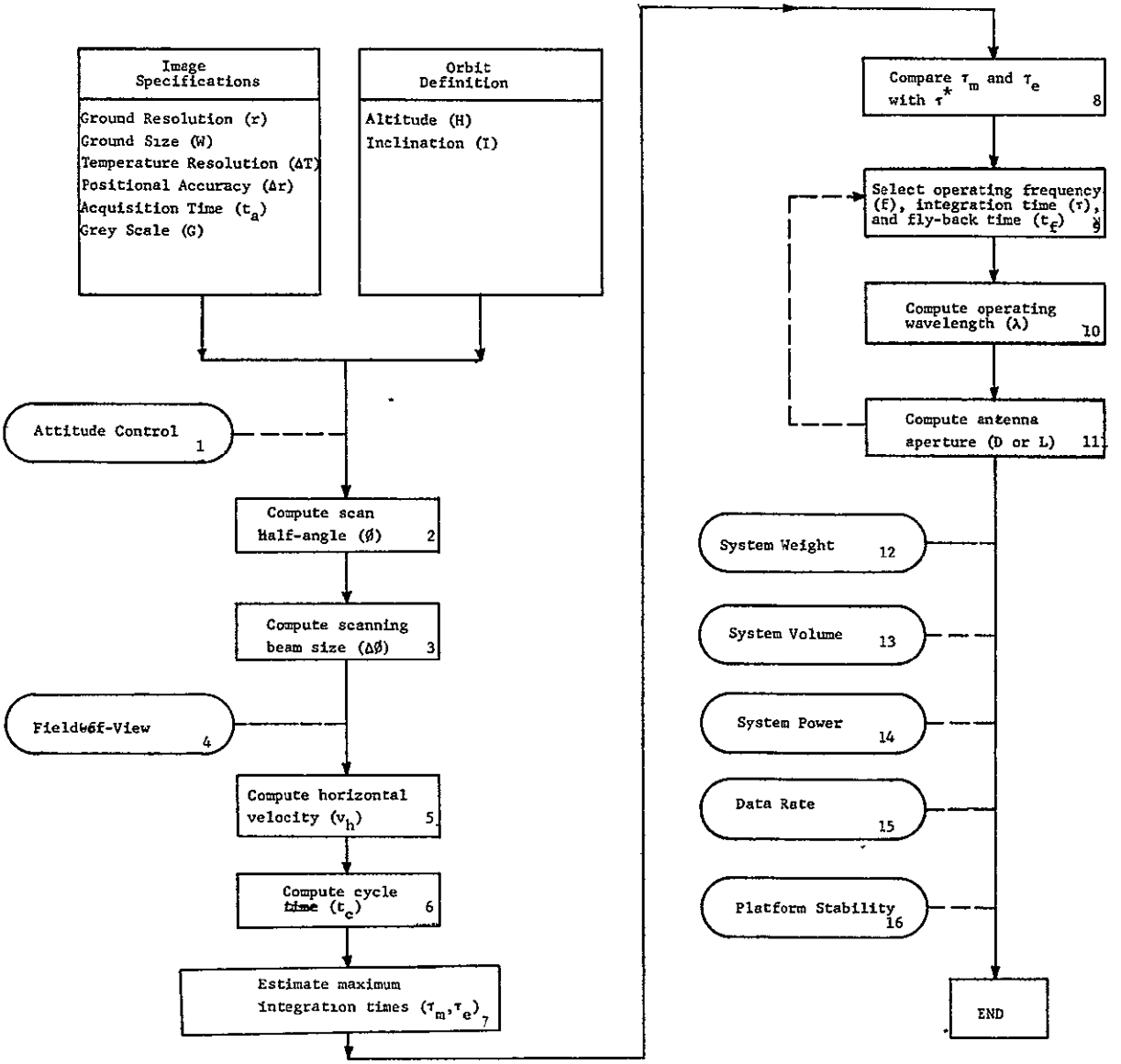

FIGURE 7-10 LOGIC DIAGRAM FOR PASSIVE MICROWAVE SYSTEMS

8. NONCOHERENT RADAR SYSTEMS

8.1 Design Equations

This section describes the physical and mathematical relations useful in estimating design variables of side-looking noncoherent radar imaging systems intended for orbital spacecraft experiments. Much of the development is based upon Appendix D of reference 89, although other references are cited whenever appropriate. Section 8.2 presents empirical data useful in estimating support requirements, while Section 8.3 summarizes a suggested design procedure for noncoherent radar systems.

8.1.1 Antenna Range Beamwidth

The planet-spacecraft spatial relationship has been discussed in Section 1.3, where it was shown that the field-of-view angle subtended at the altitude H by a great-circle arc-length W on the planetary surface is given by

$$\beta_r^* = \tan^{-1}\left[\frac{W' \sin(\Psi_2 + \delta)}{R_2 - W' \cos(\Psi_2 + \delta)}\right], \qquad (8\text{-}1)$$

where

$$W' = 2R \sin\frac{W}{2R}, \qquad (8\text{-}2)$$

$$\Psi_2 = \cos^{-1}\left(\frac{R+H}{R}\cos\alpha\right), \qquad (8\text{-}3)$$

$$\delta = \frac{W}{2R}, \qquad (8\text{-}4)$$

$$R_2 = \frac{R \sin(\alpha - \Psi_2)}{\cos\alpha} \qquad (8\text{-}5)$$

with β_r^* = minimum angular field-of-view,

W' = chord length associated with W,

R_2 = slant range to far end of W,

Ψ_2 = grazing angle at far end of W,

δ = half-angle subtended at planet center by W,

R = planet radius,

α = antenna depression angle.

as shown in Figure 8-1. The minimum angular field-of-view β_r^* may be regarded as equivalent to the radar antenna 3 dB range beamwidth and W as the swath width seen by the antenna. The value of β_r^* is uniquely determined by H/R, W/R, and the antenna depression angle α. The planet radius R is a known constant, the altitude H is determined by the representative orbit selections given in Volume III, minimum values of W are given by the image specifications in Volume I, but the depression angle α is somewhat arbitrary. In the limit as Ψ_2 approaches zero, a radar target will not produce a pulse return detectable by the antenna and receiver. Therefore α should be at least about two degrees larger than the depression angle to the planetary horizon:

$$\alpha_h = \cos^{-1}\left(\frac{R}{R+H}\right) . \tag{8-6}$$

On the other hand, α must not be so large that part of the swath width lies directly under the spacecraft. Thus α is constrained by

$$\frac{\pi}{2} - \beta_r^* > \alpha > \cos^{-1}\left(\frac{R}{R+H}\right). \tag{8-7}$$

The physical height of the antenna is related to the range beamwidth by

$$D_r = \frac{K_2\,\lambda}{\beta_r} , \tag{8-8}$$

where D_r is the antenna height, K_2 is a beamwidth factor, λ is the radar operating wavelength (in same units as D_r), and

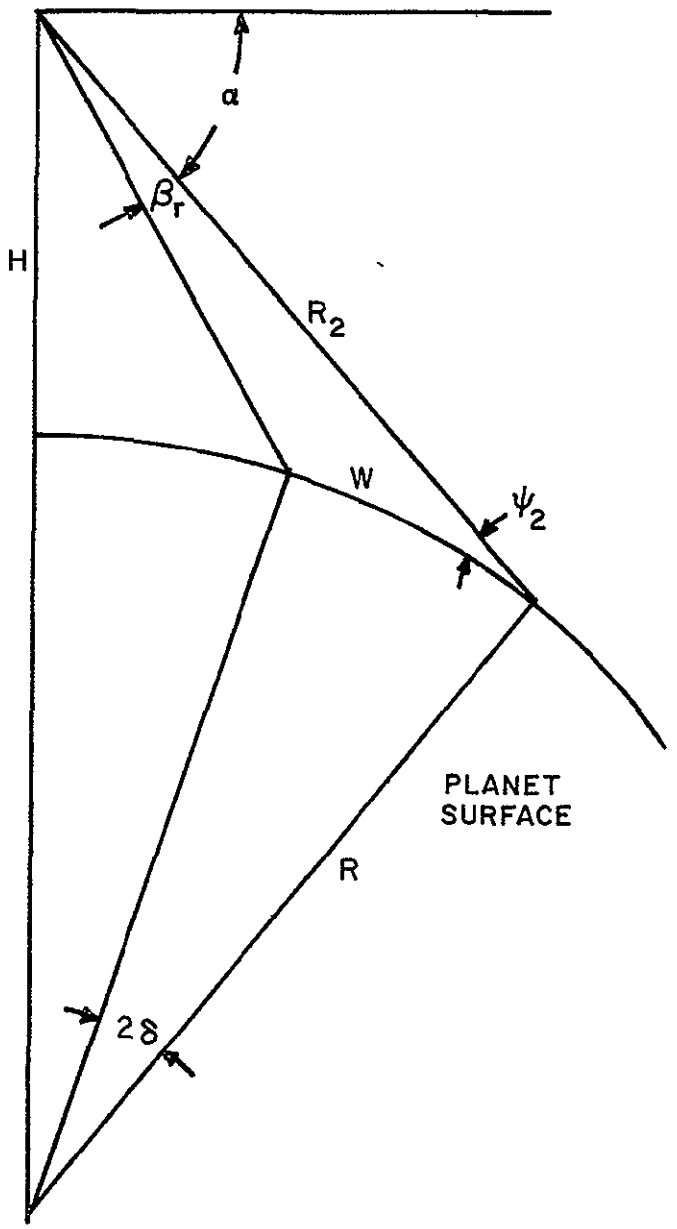

FIGURE 8-1. SIDE-LOOKING RADAR GEOMETRY

β_r is the antenna range beamwidth. The value appropriate for K_2 depends upon the antenna sidelobe configuration; for sidelobes down 25 dB from the main beam a value of 1.25 should be used[90] for K_2.

8.1.2 . Antenna Azimuth Beamwidth

For noncoherent processing of radar returns, the attainable ground resolution in the azimuth plane (the plane lying within β_r, but normal to the plane of Figure 8-1 and containing the point representing the spacecraft) is related to the antenna azimuth beamwidth. The linear azimuth resolution r_a at the slant range R_s provided by an azimuth beamwidth β_a is given by

$$r_a = K_3 \beta_a R_s , \tag{8-9}$$

where K_3 is a numerical constant ranging from about 1.1 to 1.2, and taken in this study as 1.15. For a fixed azimuth beamwidth, the azimuth resolution degrades (increases) with slant range. If a ground resolution of r is desired throughout the imagery, then the antenna azimuth beamwidth is constrained by

$$\beta_a \leq \frac{r}{K_3 R_2} . \tag{8-10}$$

The antenna length is related to the azimuth beamwidth in a manner analogous to eq. (8-8). Thus to achieve the resolution r, the antenna length is constrained by

$$D_a \geq \frac{K_2 K_3 \lambda R_2}{r} = \frac{1.44 \lambda R_2}{r} . \tag{8-11}$$

If high-quality resolution is demanded, then a long antenna may be required.

Antenna lengths of up to twenty feet are not unusual for high-resolution mapping radar systems currently operational

in some aircraft. Unfortunately no data on space-qualified antenna lengths are available. Rider and Sung[76] have surveyed the state-of-art in spaceborne antenna technology and have concluded that a fifty-foot diameter circular (or paraboloidal) antenna is within the reach of a short development effort. Presumably antenna lengths of greater than fifty feet are attainable for rectangular antenna arrays. Some spacecraft radar designs[91] have suggested eight meter long antennas at an operating frequency of eight GHz. Titus[84] has constructed a 24 feet by 40 inch unfolding mechanically-scanned antenna as a feasibility demonstration for a satellite-borne radar. The measured rms surface accuracy of this antenna was 0.4 cm, giving a value of about 2×10^3 for the ratio of antenna length to rms surface accuracy. It is assumed here that if particular care is taken in the fabrication process, a value of about 1.5×10^4 would be representative of the current state-of-art. Titus achieved a value of about $\lambda/50$ for the rms surface deviations, and notes that a tolerance of about 3/16-inches would be acceptable for S-band operation. This corresponds to rms deviations in the range from $\lambda/12$ to $\lambda/40$. By assuming that the required rms surface tolerance is $\lambda/15$, and that antenna lengths of 1.5×10^4 times the tolerance are attainable with the current state-of-art, the maximum antenna length may be related to the operating frequency as shown in Figure 8-2. However, antenna lengths of greater than 500 feet are regarded as unfeasible at any operating frequency. It should be emphasized that although Figure 8-2 implies that antenna lengths which are not feasible at one wavelength may be reasonable at a longer wavelength, the minimum required length also increases with wavelength. That is, if the minimum antenna length required to achieve a specified ground resolution is beyond the state-of-the-art, use of a longer wavelength will not circumvent the problem.

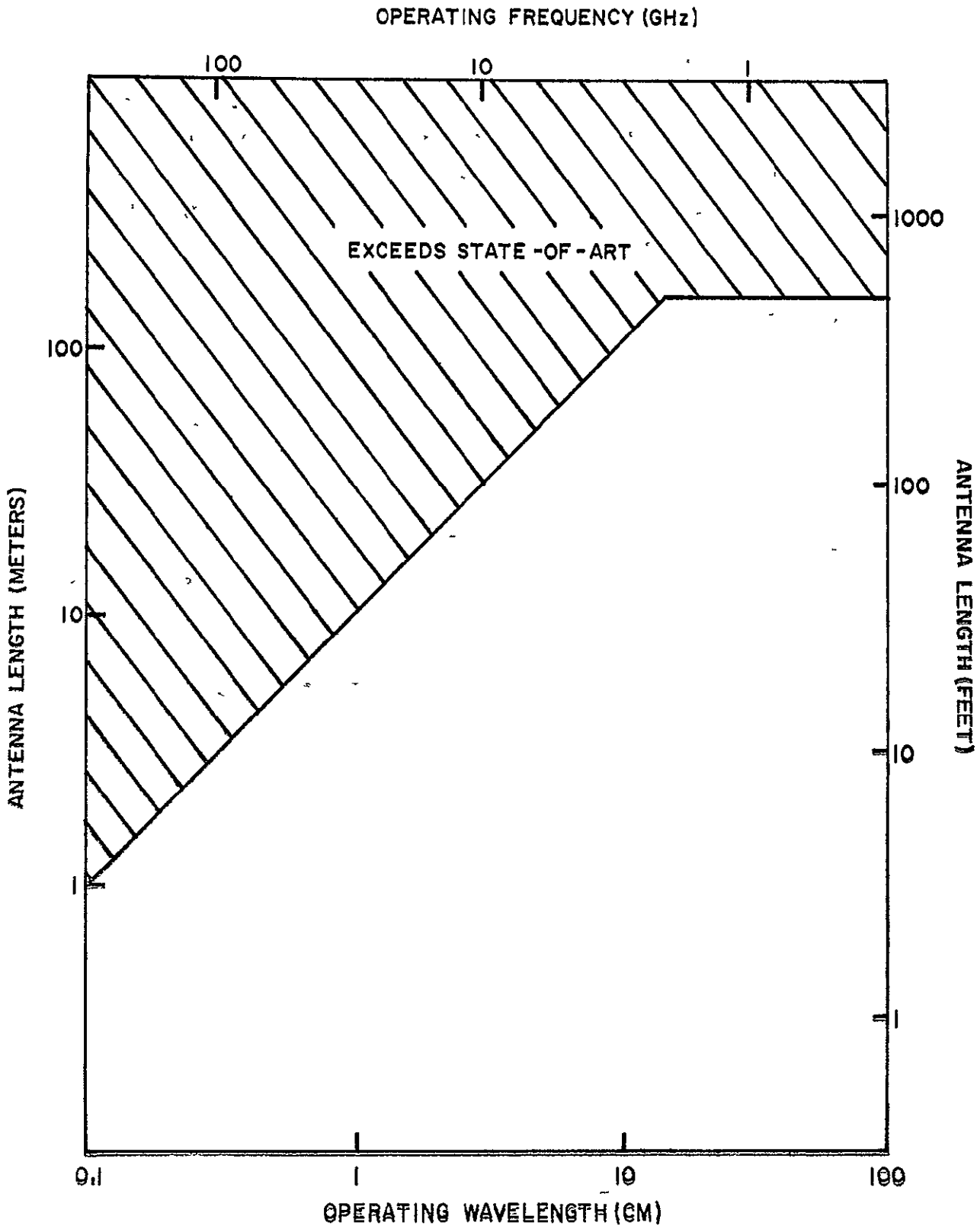

FIGURE 8-2. MAXIMUM ANTENNA LENGTHS

The antenna azimuth beamwidth is also related to the pulse transmission and reception timing. In particular, the azimuth beamwidth must be broad enough that the proper number of pulse returns are received before the antenna has traveled too far to detect the reflected pulses. For a non-rotating planet, Baldauf and Leef[92] have shown that the time interval t_o during which a target at slant range R_s lies within the physical beamwidth of the antenna is approximately

$$t_o = \frac{2(H+R)}{v_s} \sin^{-1}\left[\frac{R_s \sin(\beta_a/2)}{H+R - R_s \sin\alpha_s}\right] , \quad (8\text{-}12)$$

where v_s is the horizontal speed of the spacecraft normal to R_s, α_s is the depression angle associated with the slant range R_s, and the other symbols have been defined previously. Since targets at short range will spend less time in the beam than targets at long range, and using eq. (1-46) to account approximately for the effects of planet rotation, the minimum time which targets in the swath width W will spend in the beam is

$$t_o = \frac{2R}{v_h} \sin^{-1}\left[\frac{R_1 \sin(\beta_a/2)}{H+R - R_1 \sin(\alpha + \beta_r^*)}\right] , \quad (8\text{-}13)$$

where v_h is the maximum apparent horizontal velocity of the planetary surface along the heading line as seen by the antenna, and is given by eq. (1-46). R_1 is the slant range to the near edge of the swath width,

$$R_1 = \frac{W' \sin(\Psi_2 + \delta)}{\sin\beta_r^*} . \quad (8\text{-}14)$$

Clearly, from eq. (8-13), increasing the antenna azimuth beamwidth β_a will permit targets to be observed for longer periods of time.

8.1.3 Pulse Length

The transmitted pulse length must be short enough that the desired ground resolution is achieved. The slant range resolution capability of the radar system is $\frac{1}{2}$ $c\tau$, where c is the velocity of radar wave propagation, and τ is the pulse width. The ground range resolution capability r_r is then

$$r_r = \frac{c\,\tau}{2\cos\Psi} , \tag{8-15}$$

where Ψ is the grazing angle. Since, for a fixed altitude and planet radius, the cosine of the grazing angle increases with slant range, the range resolution capability of the system improves with slant range. This behavior is opposite to that of the azimuth resolution capability, as expressed by eq. (8-9), which degrades with increasing slant range. It should also be noted that directly underneath the spacecraft, where cos Ψ vanishes, the system has no ground range resolution capability. For this reason, the swath width W should not include the area directly beneath the spacecraft. If the ground resolution r is desired throughout the swath width, then the pulse width is constrained by

$$\tau \leq \frac{2\,r\cos\Psi_1}{c} , \tag{8-16}$$

where Ψ_1 is the grazing angle at the near edge of the swath width. It has been shown in Section 1.3 that

$$\Psi_1 = \Psi_2 + \beta_r^* + \frac{W}{R} , \tag{8-17}$$

and Ψ_2 has been given explicitly by eq. (8-3).

The use of pulse-compression techniques[93] permits a better range resolution than that implied by eq. (8-15). Relatively long pulses can be transmitted, the echoes received,

and the long pulse length data processed to appear as if much shorter pulses had been used. Eqs. (8-15) and (8-16) are applicable when pulse compression is used, provided that τ is interpreted as the compressed pulse length τ_c. The pulse compression ratio C is defined as the ratio of the uncompressed pulse length to the compressed pulse length,

$$C = \frac{\tau}{\tau_c} . \tag{8-18}$$

Pulse compression ratios of 200, and uncompressed pulse lengths as short as 10^{-9} seconds, appear to be attainable with the current state-of-art.[93]

Receiver bandwidths are related to the pulse length, and are currently limited to about ten percent or less of the operating frequency. That is, the current state-of-art[74,79] limits the maximum attainable bandwidth to ten percent of the operating frequency. Since the receiver bandwidth, for a matched system, is simply the reciprocal of the compressed pulse length[94], this implies that

$$\tau_c \geq \frac{10}{f} = \frac{10\lambda}{c} , \tag{8-19}$$

where f is the operating frequency, and c is the speed of light. This state-of-art constraint is often more stringent than that implied by a nanosecond uncompressed pulse length and a maximum compression ratio of 200.

For rapidly-rotating planets, such as Jupiter, target motion due to planetary rotation will result in a Doppler-shift of the transmitted frequencies. The maximum fractional Doppler shift is

$$\frac{\Delta f}{f} \simeq \frac{2\, v_r}{c} , \tag{8-20}$$

where v_r is the apparent target velocity due to planet rotation. If the maximum acceptable Doppler shift is ten percent of the receiver bandwidth, and if the bandwidth is taken as the reciprocal of the compressed pulse width, then

$$\tau_c \leq \frac{0.05\lambda}{v_r} \quad . \tag{8-21}$$

In some cases, this may be a more severe constraint upon the pulse length than the resolution requirement expressed by eq. (8-16).

8.1.4 Pulse Repetition Frequency

Range ambiguities will result if pulse returns from the near edge of the swath width interfere with returns from the far edge. The pulse repetition frequency should be low enough that only one pulse is traveling through the swath width at a time. This condition limits the acceptable pulse repetition frequency p to

$$p \leq \frac{c}{2 W \cos \Psi_2} \quad . \tag{8-22}$$

On the other hand, the pulse rate must be sufficient to provide at least one pulse return per azimuth resolution element. Thus if m hits per target are required, the pulse repetition rate is constrained by

$$p \geq \frac{m}{t_o} \quad , \tag{8-23}$$

where t_o is the time required for a point target to traverse the beamwidth, and was given by eq. (8-13). Pulse travel time is neglected in eq. (8-23). Since eq. (8-13) is an approximation which slightly underestimates the travel time, eq. (8-23) is a slight overestimate, and this tends to compensate for the neglect of the pulse travel time. The pulse rates

attainable with currently available equipment are limited to something on the order of 10^6 pulses per second.

The two pulse rate constraints given above are general conditions which must be satisfied, regardless of the details of the pulse transmission and reception timing. There are additional constraints on the pulse rate, which do depend upon such details[94]. The first return, from a transmitted pulse, which reaches the antenna is due to specular reflection from the planetary surface directly underneath the spacecraft. Although the antenna gain may be low in this direction, the backscatter coefficient of the target may be sufficiently large that this sidelobe return may interfere with the pulse return from the swath width of interest. Since the spacecraft altitude is H, the leading edge sidelobe return will be detected 2H/c seconds after the start of the pulse transmission. The length of the sidelobe return may be approximated by the difference in travel time between a direction in the center of the azimuth beamwidth and a direction along the edge of the azimuth beamwidth. Thus the duration of the sidelobe return is roughly

$$\frac{1}{c}\left(\frac{2H}{\cos\frac{\beta_a}{2}} - 2H\right) = \frac{2H}{c}\left[\sec\left(\frac{\beta_a}{2}\right) - 1\right] . \qquad (8\text{-}24)$$

In order that the pulse return from the near edge of the swath width not be confused with the sidelobe return,

$$\frac{2H}{c} + \frac{2H}{c}\left[\sec\left(\frac{\beta_a}{2}\right) - 1\right] < \frac{2R_1}{c} . \qquad (8\text{-}25)$$

This condition constrains the azimuth beamwidth to

$$\beta_a < 2\cos^{-1}\left(\frac{H}{R_1}\right) , \qquad (8\text{-}26)$$

which is almost always less stringent than the resolution constraint.

A mode of pulse timing which results in reception of a complete pulse return from the entire swath width before transmission of the succeeding pulse is shown schematically in Figure 8-3(a). Since the return from the leading edge of the pulse striking a target at the near edge of the swath width arrives at the antenna $2\ R_1/c$ seconds after the start of pulse transmission, and the return from the trailing edge of the pulse striking a target at the far end of the swath width arrives at the antenna $(2R_2/c) + \tau$ after the start of pulse transmission, the duration of pulse return is

$$\tau + \frac{2\ (R_2 - R_1)}{c} .$$

If the succeeding pulse transmission is not to interfere with the pulse return, then

$$\frac{1}{p} \geq \tau + \frac{2\ R_2}{c} , \tag{8-27}$$

or

$$p \leq \frac{c}{2\ R_2 + c\ \tau} . \tag{8-28}$$

This constraint is clearly more stringent than the range ambiguity constraint given by eq. (8-22).

If the swath pulse return is shorter than the time between the end of pulse transmission and the commencement of the sidelobe return, this time may be utilized for swath pulse return as shown in Figure 8-3(b). That is, if

$$\tau + \frac{2\ (R_2 - R_1)}{c} \leq \frac{2H}{c} - \tau , \tag{8-29}$$

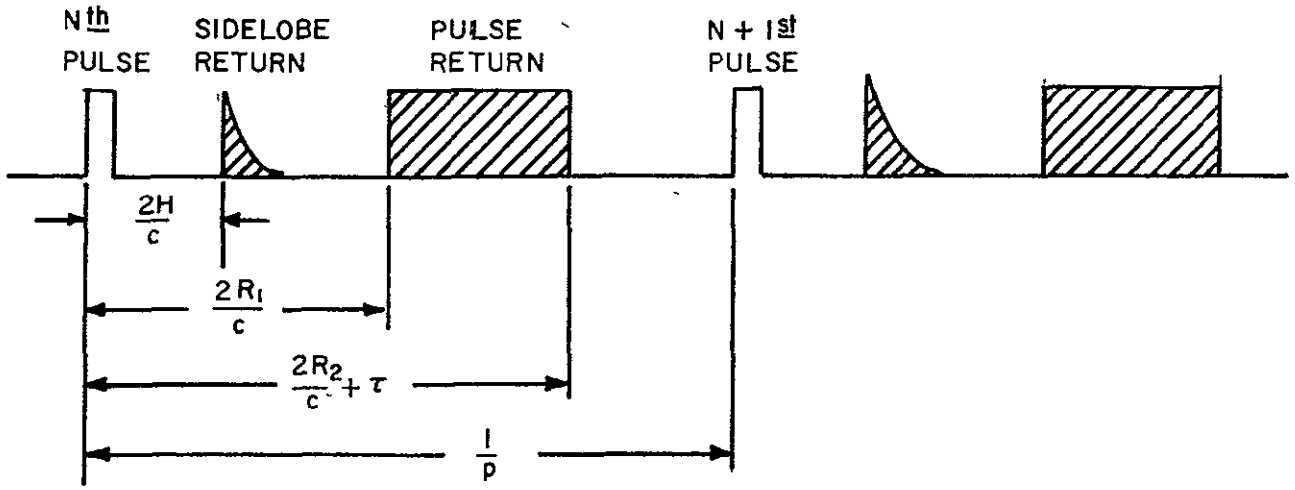

(a) SUCCESSIVE PULSES AND RETURNS

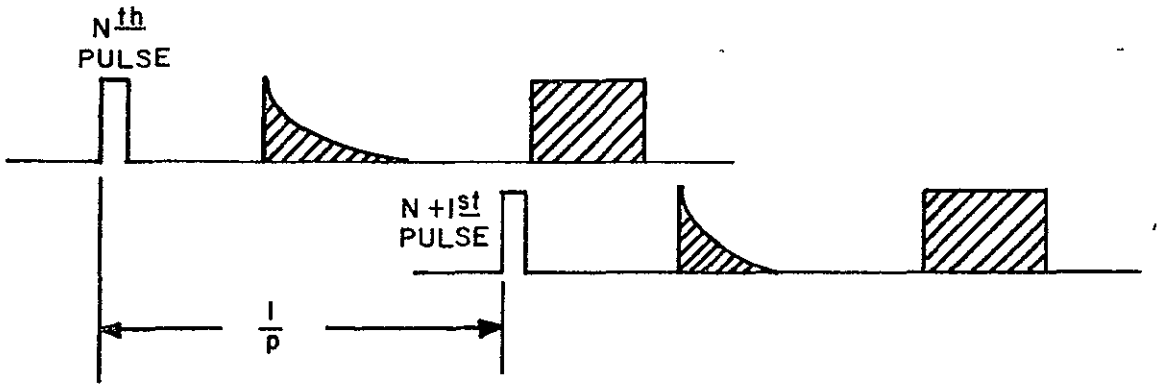

(b) NEXT PULSE TRANSMISSION BEFORE PULSE RETURN

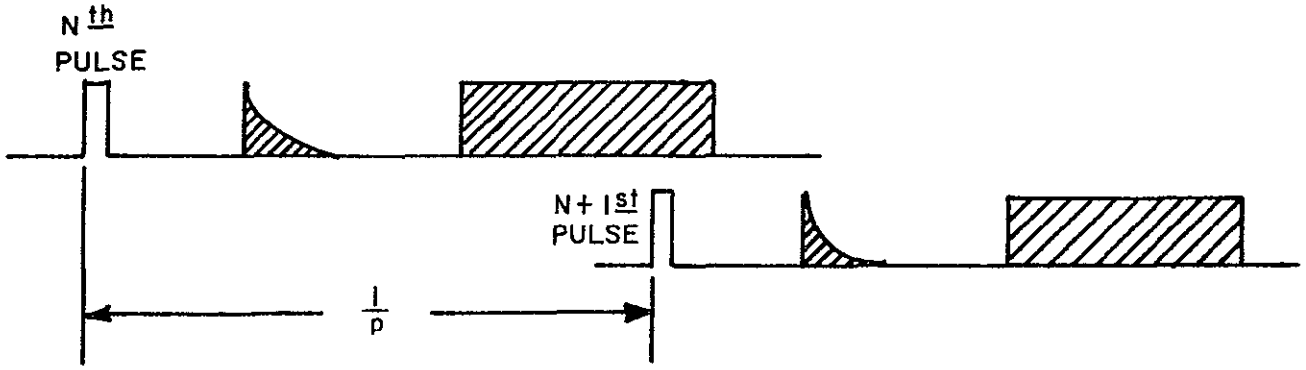

(c) PULSE TRANSMISSION DURING RECEPTION

FIGURE 8-3 MODES OF PULSE TIMING

or

$$R_2 - R_1 \leq H - c\,\tau \,, \tag{8-30}$$

then in order for the pulse transmission not to interfere with swath pulse return reception,

$$\frac{1}{p} \geq \tau + \frac{2\,(R_2 - R_1)}{c} \,, \tag{8-31}$$

or

$$p \leq \frac{c}{2\,(R_2 - R_1) + c\,\tau} \,. \tag{8-32}$$

Again, this constraint is more stringent than the range ambiguity constraint.

If the pulse transmission time is much shorter than the swath return reception time, the pulse can be transmitted during the reception time without appreciable loss of signal. To allow for switching time, the time required for pulse transmission is taken as 2τ, and if a five percent loss of signal is acceptable, the pulse length must satisfy

$$2\tau \leq 0.05 \left[\tau + \frac{2\,(R_2 - R_1)}{c} \right] . \tag{8-33}$$

or

$$R_2 - R_1 \geq 20\, c\,\tau \,, \tag{8-34}$$

to permit the timing mode shown in Figure 8-3(c). In order that the sidelobe return not interfere with the swath return,

$$\frac{1}{p} + \frac{2H}{c} \geq \tau + \frac{2\,R_2}{c} \,, \tag{8-35}$$

or

$$p \leq \frac{c}{2(R_2 - H) + c\tau} . \qquad (8\text{-}36)$$

Yet again, this constraint is more stringent than the range ambiguity constraint.

To summarize, it is essential to pulse at a rapid rate in order to hit each target one (or more) times before the target passes out of the azimuth beamwidth. The maximum allowable pulse rate is afforded by the mode shown in Figure 8-3(b), but this mode is possible only if $R_2 - R_1$ is less than $H - c\tau$. If $R_2 - R_1$ is not this small, but is larger than $20\ c\tau$, the maximum pulse rate is afforded by the mode shown in Figure 8-3(c). Finally, if $R_2 - R_1$ does not satisfy either condition, the pulse timing mode represented by Figure 8-3(a) is required. The maximum pulse repetition frequencies for these different modes are summarized in Table 8-1.

Table 8-1

Maximum Pulse Rates

Figure	$R_2 - R_1$	Maximum Pulse Rate
8-3(b)	$\leq H - c\tau$	$\frac{c}{2(R_2 - R_1) + c\tau}$
8-3(c)	$\geq 20\ c\tau$	$\frac{c}{2(R_2 - H) + c\tau}$
8-3(a)	none of above	$\frac{c}{2R_2 + c\tau}$

8.1.5 Transmitted Power

The signal power returned from a target is

$$S = \frac{P_t G^2 \lambda^2 \sigma e^{-2\rho R_s}}{(4\pi)^3 R_s^4} \qquad (8\text{-}37)$$

where

P_t = transmitted peak power,
G = antenna power gain,
λ = operating wavelength,
σ = target radar cross section,
ρ = one-way atmospheric attenuation coefficient,
R_s = slant range to target.

The noise power N associated with the radar system is[89]

$$N = F_o kTB , \qquad (8\text{-}38)$$

where F_o = system noise figure,
k = Boltzmann's constant (1.381×10^{-23} joules/de
T = effective input noise temperature,
B = receiver noise bandwidth.

If S/N is the required signal-to-noise ratio, the required signal power is (S/N) times N for a single pulse return. The noncoherent integration of m pulse returns from a specific target reduces the effective noise by $m^{\frac{1}{2}}$. Using eqs. (8-37) and (8-38),

$$P_t = \frac{(4\pi)^3 (S/N) F_o kTB R_s^4 e^{2\rho R_s}}{m^{\frac{1}{2}} G^2 \lambda^2 \sigma} . \qquad (8\text{-}39)$$

The antenna gain is related to the antenna aperture by

$$G = \frac{K_1 D_a D_r}{\lambda^2} \qquad (8\text{-}40)$$

where K_1 is a constant equal to 4π times the antenna aperture efficiency, and is approximately eight (i.e., the aperture efficiency is about 0.64). The target cross section is the product of the backscatter coefficient η and the size of the target seen by the radar pulse,

$$\sigma = \eta(K_3 \beta_a R_s)\left(\frac{c\tau}{2 \cos \Psi}\right), \qquad (8\text{-}41)$$

where eqs. (8-9) and (8-15) have been used. It is usually convenient to replace B by $(B\tau_c)/\tau_c$, since for a matched system the quantity $B\tau_c$ is unity. Finally, since P_t increases with slant range, it is necessary to evaluate P_t at the slant range to the far edge of the swath width. Using eqs. (8-8), (8-40) and (8-41), eq. (8-39) becomes

$$P_t = \frac{(10^{-30}) \cdot (S/N) F_o T (B\tau_c) R_2^3 \beta_a \beta_r^2 \cos \Psi_2 \cdot e^{2\rho R_2}}{\tau \tau_c \eta m^{\frac{1}{2}} \lambda^2} \qquad (8\text{-}42)$$

in MKS units. For continuous operation at a pulse repetition frequency p, the average radiated power is

$$\overline{P} = \tau p P_t . \qquad (8\text{-}43)$$

When the time required for a target to pass through the azimuth beamwidth is large compared to the time required to transmit m pulses, it may be expedient to place the transmitter on standby until new resolution elements enter the azimuth beamwidth. In this case, the duty cycle of the transmitter is $(m/p)/t_o$, where t_o is given by eq. (8-13), and then the average power transmitted is

$$\bar{P} = \frac{m\tau}{t_o} P_t \ . \qquad (8\text{-}44)$$

Peak power of 3 megawatts at 1.3 GHz have been achieved in laboratory demonstration[95], for nanosecond pulses. Peak powers of 100 megawatts, at 25 cm wavelengths, appear attainable in the near future. Power generation is somewhat more difficult at shorter wavelengths, the attainable power being rather roughly proportional to the wavelength.

In order to use eq. (8-42), appropriate values must be determined for the signal-to-noise ratio, the system noise figure, the input noise temperature, the atmospheric attenuation coefficient, and the target backscatter coefficient. These topics are discussed in the following section.

8.1.6 System Noise

Data on receiver noise figures reflecting the current state-of-art have been reported by the Willow Run Laboratories of the University of Michigan[89]. Figure 8-4 is reproduced from their report. The dashed lines indicate the spread in attained noise figures as a function of wavelength. An approximate fit to these data is

$$\ln F_o = 2.42 - 0.344 \ln \lambda \ , \qquad (8\text{-}45)$$

where F_o is in absolute units, not decibels, and λ is in centimeters. In addition to receiver noise, other power losses include system degradation and transmission line effects. The total effect of these other losses is taken here as six dB. Thus the system noise figure (excluding input noise) is approximately given by

$$\ln F_o = 3.80 - 0.344 \ln \lambda \ . \qquad (8\text{-}46)$$

For convenience, F_o based on this expression is shown in Figure 8-5.

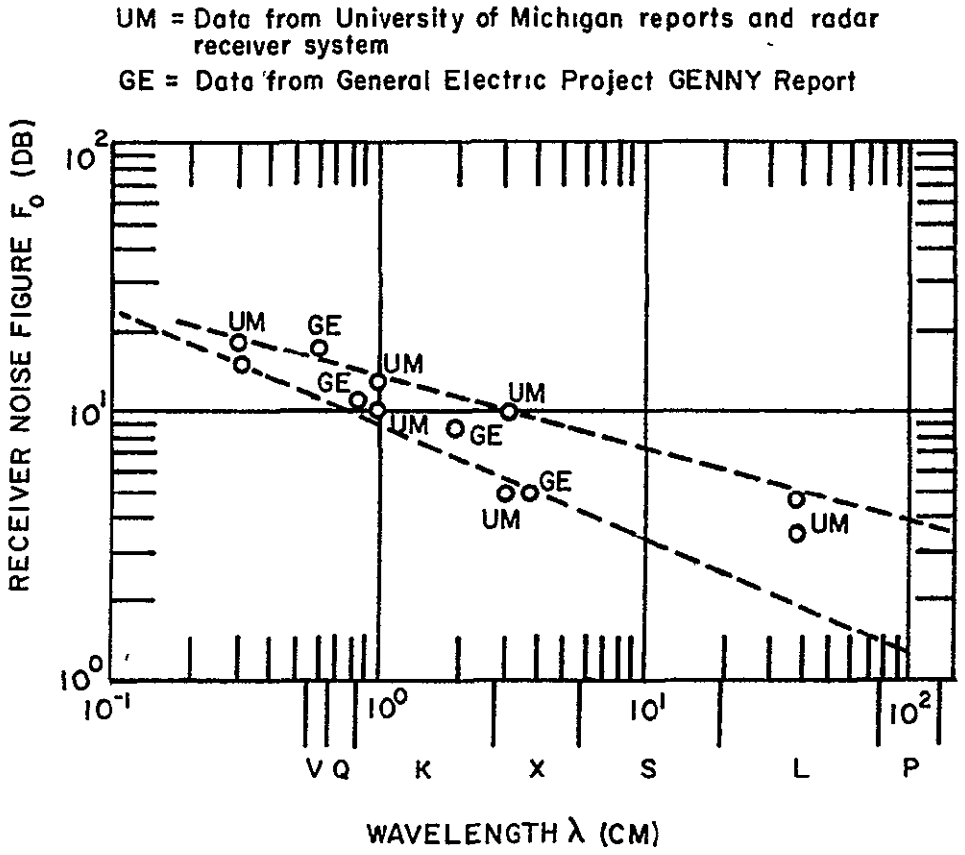

FIGURE 8-4 RECEIVER NOISE FIGURES

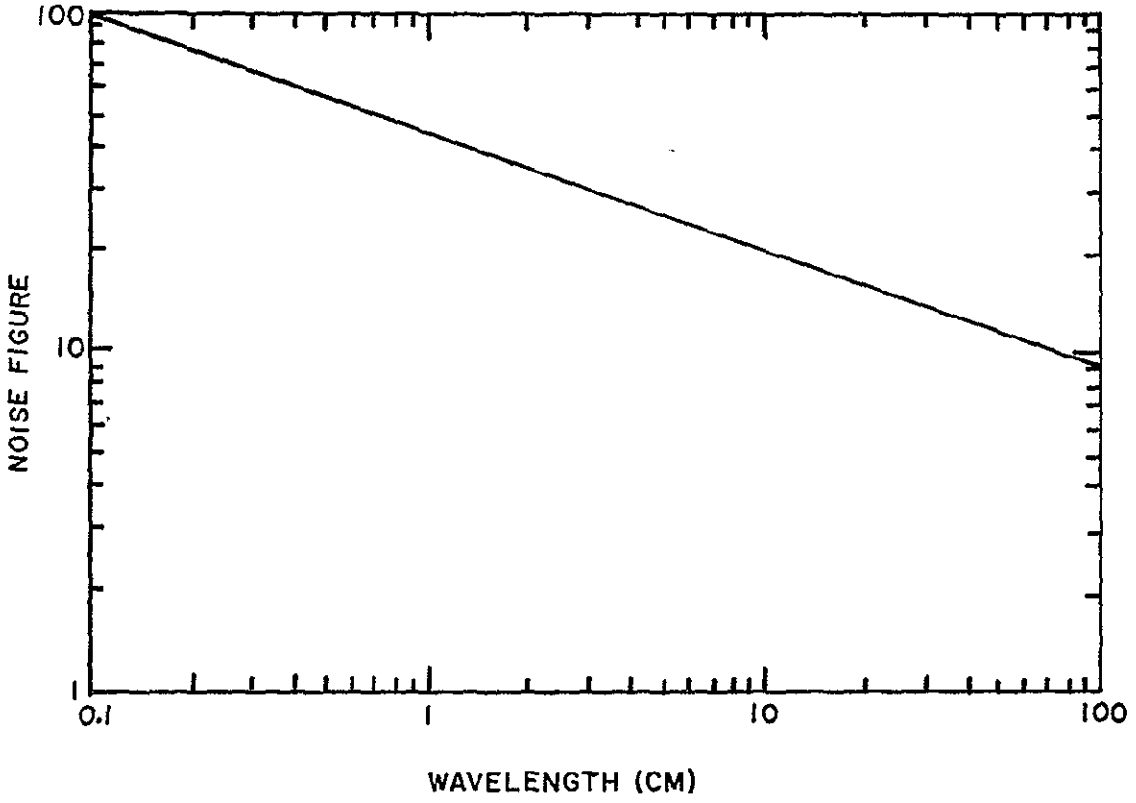

FIGURE 8-5. SYSTEM NOISE FIGURE

The input noise temperature arises from cosmic, solar, and planetary noise contributions. For a perfect antenna, only the planetary noise will be significant. Thus, as a first approximation, the input noise temperature may be taken as the maximum observed planetary temperature. Values for the planets are given in Table 8-2.

Table 8-2

Planetary Temperature

Planet	Temperature (deg K)
Moon	400
Mercury	600
Venus	700
Mars	300
Jupiter	200 (?)

It is not known whether the planetary surfaces will appear as high contrast or low contrast targets to a radar imaging system, and little guidance is available for determination of an acceptable signal-to-noise ratio. By analogy with imaging systems operating in other spectral regions, it would appear that a signal-to-noise ratio of about three would provide adequate imagery for high-contrast targets. However, signal-to-noise ratios of ten have been suggested in other studies[89] of satellite-borne imaging radar systems, and that value is recommended here.

8.1.7 Backscatter Coefficient

The required transmitter power is inversely proportional to the target backscatter coefficient. Although

backscatter coefficients are reasonably well determined as a function of grazing angle and operating wavelength for a variety of terrestrial targets, little information is available for extraterrestrial surfaces. Figure 8-6 is an example[96] of terrestrial data. Assuming that at least the Moon, Mercury, and Mars behave similar to arid desert sand, a target backscatter coefficient of 10^{-3} might be appropriate, although other studies[89] have used a backscatter coefficient of 10^{-4}. A value of 5×10^{-4} would appear to be a conservative compromise, and is recommended here. Because of this uncertainty, any attempt to assign a wavelength or grazing angle dependence to the backscatter coefficient is pretentious.

8.1.8 Atmospheric and Ionospheric Effects

The Moon, Mercury, and Mars are assumed to have sufficiently thin atmospheres and ionospheric electron layers that microwave attenuation (for either active or passive sensor systems) can be ignored. This is not the case for Venus or Jupiter. This section estimates the severity of such absorption, so that the transmitted radar pulse power can be corrected for pulse attenuation.

Venus

The one-way microwave attenuation factor is of the form

$$e^{-\int \alpha(s)ds}$$

where $\alpha(s)$ is the attenuation coefficient, and ds is an element of path length. The integration is performed through the entire Venusian atmosphere. Ho, et al.[97], have measured the microwave absorption in atmospheres containing CO_2, N_2, A, and Ne over a range of temperatures and pressures anticipated at Venus. They conclude that

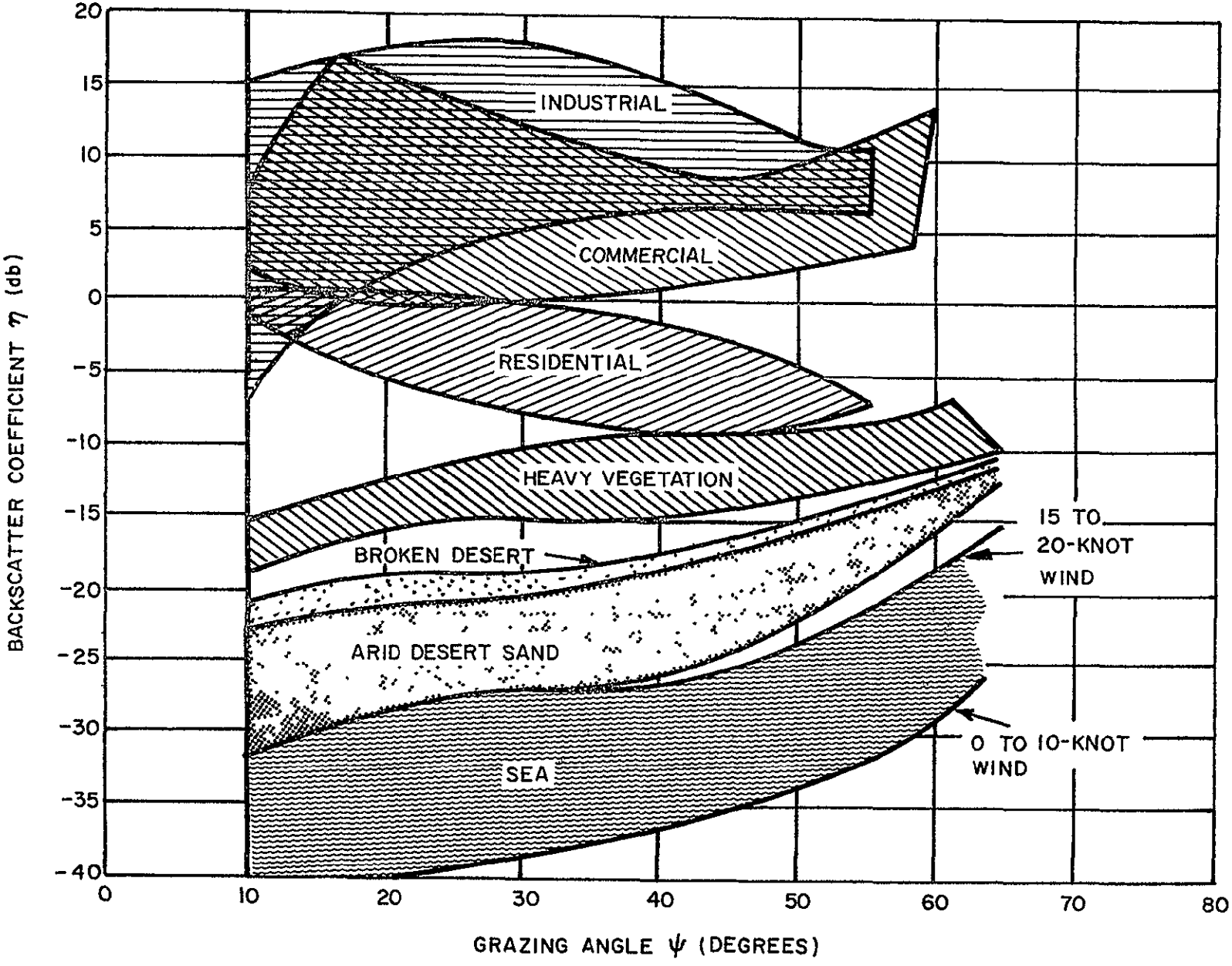

FIGURE 8–6 TERRAIN RETURN ANALYSIS PROGRAM DATA SUMMARY, X-BAND

$$\alpha = p^2 \bar{\nu}^2 \left(\frac{273}{T}\right)^5 (15.7\ f_{CO_2}^2 + 3.90\ f_{CO_2}\ f_{N_2}$$

$$+ 2.64\ f_{CO_2}\ f_A + 0.085\ f_{N_2}^2 + 1330\ f_{H_2O}) \times 10^{-8} cm^{-1}. \quad (8\text{-}47)$$

Here α is the attenuation coefficient, p is the pressure in atmospheres, $\bar{\nu}$ is the frequency in wave numbers, T is the temperature in degrees Kelvin, and f_{CO_2}, etc., are the various molar fractions. The origin of the absorption represented by eq. (8-47) is in the transient electric dipole moments induced by molecular collisions occurring under high pressure conditions. The water contribution term is strictly correct only in nitrogen-rich atmospheres, and ignores the resonant contribution from the 1.35 cm water vapor line (significant only at low pressure). It remains now to determine the pressures, temperatures, and constituents of the Venusian atmosphere.

An early analysis of the Venera 4 data by Reese and Swan[98] indicated that a simple constant-lapse-rate atmospheric model could be used to interpret the Venera 4 results. The model is simplified even further here, for purposes of microwave absorption estimation, by neglect of the isothermal stratosphere. That is, a polytropic atmosphere model is assumed valid from the surface to an extrapolated altitude at which the pressure and temperature vanish. If p_s and T_s are the surface pressure and temperature, respectively, then according to the polytropic model,

$$\frac{p}{p_s} = \left(\frac{T_s - \gamma Z}{T_s}\right)^{\frac{mg}{k\gamma}} \quad (8\text{-}48)$$

where γ is the temperature lapse rate, Z is the altitude, m is the mean molecular weight, g is the gravitational constant, and k is Boltzmann's constant. Using a lapse rate of 10°K/km[98], a mean molecular weight of 40 amu[99], and a gravitational constant of 870 cm/sec^2,

$$\frac{p}{p_s} \simeq \left(\frac{T_s - \gamma Z}{T_s}\right)^4 \quad . \tag{8-49}'$$

Jastrow[99], in comparing the Venera 4 data with the Mariner V results, has suggested a surface pressure of 40 atmospheres and a surface temperature of 700°K, the latter being a suitable average between day and night temperatures. These surface conditions assume that the Venera 4 landed on a 10 km high mountain. If the capsule indeed impacted the surface, the attenuation computed here will be an overestimate. The crude model used here implies a 70 km thick atmosphere. Now assuming an atmosphere of 90 percent carbon dioxide and 5 percent nitrogen[99], eq. (8-47) yields

$$\alpha = \frac{0.186}{\lambda^2}\left(\frac{T_s - \gamma Z}{T_s}\right)^3 \text{ km}^{-1} \quad , \tag{8-50}$$

where λ is the wavelength in centimeters, and contributions from other than CO_2 and N_2 have been ignored.

An interesting, if not entirely convincing, check on the validity of this estimate may be obtained by assuming a surface brightness temperature of 700°K, correcting for the one-way radiation attenuation, and comparing the result to the measured brightness temperature as a function of wavelength. Figure 8-7 shows the measured microwave temperatures[97,100], where the error bars indicate estimates of typical measurement errors. The solid line is the result of correcting the surface microwave emission for attenuation

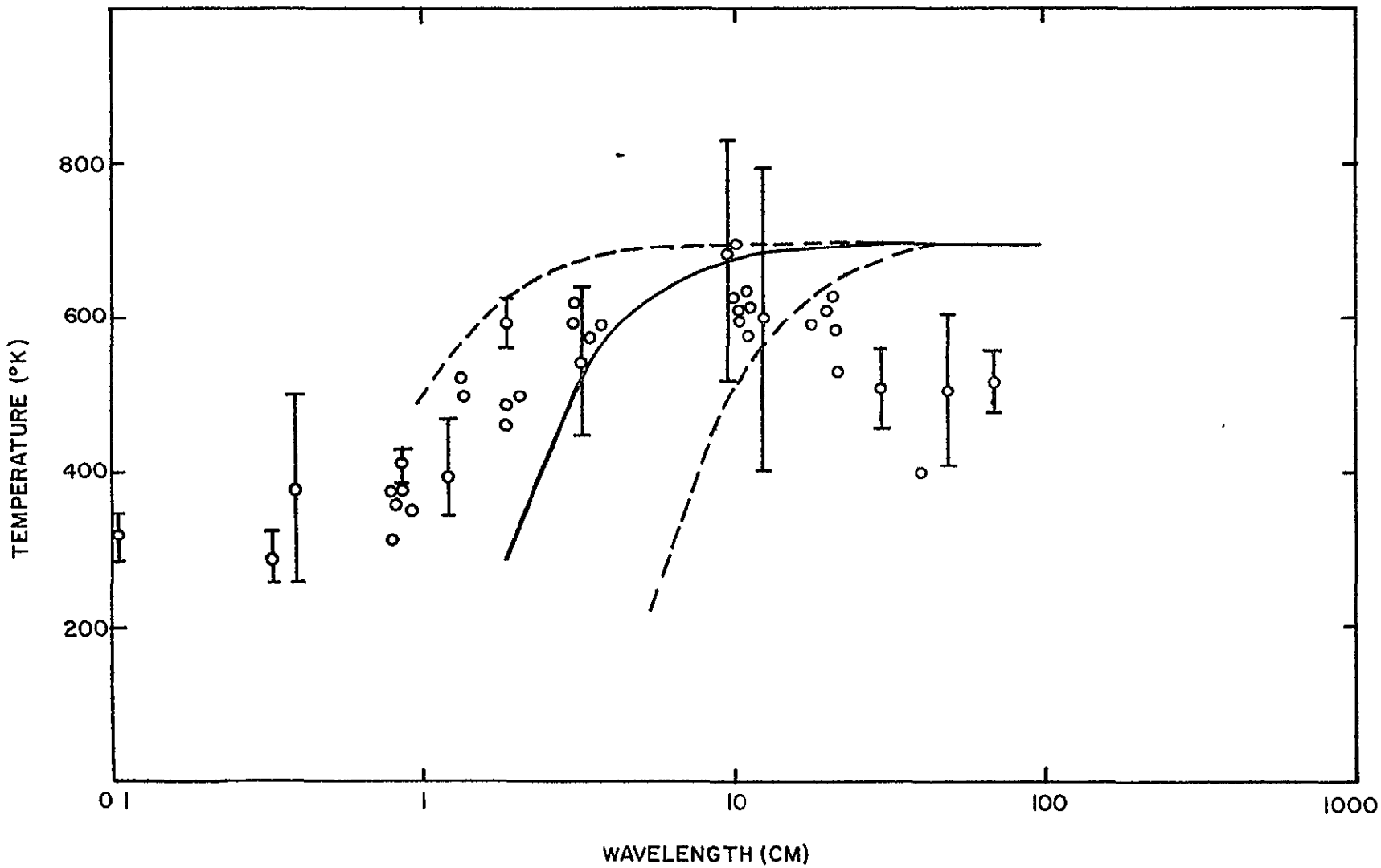

FIGURE 8-7. VENUS MICROWAVE TEMPERATURE

using eq. (8-50) for the attenuation coefficient. The dashed lines show the results of similar calculations, but with an attenuation coefficient a factor of ten larger in one case, and smaller in the other, than implied by eq. (8-50). These results suggest that the attenuation coefficient derived here is a reasonable one.

For a side-looking radar, the attenuation factor may be estimated by using eq. (8-50) i.e.,

$$e^{-2\int \alpha(s)ds} = e^{-\frac{.372}{\lambda^2}\int_o^H \left(\frac{T_s - \gamma Z}{T_s}\right)^3 \frac{dz}{\sin \Psi_2}}$$

where H is the atmospheric thickness (70 km), and Ψ_2 is the grazing angle at the far edge of the swath width. The factor $1/\sin \Psi_2$ simply corrects for the atmospheric path length being non-vertical. Thus the attenuation factor is

$$e^{-\frac{6.5}{\lambda^2 \sin \Psi_2}}$$

where λ is the wavelength in centimeters. An attenuation factor of unity corresponds to no absorption. The radar support requirements estimated in this study for experiments at Venus have been based on this attenuation factor.

It should be noted that the only attenuation mechanism considered here is that of molecular absorption by carbon dioxide and nitrogen. Absorption by dust clouds, water vapor, and ionospheric electrons has been considered insignificant. If the atmospheric water concentration is 0.1 percent, which is roughly the upper limit deduced from microwave emission data, the absorption coefficient would be increased by ten percent over that used above. Mariner V data indicates a peak ionospheric electron density of 5×10^5 cm^{-3} with a density profile

half-width of about 20 kilometers. In the terrestrial D-layer, the electron density is about 10^4 cm^{-3} and the collision frequency is on the order of 10^6 sec^{-1}. Assuming that the collision frequency is crudely proportional to the electron density, the collision frequency appropriate for Venus is on the order of 5×10^7 sec^{-1}. Evans and Hagfors[101] have shown that when the operating frequency is much greater than the collision frequency (and the gyrofrequency), the power absorption coefficient is approximately

$$\alpha = 2.7 \times 10^{-7} \frac{N\nu}{f^2} \quad m^{-1} \qquad (8\text{-}51)$$

where N is the electron density (per cubic meter), ν is the collision frequency, and f is the operating frequency. Thus at a wavelength of ten centimeters, the maximum signal loss due to ionospheric electron absorption at Venus is roughly 0.1 dB, which is regarded as insignificant.

Jupiter

An estimate of the one-way microwave absorption in Jupiter's upper atmosphere has been given by Chandra and Srivastava[102] as 6.4 db at 3 cm and 0.5 db at 10 cm. This corresponds to a radar attenuation factor of

$$e^{-\frac{26.6}{\lambda^2 \sin \Psi_2}}$$

The attenuation model assumes the absorption is due entirely to the 1.25 cm ammonia line and apparently considers absorption down to, but not including, the visible cloud cover. The attenuation coefficient of the lower atmosphere is taken here as ten times that of the upper atmosphere, and hence the attenuation factor for radar experiments is

$$e^{-\frac{266}{\lambda^2 \sin \Psi_2}}.$$

In addition to atmospheric attenuation, the radiation belts must be considered. Chang and Davis[103] have suggested a synchrotron model and obtained different properties of the belts, depending upon whether the magnetic field is 0.1, 1, or 10 gauss. They suggest that the one gauss model may be the most reasonable, in which case the electron density is about 2×10^{-3} cm^{-3}, for a radiation belt volume ten times the volume of Jupiter itself. For a one gauss field, the gyrofrequency is about 3 MHz. Since the collision frequency is crudely proportional to the electron density, the collision frequency is taken here as one collision/second at most. For a one-meter radar wavelength, the operating frequency is 300 MHz. Using eq. (8-51), and assuming a radiation belt thickness of two Jupiter radii, the attenuation due to the radiation belts can be shown to be entirely insignificant.

8.2 Support Requirements

8.2.1 System Weight

The dependence of the support requirements upon the radar system design variables discussed above may be determined approximately by analysis of existing design data for spacecraft imaging radar systems. In addition to the design data (91) summarized in Table 8-3 for three similar radar systems, incomplete data is available for three other radar systems. A modified APQ-102 is reported[104] to operate on a 3 cm wavelength with a peak transmitter power of 12.6 kW and a system weight of 80 pounds, excluding antenna and recorder. A JPL design[105] is reported to operate at 1215 MHz with a transmitted power of 3 kW and a system weight of 120 pounds,

excluding antenna and recorder. The azimuth and range resolutions are reported as 150 m and 250 m respectively. Finally, an LMSC design[106] is reported with an antenna size of 26 x 1.5 x 0.33 feet and an antenna weight of 100 pounds. Although the design data given in Table 8-3 refer to coherent radar systems, the weight scaling coefficients will be shown to be the same for non-coherent and coherent systems

Table 8-3

Radar Parameters

System No.	1	2	3
Frequency (GHz)	8	8	8
Altitude (km)	80	80	370
Swath Width (km)	40	40	40
Resolution (m)	15	15	15
Azimuth Aperture (m)	8	8	8
Range Beamwidth (deg)	18.4	13.7	4.8
Antenna Pointing Angle (deg)	35.7	33.3	28.9
Average Transmitted Power (w)	0.5	1.5	16.7
Pulse Width (nanoseconds)	53	450	53
Pulse Repetition Frequency (pps)	4200	4200	4200
Average Input Power (w)	100	100	150
Average Recorder Power (w)	350	350	350
Radar Size (cu. ft.)	7	7	7
Radar Weight (lbs.) (with antenna)	100	100	150
Recorder Size (cu. ft.)	6	6	6
Recorder Weight (lbs.)	60	60	60

The LMSC radar design suggests that spacecraft radar antennas have densities of about 2.5 pounds per square foot of antenna. A recent study[76] implies that antenna densities

of about 1.5 pounds per square foot of aperture are now attainable, and that development of inflatable antennas may result in densities approaching 0.1 pounds per square foot. The mechanically-scanned unfolding antenna constructed by Titus[84] weighs about 0.85 pounds per square foot. The support requirements estimated in this study are based on one pound per square foot, which is assumed accurate (within a factor of two) for all antenna sizes indicated as feasible in Figure 8-2.

To obtain data relating to system weights excluding the antenna, the radar system weights given in Table 8-3 may be modified by subtracting estimated antenna weights. Since the data of Table 8-3 are contemporary with the LMSC design, an antenna density of 2.5 pounds per square foot is assumed. The results of this calculation are given in Table 8-4. In an effort to relate the radar system weight (excluding the antenna) to the system design parameters, it is assumed here that radar system weights increase with increasing peak transmitter power and with increasing wavelength. Figure 8-8 shows the dependence of radar system weight upon the product of peak power and wavelength for the design data available. As previously stated, the APQ-102 has a peak power of 12.6 kilowatts at 3 cm wavelength, while the JPL design indicates a peak power of 3 kilowatts at 25 cm wavelength. The systems described in Table 8-3 all operate at 3.75 cm wavelength, and have peak powers of 2.25, 0.8, and 75 kilowatts for designs 1, 2, and 3, respectively. These peak powers were estimated from the given data by dividing the average transmitted power by the product of the pulse width and pulse repetition frequency. The weight of system #3 appears to be anomalously low. It may be that too much weight was ascribed to the antenna for this system. Curiously, if the reported radar weight for this design given in Table 8-3 does not in fact include the antenna, the data point in Figure 8-8 would fall very close to the

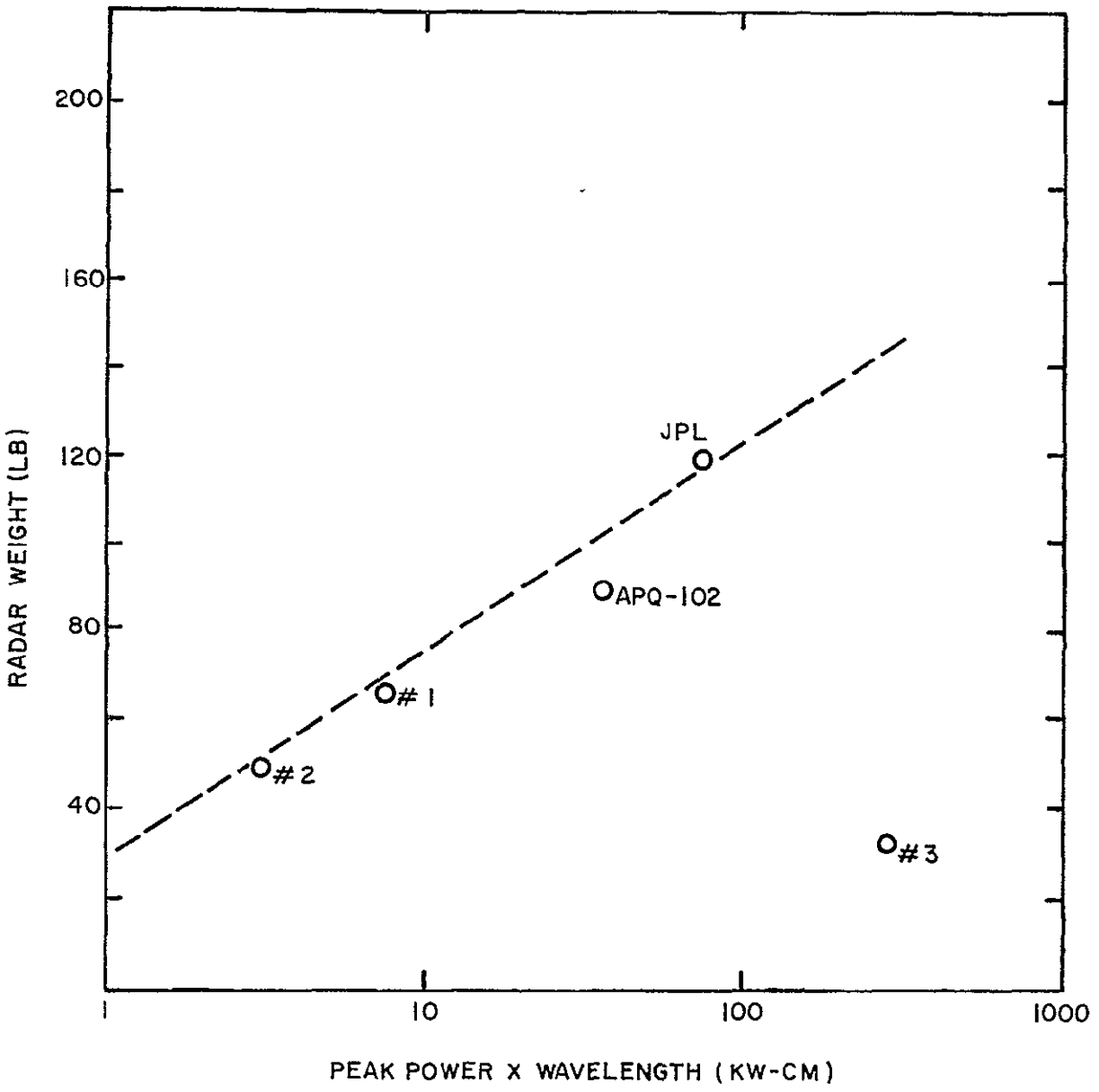

FIGURE 8-8. RADAR SYSTEM WEIGHTS (EXCLUDING ANTENNA)

dashed line. The dashed line appears to be a reasonable fit to the data, and leads to the scaling law for radar weights (excluding antenna and data storage):

$$M_r(\text{lbs}) = 30 + 20 \ln (P_t\lambda) , \qquad (8\text{-}52)$$

where $P_t\lambda$ is in units of kilowatt-centimeters. If the logarithmic term comes out negative, it should be ignored. That is, the minimum radar weight is thirty pounds. This scaling law has been derived from data implying peak powers in the range 1-75 kilowatts and wavelengths in the range 3-25 centimeters, but is probably accurate to within a factor of two or three for values of $P_t\lambda$ from 1 to 1000 kW-cm, except possibly for the combination of high powers (greater than one megawatt) and short wavelengths (less than one centimeter). The total system weight is simply the sum of the radar and antenna weights.

Table 8-4

Antenna Parameters

System No.	1	2	3
Azimuth Aperture, D_a (ft)	26	26	26
Range Beamwidth (°)	18.4	13.7	4.8
Range Aperture, D_r (ft)	0.46	0.72	1.8
Antenna Weight (lb)	30	48	120
Radar Weight (lb) (w/o Antenna)	70	52	30

9.2.2 System Volumes

Limited information has been collected permitting development of an empirical relation between radar weight and radar volume. The density of radar system #1 of Table 8-3

is apparently 70 lb/7 cu ft or 10 lbs/cu ft, while that of system #2 is 52 lbs/7 cu ft or 7.5 lbs/cu ft. The LMSC design yields a density of 150 lbs/5 cu ft or 30 lbs/cu ft. Omitting consideration of system #3, which has been shown to have an anomalously low weight, the average packing density is about 16 lb/cu ft. Thus, the radar system volume may be estimated from the weight according to

$$V_r(\text{cu ft}) = \frac{M_r(\text{lb})}{16} \quad . \tag{8-53}$$

The resulting estimated volumes are probably correct to within a factor of two. Antenna storage volumes may be estimated by noting that the unfolding 24 feet by 40 inch antenna (80 square feet) referred to earlier[84] is stowable in a space 3 by 4 by 9 feet (108 cubic feet). Thus the antenna stowage volume (in cubic feet) is approximately numerically equal to the antenna area (in square feet).

8.2.3 System Power Requirements

The average power required by the radar sensor system may be correlated with the average transmitted power as shown in Figure 8-9. The data points shown are from Table 8-3. The dashed line in the figure is a representation of

$$P_{in} = 100 + 3\,\overline{P} \text{ watts} \quad , \tag{8-54}$$

where P_{in} is the average power demanded by the radar system (excluding a recorder) and $\overline{P}$ is the average transmitted power. Rider and Sung[76] have suggested a similar scaling law, but with a constant term of 300, rather than 100 watts; presumably the 300 watt value includes a power requirement for on-board data conversion and recording. Eq. (8-54) should be valid for all average powers of interest. Although the data leading to eq. (8-54) is confined to coherent systems, the scaling law is expected to be equally valid for noncoherent systems.

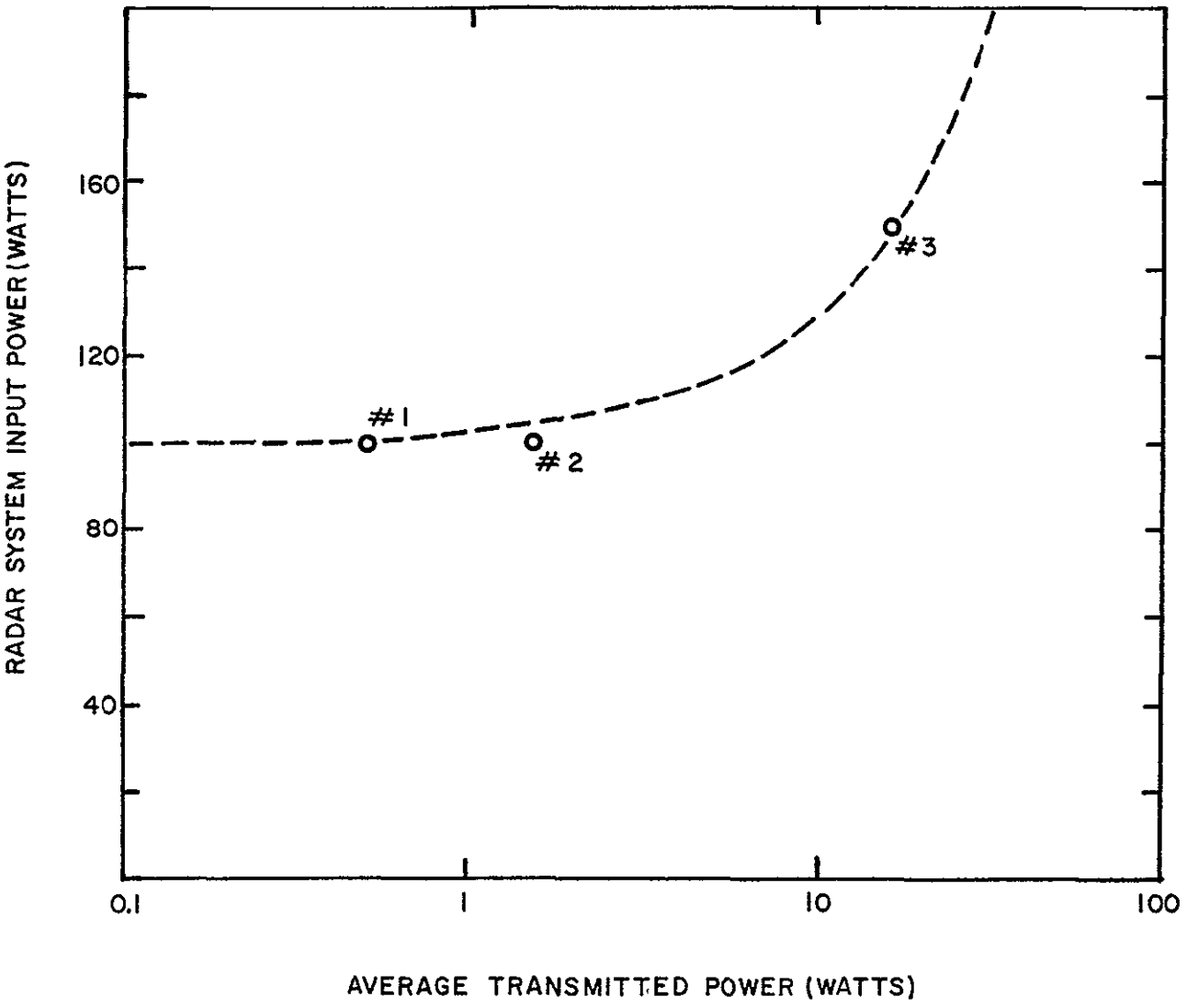

FIGURE 8-9. RADAR SYSTEM POWER REQUIREMENT

8.2.4 Data Acquisition Rate

The swath width W may be regarded as composed of a chain of range resolution elements, each of length $c\tau_c/2 \cos \Psi$, where τ_c is the compressed pulse width, and Ψ is the grazing angle. The azimuthal size of each range resolution element is determined by the antenna azimuth beamwidth, and a new chain of range resolution elements is observed every t_o seconds, where t_o has been given by eq. (8-13). If the accumulated echo from m pulses striking a resolution element is described by G binary bits, the data acquisition rate is approximately

$$DR = \frac{WG}{\bar{r}_r t_o} , \tag{8-55}$$

where $\bar{r}_r$ is the average size of a range resolution element. t_o is analogous to the cycle time as used in describing film or television imaging systems. For 64 shades of grey in the processed imagery, G has the value 6, which has been used for all estimates of data rates in this study.

Since the length of a ground range resolution element is inversely proportional to the grazing angle Ψ, $\bar{r}_r$ is found by averaging 1/cos Ψ over the swath width W. This leads to

$$DR = \frac{2WG(\beta_r^* + 2\delta)}{c\,\tau_c\,t_o \ln\left[\dfrac{\tan \frac{1}{2}\left(\frac{\pi}{2} + \Psi_1\right)}{\tan \frac{1}{2}\left(\frac{\pi}{2} + \Psi_2\right)}\right]} . \tag{8-56}$$

A simpler expression, which yields an upper limit to the data rate, may be obtained by using the smallest range resolution element in eq. (8-55), rather than the average. Thus

$$DR \leq \frac{2WG \cos \Psi_2}{c\,\tau_c\,t_o} \tag{8-57}$$

and similarly, by using the largest range resolution element,

$$DR \geq \frac{2WG \cos \Psi_1}{c \tau_c t_o} \quad . \tag{8-58}$$

A good approximation to the cumbersome eq. (8-56) is

$$DR = \frac{WG}{c\tau_c t_o} (\cos \Psi_1 + \cos \Psi_2) \quad . \tag{8-59}$$

In any event, it has been assumed that data from m pulses is accumulated by on-board integration. If this is not the case, the data rates given above must be multiplied by the factor m.

8.2.5 Pointing

If Δr is the allowable error in location of the principal point of the image, and $\Delta\theta$ is the corresponding error in the antenna pointing angle, then

$$\Delta r = R_s \Delta\theta \quad , \tag{8-60}$$

where R_s is the slant range to the center of the projected image on the ground. Approximating R_s by $\frac{1}{2}(R_1 + R_2)$, where R_1 and R_2 are the slant ranges to the near and far edges, respectively, of the swath width and are given by eqs. (8-14) and (8-5), the allowable error in pointing angle is

$$\Delta\theta = \frac{2 \Delta r}{R_1 + R_2} \quad . \tag{8-61}$$

8.2.6 Platform Stability

Maximum allowable roll and yaw rates may be estimated by assuming that the antenna should not be permitted to roll or yaw farther than one beamwidth during the time required for m pulses to be transmitted and received. Figure 8-3 shows that for all pulse timing modes, the time required to transmit

and receive m pulses is about m/p. Thus the allowable roll rate is

$$\dot{\theta} = \frac{p\,\beta_r}{m} . \tag{8-62}$$

Similarly, the allowable yaw rate is

$$\dot{\phi} = \frac{p\,\beta_a}{m} . \tag{8-63}$$

For m = 1, a more accurate estimate is provided by:

$$\dot{\theta} = \frac{c\,\beta_r}{2R_2 + c\tau} \tag{8-64}$$

$$\dot{\phi} = \frac{c\,\beta_a}{2R_2 + c\tau} . \tag{8-65}$$

8.2.7 State-of-Art Constraints

The most important limitation that the current technological capability places upon the use of noncoherent radar imaging systems for planetary exploration arises from antenna length considerations. Assuming that rms surface deviations of less than $\lambda/15$ are required, and that the maximum antenna length which is currently feasible is about 1.5×10^4 times the allowable surface deviation, then antennas about one thousand wavelengths long are reasonable. There is probably some upper limit independent of wavelength, and five hundred feet has been selected here. It can be shown that an antenna length 1000λ will provide angular resolutions of about 1.5 milliradians. That is, for a 1000 km orbital altitude, the maximum ground resolution which can be hoped for a noncoherent radar system is about 1.5 kilometers. If better performance is required, the most reasonable

solution is to attempt synthetic generation of longer antenna lengths as discussed in the following Section 9.

Receiver state-of-art limits the bandwidth to about ten percent of the operating frequency. This implies that the compressed pulse length must be longer than about ten times the reciprocal of the operating frequency. Since the maximum attainable range resolution is $c\tau_c/2$, at best, the range resolution is limited to about five times the wavelength. Thus for any conceivable orbit altitude, the limiting range resolution is much better than the limiting azimuth resolution. Although the azimuth resolution can be improved by use of a synthetic aperture system, the limiting range resolution cannot be improved upon, except by those advances in the state-of-art which lead to a broader bandwidth capability.

Peak transmitter powers on the order of four megawatts per centimeter of wavelength should be achievable in the very near future. This constraint may be circumvented, when necessary, by using many hits per target (large m) thereby reducing the power in each pulse. Uncompressed pulse lengths of nanosecond duration are possible, but not usually required, since compression ratios of about 200 are possible with current equipment. Pulse repetition frequencies on the order of one million pulses per second appear attainable, and may be required to alleviate the imposition due to peak transmitted power. Finally, Figure 8-5 has summarized system noise figures based on the current state-of-art. These estimates may be conservative in that six dB have been allowed for losses in components other than the receiver.

8.3 Experiment Design Procedure

Figure 8-10 summarizes a logical procedure for the approximate determination of noncoherent radar imaging system design variables and the estimation of experiment support requirements. Figure 8-11 summarizes the scaling laws and design equations. There is a one-to-one correspondence between the numbered boxes in Figure 8-10 and the numbered blocks

in Figure 8-11. The constants incorporated in the equations shown in Figure 8-11 presume use of MKS units.

Image specifications for radar imaging experiments useful in planetary orbital exploration have been provided in Volume I. Those specifications which affect the design of the radar imaging system are enumerated in Figure 8-10. Similarly, Volume III has provided definition of selected orbits which appear to be appropriate for radar imaging experiments. Radar system design is predicated upon a set of image specifications and a specific orbit selection. A small operating wavelength is normally selected in an effort to minimize the required antenna length. At Venus and Jupiter, however, short wavelength systems will not penetrate deeply into the planetary atmosphere. It should also be noted that the peak transmitted power is inversely proportional to the square of the wavelength, hence there is a tradeoff between antenna weight and receiver/transmitter weight which depends upon the wavelength. In cases where high resolution experiments require antenna lengths exceeding the current state-of-art limitations, it is likely that synthetic aperture radar systems can be used to advantage.

Some design iteration may be required to select an appropriate depression angle. The range beamwidth should be oriented below the planetary horizon, but should not include the subsatellite point (where the ground range resolution becomes infinite). To minimize antenna size and weight, the largest possible azimuth and range beamwidths should be used. The azimuth beamwidth is constrained by the desired ground resolution (step #5). The range beamwidth is not constrained, but since the peak transmitted power increases as the square of the range beamwidth, very large range beamwidths should be avoided. In many cases, use of the largest possible azimuth beamwidth and the smallest possible range beamwidth results in a sensor system design which is not far from an optimum

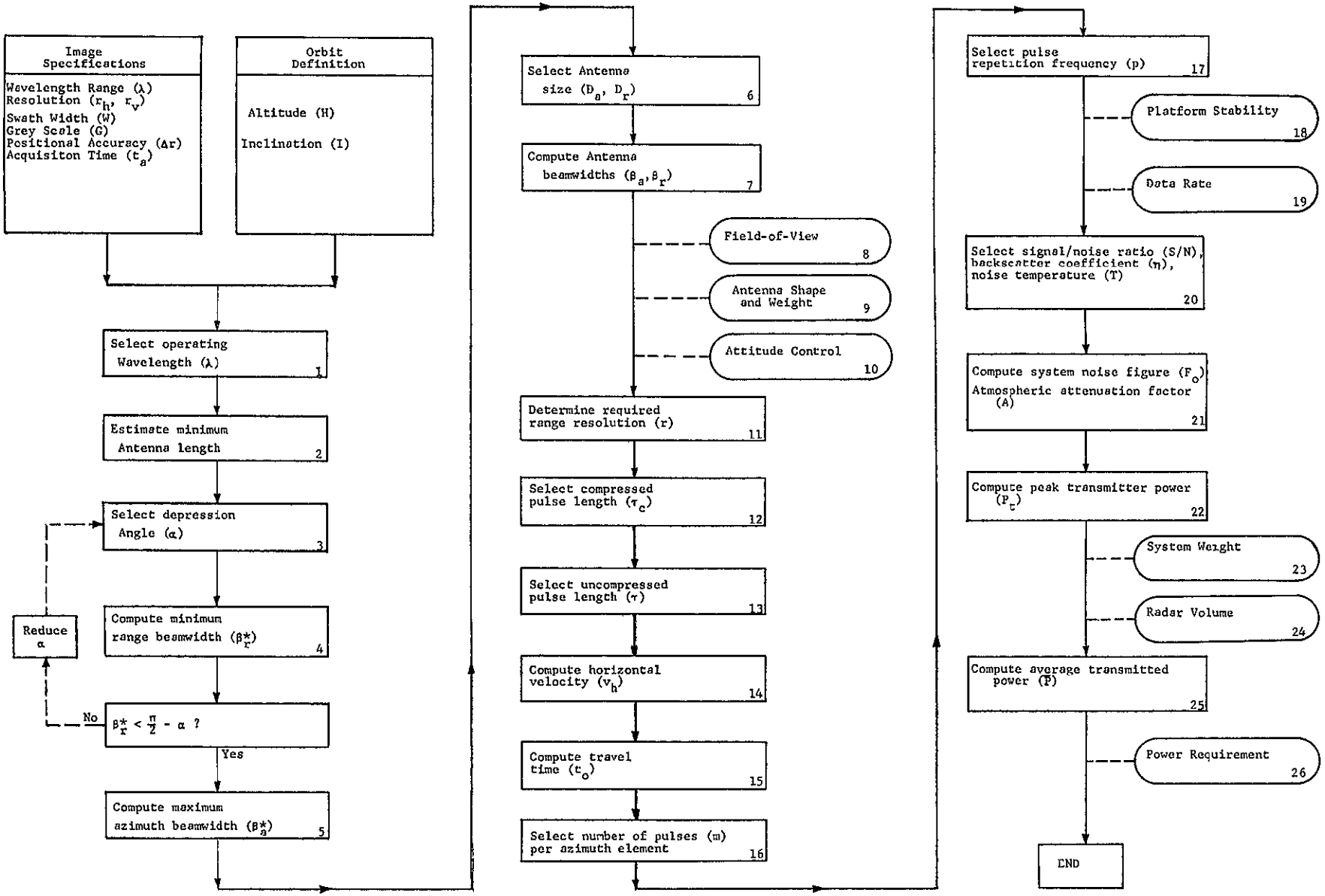

FIGURE 8-10 LOGIC DIAGRAM FOR NONCOHERENT RADAR SYSTEMS

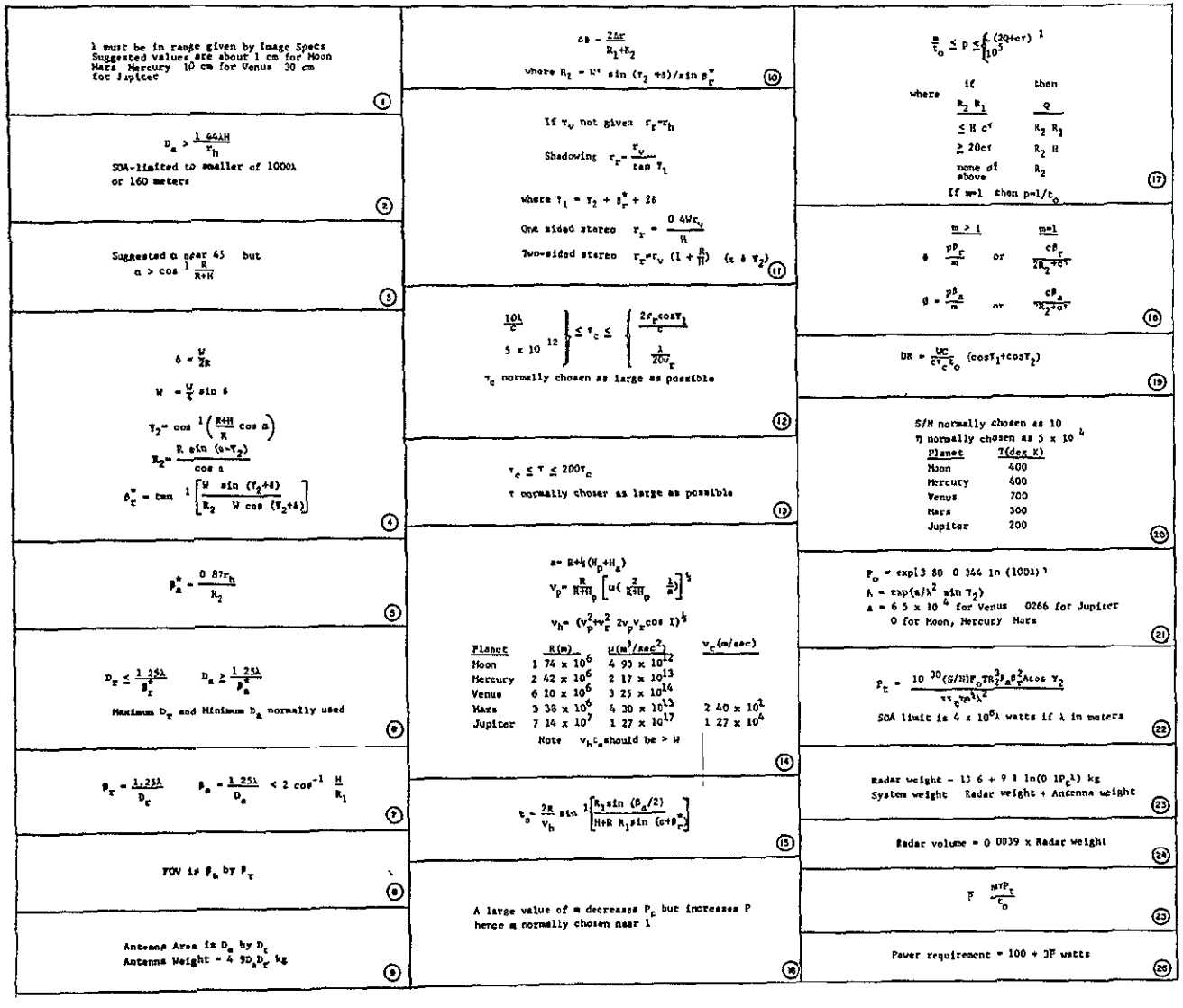

FIGURE 8-11 SCALING LAWS FOR NONCOHERENT RADAR SYSTEMS

NOMENCLATURE
(MKS units used throughout)

a orbit semi major axis
A atmospheric attenuation factor
c speed of light (3×10^8m/sec)
D_a antenna azimuth aperture (length)
D_r antenna range aperture (width)
DR data acquisition rate (bits/sec)
F_o system noise figure
FOV field of view
G bits per resolution element (normally 6)
H sensor system altitude
H_a orbit apoapse altitude
H_p orbit periapse altitude
I orbit inclination
m no. of pulses per azimuth element
p pulse repetition frequency
P average transmitted power
P_t peak transmitted power
r_h desired horizontal ground resolution
r_r ground range resolution
r_v desired vertical ground resolution
R planet radius
R_1 slant range to near edge of swath
R_2 slant range to far edge of swath
S/N signal to noise ratio
SOA state-of-art
T_a maximum acquisition time
T_o observation time per azimuth element
T input noise temperature
v_h apparent horizontal ground speed
v_p ground speed at periapse
v_r planet equatorial rotation speed
W swath width on planet surface
α antenna depression angle
β_a antenna azimuth beamwidth
β_r antenna range beamwidth
β_a^* maximum azimuth beamwidth
β_r^* minimum range beamwidth
ζ half angle of W at planet center
η backscatter coefficient
ΔR maximum antenna pointing error
δr desired positional accuracy
η backscatter coefficient
ζ allowable antenna roll rate
λ operating wavelength
μ planet gravitational constant
τ transmitted pulse length
τ_c compressed pulse length
φ allowable antenna yaw rate
γ_1 grazing angle at near edge of swath
γ_2 grazing angle at far edge of swath

from power and weight considerations. The system field-of-view (step #8), and the antenna shape and weight (step #9) can be estimated once the beamwidths are selected. The attitude control requirement (step #10) depends upon the desired positional accuracy of the image and the slant range.

The range resolution required (step #11) depends upon the manner in which vertical height differences are to be inferred from the imagery. If no vertical height information is required, the ground range resolution is equal to the ground resolution given by the image specifications. If vertical height information is required, the necessary range resolution depends upon whether height differences are to be determined by measurement of radar shadows or stereo parallax. The compressed pulse length (step #12) is normally chosen as large as is consistent with the required range resolution and the Doppler shift due to planet rotation, since the peak transmitted power increases with decreasing pulse length. The uncompressed pulse length (step #13) is simply the compression ratio times the compressed pulse length. Compression ratios as large as 200 are consistent with the current state-of-art.

The apparent ground speed (step #14) is computed in the same manner as for other sensor systems, and is required to estimate the target travel time (step #15). The travel time is the length of time a point target can be observed as it moves through the azimuth beamwidth. The pulse repetition frequency (step #16) must be high enough that at least one pulse is transmitted and received in the time for a target to traverse the azimuth beamwidth. On the other hand, the repetition rate must be low enough to avoid confusion between pulse returns from different portions of the swath width or from different transmitted pulses. Current transmitter capability limits the pulse rate to something on the order of 100,000 pulses per second. The pulse rate,

travel time, and number of pulses processed per azimuth resolution element must be such that the number of pulses is equal to or less than the pulse rate times the travel time. Although the peak transmitted power required decreases as the number of pulses increases, the average transmitted power (and hence the sensor system power requirement) increases with the number of pulses. For noncoherent radar systems, near-minimum weight and power requirements will result if only one pulse per azimuth resolution element is processed. The pulse repetition rate in this case is simply the reciprocal of the travel time.

Estimation of platform stability requirements (step #18) and the data acquisition rate (step #19) is straightforward, as is the selection of the signal-to-noise ratio, backscatter coefficient, and noise temperature (step #20) and the computation of the system noise figure, atmospheric attenuation factor, and the peak transmitted power (steps #21 and #22). Current and near-future transmitter technology limits the peak transmitted power to about four megawatts per centimeter of wavelength. If the computed peak power exceeds this limit, and if the radar system design variables have been chosen in a reasonably skillful manner, the only recourse is to increase the number of pulses per azimuth resolution element (which will increase the system power requirement) or to increase the operating wavelength (which will increase the antenna size and weight). Increasing the wavelength is usually the most effective technique, as this not only reduces the peak power required but increases the limiting capability, but may require antenna lengths in excess of the current state-of-art. If this occurs, the system designer may well consider use of synthetic aperture radar. Once the peak transmitted power is within acceptable bounds, the radar weight (step #23), the radar volume (step #24) excluding the antenna, the average transmitted power (step #25), and the system power requirement (step #26) may be estimated.

A numerical example of this design procedure is provided in Section 6 of Volume I.

9. SYNTHETIC APERTURE RADAR SYSTEMS

9.1 Design Equations

This section develops the mathematical and physical relationships necessary to the design of coherent synthetic aperture radar systems. This analysis considers two modes of operation: the coherent focused mode, and the coherent unfocused mode. Noncoherent processing and operation in the semi-focused mode are not considered, since the analysis presented in this section, and the last section, should provide an adequate guide to the limitations and support requirements of planetary imaging radar systems. Section 9.1 is organized in a similar manner to Section 8.1, and although all the essential relationships are presented here, exposition which would merely repeat that given in Section 8.1 has been omitted. Section 9.2 presents scaling laws which relate support requirements to sensor system design parameters. Since the empirical bases of these scaling laws, and indeed the scaling laws themselves, are identical to those given in Section 8.2, the scaling laws are merely listed, without embellishment, for the convenience of the reader. Finally, Section 9.3 summarizes the design procedure and estimation of support requirements for synthetic aperture radar systems.

9.1.1 Antenna Range Beamwidth

As with the noncoherent radar system, the minimum range beamwidth required to subtend a great-circle arc-length W on the planetary surface is

$$\beta_r^* = \tan^{-1}\left[\frac{W' \sin(\Psi_2 + \delta)}{R_2 - W' \cos(\Psi_2 + \delta)}\right], \qquad (9\text{-}1)$$

where

$$W' = 2R \sin\frac{W}{2R}, \qquad (9\text{-}2)$$

$$\Psi_2 = \cos^{-1}\left(\frac{R+H}{R}\cos\alpha\right) , \tag{9-3}$$

$$\delta = \frac{W}{2R} , \tag{9-4}$$

$$R_2 = \frac{R \sin(\alpha-\Psi_2)}{\cos\alpha} \tag{9-5}$$

with

β_r^* = minimum range beamwidth,
W' = chord length associated with W,
R_2 = slant range to far end of W,
Ψ_2 = grazing angle at far end of W,
δ = planetocentric half-angle subtended by W,
R = planet radius,
α = antenna depression angle.

The depression angle must lie in the range

$$\frac{\pi}{2} - \beta_r^* > \alpha > \cos^{-1}\left(\frac{R}{R+H}\right) , \tag{9-6}$$

in order that power not be wasted by transmitting over the planet horizon, and that adequate range resolution be obtained at the near edge of the swath width.

The antenna height is related to the antenna range beamwidth β_r by

$$D_r = \frac{1.25\,\lambda}{\beta_r} , \tag{9-7}$$

where D_r is the antenna height, and λ is the operating wavelength.

9.1.2 Synthetic Aperture Length

Superior angular resolution is achieved in a synthetic aperture radar system by synthetically creating a large linear antenna. The resulting angular (azimuth) resolution can be much

narrower than the angular dimensions of the azimuth beamwidth emanating from the real antenna azimuth aperture. Since the antenna is moving along a known path with respect to the target, the real antenna becomes a new element of the synthetically-generated antenna with each pulse transmission. In the focused mode, a phase shift is applied to each pulse return to account for the fact that the received wave is spherical rather than planar. The azimuth resolution in the focused mode is[107] approximately

$$r_a = \frac{\lambda R_s}{2 D_{sa}} , \tag{9-8}$$

where r_a is the length of an azimuth resolution element. R_s is the slant range, and D_{sa} is the length of the synthetic aperture. Although eq. (9-8) implies that the azimuth resolution degrades (increases) with range, it will be shown below that D_{sa} can be made to increase linearly with range, and hence the azimuth resolution remains constant with range. If m pulses are processed to create the synthetic array, and if d is the distance moved by the real antenna between pulse transmissions, then

$$D_{sa} = m\, d . \tag{9-9}$$

If v_h is the relative antenna-target velocity along the heading line, and if p is the pulse repetition frequency, d is simply v_h/p. Substituting eq. (9-9) into eq. (9-8),

$$r_a = \frac{\lambda\, p\, R_s}{2\, m\, v_h} \tag{9-10}$$

which implies that the azimuth resolution degrades with slant range. To achieve a constant azimuth resolution throughout the swath width, the signal return data is usually processed

so that m increases linearly with slant range. If r is the desired ground resolution, eq. (9-10) indicates that

$$m \geq \frac{\lambda\, p\, R_s}{2\, r\, v_h} \qquad (9\text{-}11)$$

in order to achieve the desired resolution. An upper limit on m arises from the need to observe the target continuously, as will be shown later.

For an unfocused system, the pulse return is not corrected to account for non-planarity of the returning wave. Therefore, the round-trip distance from the ends of the synthetic aperture to the target should be no more than one-quarter wavelength greater than the round-trip distance from the center of the synthetic aperture to the target. Thus the synthetic aperture length which can be used in a unfocused system is approximately

$$D_{sa} \leq (R_s \lambda)^{\frac{1}{2}} . \qquad (9\text{-}12)$$

Use of eq. (9-8) shows that the best azimuth resolution which can be achieved is then

$$r_a \geq \tfrac{1}{2}(R_s \lambda)^{\frac{1}{2}} . \qquad (9\text{-}13)$$

Eq. (9-11) is valid for either a focused or unfocused system. However, for an unfocused system, m is constrained by

$$m \leq \frac{p}{v_h} (R_s \lambda)^{\frac{1}{2}} , \qquad (9\text{-}14)$$

which follows from eq. (9-9) and (9-12).

9.1.3 Pulse Length

Pulse compression techniques can be used with synthetic aperture systems, just as with real aperture systems.

As discussed in Section 8.1.3 above, if the ground resolution r is desired throughout the swath width, the compressed pulse length τ_c must satisfy

$$\tau_c \leq \frac{2r \cos \Psi_1}{c} , \tag{9-15}$$

where

$$\Psi_1 = \Psi_2 + \beta_r^* + \frac{W}{R} . \tag{9-16}$$

Current limitations on transmitter state-of-art limits the uncompressed pulse length to about one nanosecond. Since compression ratios of 200 appear attainable, the compressed pulse length is limited to about 5×10^{-12} seconds. However, receiver technology constrains the receiver bandwidth to something on the order of ten percent of the operating frequency, which implies that

$$\tau_c \geq \frac{10 \lambda}{c} . \tag{9-17}$$

For one cm wavelength, this limits the compressed pulse length to greater than about one-third nanoseconds.

For rotating planets, the pulse length may be constrained by the allowable Doppler shift due to target motion associated with the planet rotation. Assuming that a shift of ten percent of the receiver bandwidth is acceptable,

$$\tau_c \leq \frac{0.05 \lambda}{v_r} . \tag{9-18}$$

For Mars and Jupiter, this may be a more stringent limitation than the resolution constraint expressed by eq. (9-15).

9.1.4 Pulse Repetition Frequency

As with real aperture systems, the highest pulse rate can be achieved if the swath width return of the n^{th} pu occurs between transmission of the n + 1st pulse and its sid lobe return (see Figure 8-3b). That is, if

$$R_2 - R_1 \leq H - c\tau \ , \qquad (9\text{-}1$$

then

$$p \leq \frac{c}{2(R_2 - R_1) + c\tau} \ . \qquad (9\text{-}2$$

If the pulse transmission time (taken as 2τ to allow for switching time) is short enough, say five percent of the swa width return time, i.e., if

$$R_2 - R_1 \geq 20\, c\tau \ , \qquad (9\text{-}2$$

then little loss of signal return results if the transmissio time blocks out the pulse reception. In this case, the puls rate must satisfy

$$p \leq \frac{c}{2(R_2 - H) + c\tau} \ . \qquad (9\text{-}2$$

Finally, if the pulse transmissions and swath returns are no intermixed,

$$p \leq \frac{c}{2R_2 + c\tau} \ . \qquad (9\text{-}2$$

It will be shown below that for synthetic aperture systems, the minimum antenna length is inversely proportional to the pulse repetition frequency. Pulse rates approaching 10^6 per second are attainable with the current state-of-art.

9.1.5 Antenna Azimuth Beamwidth

The antenna length D_a is related to the azimuth beamwidth β_a by

$$D_a = \frac{1.25\,\lambda}{\beta_a} \qquad (9\text{-}24)$$

During creation of the synthetic aperture, the real antenna travels the distance d between pulses. Angular ambiguities will result if $d - D_a$ is not small enough that the sidelobe of the synthetic aperture gain pattern falls outside the main lobe of the real aperture gain pattern. Greenberg[107] has shown that such angular ambiguities will be eliminated if

$$D_a \geq \frac{4\,v_h}{p} \,. \qquad (9\text{-}25)$$

To eliminate Doppler ambiguities,

$$D_a \geq \frac{2\,K_2\,v_h}{p} \qquad (9\text{-}26)$$

which is automatically satisfied if eq. (9-25) is observed, since K_2 is about 1.25.

The time required for a target to move through the real aperture beamwidth β_a is approximately[92]

$$t_o = \frac{2R}{v_h} \sin^{-1}\left[\frac{R_s \sin(\beta_a/2)}{H + R - R_s \sin \alpha_s}\right] , \qquad (9\text{-}27)$$

where R_s is the slant range (not to be confused with the planet radius R), and α_s is the depression angle corresponding to R_s. In order to transmit and receive m pulses from a target, the real aperture beamwidth must be broad enough that, approximately,

$$\frac{m}{p} \leq \frac{2R}{v_h} \sin^{-1}\left[\frac{R_s \sin(\beta_a/2)}{H + R - R_s \sin\alpha_2}\right] . \qquad (9\text{-}28)$$

Rearranging,

$$\beta_a \geq 2 \sin^{-1}\left[\frac{H + R - R_s \sin\alpha_s}{R_s} \cdot \sin\frac{m v_h}{2 p R}\right] . \qquad (9\text{-}29)$$

For a flat planet, $R_s \sin\alpha_s$ is equal to H. Then by taking the sines and arcsines equal to their arguments, one arrives at the approximate condition:

$$\beta_a \geq \frac{m v_h}{p R_s} . \qquad (9\text{-}30)$$

If m is chosen to increase linearly with R_s, as is usually the case, the minimum azimuth beamwidth is independent of range. Eq. (9-30) may be rewritten in terms of the antenna length D_a, and the resulting contraint may be combined with eq. (9-25) to show that the antenna length must lie in the approximate range

$$\frac{4 v_h}{p} \leq D_a \leq \frac{1.25 R_2 \lambda p}{m v_h} , \qquad (9\text{-}31)$$

provided that m is the number of pulses processed for targets at the far edge of the swath (at range R_2).

The right-hand-side of this inequality may be related to the achieved azimuth resolution at slant range R_2. Using eq. (9-10),

$$r_a = \frac{\lambda p R_2}{2m v_h} \qquad (9\text{-}32)$$

for the azimuth resolution at R_2. The inequality expressed by eq. (9-31) then yields

$$r_a \geq \frac{D_a}{2} , \qquad (9\text{-}33)$$

if the constant K_2 (occuring in $D_a = K_2\lambda/\beta_a$) is taken as unity rather than 1.25. Eq. (9-33) is the expression usually seen[107] for the limiting azimuth resolution of a synthetic aperture system. Although it might appear from eq. (9-33) that the resolution can be improved without bound simply by decreasing the real antenna length, eq. (9-31) has shown that this cannot be done without limit, since D_a is constrained. It is seen however, that using the maximum possible pulse rate permits a shorter antenna, and hence a better azimuth resolution.

A final restriction on the antenna length results from requiring that the specular return from the planet surface directly beneath the spacecraft not interfere with the swath width return, as discussed in Section 8.1.4. Rewritting eq. (8-28) in terms of the antenna length,

$$D_a > 2.5 \lambda \cos^{-1} \left(\frac{H}{R_1}\right) . \qquad (9\text{-}34)$$

In addition to the operational constraints discussed above, the antenna length is subject to state-of-art limitations. As discussed in Section 8.1.2, the maximum feasible antenna length is taken here as 1000 λ, except that antennas longer than 500 feet are regarded as impractical at any wavelength.

9.1.6 Transmitted Power

An expression for the peak transmitted power may be derived in a manner virtually identical to that used in Section 8.1.5. However, in integrating m pulses coherently, the signal-to-noise ratio in the processed data varies linearly with m. The peak transmitted power is then

$$P_t = \frac{2.35 \times 10^{-30}(S/N)\, F_o T(B\tau_c)\, v_h\, R_2^3\, \beta_a^2\, \beta_r^2 \cos \Psi_2 \cdot e^{2\rho R_2}}{p\, \tau\, \tau_c\, \eta\, \lambda^3} \qquad (9\text{-}35)$$

in MKS units, where

(S/N)	=	signal-to-noise ratio,
F_o	=	system noise figure,
T	=	input noise temperature ,
B	=	receiver noise bandwidth,
ρ	=	atmospheric attenuation coefficient,
η	=	backscatter coefficient,

and the other symbols have been defined previously. The peak transmitted power has been evaluated at the slant range to the far edge of the swath width, since the power increases with slant range.

The evaluation of the quantities listed above has been discussed in Sections 8.1.6 through 8.1.8. To summarize, a value of ten is recommended for the signal-to-noise ratio, the system noise figure is approximated according to

$$\ln F_o = 3.80 - 0.344 \ln \lambda , \qquad (9\text{-}36)$$

for λ in centimeters, and the input noise temperature is taken as the maximum expected planetary temperature. Values have been given in Table 8-2. For a matched system, the product $B\tau_c$ is unity. The backscatter coefficient is about 5×10^{-4}, while the atmospheric attenuation factor is

$$2\rho R_2 = \frac{6.5}{\lambda^2 \sin \Psi_2} \qquad (9\text{-}37)$$

for Venus, and

$$2\rho R_2 = \frac{266}{\lambda^2 \sin \Psi_2} \qquad (9\text{-}38)$$

for Jupiter, where again λ is in centimeters. Atmospheric attenuation is neglected for the Moon, Mars, and Mercury.

The average transmitted power is

$$\overline{P} = \frac{m\tau}{t_o} P_t , \qquad (9\text{-}39)$$

where m is the number of transmitted pulses in the time t_o. The value of m must be large enough to provide the desired resolution at the range R_2, while t_o is the time required for a target at R_1 to travel through the real antenna azimuth beamwidth.

9.2 Support Requirements

The dependence of sensor system support requirements upon the system design variables of synthetic aperture radar systems are identical to that of real aperture noncoherent radar systems, and are summarized here for the convenience of the reader. A complete discussion has been given in Section 8.2.

The antenna weight is estimated by assuming an antenna density of one pound per square foot of antenna aperture. This estimate should be accurate within a factor of two for all antennas of feasible size. The radar system weight (excluding the antenna and elaborate data processing equipment) is estimated by

$$M_r(\text{lbs}) = 30 + 20 \ln (P_t\lambda), \qquad (9\text{-}40)$$

where $P_t\lambda$ is in kilowatt-centimeters. This estimate should be accurate within a factor of two or three for values of $P_t\lambda$ in the range from 1 to 1000.

The volume (in cubic feet) required for antenna stowage is taken as numerically equal to the antenna aperture area (in square feet). The radar system volume, excluding the antenna, is approximately

$$V_r(\text{cu ft}) = \frac{M_r(\text{lbs})}{16} \quad . \tag{9-41}$$

The radar system power requirement is

$$P_{in} = 100 + 3\,\overline{P} \text{ watts}, \tag{9-42}$$

which should be valid for all average powers of interest. The data acquisition rate is approximately

$$DR = \frac{m\,W\,G}{c\,\tau_c\,t_o}\,(\cos\,\Psi_1 + \cos\,\Psi_2) \quad , \tag{9-43}$$

where G is the number of binary bits per resolution element (taken as six in this study). A more accurate expression is given by eq. (8-58), which should be multiplied by m for application to synthetic aperture systems. It is assumed here that the elaborate data processing required for synthetic aperture systems is <u>not</u> performed on board the spacecraft.

The antenna pointing requirement is approximately

$$\Delta\theta = \frac{2\,\Delta r}{R_1 + R_2} \quad , \tag{9-44}$$

where Δr is the allowable ground error in location of the image center. The allowable roll rate is

$$\dot{\theta} = \frac{p\,\beta_r}{m} \quad , \tag{9-45}$$

while the allowable yaw rate is

$$\dot{\phi} = \frac{p\,\beta_a}{m} . \qquad (9\text{-}46)$$

System constraints arising from current technological capabilities have been mentioned throughout the preceeding section, wherever appropriate. A summary of such limitations has been given in Section 8.2.7. The limitations are equally applicable to synthetic aperture systems.

9.3 Experiment Design Procedure

A suggested logical procedure for the design of space-orbital synthetic aperture radar imaging systems is summarized in Figure 9-1. The design equations and scaling laws are summarized in Figure 9-2, which is designed for use with the logic diagram. The design procedure down through selection of the pulse length is similar to the noncoherent radar system design procedure. The selection of the pulse repetition frequency and the minimum number of pulses processed per azimuth resolution element is handled in a somewhat different manner because the minimum antenna length is now inversely proportional to the pulse repetition frequency. For this reason, and also because the peak transmitted power is also inversely proportional to the pulse rate, a convenient initial design choice is to select the maximum possible pulse repetition frequency (step #7). The minimum number of pulses required is estimated (step #9). For unfocused systems, there is also a maximum number of pulses which can be processed properly. The design value selected for the number of pulses should be close to the minimum value, as this will minimize the data acquisition rate. That is, there appears to be no reason why more pulse returns should be processed than is absolutely necessary, for a fixed pulse repetition frequency.

The constraints upon antenna length are evaluated (step #10) and a nominal value chosen for the antenna length.

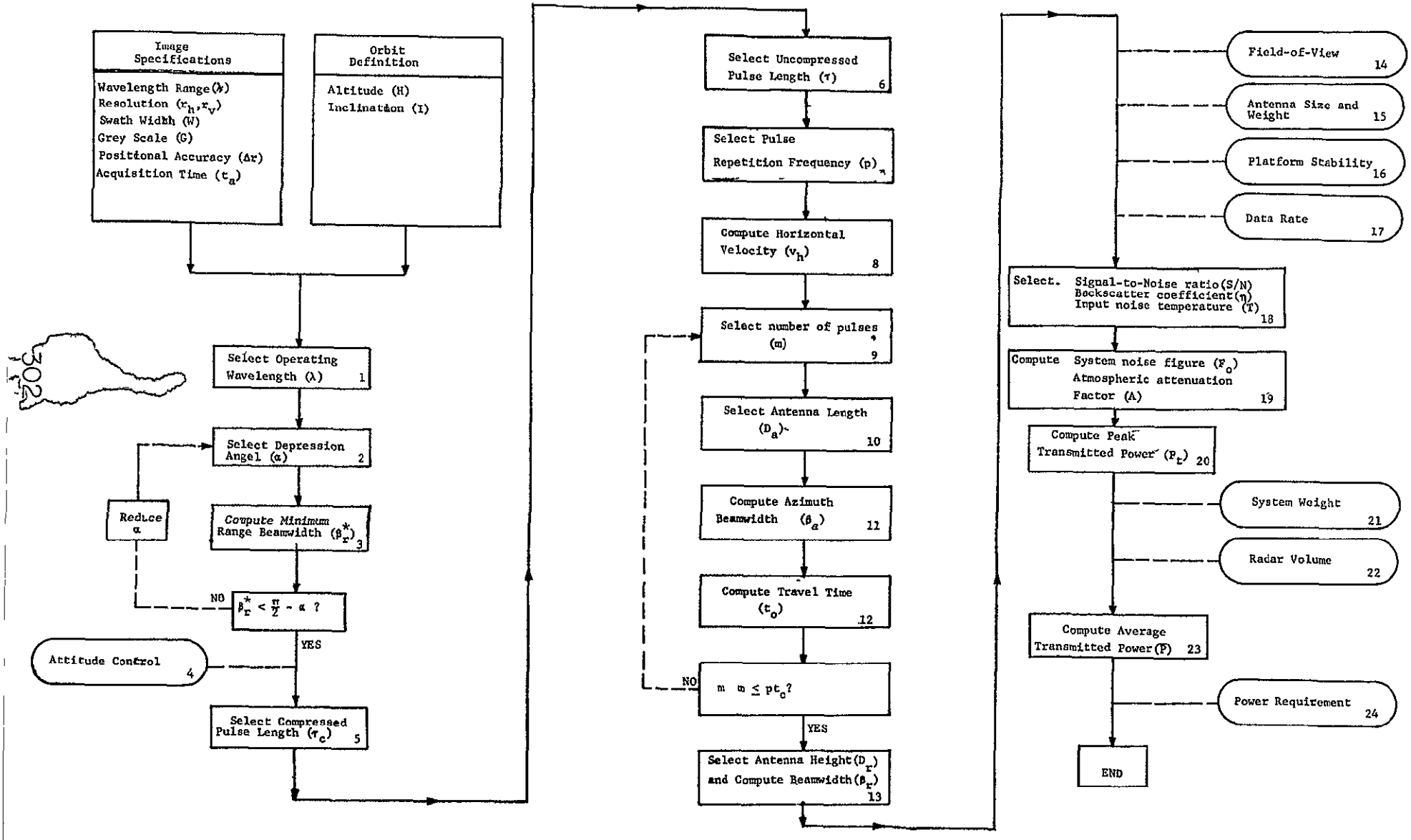

FIGURE 9-1 LOGIC DIAGRAM FOR SYNTHETIC APERTURE RADAR SYSTEMS

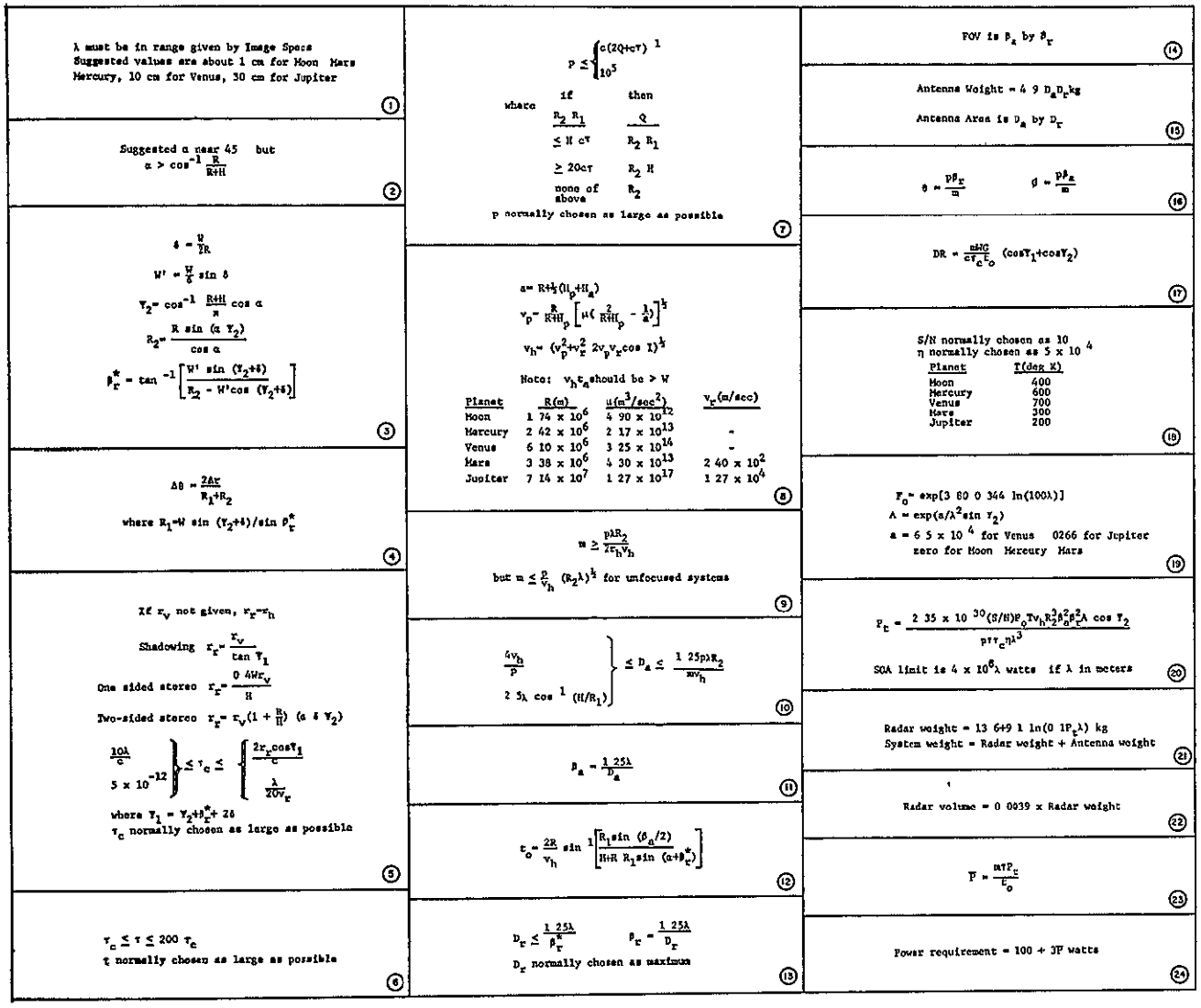

FIGURE 9-2 SCALING LAWS FOR SYNTHETIC APERTURE RADAR SYSTEMS

NOMENCLATURE

(MKS units used throughout)

a orbit semi major axis
A atmospheric attenuation factor
c speed of light (3×10^8 m/sec)
D_a-antenna azimuth aperture (length)
D_r antenna range aperture (width)
DR data acquisition rate (bits/sec)
F_o-system noise figure
FOV field of view
G bits per resolution element (normally 6)
H sensor system altitude
H_a orbit apoapse altitude
H_p orbit periapse altitude
I orbit inclination
m no. of pulses per azimuth element
p pulse repetition frequency
$\bar{P}$ average transmitted power
P_t peak transmitted power
r_h desired horizontal ground resolution
r_r ground range resolution
r_v desired vertical ground resolution
R planet radius
R_1 slant range to near edge of swath
R_2 slant range to far edge of swath
S/N signal to noise ratio
SOA state of art
t_a maximum acquisition time
t_o observation time per azimuth element
T input noise temperature
v_h apparent horizontal ground speed
v_p ground speed at periapse
v_r planet equatorial rotation speed
W swath width on planet surface
α antenna depression angle
β_a-antenna azimuth beamwidth
β_r antenna range beamwidth
β_a^* maximum azimuth beamwidth
β_r^* minimum range beamwidth
δ half angle of W at planet center
Δθ maximum antenna pointing error
Δr-desired positional accuracy
η backscatter coefficient
θ allowable antenna roll rate
λ-operating wavelength
μ-planet gravitational constant
τ transmitted pulse length
τ_c compressed pulse length
β-allowable antenna yaw rate
γ_1-grazing angle at near edge of swath
γ_2-grazing angle at far edge of swath

State-of-art constraints on the antenna length have been provided in Figure 9-2. If the maximum pulse repetition frequency has been chosen in step #7, the minimum antenna length computed in step #10 is an absolute minimum. That is, no amount of design iteration will result in smaller antenna lengths. If it appears that the minimum antenna length will result in a light antenna weight, the design value actually selected for the antenna length may be increased, as this will reduce the peak transmitted power and also the radar weight (excluding the antenna). After the target travel time is estimated (step #12), the number of pulses transmitted during the travel time should be compared to the number of pulses which must be processed. If an insufficient number of pulses are transmitted, either the travel time must be increased, or the number of pulses processed must be reduced. Increasing the pulse rate is usually not of much use, since the number of pulses which must be processed increases linearly with the pulse rate. The travel time may be increased by broadening the antenna azimuth, which requires decreasing the antenna length. The number of pulses which must be processed can be reduced by decreasing the wavelength. However, this will also reduce the peak power which can be transmitted (at the current state-of-art) and may increase substantially the amount of atmospheric absorption at Venus and Jupiter.

Once a consistent set of values has been selected for the pulse rate, the number of processed pulses, the travel-time, and the antenna size, the design proceeds as for noncoherent radar systems. The required peak transmitted power is estimated using a slightly different formula than for noncoherent systems. If the required peak power exceeds four megawatts per centimeter of operating wavelength, the required power may be reduced by decreasing the antenna beamwidths (which will, of course, increase the antenna size and weight), increasing the operating wavelength (which will also increase the antenna size and weight), or by increasing the pulse

repetition frequency (which will increase the minimum number of processed pulses). The estimation of the remaining support requirements is performed exactly as for noncoherent systems. A numerical design example is given in Volume I, Section 6.

REFERENCES

1. Widger, W. K., Jr.: Orbits, Altitudes, Viewing Geometry, Coverage, and Resolution Pertinent to Satellite Observations of the Earth and its Atmosphere. Proceedings of the Fourth Symposium on Remote Sensing of Environment, Report No. 4864-11-X, Infrared Physics Lab., Univ. of Michigan, 1966, pp. 489-537.

2. Jensen, J.; Townsend, G.; Kork, J.; and Kraft, K,: Design Guide to Orbital Flight. McGraw-Hill Book Co., Inc., 1962.

3. Robinson, N.: Solar Radiation. Elsevier Publishing Co., 1966.

4. Burkhard, D. G.; and Ashby, N.: Study of Radiative Aspects of Lunar Materials. NASA CR-61481, 1967.

5. Rennilson, J. J.; Holts, H. E.; and Morris, E. C.: In Situ Measurements of the Photometric Properties of an Area on the Lunar Surface. J. Opt. Soc. Am., Vol. 58, No. 6, June 1968, pp. 747-755.

6. Orlova, N. S.; Akad. Nauk. Astro. Zh., vol. 33, no. 1, 1956.

7. Hapke, B.: A Theoretical Photometric Function for the Lunar Surface. J. Geophys. Res., vol. 68, no. 15, 1 Aug. 1963, pp. 4545-4570.

8. Hapke, B.: An Improved Theoretical Lunar Photometric Function. Astron. J., vol. 71, no. 5, June 1966, pp. 333-339.

9. Harris, D. L.: Photometry and Colorimetry of Planets and Satellites. Planets and Satellites, G. P. Kuiper and B. M. Middlehurst, ed., Univ. of Chicago Press, 1961, pp. 272-342.

10. Danjon, A.: Bull. Astro., vol. 14, 1949, p. 315ff.

11. de Vaucouleurs, G.: Geometric and Photometric Parameters of the Terrestrial Planets. Icarus, vol. 3, Sept. 1964, pp. 187-235.

12. Tull, R. G.: The Reflectivity Spectrum of Mars in the Near-Infrared. Icarus, vol. 5, no. 5, Sept. 1966, pp. 505-514.

13. Jenkins, E. B.; et. al.: Rocket Spectra of Venus and Jupiter from 2000 to 3000 A. Princeton University publication, 1968.

14. Stecher, T. P.: Ultraviolet Reflectivity of Jupiter. Astrophys. J., vol. 142, no. 3, 1 Oct. 1966, pp. 1186-1190.

15. Hayakawa, S.; et. al.: Infrared Observations of the Moon. Icarus, vol. 9, no. 2, Sept. 1968, pp. 357-359.

16. Binder, A. B.; and Jones, C. J.; personal communication, IIT Research Institute, Chicago, Illinois.

17. Kruse, P. W.; McGlauchlin, L. D.; and McQuistan, R. B.: Elements of Infrared Technology: Generation, Transmission, and Detection. John Wiley and Sons, Inc., 1962.

18. Wolfe, W. L., ed.: Handbook of Military Infrared Technology, U. S. Government Printing Office, 1965.

19. Holter, M. R.; et. al.: Fundamentals of Infrared Technology, Macmillan Co., 1962.

20. Chase, R. H.; and Kaisler, F. J.: Problems Associated with High-Speed Scanning. Proc. IRIS, vol. 5, no. 1, Jan. 1960, pp. 515-522.

21. Heath, D. F.; and Sacher, P. A.: Effects of a Simulated High Energy Electron Space Environment on the Ultraviolet, Transmittance of Optical Materials between 1050 and 3000 A. NASA TM X-55337, 1965.

22. Eberhardt, E. H.: Noise in Multiplier Phototubes. Application Note E-8, ITT Industrial Labs., Fort Wayne, Ind., 1965.

23. Anon.: Threshold Sensitivity and Noise Rating of Multiplier Phototubes. Application Note E-2, ITT Industrial Labs., Fort Wayne, Ind., 1964.

24. Jamieson, J. A.: Infrared Physics and Engineering. McGraw-Hill Book Co., Inc., 1963.

25. Van Slyke, N. E.: A Compendium of Optical Radiation Detectors. Mis. Publ. MP-67-13, (ASTIA No. AD 659986), U. S. Naval Missile Center, Point Mugu, Calif., 1967.

26. Schultz, M. L.; and Harty, W. E.: Solid State Ultraviolet Photodetectors. Tech. Report AFAL-TR-68-112, (ASTIA No. AD 836667), Air Force Avionics Lab., Air Force Systems Command, Wright-Patterson Air Force Base, Ohio, 1968.

27. Hawkins, J. A.: Generalized Figures of Merit for Infrared Imaging Systems. Report No. DRL-TR-68-12, (ASTIA No. AD 832158), Defense Research Lab., Univ, of Texas, Austin, 1968.

28. Smith, C. V.; and Wood, R. W.: High Performance Aircraft Defense Techniques, Vol. III, A Theoretical and Experimental Investigation of Laser Illuminated Imaging. Tech. Report AFAL-TR-65-322, (ASTIA No. AD 479986), Air Force Avionics Lab., Air Force Systems Command, Wright-Patterson Air Force Base, Ohio, 1966.

29. Slater, P. N.; and Johnson, G.: A Study of Photographic and Spectrometric Subsystems for Voyager. Tech. Memo. S-1, Astro Sciences Center, IIT Research Institute, Chicago, 1965.

30. Bashe, R.; and Kennedy, S.· Martian Orbital Photographic Study, Technical Summary Report. NASA CR-61854, 1967.

31. Published data from Cook Electric Co., Tech-Center Div., Morton Grove, Ill.

32. Dornin, W. A.; personal communication, Univ. of Colorado.

33. Anon.: Chopperless Infrared Sensors Developed. Aerospace Technology, 15 Jan. 1968, pp. 44-45.

34. Malling, L. R.: Space Photography and Colorimetry. Space Programs Summary No. 37-28, Vol. IV, Supporting Research and Development, Jet Propulsion Lab., California Inst. of Tech., Aug. 1964, pp. 95-100.

35. Smith, J. T., Jr., ed.· Manual of Color Aerial Photography. Amer. Soc. of Photogrammetry, Fallo Church, Va., 1968.

36. Rose, A.: The Sensitivity Performance of the Human Eye on an Absolute Scale. J. Opt. Soc. Am., vol. 38, no. 2, Feb. 1948, pp. 196-205.

37. Morton, G. A.: Image Intensifiers and the Scotoscope. Appl. Opt., vol. 3, no. 6, June 1964, pp. 651-672.

38. Sadashige, K.: Image Intensifier TV Camera System, its Performance and Applications. Appl. Opt., vol. 6, no. 12, Dec. 1967, pp. 2179-2190.

39. Scott, R. M.: Contrast Rendition as a Design Tool. Photographic Sci. and Engr., vol. 3, no. 5, Sept. 1959, pp. 201-209.

40. Hall, H. J.; and Howell, H. K., ed: Photographic Considerations for Aerospace. Itek Corp., Lexington, Mass., 1965.

41. Anon.: RCA Vidicons. Report CAM-700, Electronic Components and Devices Div., Radio Corporation of America, Harrison, N. J.

42. Anon.: WX-30654 SEC Camera Tube. Report TD 86-820, Electronic Tube Div., Westinghouse Electric Corp., Elmira, N. Y., 1968.

43. Anon.: Space Television Cameras Data Sheet. Astro Electronics Div., Radia Corporation of America.

44. Van Buren, R.: Mariner Mars 1964 Handbook. NASA CR-80953, 1965.

45. Montgomery, D. R.; and Wolf, F. J.: The Surveyor Lunar Landing Television System. IEEE Spectrum, vol. III, no. 8, Aug. 1966, pp. 54-61.

46. Schutz, F. L.; et al.: Mariner Mars Science Subsystem. NASA CR-77906, 1966.

47. Kindt, D. H.; and Staniszewski, J. R.: The Design of the Ranger Television System to Obtain High-Resolution Photographs of the Lunar Surface. Tech. Report 32-717, Jet Propulsion Lab. Calif. Inst. of Tech., 1965.

48. Becker, R. A.: Design and Test Performance of Mariner IV Television Optical System. Tech. Report 32-773, Jet Propulsion Lab., Calif. Inst. of Tech., 1965.

49. Campen, C. F.; and Stallkamp, J. A.: Preliminary Study of Effects of Spacecraft and Orbit Parameters on Voyager Orbiter Photographic Experiments. Unpub. report, Jet Propulsion Lab., Calif. Inst. of Tech., 1965.

50. Crane, R., Jr.: An Experimental Twenty-inch Segmented Active Mirror. IEEE Trans. on Aerospace and Electronic Systems, vol. 5, no. 2, March 1969, pp. 323-329.

51. Anon.: A Study of Jupiter Flyby Missions, Final Technical Report. Report FZM-4625, Fort Worth Div., General Dynamics Corp., 1966.

52. Anon.: Study of Applicability of Lunar Orbiter Subsystems to Planetary Orbiters. NASA CR-66302, 1967

53. Bashe, R.; and Schwartz, I.: Planetary Film Reconnaissance System. NASA CR-1358, 1969.

54. Anon.: Airborne Photographic Equipment, Volume I-Cameras, Magazines, and Mounts. Report RC-013200(1), Air Force Avionics Lab., Air Force Systems Command, Wright-Patterson Air Force Base, Ohio, 1965.

55. Hill,C. W.; Ritchie, W. B.; and Simpson, K. M., Jr.: Data Computation and Evaluation of Space Shielding Problems: Volume III, Radiation Hazards in Space. Report ER-7777, Lockheed Nuclear Products, Lockheed-Georgia Co., 1966.

56. Watts, H. V.; and Lewis, J. C.: Effects of Nuclear Radiation on the Sensitometric Properties of Reconnaissance Films. Report AFAL-TR-65-113, Air Force Avionics Lab., Air Force Systems Command, Wright-Patterson Air Force Base, Ohio, 1965.

57. Kolsofsky, L. J.; and Broome, G. C.: Lunar Orbiter-A Photographic Satellite. NASA TM X-56207, 1965.

58. Anon.: Study of the Lunar Orbiter Regarding Its Adaptability to Other Scientific Investigations. NASA CR-66448, 1967.

59. Shephard, O.; and Davidson, G.: An Infrared Skymapper System. Report AFCRL-66-250, (ASTIA No. AD 482524), Air Force Cambridge Research Labs., Bedford, Mass., 1966.

60. Anon.: Improved Forward-Looking Infrared Reconnaissance Detector-Cooler and Display Components Development. Report AFAL-TR-68-88 (Confidential), (ASTIA No. AD 390220), Air Force Avionics Lab., Air Force Systems Command, Wright-Patterson Air Force Base, Ohio, 1968.

61. Schenkel, F. W.; and Anand, D. K.: Infrared Imaging in the 10-12.6 Micron Band from a Synchronous Altitude Earth Satellite. Report TG-948, (ASTIA No. AD 663265), Applied Physics Lab., Johns Hopkins Univ., 1967.

62. Soref, R. A: Extrinsic IR Photoconductivity of Si Doped with B, Al, Ga, P, As, or Sb., J. Appl. Phys., vol. 38, 1967, pp. 5201-5209.

63. Hummer, R. F.; and Malinowski, F. R.: Nimbus Five-Channel Scanning Radiometer. Proc. IRIS, August 1963, pp. 43-49.

64. Chase, S. C.; Kaplan, L. D.; and Neugebauer, G.: The Mariner II Infrared Radiometer Experiment. NASA CR-53078, 1964.

65. Mortensen, C. A.; et. al.: Dual-Channel Satellite Radiometer. Report AFCRL-65-491, Air Force Cambridge Research Labs., Bedford, Mass., 1965.

66. Stanfill, D. F.; et. al.: Horizon Scanner for Venus and Mars. NASA CR-56511, 1964.

67. Sachs, H.: Infrared Grating Spectrophotometer for Space Application. Proc. IRIS, October 1961, pp. 89-96.

68. Foshee, L. I.; Goldberg, I. L.; and Catoe, C. E.: The High Resolution Infrared Radiometer (HRIR) Experiment. Observations from the Nimbus I Meteorological Satellite, NASA SP-89, 1965.

69. Chase, S. C., Jr.: Infrared Radiometer for the 1969 Mariner Mission to Mars. Appl. Optics, vol. 8, 1969, pp. 639-643.

70. Anon.: A Day-Night High Resolution Infrared Radiometer Employing Two-Stage Radiant Cooling, Fifth Quarterly Report. Report ITTZL No. 67-1035, ITT Industrial Labs., Fort Wayne, Indiana, 1967.

71. Anon.: Design Study Report for Infrared Filter-Wedge Spectrometer Instrument for Nimbus D Satellite, First Quarterly Report. NASA CR-91079, 1967.

72. Gross, U. E.; and Weinstein, A. I.· A Cyrogenic-Solid Cooling System. Proc, IRIS, January 1964, pp. 23-28.

73. Falco, C. V.; and Oister, G.: Final Report for Microwave Radiometer Design and Development. NASA CR-92670, 1967.

74. Findlay, J. W.: Antennas and Receivers for Radio Astronomy. Vol. 2 of Advances in Radio Research, J. A. Saxton, ed., Academic Press, 1964, pp. 37-119.

75. Hiatt, R.; and Larson, R. W.: Survey of High Gain Broadband, Passive Deployable Antennas with Scanning Capabilities for Installation in a Manned Satellite. Memo 6734-502-M, University of Michigan, 1964.

76. Rider, L.; and Sung, R.: Radar Satellite Surveillance of Surface Shipping, Vol. II: Detailed Studies. Report No. ATR-68 (7090)-1, Vol. II (Secret), (ASTIA No. AD 388302 L), Aerospace Corporation, 1968.

77. Caruso, P. J.: and Ewing, L. R.: First Quarterly Report for Microwave Radiometer Design and Development. NASA CR-71883, 1966.

78. Johnson, H. A.: Detection, Sensitivity, and Related Statistics of Microwave Radiometry. Report 735, (ASTIA No. AD 822457), Naval Weapons Center Corona Labs., 1967.

79. Ewen, H. I.: State of the Art of Microwave and Millimeter Wave Radiometric Sensors. Proceedings of the Symposium on Electromagnetic Sensing of the Earth from Satellites, R. Zirklind, ed., Polytechnic Press of the Polytechnic Inst. of Brooklyn, 1967.

80. Matthei, W. G.: Recent Developments in Solid-State Microwave Devices. Tech. Rep. ECOM-2676, U. S. Army Electronics Command, Fort Monmouth, N. J., 1966.

81. Frazier, L., private communication, Autonetics Division, Philco-Ford Corporation, Anaheim, Calif.

82. Pascalar, H., private communication, Aerojet-General Corporation, El Monte, Calif.

83. Anon.: AN/AAR-33 Airborne Radiometer System. Report SJ 230-4980-1 (ASTIA No. AD 674780), Sperry Microwave Electronics Div., Sperry Rand Corp., Clearwater, Fla., 1967.

84. Titus, J. W.: An Unfolding Mechanically Scanned Antenna for a Satellite-Borne Radar. NRL Report 6480, (ASTIA No. AD 806473), Naval Research Lab., Washington, D. C., 1966.

85. Catoe, C.; Nordberg, W.; Thaddeus, P.; and Ling, G.: Preliminary Results from Aircraft Flight Tests of an Electrically Scanning Microwave Radiometer. NASA TM X-55893, 1967.

86. Somerlock, C. R.; and Krustins, J.: A Precision Spacecraft Radiometer for Hectometer Wavelengths. NASA TN D-4634, 1968.

87. Jones, D. E.: The Mariner II Microwave Radiometer Experiment. NASA CR-69916, 1966.

88. Staelin, D. H.: Passive Remote Sensing at Microwave Wavelengths. IEEE Proc., vol. 57, no. 4, April 1969, pp. 427-439.

89. Anon.: Peaceful Uses of Earth-Observation Spacecraft. Vol. III: Sensor Requirements and Experiments. Infrared and Optical Sensor Lab., Willow Run Labs., Inst. of Sci. and Tech., U. of Mich., 1966.

90. Silver, S.: Microwave Antenna Theory and Design. Dover Press, 1965.

91. Earth Resources Radar Team submission to NASA for review by Planetology Subcommittee, 1965 (R. K. Moore, U. of Kansas).

92. Baldauf, R. K.; and Leef, A. E.: Ocean Surveillance Radar Parametric Analysis, Case III - Synthetic Aperture Side-looking Radar. Memo. Report 1898 (Secret), (ASTIA No. 392079), Naval Research Lab., Washington, D. C., 1968.

93. Liskow, C. L.; and Young, W. E.: Interpretation of Synthetic-Aperture Radar Imagery. Tech. Report ECOM-00013-127 (Secret), (ASTIA No. 395317), U. S. Army Electronics Command, Fort Monmouth, N. J., 1968.

94. Angyal, S.; Hemenway, D. F.; and Zuro, S. A.: Ocean Surveillance Radar Parametric Analysis, Case II - Non-coherent Sidelooking Radar. Memo. Report 1874 (Secret), (ASTIA No. 391513), Naval Research Lab., Washington, D. C., 1968.

95. Proud, J. M.; Huber, H. J.; and Hirtle, W. W.: A Megawatt L-Band Travatron for Direct Generation of Nanosecond Pulses. Tech. Report No. RADC-TR-68-254, (ASTIA No. 838898), Rome Air Development Center, Air Force Systems Command, Griffiss Air Force Base, N. Y., 1968.

96. Arnovick, G. N.; et. al.: A Compendium of Multisensor Data for Evaluating and Predicting Tactical Reconnaissance Sensor Performance. Tech. Report No. RADC-TR-66-493 (Secret), (ASTIA No. 383699), Rome Air Development Center, Air Force Systems Command, Griffiss Air Force Base, N. Y., 1967.

97. Ho, W.; Kaufman, I. A.; and Thaddeus, P.: Laboratory Measurement of Microwave Absorption in Models of the Atmosphere of Venus. J. Geophys. Res., vol. 71, no. 21, Nov. 1966, pp. 5091-5108.

98. Reese, D. E.; and Swan, P. R.: Venera 4 Probes Atmosphere of Venus. Science, vol. 159, 25 Jan. 1968, pp. 1228-1230.

99. Jastrow, R.: The Planet Venus. Science, vol. 160, 28 1968, pp. 1403-1410.

100. Barrett, A. H.; and Staelin, D. H.: Radio Observations Venus and the Interpretations. Space Sci. Rev., vol. 3 no. 1, July 1964, pp. 109-135.

101. Evans, J. V.; and Hagfors, T.: Radio Astronomy. McGra Hill Inc., 1968.

102. Chandra, S.; and Srivastava, B. P.: Z. Astrophys., vol 1959, pp. 127-131.

103. Chang, D. B.; and Davis, L., Jr.: Synchrotron Radiatio as the Source of Jupiter's Polarized Decimeter Radiatio Astrophys. J., vol. 136, no. 2, Sept. 1962, pp. 567-581

104. Moore, R.K., private communication, U. of Kansas.

105. Brown, W., private communication, Jet Propulsion Lab., Cal. Tech.

106. Anon.: Experimental Definition - Volume II, Systems Analysis and Spacecraft Integration. Report LMSC-89549 II, Lockheed Missiles and Space Corp., Sunnyvale, Calif 1966.

107. Greenberg, J. S.: A Systems Look at Satellite-Borne High-Resolution Radar. RCA Review, Dec. 1967, pp. 679-709.